THE MORRIS-LECAR EQUATIONS WITH DELAY

ROBIN SWAIN

National Library
of Canada

Bibliothèque nationale
du Canada

Acquisitions and
Bibliographic Services

Acquisisitons et
services bibliographiques

395 Wellington Street
Ottawa ON K1A 0N4
Canada

395, rue Wellington
Ottawa ON K1A 0N4
Canada

In compliance with the Canadian Privacy Act some supporting forms may have been removed from this dissertation.

Conformément à la loi canadienne sur la protection de la vie privée, quelques formulaires secondaires ont été enlevés de ce manuscrit.

While these forms may be included in the document page count, their removal does not represent any loss of content from the dissertation.

Bien que ces formulaires aient inclus dans la pagination, il n'y aura aucun contenu manquant.

Canadä

THE MORRIS–LECAR EQUATIONS WITH DELAY

by

©Robin Swain

A Thesis Submitted to the School of
Graduate Studies in partial fulfillment of
the requirement for the degree of Master
of Science

Department of Mathematics and Statistics
Memorial University of Newfoundland

August 2003

St. John's, Newfoundland, Canada

Abstract

In this thesis we study the Morris–Lecar equations with delay. We modify the original Morris–Lecar ODE model to simulate delayed recurrent (inhibitory and excitatory) feedback in a appropriate neuro–muscular feedback loop. The loop consists of two neurons and a muscle fibre, whereby a neuron excites a muscle fibre, which influences a second neuron which in turn excites or inhibits the first neuron. The effects of feedback are described in terms of the voltage across the membrane of the muscle fibre. The model is formulated in terms of delay differential equations with a single discrete time delay to account for impulse conduction and synaptic delays, and assumes the muscle fibre possesses two noninactivating conductances, one for Ca^{2+} and one for K^+. Each single–ion conductance system with delay is studied before analysing the model with both conductances operational. A dynamical systems approach is used to analyse the bifurcation structure of the systems as the delay parameters (μ and τ) are varied, using both analytical and numerical techniques. The systems with delay are more complex than their non–delayed counterparts, and exhibit stability switching of equilibria, Hopf bifurcation leading to stable soft and hard oscillations, and multistability. The direction and stability of Hopf bifurcations are determined by applying the normal form theory and

the centre manifold theorem. Biophysical interpretation of results are also included. Applicability and limitations of the model are discussed, along with suggestions for future research.

Acknowledgments

List of Figures

List of Tables

Contents

Chapter 1

Introduction

Physiological systems use feedback as a control mechanism to regulate important functions. Virtually all essential processes employ feedback, including enzyme synthesis, production of red blood cells, and neural interactions. A feedback model for the regulation of enzyme synthesis was introduced by Goodwin [15], and modified by Landahl [23] and MacDonald [27]. Models describing the control of production of red blood cells were initially studied by Chow [5], and subsequently modified by Mackey and Glass [28]. The subject of neural feedback loops has a rich and extensive literature. A survey of results and literature in this area appears in [2]. As most biological cycles and interactions involve electrical and/or chemical signals from the nervous and endocrine systems, most feedback loops are subject to temporal delays arising from transport and processing of such signals. For a nice overview of delays and feedback in physiological systems, see [1] and references therein.

Delay differential equations (DDEs) provide an appropriate setting in which to formulate models with inherent time delay, since they incorporate non-

1

instantaneous interactions. Many models have been developed which demonstrate the profound influence which time delays can have on the qualitative behavior of biological systems. Delay equations are capable of richer dynamics than ordinary differential equations (ODEs). Introducing a delay to an ODE system can lead to instabilities in the solutions, and even lead to oscillations or chaotic behavior in such models.

In this thesis, we investigate an electrophysiology model with delayed recurrent feedback, a phenomenon commonly encountered in the nervous system used to coordinate electrical and mechanical processes. In particular, we consider a neuro–muscular feedback loop involving two neurons and a muscle fibre. An excitatory neuron E activates a muscle fibre M, which in turn influences a second neuron (or interneuron) I, that either excites or inhibits the firing of E. Due to finite conduction velocities and synaptic transmission, the influence of I on E and then E on M, is not instantaneous, and depends on the activity of M at a time τ in the past. The effects of the recurrent feedback are studied by examining the potential difference (voltage) across the cellular membrane of the muscle fibre. The differential equations used to describe the voltage across the muscle fibre membrane are based on the Morris–Lecar Equations [24]. The original Morris–Lecar model is based on the historical model developed by Hodgkin and Huxley [21] to describe conduction and excitation in nerve. In the following sections, we introduce both the Hodgkin–Huxley and Morris–Lecar models, and formulate our model of the Morris–Lecar equations, modified to simulate delayed recurrent feedback.

1.1 The Hodgkin–Huxley Equations

In the 1950's, Hodgkin and Huxley [21] developed a physiologically based, quantitative model describing the propagation of an electric signal along a squid giant axon. The first of its kind, their model accurately detailed the dynamics of the action potential from a phenomenological viewpoint, and is therefore capable of explaining the behavior of excitable cells. Excitable cells, such as neurons and muscle cells, respond to a sufficiently strong stimulus (applied current or synaptic input) whereby the membrane potential goes through a large excursion before returning to rest. This large excursion is an action potential, which is an electrical signal. The ground–breaking work of Hodgkin and Huxley was an important landmark, and not only had a major influence on electrophysiology, but on the applied mathematics of excitable systems as well.

The general approach taken by Hodgkin and Huxley was to model the cellular membrane as a capacitor in parallel with an ionic current. In particular, the Hodgkin–Huxley neuron model incorporates two nonlinear voltage– and time–dependent ion conductances, one to describe the fast sodium (Na^+) current, and one for the slow potassium (K^+) current. The remaining ions present, which play no significant role, are lumped together into a membrane leakage conductance. The parameters and functions governing these conductance systems were measured and fitted from empirical data based on space–clamp and voltage–clamp experiments conducted by Hodgkin and Huxley. The full nonlinear system involves four ODEs, one describing the membrane potential which is coupled to three auxiliary equations used to describe membrane gating variables which affect the ionic conductances (commonly known as "relaxation

variables"). The full Hodgkin–Huxley system is given by

$$C\dot{V}(t) = -\bar{g}_{\text{Na}}m^3 h(V - V_{\text{Na}}) - \bar{g}_{\text{K}}n^4(V - V_{\text{K}}) - \bar{g}_{\text{L}}(V - V_{\text{L}}) + I_0,$$

$$\dot{m}(t) = \alpha_m(V)(1 - m) - \beta_m(V)m,$$

$$\dot{n}(t) = \alpha_n(V)(1 - n) - \beta_n(V)n,$$ \quad (1.1.1)

$$\dot{h}(t) = \alpha_h(V)(1 - h) - \beta_h(V)h.$$

The functions α and β describe the kinetics of the relaxation variables, and are logistic and exponential functions given by

$$\alpha_m(V) = 0.1\frac{25 - V}{e^{\frac{25-V}{10}} - 1},$$

$$\beta_m(V) = 4e^{-\frac{V}{18}},$$

$$\alpha_h(V) = 0.07e^{-\frac{V}{20}},$$

$$\beta_h(V) = \frac{1}{e^{\frac{30-V}{10}} + 1},$$ \quad (1.1.2)

$$\alpha_n(V) = 0.01\frac{10 - V}{e^{\frac{10-v}{10}} - 1},$$

$$\beta_n(V) = 0.125e^{-\frac{V}{80}}.$$

In (1.1.1), V is the membrane potential, m, n, and h are ion gating variables, I_0 is the applied current, and V_{Na}, V_{K}, V_{L} are equilibrium potentials. The sodium conductance is a function of the m and h gating variables, and is of the form $g_{\text{Na}} = \bar{g}_{\text{Na}}m^3 h$. Here, the $\bar{g}_{\text{Na}}$ is a conductance constant and the term $m^3 h$ describes the fraction of open Na$^+$ channels, where each channel consists of three m gates and a single h gate. Each potassium channel consists of four n gates, and so the n^4 term indicates the fraction of open K$^+$ channels. The overall potassium conductance is described by the equation $g_{\text{K}} = \bar{g}_{\text{K}}n^4$. Furthermore, the sodium conductance is inactivating, meaning that when the membrane potential is high, the Na$^+$–ion gates close to shut down the sodium

conductance. The variable m is the sodium activation variable, and h is the inactivation variable. The potassium conductance does not display this feature, and so this conductance is noninactivating, with n as the activation variable.

Mathematical analysis of the Hodgkin–Huxley system (1.1.1) is difficult, since the system is 4-dimensional. However, many researchers have modified the equations so that they are easier to study, but successfully capture the dynamics of the full system. One route popularized by FitzHugh [12, 13], and Nagumo [31] in the 1960's involves analysing a 2-dimensional analogue of (1.1.1), by taking advantage of the different time scales of the two conductance systems. The V and m variables are fast–acting while n and h are slow. This allows one to reduce the dimension and consider a fast–fast sub–system, where V and m are varied and n and h are essentially fixed, and a fast–slow sub–system, where the slow variables are combined and the fast variable m is considered to act instantaneously. There has been considerable work done on both of these simplified systems, and both successfully reduce the dimension of the system while retaining some of the key features. There is a vast literature devoted to the analysis of the Hodgkin–Huxley equations, and the bifurcation structure of the model has been investigated in detail. Refer to [33] and references therein for more details.

1.2 The Morris–Lecar Equations

The Morris–Lecar model [24] is a Hodgkin–Huxley type model developed to describe voltage oscillations in barnacle giant muscle fibre. The model employs two nonlinear, non–inactivating, voltage–dependent conductance systems, one

for calcium Ca^{2+} and one for potassium K^+. Calcium and potassium play important roles in electrical activity in muscle, in contrast to sodium and potassium in the Hodgkin–Huxley neuron model. Like the Hodgkin–Huxley model, the Morris–Lecar model is quantitative and physiologically based, developed using voltage– and space–clamp experimental techniques. The system consists of the following three non–linear differential equations

$$C\frac{dV}{dt} = -g_{Ca}m(V - V_{Ca}) - g_{K}n(V - V_{K}) - g_{L}(V - V_{L}) + I$$
$$\dot{m}(t) = \lambda_m(V)\left[m_\infty(V) - m\right] \tag{1.2.1}$$
$$\dot{n}(t) = \lambda_n(V)\left[n_\infty(V) - n\right],$$

where $V = V(t)$ represents the voltage across the membrane, and the variables $m = m(V(t))$ and $n = n(V(t))$ represent the fraction of open Ca^{2+} and K^+ channels, respectively. The functions $\lambda_m(V)$, $\lambda_n(V)$, $m_\infty(V)$ and $n_\infty(V)$, fitted using experimental data, are given by

$$\begin{cases} \lambda_m(V) = \overline{\lambda_m}\cosh\left(\dfrac{V - V_1}{2V_2}\right) \\[3mm] m_\infty(V) = \dfrac{1}{2}\left[1 + \tanh\left(\dfrac{V - V_1}{V_2}\right)\right] \end{cases} \tag{1.2.2}$$

$$\begin{cases} \lambda_n(V) = \overline{\lambda_n}\cosh\left(\dfrac{V - V_3}{2V_4}\right) \\[3mm] n_\infty(V) = \dfrac{1}{2}\left[1 + \tanh\left(\dfrac{V - V_3}{V_4}\right)\right]. \end{cases} \tag{1.2.3}$$

The gating variables m and n are analogous to the m and n activation variables in Equation (1.1.1), but here each calcium and potassium channel are both composed of a single gate. The model parameters are listed below, and parameter values used in [24] are based on experimental data.

List of Model Parameters

V = membrane potential in millivolts, (mV)

m, n = fraction of open Ca^{2+} and K^+ channels, respectively

g_L, g_K, g_{Ca} = instantaneous conductance values for leak, K^+, and Ca^{2+} pathways, respectively ($mmho/cm^2$)

V_L, V_K, V_{Ca} = equilibrium potentials corresponding to leak, K^+, and Ca^{2+} conductances, respectively (mV)

$m_\infty(V), n_\infty(V)$ = fraction of open Ca^{2+} and K^+ channels at steady state

$\lambda_m(V), \lambda_n(V)$ = rate constant for opening of Ca^{2+} and K^+ channels, (s^{-1})

$\overline{\lambda_m}, \overline{\lambda_n}$ = maximum rate constants for Ca^{2+} and K^+ channel opening (s^{-1})

V_1, V_3 = potentials at which $m_\infty = 0.5, n_\infty = 0.5$, respectively (mV)

V_2, V_4 = reciprocal of slope of voltage dependence of m_∞ and n_∞, resp. (mV)

C = membrane capacitance, $(\mu F/cm^2)$

I = applied current $(\mu A/cm^2)$

Morris and Lecar compared numerical simulations of (1.2.1) to their own experimental results, and found that they were in good agreement. Therefore their model had the power to accurately describe voltage responses of muscle fibre. To simplify the analysis, they first considered separately the dynamics of each conductance system in isolation from the other. This was done to gauge the contribution of each conductance system to the model with both systems operational. To prove that voltage oscillations are possible with both conductance systems active, Morris and Lecar successfully reduced the dimension of the system to two, and in doing so were able to invoke the theory of Poincaré and Bendixson. They were also able to establish domains of oscil-

latory behavior by varying certain model parameters, and to interpret their results biologically. Mathematical analysis of the original ion conductance systems, as well as the full two–dimensional Morris–Lecar model, is included in this thesis for comparison with the Morris–Lecar model with delay.

The Morris–Lecar model, although relatively simple with only two non-inactivating conductance systems, is quite versatile and exhibits a diverse spectrum of behavior when considered over a broad range of parameters. These include bistability and hysteresis, excitability and threshold behavior, and beating and bursting oscillations. A detailed study of these behaviors, as well as the bifurcation structure of the Morris–Lecar model, is conducted by Rinzel and Ermentrout in [34]. Tsumoto *et al.* further investigate bifurcations of the Morris–Lecar model in [39]. Most work done using this model has been done treating I, the applied current, as a bifurcation parameter. External stimulus, while artificial, can effectively simulate excitatory synaptic input.

1.3   Formulation of the Model

The model we propose is derived from the pre–existing Morris–Lecar ODE model. We intend to modify the Morris–Lecar equations by adding a suitable delay term to simulate the effects of delayed recurrent feedback . Here, we discuss physiological models with delayed feedback as a means to motivate our modification of the Morris–Lecar equations.

The phenomenon we consider is a time–delayed recurrent loop composed of a muscle fibre and two neurons, depicted schematically in Figure 1.1. The excitatory nerve cell E initiates an action potential which stimulates the muscle

fibre M. If the signal received by the fibre M is above a certain threshold, then an action potential is generated, and will propagate along with membrane of the muscle fibre, causing muscle contraction. The depolarization of the membrane excites the interneuron I in close proximity to the muscle fibre. The synapses of I impinge upon E after a time delay τ, and either excite or inhibit it. This completes the feedback loop, and in this way contraction of the muscle fibre is controlled through delayed feedback.
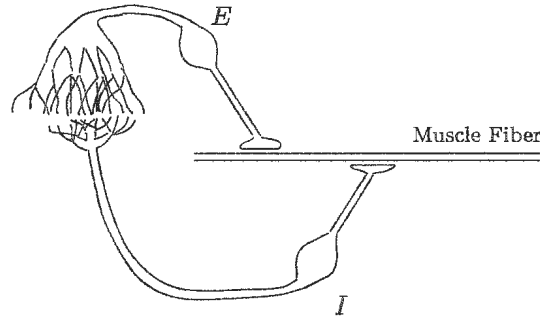
Figure 1.1: Schematic diagram representing the time–delayed recurrent neuro-muscular feedback loop.

We note that the phenomenon of recurrent inhibition is more commonly observed in physiological systems than excitation [29, 32]. Plant [32] comments that recurrent neural excitation might be responsible for causing seizures in the hippocampus. This might indicate that, in some physiological systems, recurrent excitation can have a destructive rather than a mediating influence, and may lead to unstable behavior.

A model describing recurrent neural feedback in a system of two neurons

is considered by Plant [32] by implementing a delay into the FitzHugh equation [13]

$$\dot{v} = v - \frac{1}{3}v^3 - w + I,$$
$$\dot{w} = \rho[v + a - bw].$$

(1.3.1)

In (1.3.1), v represents membrane potential, w is an inactivation variable, a, b, and ρ are parameters, and I represents the membrane current. In this model, neuron 1 excites neuron 2, which in turn excites or inhibits neuron 1. To simulate synaptic feedback, Plant proposes the following modification:

$$\dot{v}(t) = v(t) - \frac{1}{3}v^3(t) - w(t) + \mu[v(t - \tau) - v_0],$$
$$\dot{w}(t) = \rho[v(t) + a - bw(t)].$$

(1.3.2)

In (1.3.2), the magnitude of μ measures the strength of the feedback, and $\mu > 0$ represents excitatory feedback, while $\mu < 0$ inhibitory feedback. The time delay $\tau > 0$ is to account for the delay due to conduction time(s) and synaptic delay. The appearance of v_0 in the delay term $\mu[v(t - \tau) - v_0]$ results from the assumption that the magnitude of the current induced by the feedback is proportional to the distance of the voltage v from the resting potential v_0 of the system in the absence of feedback. Furthermore, Plant considers only "moderate" values of μ and τ, and imposes the restriction

$$\tau > \frac{1}{\rho b},$$

where $\frac{1}{\rho b}$ measures the relaxation time of the system. This is based on an assumption that combined synaptic and conduction delays in a neural feedback circuit are greater than the duration of a single action potential.

In his investigation of (1.3.2), Plant focused on equilibrium point stability for $\tau > 0$, and treating μ and τ as bifurcation parameters, on the appearance of periodic solutions via Hopf bifurcation. Direction and stability of the Hopf bifurcation(s) was also studied, using the normal form method and the center manifold theory developed by Hassard, Kazarinoff and Wan [20]. The results indicated that Hopf bifurcation occurs in the presence of both inhibitory and excitatory feedback, and both bifurcations are supercritical and branch to stable oscillations. Furthermore, the Hopf bifurcation structure of the model depends on the pair of delay parameters μ and τ. Similar results for both $\mu > 0$ and $\mu < 0$ are most likely due to symmetry in this simple system. Stable oscillations resulting from delayed recurrent inhibition are a result of anode break excitation, a commonly encountered phenomenon whereby the membrane rebounds from a strong hyperpolarization to generate an action potential upon removal of that hyperpolarization [32]. Plant comments that, while this model and assumptions are restricted in their application to actual physiological systems, it does successfully describe the dynamics of recurrent neural feedback, and does provide insight into the behavior of more complex models.

To investigate the properties of multistability arising in delayed recurrent loops, Foss *et al.* [14] looked at a simple integrate–and–fire neuron model with delay, and, more notably, the classic Hodgkin–Huxley model with delay. Interested primarily in recurrent inhibition between a population of two neurons, their research largely consisted of numerical simulations to study the possibility of encoding memory into temporal patterning of neural spike trains. They found that multistability in delayed recurrent loops can arise from two different

mechanisms, depending on whether the neuron is in the excitable or periodic regime in the absence of recurrent input, which is determined by the value of the applied input current. They considered a loop with a time delay τ, and commented on results obtained by selecting τ less than and greater than the response time of the system. However, their main interest was to identify how changes in the initial function ϕ on the delay interval $[-\tau, 0]$ propagate in the solution, where ϕ is given the form of neural spike trains.

The modification to the Hodgkin–Huxley equations Foss *et al.* proposed to simulate this delayed recurrent feedback was the following

$$\begin{aligned}
C\dot{V}(t) &= -g_{\text{Na}}m^3h(V - V_{\text{Na}}) - g_{\text{K}}n^4(V - V_{\text{K}}) - g_{\text{L}}(V - V_{\text{L}}) + I_0 \\
&\quad - \mu V(t - \tau) \\
\dot{m}(t) &= \alpha_m(V)(1 - m) - \beta_m(V)m \\
\dot{n}(t) &= \alpha_n(V)(1 - n) - \beta_n(V)n \\
\dot{h}(t) &= \alpha_h(V)(1 - h) - \beta_h(V)h,
\end{aligned} \tag{1.3.3}$$

where the functions α, β, variables and model parameters are given in (1.1.2). The term $-\mu V(t - \tau)$ is a feedback function which simulates delayed recurrent feedback with time delay $\tau > 0$, $|\mu|$ denotes the strength of the feedback, which is inhibitory for $\mu > 0$, and excitatory for $\mu < 0$. Note that the sign convention of μ is opposite to that employed by Plant [32]. System (1.3.3) represents the simplest modification of the original Hodgkin–Huxley system to incorporate delayed recurrent feedback.

Mackey and an der Heiden investigate the dynamics of recurrent inhibition in [29]. They propose a model for a recurrent inhibitory neural feedback system using nonlinear DDEs. The model consists of three populations of neurons: presynaptic fibres which excite the postsynaptic cells, and inhibitory

interneurons which are activated by the postsynaptic cells. In turn, the inhibitory interneurons inhibit the postsynaptic cells. In particular, Mackey and an der Heiden model the dynamics of the inhibitory post synaptic potential (IPSP), to relate the frequency of arrival of action potentials at the interneuron synaptic terminals to the frequency of generation of action potentials in the postsynaptic cell. The feedback loop is delayed, since a finite time delay is required for activity in the postsynaptic cell to be translated into activity at the synaptic terminals of the inhibitory interneuron.

As a specific example, recurrent inhibitory feedback with delay is used to describe the excitatory–inhibitory neuronal interactions involving three populations of neurons of the hippocampus. Here, the presynaptic mossy fibres excite the CA3 pyramidal cells, which in turn excite the interneural basket cells. The basket cells then inhibit the pyramidal cells via the neurotransmitter GABA (γ–amino butyric acid) after a finite time delay $\tau(>0)$, to account for impulse conduction and synaptic transmission. Their model is of the form

$$\frac{dx}{dt} = f(x(t - \tau)) - ax(t), \tag{1.3.4}$$

where the feedback function f is a non–monotone, "humped" function of $x(t - \tau)$. This implies that the the feedback is of mixed type, a combination of both positive and negative feedback. Using analytical and numerical methods, they detected interesting behavior, including periodicity and deterministic chaos. The model proposed in [29] does not simulate exactly the same type of feedback as we are interested in, nor does it directly involve voltage across cellular membranes. It does, however, involve the process of recurrent inhibition in a population of more than two neurons, and therefore serves as a good example of this process which we hope to implement in our model.

Longtin and Milton [26] use a nonlinear DDE to model the human pupil light reflex with negative feedback. This reflex is governed by a neural feedback control mechanism, and exhibits a wide range of dynamical behaviors.

The feedback loop operates as follows. Pupil size is controlled by a balance between constricting and dilating mechanisms. Constriction is caused by contraction of the pupillary constrictor muscle. This muscle is innervated by parasympathetic fibres, and is controlled by the Edinger–Westphal motor nucleus (in the oculomotor complex in the midbrain). According to Longtin and Milton, retinal light flux is transformed, after a time delay τ_r, into neural action potentials which travel along the optic nerve. The afferent neural action potential rate gives rise to an efferent neural signal which is produced by the Edinger–Westphal nucleus after a time delay, τ_t. The efferent neural signal is conducted to the pupillary constrictor muscle by parasympathetic fibres which generate muscle action potentials via the neurotransmitter acetylcholine. This initiates contraction of the pupillary constrictor muscle, after a time delay τ_m. Pupil dilation is then regulated by two neural mechanisms, one which operates by inhibition of the activity of the Edinger–Westphal nucleus by sympathetic fibres. This inhibition then decreases the efferent neural signal which initiates contraction of the pupillary constrictor muscle.

Thus, the pupil–light reflex functions as a time–delayed negative feedback system. This system involves two populations of neurons (the Edinger–Westphal nucleus along with the parasympathetic fibres, and the sympathetic fibres) and a muscle fibre, and controls the size of the pupil, thereby regulating the amount of light which enters the eye. The total time delay of the model, the pupil latency time, is simply the sum of the time delays discussed, *i.e.*

$\tau = \tau_r + \tau_t + \tau_m$. The nonlinear DDE model developed by Longtin and Milton is of the form (1.3.4), and stability and bifurcation analysis of their model revealed that stable periodic solutions arise via supercritical Hopf bifurcation as the equilibrium point of the system loses stability. This was observed in both cases of symmetric and asymmetric pupil light reflex. While no additional bifurcations were detected after the Hopf bifurcation in numerical simulations, they point out that other bifurcations leading to additional periodic, quasiperiodic, and chaotic dynamics may occur as parameters are varied.

The model formulated and analysed in [26] does not study the pupil–light reflex in terms of voltage across the membrane of the pupillary constrictor muscle. However, the reflex does involve neuro–muscular interactions in a delayed negative feedback loop, involving multiple neurons (or populations of neurons) and the pupillary constrictor muscle. This is, in principle, the anatomical phenomenon we are hoping to model by adding a delay to the Morris–Lecar equations, and therefore represents an actual physiological process to which our model might be applied. It also provides insight into the stability and bifurcation analysis of a physiological model involving nonlinear DDEs.

These observations suggest that an appropriate modification to the Morris–Lecar equations to simulate delayed recurrent feedback is

$$C\frac{dV}{dt} = -g_{Ca}m(V - V_{Ca}) - g_K n(V - V_K) - g_L(V - V_L) + \mu V(t - \tau)$$
$$\dot{m}(t) = \lambda_m(V)\left[m_\infty(V) - m\right] \tag{1.3.5}$$
$$\dot{n}(t) = \lambda_n(V)\left[n_\infty(V) - n\right]$$

where the functions $m_\infty(V)$, $n_\infty(V)$, $\lambda_m(V)$ and $\lambda_n(V)$ are given in (1.2.2), (1.2.3), and model parameters are introduced in the List of Model Parameters

in section 1.2. The term $\mu V(t - \tau)$ represents the feedback function of the system, $F(V(t - \tau)) = \mu V(t - \tau)$. The parameter $|\mu|$ measures the strength of the feedback signal: $\mu > 0$ represents excitatory feedback, for which the feedback function is monotone increasing, while F is monotone decreasing for $\mu < 0$, which corresponds to inhibitory feedback. In either case, the feedback signal is subject to a time delay $\tau > 0$, which recognizes the non–instantaneous interactions associated with the feedback. Note that the applied current, I, which plays and important role in the original Morris–Lecar equations (1.2.1) without delay, does not appear in the delay model (1.3.5). Therefore, our analysis of the Morris–Lecar model with delayed recurrent feedback is carried out in the absence of applied current. This is done to limit the number of parameters which influence the system. Furthermore, we consider two distinct types of model parameters. Static parameters, which we do not vary, are those which are described in the List of Model Parameters. For these parameters we select a standard reference set of typical parameter values, cited in [24]. The dynamic parameters, which we do vary in our analysis, are those associated with the additional feedback term in (1.3.5), namely μ and τ. We wish to study the dynamics of the model as these parameters are varied, and in doing so we hope to isolate the effects of the delayed recurrent feedback, and compare them to the original model without delay. We note that system (1.3.5) does not account for spatio–temporal aspects of a distributed muscle fibre membrane. Therefore the investigation of the model in this thesis applies only to a space–clamped patch of sarcolemma membrane.

Of course, there are limits on the values of μ and τ for which (1.3.5) could be considered physiologically realistic. For example, the strength of the

feedback signal $|\mu|$ would certainly be bounded, as well as the value of the time delay τ. However, establishing suitable parameter ranges on μ and τ is of secondary concern here, and the main goal is to study the dynamics of the model, to determine whether a physiologically based, quantitative model such as the Morris–Lecar equations (1.2.1) can support delayed recurrent feedback. Therefore, in our investigation we do not impose too many restrictions on these dynamic parameters. In particular, we consider $\mu \in \mathbb{R}$, and only require that the time delay be positive, $\tau > 0$. Note that we do not impose the restriction that τ be larger than the response time of the system, as Plant does in [32]. Since we are using a specific set for the other model parameters, the results obtained are largely restricted to that particular set. However, in the analysis, an attempt is made to generalize the results to an arbitrary set of model parameters (which obey certain physiological criteria) whenever possible.

System (1.3.5) is a set of three differential equations, two ODEs both coupled to a DDE with a single discrete time delay. The results obtained from other nonlinear delay differential equation models describing delayed feedback indicate the presence of rich dynamics and bifurcation structure, with multistability and periodicity being the most common and widely observed. In our analysis of (1.3.5), we interest ourselves primarily in the number, location, and stability of equilibria of the system, as μ and τ are varied. To investigate these properties we use both analytical and numerical techniques. Also, since the main motivation behind the development of the original Morris–Lecar model was to describe voltage oscillations in muscle fibre, and given the propensity to which similar models display periodicity, we take a vested interest in examining the potential for oscillations in the model with delay. Of course, the

presence of additional dynamical phenomena arising as a result of the feedback will also be addressed.

In [24], Morris and Lecar first analyse the potassium and calcium conductance systems in isolation before considering the model with both conductances operational. Determining the dynamics of each sub–system before combining them provides insight into the contribution of each component to the full model. Then, Morris and Lecar study a reduced, two–dimensional model which incorporates both nonlinear, voltage-dependent potassium and calcium conductance systems. This reduction, described in Chapter 4, simplifies the analysis of the model dynamics, by confining them to the (V, n)–phase plane. In the same fashion, we follow similar steps in our investigation of the model with delay, in that we provide a detailed analysis of each isolated conductance system, and then turn to the two–dimensional reduced model employing both conductances.

With the derivation of the modeling equations in place, we present a brief discussion of DDEs before our analysis of the Morris–Lecar equations with delay.

1.4 Delay Differential Equations (DDEs)

Autonomous ODEs with independent variable time t are of the form

$$\dot{x}(t) = f(x(t), \eta), \qquad (1.4.1)$$

where $x(t) \in \mathbb{R}^n$, $\eta \in \mathbb{R}^k$, and $f : \mathbb{R}^n \times \mathbb{R}^k \to \mathbb{R}^n$. In (1.4.1), $\eta \in \mathbb{R}^k$ is a k–dimensional vector containing real parameters, and the n components of $x(t)$ are all real–values functions of t. Within systems of ODEs, both the

state variable x and its derivative $\dot{x}$ depend only on t, the current time of the system, and so interactions between the state of the system and rate of change of that state with respect to t are assumed to be instantaneous. Furthermore, solutions of (1.4.1) are uniquely determined by the value of $x(t)$ at some fixed time t_0, denoted by $x(t_0) = x_0$, assuming f is moderately well–behaved, at least Lipschitz continuous. Since (1.4.1) is autonomous, any initial time t_0 should suffice, however for our purposes we shall consider $t_0 = 0$. For (1.4.1), the phase space is $\mathbb{R}^n$, which is real and has finite dimension n.

However, the story becomes much more interesting if we incorporate a time delay into the system, and allow the state variable x to depend not only on the current time t of the system, but also on some time(s) in the past. This can be done in a number of different ways. The entire history of the system can be considered, which results in a system of integro–differential equations, and the importance of certain delay times or intervals can be specified by an appropriate kernel, or distribution function(s). If the state variable x depends on a finite interval of time in the past, a system of distributed delay equations results. Thirdly, if x only depends on one or more specific time values in the past, then we obtain a system of DDEs with discrete time delay(s). All three types mentioned are all part of a larger class of equations known as functional differential equations. In this paper, we only consider the latter, that is, autonomous delay equations with a finite number of discrete time delay(s).

Delay equations of this type are of the form

$$\dot{x}(t) = f(x(t), x(t - \tau_1), x(t - \tau_2), \ldots, x(t - \tau_m), \eta), \qquad (1.4.2)$$

where $x(t) \in \mathbb{R}^n$, $\eta \in \mathbb{R}^k$, and $f : \mathbb{R}^{n \times (m+1)} \times \mathbb{R}^k \to \mathbb{R}^n$. In this case, the state

variable x depends not only the current time of the system, t, but on the m discrete times in the past, denoted by $\tau_1, \tau_2, \ldots, \tau_m$. Note that the derivative of the state variable, $\dot{x}$, depends only on the current time of the system and not on times in the past. Equations where the (highest order) derivative depends on time(s) in the past are called neutral functional differential equations, and are not considered here. Due to the dependency on the past, rather than prescribing a single value of $x(t)$ at a fixed time t_0, an initial function $\phi(\theta)$, $\theta \in [-\tau, 0]$, must be specified on an interval of length $\tau = \max_{i=1,\ldots,m} \{\tau_i\}$ to ensure uniqueness of solutions. The initial function segment belongs to $C = C([-\tau, 0], \mathbb{R}^n)$, the infinite–dimensional function space of continuous functions mapping the maximal delay interval $[-\tau, 0]$ into $\mathbb{R}^n$. If we integrate (1.4.2) to some time t, the function $x_t \in C$ with $x_t(\theta) = x(t - \theta)$, $\theta \in [-\tau, 0]$ defines the state of the system which then uniquely determines the future of the system. In this manner, delay equations of the form (1.4.2) are infinite–dimensional systems, and the phase space is C, an infinite–dimensional function space.

A consequence of the transition from finite– to infinite–dimensional phase space is that DDEs are capable of exhibiting richer dynamics than ODEs. For example, a scalar delay equation may be capable of periodic, quasi–periodic, and chaotic behavior, which is not possible for scalar ODEs. This also implies that incorporating a delay into a system of ODEs may significantly complicate the dynamics. One of the most well–known instances of this involves the logistic equation, whereupon introduction of a delay leads to periodic solutions if the delay is above a certain threshold, which depends on the parameters of the system. In fact, periodicity is commonly observed as a result of introducing a delay into a system of ODEs, and usually arise via Hopf bifurcation in the

system.

Consider next an example which will play a prominent role in this paper, the all–potassium conductance system of the Morris–Lecar equations:

$$C\dot{V}(t) = -g_{\mathrm{L}}(V - V_{\mathrm{L}}) - g_{\mathrm{K}}n(V - V_{\mathrm{K}})$$
$$\dot{n}(t) = \lambda_n(V)\left[n_\infty(V) - n\right], \qquad (1.4.3)$$

where $n_\infty(V)$, and $\lambda_n(V)$ are given in a previous section. This planar system consists of two coupled ODEs, with $x(t) = [V(t), n(t)]^{\mathrm{T}} \in \mathbb{R}^2$, $\eta = [g_{\mathrm{L}}, g_{\mathrm{K}}, V_{\mathrm{L}}, V_{\mathrm{K}}, V_3, V_4, C, \overline{\lambda_n}]^{\mathrm{T}} \in \mathbb{R}^8$. Therefore, an initial condition $V(0) = V_0$, $n(0) = n_0 = n_\infty(V_0)$ uniquely determines the solution for all time $t \geq 0$, and the dynamics of the system are confined to the (V, n)–phase plane. Furthermore, in the phase plane, trajectories must satisfy properties common to all ODEs, that is they must cross nullclines in a certain manner, they cannot cross each other, a closed curve in the phase space represents a periodic solution, etc. To simulate delayed recurrent feedback in the all–potassium system (1.4.3), we add a delay term to obtain

$$C\dot{V}(t) = -g_{\mathrm{L}}(V - V_{\mathrm{L}}) - g_{\mathrm{K}}n(V - V_{\mathrm{K}}) + \mu V(t - \tau)$$
$$\dot{n}(t) = \lambda_n(V)\left[n_\infty(V) - n\right]. \qquad (1.4.4)$$

Thus we now have a single DDE with a single discrete time delay $\tau > 0$ coupled to an ordinary differential equation. There are still only two equations in the system, but because of the $\mu V(t - \tau)$ term, to solve this system we must prescribe initial functions $V(\theta)$, $n(\theta) = n_\infty(V(\theta))$, $\theta \in [-\tau, 0]$ on the delay interval $[-\tau, 0]$, and so the system is indeed infinite–dimensional. As such, the dynamics of the system are no longer confined to the (V, n)–phase plane. But we may project the system onto this plane, and in doing so gain some valuable

insight into the behavior of the system. Steady state solutions, or equilibrium points, (V^*, n^*) of the system are independent of the value of the delay τ, and are merely given by the intersection points of the nullclines of (1.4.4) with $\tau = 0$ in the (V, n)–plane. Studying the nullclines in this plane therefore reveals the number and value of steady state solutions of (1.4.4). However, it is important to realize that trajectories of the DDE (1.4.4) in the phase plane are not subject to the same rules as those of the ODE (1.4.3), and so closed curves in the plane do not necessarily represent periodic solutions, and trajectories do not have to cross nullclines in a specific manner, and can cross each other in the plane. In the actual infinite–dimensional phase space, trajectories may not cross each other, however, but may appear to in the (V, n)–plane since this is merely a projection of the trajectory onto the plane. To analyse periodic solutions, we will make use of the "delay phase plane" of (1.4.4), a convenient construction which plots the delay $V(t - \tau)$ versus $V(t)$. Closed curves in the delay phase plane are indicative of periodic orbits of the system. In going from (1.4.3) to (1.4.4) we merely included a single discrete delay term. We shall see later on that this subtle addition significantly enriches the dynamics of the all–potassium system of the Morris–Lecar equations.

This section has briefly discussed DDEs, and in doing so introduced the setting for our investigation of the Morris–Lecar equations with delay. Some additional properties of delay equations are presented throughout the course of our study, when these details are pertinent.

Chapter 2

The all–K$^+$ Conductance System

The equations describing the all–K$^+$ conductance system with delay ($\mu \neq 0$) are

$$C\dot{V}(t) = -g_{\mathrm{L}}(V - V_{\mathrm{L}}) - g_{\mathrm{K}}n(V - V_{\mathrm{K}}) + \mu V(t - \tau)$$

$$(2.0.1)$$

$$\dot{n}(t) = \lambda_n(V)\left[n_\infty(V) - n\right],$$

where $n_\infty(V)$, and $\lambda_n(V)$ are given by

$$
\begin{cases}
n_\infty(V) = \dfrac{1}{2}\left[1 + \tanh\left(\dfrac{V - V_3}{V_4}\right)\right], \\[4mm]
\lambda_n(V) = \overline{\lambda_n}\cosh\left(\dfrac{V - V_3}{2V_4}\right).
\end{cases}
\qquad (2.0.2)
$$

Here the Ca^{2+}–conductance system has been blocked, so that $m = 0$. Before investigating the all–potassium system with delay, we address the original all–potassium conductance system without delay.

2.1 The all–K$^+$ Conductance System without Delay

In their model without delay, Morris and Lecar found that muscle fibres in Ca^{2+}–free solutions produce no voltage oscillations, even in the presence of external applied current. Their investigation revealed that the all–K$^+$ system exhibits a graded response with a transient peak followed by a decay to a voltage plateau. Consider system (2.0.1) with $\mu = 0$:

$$C\dot{V}(t) = -g_{\text{L}}(V - V_{\text{L}}) - g_{\text{K}}n(V - V_{\text{K}})$$

(2.1.1)

$$\dot{n}(t) = \lambda_n(V)\left[n_\infty(V) - n\right],$$

with $n_\infty(V)$ and $\lambda_n(V)$ as given in (2.0.2). This is simply the equations describing the all–K$^+$ conductance system without delay, studied by Morris and Lecar. We shall show that this system admits a single stable equilibrium point (node). Equilibria (V^*, n^*) are given by the intersection of the nullclines

$$V(n) = \frac{g_{\text{L}}V_{\text{L}} + g_{\text{K}}V_{\text{K}}n}{g_{\text{L}} + g_{\text{K}}n} \quad \text{and} \quad n(V) = n_\infty(V) = \frac{1}{2}\left[1 + \tanh\left(\frac{V - V_3}{V_4}\right)\right],$$

where $V(n)$ is monotone decreasing for $0 \le n \le 1$, and $n(V)$ is a monotone increasing function. Therefore the nullclines may intersect at most once for $0 \le n \le 1$, yielding at most one equilibrium point. Figure 2.1(b) shows the phase plane for the system with $\mu = 0$, and indicates that the system admits a single equilibrium point. Taking $x = V - V^*$ and $y = n - n^*$, the linearised system with equilibrium shifted to the origin is

$$\dot{x}(t) = -ax + by$$

(2.1.2)

$$\dot{y}(t) = cx - dy,$$

where

$$a = \frac{g_{\mathrm{L}} + g_{\mathrm{K}} n^*}{C}, \qquad b = \frac{g_{\mathrm{K}}(V_{\mathrm{K}} - V^*)}{C}, \qquad d = \overline{\lambda_n} \cosh\left(\frac{V^* - V_3}{2V_4}\right),$$

$$c = \frac{\overline{\lambda_n}}{2V_4} \cosh\left(\frac{V^* - V_3}{2V_4}\right) \operatorname{sech}^2\left(\frac{V^* - V_3}{V_4}\right).$$

A detailed linearisation of the system with delay is included in section 2.2.2 — the linearisation presented here follows directly from that by setting $\mu = 0$. The characteristic equation for system (2.1.2) is

$$\lambda^2 + (a + d)\lambda + (ad - bc) = 0.$$

The equation has two roots, given by

$$\lambda_{\pm} = \frac{-(a + d) \pm \sqrt{(a + d)^2 - 4(ad - bc)}}{2}.$$

The equilibrium point (V^*, n^*) is stable provided both eigenvalues have negative real parts. By the Routh–Hurwitz [3] conditions, this is satisfied as long as

(i). $a + d > 0 \quad \Rightarrow \quad a > -d$, and

(ii). $ad - bc > 0 \quad \Rightarrow \quad ad > bc$.

Since there are numerous parameters in the system, we employ a standard reference set for the original model parameters to facilitate our investigation. Table 2.1 contains typical values for the parameters for the all–K$^+$ system, as reported by Morris and Lecar [24].

Note that the first Routh–Hurwitz condition is satisfied for any non-negative a and d, provided a and $\overline{\lambda_n}$ are both non–zero. That is, (i) holds

Parameter Set	
$C = 20\ \mu\mathrm{F/cm^2}$	$\overline{\lambda_n} = \frac{1}{15}\ \mathrm{s^{-1}}$
$g_\mathrm{L} = 3\ \mathrm{mmho/cm^2}$	$g_\mathrm{K} = 8\ \mathrm{mmho/cm^2}$
$V_\mathrm{L} = -50\ \mathrm{mV}$	$V_\mathrm{K} = -70\ \mathrm{mV}$
$V_3 = -1.0\ \mathrm{mV}$	$V_4 = 14.5\ \mathrm{mV}$

Table 2.1: Morris–Lecar parameter set for the all–K$^+$ conductance system.

for a general set of parameter values $g_\mathrm{L}, g_\mathrm{K}, \overline{\lambda_n}, V_3, V_4$ and C. Therefore, condition (i) is satisfied for the specific parameter values given in Table 2.1. For condition (ii), note that $(V^*, n^*) = (-50.061, 0.001)$ for the parameters in Table 2.1. Since $V^* > V_\mathrm{K}$, then $b < 0$, which implies that (ii) is satisfied. Hence both eigenvalues have negative real parts and the equilibrium (V^*, n^*) is stable. It is a stable node since both eigenvalues are real, which follows from the fact that the discriminant of the roots $\Delta = 3.98 \times 10^{-4} > 0$. Also, any combination of parameters for which $V^* > V_\mathrm{K}$ will ensure that (ii) is satisfied. Finally, this analysis is valid for any $V_\mathrm{K} < V_\mathrm{L}$.

2.2 The all–K$^+$ Conductance System with Delay

Consider the delayed system (2.0.1), with $\mu \neq 0$. Then we have a system consisting of one delay differential equation coupled to an ordinary differential equation. Since both dependent variables V and n appear in the DDE, to solve the system we must prescribe initial functions on the delay interval $[-\tau, 0]$. From a mathematical standpoint, the initial functions $V(\theta)$ and $n(\theta)$ for $\theta \in [-\tau, 0]$ can be arbitrary elements of the function space $C([-\tau, 0], \mathbb{R})$. The physiological interpretation of the state variables V and n requires initial data to be selected appropriately, that is by choosing an initial voltage function $V(\theta) = V_0$, and then calculating $n_\infty(V_0)$ for $n(\theta)$, so that the initial fraction of open K$^+$–channels corresponds to the initial voltage. For our purposes, we employ constant initial functions for $V(\theta)$ and $n(\theta)$.

Analysis of the $\dot{V}(t) = 0$ and $\dot{n}(t) = 0$ nullclines in the (V, n)–plane provides information pertaining to the number and location of equilibria of (2.0.1). In the following section we present a detailed discussion of the nullclines of the all–potassium conductance system, and how they change as μ is varied.

2.2.1 The Nullclines of the all–K$^+$ System

To study the nullclines in the (V, n)–plane, we set $\dot{V}(t) = 0$ and $\dot{n}(t) = 0$ and consider $V(t - \tau) = V(t)$:

$$V(n) = \frac{g_L V_L + g_K V_K n}{g_L + g_K n - \mu} \tag{2.2.1}$$

$$n(V) = n_\infty(V) = \frac{1}{2}\left[1 + \tanh\left(\frac{V - V_3}{V_4}\right)\right]. \tag{2.2.2}$$

We wish to determine how the nullclines change as the parameter μ is varied. The variable n represents the fraction of open K$^+$ channels, and so $0 \leq n \leq 1$. This in turn implies that the voltage $V(n)$ varies between

$$V(0) = \frac{g_{\mathrm{L}} V_{\mathrm{L}}}{g_{\mathrm{L}} - \mu} \qquad \text{and} \qquad V(1) = \frac{g_{\mathrm{L}} V_{\mathrm{L}} + g_{\mathrm{K}} V_{\mathrm{K}}}{g_{\mathrm{L}} + g_{\mathrm{K}} - \mu}.$$

Note that, for certain parameter sets, these voltage limits may become infinite for certain values of μ. In this chapter, we interested in varying only the parameters μ and τ to investigate how changes in the delay parameters affect the behavior of the system. For consistency, we use the reference parameter set listed in Table 2.1 for the remaining model parameters.

The $\dot{n}(t) = 0$ nullcline (2.2.2) does not directly depend on μ, and $n(V)$ is a sigmoidal–shaped, monotone increasing function of V for all μ, and $n(V) \to 0$ as $V \to -\infty$, while $n(V) \to 1$ as $V \to \infty$. On the other hand, the $\dot{V}(t) = 0$ nullcline (2.2.1) does depend on μ, and the qualitative behavior of $V(n)$ as a function of n changes as μ is varied. The $V(n)$ nullcline is simply a hyperbola, separated by a vertical asymptote at $V = V_{\mathrm{K}}$, except for one degenerate case, where it is reduced to a pair of vertical and horizontal lines. We are only interested in the physiological case where $0 \leq n \leq 1$, and so depending on the value of μ, one or both branches of the V–nullcline are significant. First, note that as $\mu \to \pm\infty$, we have $V \to 0$ and $n \to n_\infty(0) \approx 0.53$. For

$$\mu < g_{\mathrm{L}} \left(1 - \frac{V_{\mathrm{L}}}{V_{\mathrm{K}}} \right),$$

$V(n)$ is a monotone decreasing function of n in the interval of interest, $0 \leq n \leq 1$, and the system admits a single unique equilibrium point, (V^*, n^*). The significant branch of the hyperbola lies to the right of the vertical asymptote,

and we can ignore the lower branch of the hyperbola, which is below the V–axis. For these values of μ, we have $V_K < V^*$, and with the parameter values listed in Table 2.1, we obtain

$$g_L \left(1 - \frac{V_L}{V_K} \right) = \frac{6}{7}.$$

Figure 2.1(b) shows the nullclines in the (V, n)–plane for μ in this range $\mu < \frac{6}{7}$.

Next we evaluate $V(n)$ when $\mu = g_L \left(1 - \frac{V_L}{V_K} \right)$:

$$V(n) = \frac{g_L V_L + g_K V_K n}{g_L + g_K n - g_L + g_L \frac{V_L}{V_K}} = \frac{V_K (g_L V_L + g_K V_K n)}{g_K V_K n + g_L V_L} = V_K,$$

and so the $V(n)$–nullcline is simply a vertical line at $V = V_K = -70$ in the (V, n)–plane. Above we canceled the common factor $g_L V_L + g_K V_K n$, and in doing so, we assumed that this expression is nonzero. In the event that the factor is zero we have

$$g_L V_L + g_K V_K n = 0 \quad \Rightarrow \quad n = -\frac{g_L V_L}{g_K V_K},$$

which is a horizontal line in the (V, n)–plane. With the parameter values in Table 2.1, the horizontal line is $n = -\frac{15}{56} < 0$, which is outside the feasible range $0 \le n \le 1$. Therefore, with $\mu = g_L \left(1 - \frac{V_L}{V_K} \right) = \frac{6}{7}$, $V^* = V_K$ and the equilibrium point of the nonlinear system is $(V^*, n^*) \approx (-70, 0)$, since the $n(V)$ nullcline is nearly zero there. The nullclines of the system for $\mu = \frac{6}{7}$ are depicted in Figure 2.1(c).

The next parameter range is

$$g_L \left(1 - \frac{V_L}{V_K} \right) < \mu < g_L,$$

and with μ in this interval, we find that $V(n)$ is a monotone increasing function of n in the interval of interest. The function $V(n)$ is still a hyperbola, and we

(a) $\mu = -5$.

(b) $\mu = 0$.

(c) $\mu = \frac{6}{7}$

(d) $\mu = 2$.

(e) $\mu = 5$.

(f) $\mu = 15$.
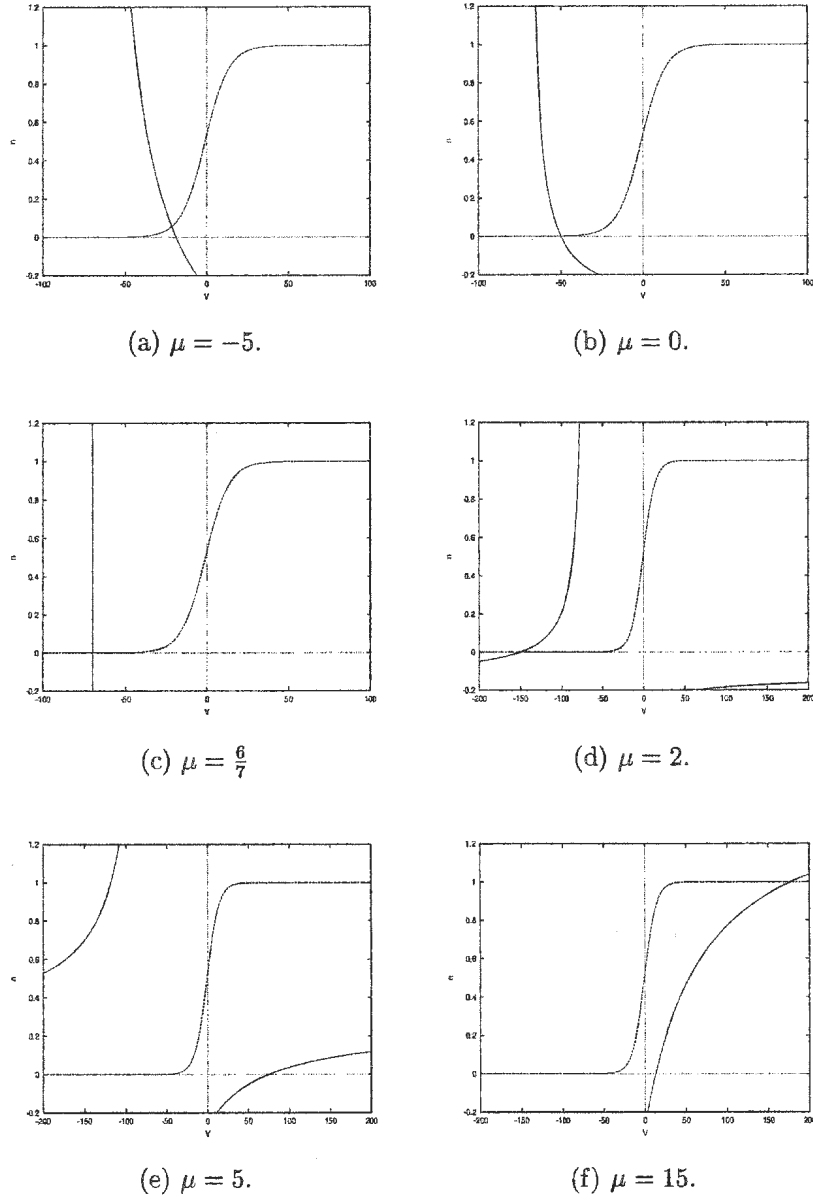
Figure 2.1: Plots of the $V(n)$ (solid) and $n(V)$ (dashed) nullclines of the all–K$^+$ system (2.0.1) for representative values of μ.

still ignore the lower branch which is below the V-axis. However, in this case the important branch is the part that is to the left of the vertical asymptote. In this range, we obtain a unique equilibrium point (V^*, n^*), with n^* still close to zero but $V^* < V_K$. Figure 2.1(d) shows the nullclines for $\mu = 2$, which is in the present range.

From equations (2.2.1) and (2.2.2), we can see that $n \to 0$ as $V \to -\infty$. Hence $(V^*, n^*) \to (-\infty, 0)$, as $\mu \to g_L$, and so when $\mu = g_L$ the system does not have a finite equilibrium point. Moreover, the system will not have an equilibrium point if μ is in the range $g_L \le \mu \le g_L + g_K$. With μ in this interval, $V(n)$ is still a strictly increasing function of n but the lower branch of the hyperbola becomes important once it crosses the V-axis (*i.e.* when μ passes g_L). For our parameter set in Table 2.1, the range of μ for which the system does not have an equilibrium point is $3 \le \mu \le 11$. This range can be obtained if we rearrange the $V(n)$ nullcline and solve for n, to obtain

$$n = \frac{g_L(V_L - V) + \mu V}{g_K(V - V_K)}.$$

This allows us to find the value of n where the voltage V becomes infinite, in other words the horizontal asymptote of the hyperbola in the (V, n)-plane:

$$\lim_{V \to \pm\infty} n(V) = \frac{\mu - g_L}{g_K}. \tag{2.2.3}$$

Hence as long as this limit is between zero and one, *i.e.* $g_L \le \mu \le g_L + g_K$, the system will not have an equilibrium point. However, as $\mu \to (g_L + g_K)$, the limit in (2.2.3) becomes 1, and here $V \to +\infty$ and $n \to 1$.

The nullclines for $\mu = 5 \in [3, 11]$ shown in Figure 2.1(e) are representative of the nullclines for the system with μ in this parameter range. If $\mu > g_L + g_K$, the lower branch of the hyperbola intersects the sigmoidal nullcline and

we regain an equilibrium point (V^*, n^*), with $n = 1^-$ and $V^* > V_{\mathrm{K}}$. In this parameter range, the branch of the nullcline which is to the right of the vertical asymptote is again significant. The nullclines for $\mu = 15$ are shown in Figure 2.1(f), where we see that, for $\mu > 11$, the system admits a single equilibrium point.

This concludes the description of the nullclines in the (V, n)–plane for $\mu \in \mathbb{R}$. The evolution of the nullclines as μ is varied is shown in Figure 2.1. Figures 2.2(a), 2.2(b) depict the bifurcation diagrams for the all–potassium conductance system, indicating how both V^* and n^* and their stability change as μ is varied (for $\tau = 0$).

(a) V vs. μ.   (b) n vs. μ.
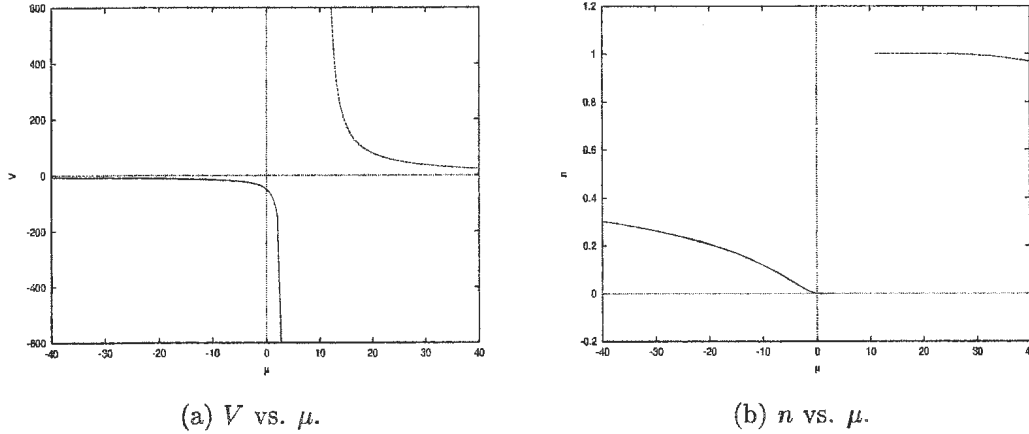
Figure 2.2: Bifurcation diagrams describing how V^* and n^* of the all–K$^+$ conductance system (2.0.1) change as μ is varied. Solid lines indicate stable equilibrium points while dashed lines represent unstable ones.

The nullcline analysis of this section can be used to prove the following theorem:

Theorem 2.2.1.1. *With parameters listed in Table 2.1, system (2.0.1) admits at most one equilibrium point (V^*, n^*) for all $\mu \in \mathbb{R}$. The value $n^* \in [0, 1]$, and $V^* > V_K$ if $\mu < g_L \left(1 - \frac{V_L}{V_K}\right)$ or $\mu > g_L + g_K$, $V^* < V_K$ if $g_L \left(1 - \frac{V_L}{V_K}\right) < \mu < g_L$, and $V^* = V_K$ if $\mu = g_L \left(1 - \frac{V_L}{V_K}\right)$. Furthermore, if $g_L \leq \mu \leq g_L + g_K$, then (2.0.1) does not possess an equilibrium point.*

2.2.2 Local Stability and Bifurcation Analysis of the all–K$^+$ System

We wish to analyse the dynamics of the isolated conductance systems in the presence of delayed recurrent feedback. Not only will this reveal how the implemented delay affects the dynamics of the systems, it should also indicate how each conductance system with delay contributes to the full delay model which incorporates both conductance systems. In this subsection, we take a look at the all–K$^+$ system, to investigate the stability of the equilibrium point (V^*, n^*) for certain parameter ranges. We shall also examine the system to determine whether or not it is capable of supporting oscillations. Periodic solutions commonly arise in delay differential equation models via Hopf bifurcation. The system studied by Plant in [32] serves as a case in point. As will become evident later, the system in [32] is very similar in form to the ion conductance systems of the Morris–Lecar model with delay. Therefore, we look for periodic solutions of (2.0.1) arising via Hopf bifurcation. It seems plausible that the Hopf bifurcation structure of the system will depend on the pair of delay parameters μ and τ.

Consider a two–dimensional autonomous delay equation with a single dis-

crete time delay,

$$\dot{x}(t) = f(x(t), x(t-\tau), \eta), \qquad (2.2.4)$$

where $x(t) \in \mathbb{R}^2$, $\eta \in \mathbb{R}^k$, and $f : \mathbb{R}^4 \times \mathbb{R}^k \to \mathbb{R}^2$. Steady state solutions, or equilibrium points, $x(t) \equiv x^* \in \mathbb{R}^2$ of (2.2.4) are obtained as solutions of the nonlinear system

$$f(x^*, x^*, \eta) = 0.$$

The number and location of steady state solutions x^* to a system of delay differential equations do not depend on the value(s) of the delay(s). However, the stability of x^* under (2.2.4) does depend on the value of the delay(s). To study the stability of an equilibrium point x^*, we linearise the nonlinear system (2.2.4) about x^* and obtain the variational equation, which is a linear delay differential equation of the form

$$\dot{y}(t) = \frac{\partial f}{\partial x^0}(x^*, x^*, \eta)y(t) + \frac{\partial f}{\partial x^1}(x^*, x^*, \eta)y(t-\tau),$$

where $f \equiv f(x^0, x^1, \eta)$. To obtain the characteristic equation of the system, we substitute solutions of the form $ve^{\lambda t}$ into the variational equation to obtain

$$\begin{cases} \left(\lambda I - \dfrac{\partial f}{\partial x^0}(x^*, x^*, \eta) + \dfrac{\partial f}{\partial x^1}(x^*, x^*, \eta)e^{-\lambda\tau} \right) v = 0 \\ \|v\| = 1. \end{cases}$$

This gives a nonlinear eigenvalue problem with characteristic matrix

$$\Delta(\lambda) = \lambda I - \frac{\partial f}{\partial x^0}(x^*, x^*, \eta) + \frac{\partial f}{\partial x^1}(x^*, x^*, \eta)e^{-\lambda\tau},$$

which we can rewrite to obtain the characteristic equation

$$\det(\Delta(\lambda)) = 0. \qquad (2.2.5)$$

Equation (2.2.5) is a transcendental equation, with an infinite number of roots. Therefore, system (2.2.4) linearised about x^* has an infinite number of eigenvalues which determine the stability of x^*. The equilibrium x^* is asymptotically stable provided all roots of (2.2.5) have negative real parts, and is unstable if there exists a root with positive real part. If $\lambda = 0$ is a root, then the system is degenerate, and the stability of the equilibrium cannot be determined in this manner. In general, the eigenvalues $\lambda \in \mathbb{C}$ and depend on the parameters η, so that $\lambda(\eta) = \alpha(\eta) + i\omega(\eta)$. As physical parameters η are varied, a bifurcation occurs when an eigenvalue crosses the imaginary axis, that is $\lambda = 0$ or $\lambda = i\omega$, $\omega \neq 0$. With this bifurcation, the stability of x^* can change, and in the case $\lambda = i\omega$, $\omega \neq 0$, a Hopf bifurcation is likely, and a branch of periodic solutions may emerge.

We now turn from discussion of steady state analysis of general delay equations of the class (2.2.4) to the specific analysis of the all–potassium system with delay (2.0.1). Assuming that $\mu \notin [g_L, g_L + g_K] = [3, 11]$, system (2.0.1) admits a single equilibrium point (V^*, n^*). To linearise the system about the origin, we shift the equilibrium point to the origin by taking $x = V - V^*$, and $y = n - n^*$. With this substitution we obtain

$$
\begin{aligned}
C\dot{x}(t) &= -g_L \left(x + V^* - V_L \right) - g_K \left(y + n^* \right) \left(x + V^* - V_K \right) + \mu \left(x(t-\tau) + V^* \right) \\
&= -g_L x - g_K xy - g_K V^* y + g_K V_K y - g_K n^* x + \mu x(t-\tau) \\
&\quad -V^* \left(g_L + g_K n^* - \mu \right) + g_L V_L + g_K V_K n^* \\
&= -g_L x - g_K xy - g_K V^* y + g_K V_K y - g_K n^* x + \mu x(t-\tau),
\end{aligned}
$$

where we used the fact that $V^*(g_L + g_K n^* - \mu) = g_L V_L + g_K V_K n^*$, and

$$\dot{y}(t) = \lambda_y(x) \left[y_\infty(x) - y - n^* \right],$$

where

$$
\begin{cases}
y_\infty(x) = \dfrac{1}{2} \left[1 + \tanh \left(\dfrac{x + V^* - V_3}{V_4} \right) \right] \\[3mm]
\lambda_y(x) = \overline{\lambda_n} \cosh \left(\dfrac{x + V^* - V_3}{2V_4} \right).
\end{cases}
$$

The nonlinear system with equilibrium point at the origin $(x^*, y^*) = (0, 0)$ is

$$C\dot{x}(t) = -(g_L + g_K n^*)x + g_K(V_K - V^*)y - g_K xy + \mu x(t - \tau)$$

$$\dot{y}(t) = \overline{\lambda_n} \cosh \left(\frac{x + V^* - V_3}{2V_4} \right) \times \qquad\qquad (2.2.6)$$

$$\left[\frac{1}{2} \left(1 + \tanh \left(\frac{x + V^* - V_3}{V_4} \right) \right) - y - n^* \right].$$

The n–coordinate of the (V^*, n^*) equilibrium point is in fact $n^* = n_\infty(V^*)$, and so in in the transformed variables, we have $n^* = y_\infty(x) = y_\infty(0)$ since $x^* = 0$.

To linearise system (2.2.6) about the origin, we linearise the hyperbolic functions using series expansion. Hence the equation for $\dot{y}(t)$ becomes

$$\dot{y}(t) = \frac{\overline{\lambda_n}}{2V_4} \cosh \left(\frac{V^* - V_3}{2V_4} \right) \operatorname{sech}^2 \left(\frac{V^* - V_3}{V_4} \right) x - \overline{\lambda_n} \cosh \left(\frac{V^* - V_3}{2V_4} \right) y$$

in the linearisation. The variational equation associated with the nonlinear system (2.0.1) linearised about the origin is then

$$C\dot{x}(t) = -(g_L + g_K n^*)x + g_K(V_K - V^*)y + \mu x(t - \tau)$$

$$\qquad\qquad (2.2.7)$$

$$\dot{y}(t) = \frac{\overline{\lambda_n}}{2V_4} \cosh(u) \operatorname{sech}^2(v) x - \overline{\lambda_n} \cosh(u) y$$

where $u = \frac{V^*-V_3}{2V_4}$, and $v = \frac{V^*-V_3}{V_4}$. Since the coefficients in the terms of (2.2.7) are constants for any given set of parameter values and equilibrium point (V^*, n^*), let

$$a = \frac{g_L + g_K n^*}{C}, \qquad b = \frac{g_K(V_K - V^*)}{C}, \qquad d = \overline{\lambda_n} \cosh(u),$$

$$c = \frac{\overline{\lambda_n}}{2V_4} \cosh(u) \operatorname{sech}^2(v), \quad \hat{\mu} = \frac{\mu}{C}.$$

The equations become

$$\dot{x}(t) = -ax + by + \hat{\mu} x(t - \tau)$$

$$(2.2.8)$$

$$\dot{y}(t) = cx - dy.$$

Note that the coefficients of the linearised system depend on the equilibrium point of the nonlinear system, which in turn depends on the value of μ.

From the restriction $0 \le n \le 1$ we see that the voltage V satisfies $V(1) < V < V(0)$ if the $V(n)$–nullcline is a monotone decreasing function of n for $n \in [0, 1]$. This is true as long as $\mu < g_L \left(1 - \frac{V_L}{V_K}\right)$. On the other hand, $V(n)$ is a monotone increasing function in the n–interval of interest if $g_L \left(1 - \frac{V_L}{V_K}\right) < \mu < g_L$, and also if $\mu > g_L + g_K = 11$. For μ in either of these ranges, the voltage V varies between $V(0) < V < V(1)$. Collectively, these cases represent the situation where only one branch of the $V(n)$ hyperbola is significant, the upper branch in the first two cases, and the lower branch in the third case. Of course, there are no upper and lower limits on the voltage if $\mu \in [g_L, g_L + g_K]$, where we have no equilibrium point, since the nullcline $V(n)$ can become infinite for certain values of n, namely, the value of the the horizontal asymptote.

Given that the coefficients of the variational equation are defined in terms of (V^*, n^*) and other parameter values, we can draw some conclusions about

the range of values these coefficients may assume. Since they are functions of the equilibrium point (V^*, n^*), they only exist for values of μ which admit a finite equilibrium point in the (V, n)–plane. From the definition of a and the parameter values in Table 2.1, we find that

$$\frac{g_{\mathrm{L}}}{C} \leq a \leq \frac{g_{\mathrm{L}} + g_{\mathrm{K}}}{C} \quad \Rightarrow \quad \frac{3}{20} \leq a \leq \frac{11}{20}$$

since n is restricted to $[0, 1]$, and $g_{\mathrm{L}}, g_{\mathrm{K}}$ are positive constants. In particular, $a > 0$ for any set of parameter values where the conductance constants are non–negative and capacitance is positive.

To estimate the bounds on c, we use the properties of hyperbolic trigonometric functions. From the definition of c we see that

$$c = \frac{\overline{\lambda_n}}{2V_4} \frac{\cosh(u)}{\cosh^2(v)}$$

where $u = \frac{V^* - V_3}{2V_4}$. Note that $v = 2u$ gives

$$c = \frac{\overline{\lambda_n}}{2V_4} \frac{\cosh(u)}{\cosh^2(2u)} = \frac{\overline{\lambda_n}}{2V_4} \frac{\cosh(u)}{(\cosh^2(u) + \sinh^2(u))^2}.$$

Also, $\sinh^2(u) \geq 0$, $\cosh(u) \geq 1 \; \forall u$, it follows that

$$\cosh(u) \leq \cosh^2(u) \leq \cosh^2(u) + \sinh^2(u) \leq (\cosh^2(u) + \sinh^2(u))^2,$$

and so

$$\frac{\cosh(u)}{(\cosh^2(u) + \sinh^2(u))^2} \leq 1 \qquad \forall u.$$

Since $\overline{\lambda_n} > 0$ in general, $\cosh(u) \geq 1 > 0 \; \forall u$, and $V_4 > 0$, we find that

$$0 < c < \frac{\overline{\lambda_n}}{2V_4} .$$

Therefore, c is positive for any set of parameter values where $V_4 > 0$. For our parameter set (Table 2.1), we obtain the bounds on c to give

$$0 < c < \frac{1}{435}$$

While a and c are in general finite positive quantities, the story is not as simple for the coefficients b and d. From the definition

$$d = \overline{\lambda_n} \cosh(u) = \overline{\lambda_n} \cosh\left(\frac{V^* - V_3}{2V_4}\right),$$

we know that in general, d is positive. If we consider values of μ for which the voltage V is bounded, that is either $V(0) < V < V(1)$ or $V(1) < V < V(0)$, then the range of values which d may assume depends on the values of $|V(0)|$ and $|V(1)|$: the values of μ for which $|V(0)| < |V(1)|$ produce the inequalities

$$\overline{\lambda_n} \le \overline{\lambda_n} \cosh\left(\frac{V(0) - V_3}{2V_4}\right) < d < \overline{\lambda_n} \cosh\left(\frac{V(1) - V_3}{2V_4}\right). \qquad (2.2.9)$$

When $|V(1)| < |V(0)|$, however, we have

$$\overline{\lambda_n} \le \overline{\lambda_n} \cosh\left(\frac{V(1) - V_3}{2V_4}\right) < d < \overline{\lambda_n} \cosh\left(\frac{V(0) - V_3}{2V_4}\right). \qquad (2.2.10)$$

In either case, we see that $d \ge \overline{\lambda_n} > 0$, and so in general d is a positive constant. However, as $\mu \to g_L$ or $\mu \to g_L + g_K$, $V^* \to \pm\infty$, and so $d \to +\infty$.

Finally, for b we have

$$\frac{g_K}{C}(V_K - V(0)) < b < \frac{g_K}{C}(V_K - V(1)) \qquad (2.2.11)$$

if $\mu < g_L\left(1 - \frac{V_L}{V_K}\right)$, which implies $V(1) < V(0)$, and

$$\frac{g_K}{C}(V_K - V(1)) < b < \frac{g_K}{C}(V_K - V(0)) \qquad (2.2.12)$$

if $g_\text{L}\left(1 - \frac{V_\text{L}}{V_\text{K}}\right) < \mu < g_\text{L}$, or if $\mu > g_\text{L} + g_\text{K}$, which implies $V(0) < V(1)$. However, as $\mu \to g_\text{L}$, $V^* \to -\infty$, and so $b \to \infty$, while $b \to -\infty$ as $\mu \to g_\text{L}+g_\text{K}$, since in this case $V^* \to +\infty$. Also, from the definition we see that the sign of the coefficient b can be either positive or negative: if $\mu < g_\text{L}\left(1 - \frac{V_\text{L}}{V_\text{K}}\right)$, then $V_\text{K} < V^*$ and so $b < 0$, if $\mu = g_\text{L}\left(1 - \frac{V_\text{L}}{V_\text{K}}\right)$, then $V_\text{K} = V^*$ and $b = 0$, and finally if $\mu > g_\text{L}\left(1 - \frac{V_\text{L}}{V_\text{K}}\right)$, then $V_\text{K} > V^*$ and so $b > 0$.

2.2.3 The Characteristic Equation

To study the stability of the equilibrium point (V^*, n^*), we examine the eigenvalues of the system using the characteristic equation. This is obtained by considering (2.2.8), and assuming solutions of the form

$$X = \begin{bmatrix} x \\ y \end{bmatrix} = e^{\lambda t} \begin{bmatrix} \xi_1 \\ \xi_2 \end{bmatrix} \quad \Rightarrow \quad \dot{X} = \begin{bmatrix} \dot{x} \\ \dot{y} \end{bmatrix} = \lambda e^{\lambda t} \begin{bmatrix} \xi_1 \\ \xi_2 \end{bmatrix}.$$

Therefore

$$\lambda \begin{bmatrix} 1 & 0 \\ 0 & 1 \end{bmatrix} \begin{bmatrix} \xi_1 \\ \xi_2 \end{bmatrix} = \begin{bmatrix} -a + \hat{\mu}e^{-\lambda\tau} & b \\ c & -d \end{bmatrix} \begin{bmatrix} \xi_1 \\ \xi_2 \end{bmatrix},$$

and so the characteristic equation for the system (2.2.8) is

$$\lambda^2 + (a + d)\lambda + (ad - bc) - \hat{\mu}\lambda e^{-\lambda\tau} - \hat{\mu}de^{-\lambda\tau} = 0. \tag{2.2.13}$$

Equation (2.2.13) closely resembles a transcendental characteristic equation studied by Plant [32], and the form of the linearised two–dimensional system obtained in that paper is similar to system (2.2.8). The characteristic equation obtained by Plant was

$$z^2 + pz + q + r(\hat{\mu})ze^{-z} + s(\hat{\mu})e^{-z} = 0,$$

which compares to our model via the substitutions $z = \lambda\tau$, $p = \tau(a + d)$, $q = \tau^2(ad - bc)$, $r(\hat{\mu}) = -\hat{\mu}\tau$ and $s(\hat{\mu}) = -\hat{\mu}d\tau^2$. However, in Plant's paper the coefficients of the linearised system are simply positive constants which do not depend on any model parameters. Therefore only the last two terms of his characteristic equation are functions of the parameter μ. Recall that all of a, b, c, and d of (2.2.8) depend on (V^*, n^*), which in turn depends on μ. Hence all coefficients of characteristic equation (2.2.13) depend on μ, and so the analysis of the characteristic equation in [32], while elegant and effective in establishing Hopf bifurcation of solutions with respect to the parameter μ, cannot be applied to our model.

To analyse (2.2.13), we use theory developed by Cooke and Grossman [6] to study stability switching in delay differential equations as the delay is varied. The application of their results requires knowledge of the stability of the equilibrium point (V^*, n^*) of (2.0.1), when it exists, with zero time delay. This information is important when carrying out a Hopf bifurcation analysis of the system, since, according to Datko [7], for retarded functional differential equations the supremum of the real parts of the roots of the transcendental equation varies continuously with the delay. Therefore, as we vary τ, a transition from stability to instability (or vice–versa) must correspond to a purely imaginary root of the characteristic equation. Hence, to determine if such a transition is possible, we must know whether the equilibrium point (V^*, n^*) of the model with $\tau = 0$ is stable or unstable.

2.2.4 The $\tau = 0$ Case

With $\tau = 0$ we obtain the characteristic equation

$$\lambda^2 + (a + d - \hat{\mu})\lambda + [(ad - bc) - \hat{\mu}d] = 0, \qquad (2.2.14)$$

a quadratic polynomial, with roots

$$\lambda_\pm = \frac{\hat{\mu} - (a + d) \pm \sqrt{[(a + d) - \hat{\mu}]^2 - 4[(ad - bc) - \hat{\mu}d]}}{2}. \qquad (2.2.15)$$

Let $\Delta = [(a + d) - \hat{\mu}]^2 - 4[(ad - bc) - \hat{\mu}d]$, the discriminant of the roots in Equation (2.2.15). The trivial solution of (2.2.6), and hence (V^*, n^*) of (2.0.1), is stable as long as both roots of (2.2.14) have negative real parts, $i.e.$ $\mathrm{Re}\lambda_\pm < 0$. This is true provided both Routh–Hurwitz conditions are satisfied:

(i). $a + d - \hat{\mu} > 0 \quad \Rightarrow \quad \hat{\mu} < a + d$, and

(ii). $(ad - bc) - \hat{\mu}d > 0 \quad \Rightarrow \quad \hat{\mu} < a - \frac{bc}{d}$.

Note that (V^*, n^*) is given by the intersection of two nonlinear nullclines, and we have no closed form expressions relating the values of V^* and n^* to the value of μ. Hence, we have no explicit formula which expresses the coefficients in terms of μ. To check conditions (i) and (ii) we must determine how the coefficients vary with μ, which we do numerically using a program written in Maple which calculates the equilibrium point as μ is varied, and then also computes the values of the coefficients and quantities in conditions (i) and (ii). Then, by plotting $\hat{\mu}$, $a + d$ and $a - \frac{bc}{d}$ versus μ we can identify the ranges of the parameter μ for which both conditions (i) and (ii) are simultaneously satisfied.

Figure 2.3 contains the plots which compare how the values of $a + d$, $a - \frac{bc}{d}$ and $\hat{\mu}$ change with respect to μ. The coefficients b and d become infinite as the

(a) $\mu \leq g_{\mathrm{L}} = 3$.

(b) $g_{\mathrm{L}} + g_{\mathrm{K}} = 11 \leq \mu$.
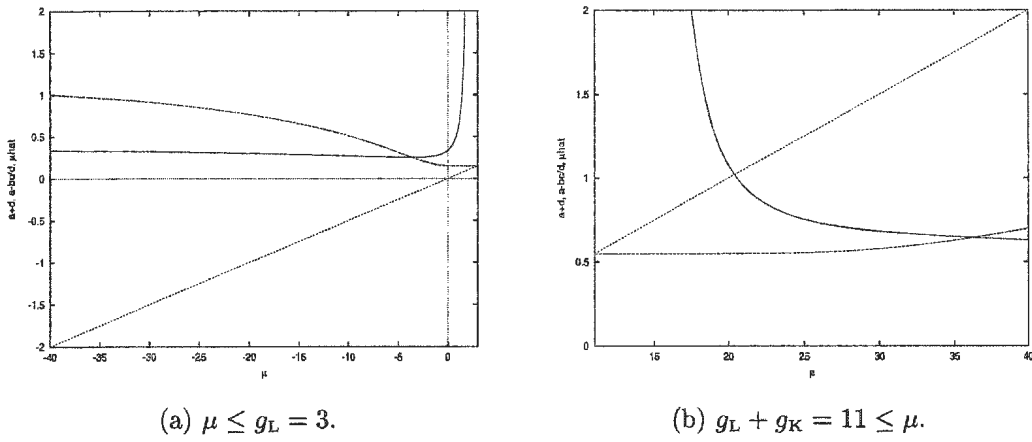
Figure 2.3: Checking the Routh–Hurwitz conditions: Plots of $a + d$ (solid curve), $a - \frac{bc}{d}$ (dashed curve), and $\hat{\mu}$ (dotted line) against μ for the two parameter ranges where system (2.0.1) (with $\tau = 0$) has a unique equilibrium point.

equilibrium voltage $V^* \to \pm\infty$, which occurs when $\mu \to g_L$ and $\mu \to g_L + g_K$. In this situation, calculating the quantity $a - \frac{bc}{d}$ in a computer program can become problematic. This can be averted by stopping the code with μ close to g_L or $g_L + g_K$, and then using a limit to show that the curves for $a - \frac{bc}{d}$ and $\hat{\mu}$ intersect as μ approaches these values. This technique is used often with this analysis, and a detailed example is given in the following section.

The plot in Figure 2.3(a) is for values of μ less than g_L. In this range we have a unique equilibrium point, and find that both conditions (i) and (ii) are satisfied. Therefore with $\mu < g_L$, both eigenvalues λ_+ and λ_- of (2.2.14) have negative real parts, and it follows that (V^*, n^*) of (2.0.1) is stable.

We may distinguish the ranges for $\mu < g_L$ for which the equilibrium (V^*, n^*) is a stable node ($\Delta > 0$) from those where it is a stable spiral ($\Delta < 0$) by checking the sign of the discriminant. To determine the sign of Δ, we plot $[(a + d) - \hat{\mu}]^2$ and $4[(ad - bc) - \hat{\mu}d]$ versus μ in Figure 2.4. We see that $[(a + d) - \hat{\mu}]^2 > 4[(ad - bc) - \hat{\mu}d] \Rightarrow \Delta > 0$ for $\mu < \mu_{\Delta_1}$, and for $\mu_{\Delta_2} < \mu < g_L$, and so for these values of μ the equilibrium point is a stable node since both λ_+ and λ_- are both real and negative. Estimating the values of μ_{Δ_1} and μ_{Δ_2}, we find that $\mu_{\Delta_1} \approx -14.0$ and $\mu_{\Delta_2} \approx -0.05$. For $\mu_{\Delta_1} < \mu < \mu_{\Delta_2}$, we have $\Delta < 0$, and so both λ_+ and λ_- are complex with negative real parts, indicating a stable spiral.

Note that there are no plots for μ between g_L and $g_L + g_K$, since for these values, (2.0.1) does not have an equilibrium point, and so we have no linearised system and hence no a, b, c, and d. Figure 2.3(b) indicates how $a + d$, $a - \frac{bc}{d}$ and $\hat{\mu}$ change with respect to μ for $\mu > g_L + g_K$. From the graph we see that condition (ii) is never met, $i.e.$ that $\hat{\mu} > a - \frac{bc}{d}$, which implies that (V^*, n^*)
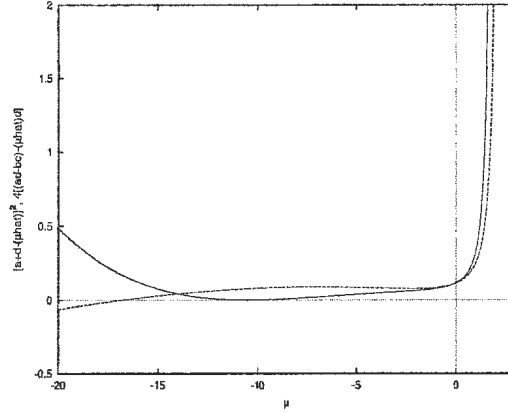
Figure 2.4: Plots of $[(a+d) - \hat{\mu}]^2$ (solid curve) and $4[(ad - bc) - \hat{\mu}d]$ (dashed curve) versus μ to determine the sign of the discriminant.

is unstable. Also, this indicates that the discriminant of the roots Δ is always positive, and so the two roots λ_+ and λ_- are always real. Therefore it follows that

$$\lambda_+ > 0 \qquad \text{and} \qquad \lambda_- < 0,$$

and so the equilibrium point is an unstable saddle point for all μ greater than $g_L + g_K$. Finally, we note that, while these results are only shown for a "small" range of the parameter μ, the programs used to obtain these results were run over larger ranges of μ and no change in the results reported were observed. Also, the results presented here pertain only to the model with the specific parameter set given in Table 2.1.

2.2.5 The System with Nonzero Delay $\tau > 0$

Now we turn to the model with nonzero delay (2.0.1) with (2.2.13) as the characteristic equation. To study the bifurcation structure of the model (2.0.1)

we apply results established by Cooke and Grossman [6] on general second order equations with a single time delay. Their equation was of the form

$$\frac{d^2x}{dt^2} + a\frac{dx}{dt} + b\frac{x(t-\tau)}{dt} + cx(t) + dx(t-\tau) = 0, \qquad (2.2.16)$$

$$a + b \neq 0, \quad c + d \neq 0$$

with characteristic equation

$$\lambda^2 + a\lambda + b\lambda e^{-\lambda\tau} + c + de^{-\lambda\tau} = 0.$$

Cooke and Grossman studied this equation in connection with a model containing delayed friction and delayed restoring force. Equations of this form can be obtained from a nonlinear system with one delay, upon linearisation. The conditions $a + b \neq 0$, $c + d \neq 0$ are required to ensure non–degenerate eigenvalues. Wei and Ruan [40] have applied the results of Cooke and Grossman to study steady state stability in a two–dimensional neural network model with delay, with equations similar in form to (2.0.1).

To see that our model is in fact of this form, we convert the system (2.2.8) to a single, second–order delay differential equation in $x(t)$ and $x(t-\tau)$:

$$\ddot{x} = -a\dot{x} + b\dot{y} + \hat{\mu}\dot{x}(t-\tau)$$

$$\ddot{x} = -a\dot{x} + b\left[cx - dy\right] + \hat{\mu}\dot{x}(t-\tau)$$

$$\ddot{x} = -a\dot{x} + b\left[cx - \frac{d}{b}\left(\dot{x} + ax - \hat{\mu}x(t-\tau)\right)\right] + \hat{\mu}\dot{x}(t-\tau)$$

$$\ddot{x} = -a\dot{x} + bcx - d\dot{x} - adx + \hat{\mu}dx(t-\tau) + \hat{\mu}\dot{x}(t-\tau)$$

$$0 = \ddot{x} + (a+d)\dot{x} - \hat{\mu}\dot{x}(t-\tau) + (ad-bc)x - \hat{\mu}dx(t-\tau)$$

Thus for our model we obtain the equation

$$\frac{d^2x}{dt^2} + (a+d)\frac{dx}{dt} + (-\hat{\mu})\frac{x(t-\tau)}{dt} + (ad-bc)x(t) + (-\hat{\mu}d)x(t-\tau) = 0, \quad (2.2.17)$$

which is simply (2.2.16) with a replaced with $a + d$, b replaced with $-\hat{\mu}$, c with $ad - bc$ and d with $-\hat{\mu}d$, with characteristic equation (2.2.13). Hence the conditions $a + b \neq 0$ and $c + d \neq 0$ are replaced with $\hat{\mu} \neq a + d$, and $\hat{\mu} \neq a - \frac{bc}{d}$, respectively. Figure 2.3 indicates that the second condition is violated when $\mu = g_L$ and $\mu = g_L + g_K$, the parameter values which lead to equilibrium voltages of $-\infty$ and $+\infty$, respectively, and that there is a single value of μ where the first condition is not met. However, these violations occur for different values of μ, and since both conditions are never violated simultaneously, the characteristic equation will possess non–degenerate roots for all μ. In the instance where $\hat{\mu} = a + d$, the coefficient of the delayed "friction" term and the instantaneous "friction" term are equal in magnitude but opposite in sign. In this case, with $\tau = 0$, the roots of the quadratic characteristic become

$$\lambda_\pm = \pm\sqrt{-[(ad-bc) - \hat{\mu}d]}\,.$$

Since $(ad - bc) - \hat{\mu}d < 0$ for this value of μ, then both roots are real, with $\lambda_+ > 0$ and $\lambda_- < 0$, indicating that (V^*, n^*) is an unstable saddle point. The value where this situation occurs is $\mu \approx 21.57$.

To find changes in stability we look for purely imaginary roots $\lambda = i\omega$ of (2.2.13). Since complex roots occur in conjugate pairs, it suffices to look for

solutions with $\omega > 0$. Hence if $\lambda = i\omega$ is a root such that $\omega \neq 0$, then

$$
\begin{aligned}
0 &= -\omega^2 + i(a+d)\omega - i\hat{\mu}\omega\left[\cos(\omega\tau) - i\sin(\omega\tau)\right] - \hat{\mu}d\left[\cos(\omega\tau) - i\sin(\omega\tau)\right] \\
&\quad +(ad - bc) \\
0 &= -\omega^2 - \hat{\mu}\omega\sin(\omega\tau) - \hat{\mu}d\cos(\omega\tau) + (ad - bc) \\
&\quad +i\left[(a+d)\omega - \hat{\mu}\omega\cos(\omega\tau) + \hat{\mu}d\sin(\omega\tau)\right].
\end{aligned}
$$

Setting separately the real and imaginary parts to zero we obtain

$$
\begin{aligned}
(ad - bc) - \omega^2 - \hat{\mu}\omega\sin(\omega\tau) - \hat{\mu}d\cos(\omega\tau) &= 0 \\
(a+d)\omega - \hat{\mu}\omega\cos(\omega\tau) + \hat{\mu}d\sin(\omega\tau) &= 0.
\end{aligned}
\tag{2.2.18}
$$

By rearranging equations (2.2.18), squaring both equations and adding, we obtain:

$$
\omega^4 + \left[(a+d)^2 - 2(ad - bc) - \hat{\mu}^2\right]\omega^2 + (ad - bc)^2 - \hat{\mu}^2 d^2 = 0.
\tag{2.2.19}
$$

The roots of this quartic equation are

$$
\begin{aligned}
\omega_\pm^2 &= \frac{1}{2}\left(\hat{\mu}^2 - a^2 - d^2 - 2bc\right) \\
&\quad \pm \left\{\frac{1}{4}\left(\hat{\mu}^2 - a^2 - d^2 - 2bc\right)^2 - \left((ad - bc)^2 - \hat{\mu}^2 d^2\right)\right\}^{\frac{1}{2}}.
\end{aligned}
\tag{2.2.20}
$$

Of course, the four roots are given by the $\pm$ square roots of ω_+^2 and ω_-^2, denoted $\pm\omega_+$ and $\pm\omega_-$, respectively.

According to Cooke and Grossman [6], there are two cases to consider:

1. $(ad - bc)^2 < \hat{\mu}^2 d^2 \quad \Rightarrow \quad \hat{\mu}^2 > \left(a - \frac{bc}{d}\right)^2$. In this case there is one imaginary root $\lambda_+ = i\omega_+$, with $\omega_+ > 0$.

2. $(ad - bc)^2 > \hat{\mu}^2 d^2 \quad \Rightarrow \quad \hat{\mu}^2 < \left(a - \frac{bc}{d}\right)^2$. Here, there are two imaginary solutions $\lambda_\pm = i\omega_\pm$, with $\omega_+ > \omega_- > 0$, provided that

    (a) $\hat{\mu}^2 - (a + d)^2 + 2(ad - bc) > 0 \quad \Rightarrow \quad \hat{\mu}^2 > a^2 + d^2 + 2bc$, and

    (b) $\left[\hat{\mu}^2 - (a + d)^2 + 2(ad - bc)\right]^2 > 4\left[(ad - bc)^2 - \hat{\mu}^2 d^2\right]$

$$\Leftrightarrow \quad \left(\hat{\mu}^2 - a^2 - d^2 - 2bc\right)^2 > 4\left((ad - bc)^2 - \hat{\mu}^2 d^2\right),$$

and no such solutions otherwise.

In Case 1, the magnitude of the coefficient of the state variable with delay $(x(t - \tau))$ in (2.2.17) is larger than that without delay, $i.e.$ the instantaneous term $x(t)$. That is, the delay term is dominant. Here, the discriminant of (2.2.20) is positive, and so $\omega_+^2 > 0$ while $\omega_-^2 < 0$. With $\omega_+^2 > 0$, we obtain two real roots, $\pm\omega_+$, one positive and one negative. For convenience, let ω_+ denote $+\omega_+$, the positive square root, since we are only interested in positive real roots of (2.2.19). The are no positive real roots of (2.2.19) associated with ω_-^2, since it is negative and its square root complex. Therefore in this case we obtain only one purely imaginary root $\lambda = i\omega_+$ of the characteristic equation (2.2.13), with $\omega_+ > 0$.

The roles of the coefficients of the delay $(x(t - \tau))$ and instantaneous $(x(t))$ state variable in (2.2.17) are reversed in Case 2, and so the non–delay term is dominant. The extra conditions (a) and (b) ensure that the discriminant of (2.2.20) is again positive, and that the term outside the square root $(\hat{\mu}^2 - (a + d)^2 + 2(ad - bc))$ is positive, so that both ω_+^2 and ω_-^2 are positive. This leads to four real roots of (2.2.19), two positive $(+\omega_\pm)$, and two negative $(-\omega_\pm)$. Hence there are two purely imaginary solutions of (2.2.13), $\lambda_\pm = i\omega_\pm$, with

$\omega_+ > \omega_- > 0$. Here, we let $\omega_+ = +\omega_+$ and $\omega_- = +\omega_-$, the positive square roots, for convenience.

Note that these conditions are independent of the coefficients of the instantaneous and delay first–derivative terms, $\dot{x}(t)$ and $\dot{x}(t-\tau)$ of (2.2.17). However, the magnitude of these coefficients does play a role in determining stability of the equilibrium point in the model with $\tau = 0$ (*cf.* Section 2.2.4). As we shall see, this will in turn influence whether or not the predicted crossings of the imaginary axis are possible. Furthermore, if in Case 2 both sub–conditions (a) and (b) are not met simultaneously, then there will be no positive roots $\omega > 0$ of (2.2.20), and hence no purely imaginary roots of (2.2.13). This, in turn implies no crossing of the imaginary axis, and therefore no change in stability of the equilibrium point.

To find the parameter ranges where the model resides in Cases 1 and 2, we must determine the values of μ for which $\hat{\mu}^2 > \left(a - \frac{bc}{d}\right)^2$, and those for which $\hat{\mu}^2 < \left(a - \frac{bc}{d}\right)^2$. We employ a graphical analysis, and plot the values $\left(a - \frac{bc}{d}\right)^2$ and $\hat{\mu}^2$ versus μ in Figure 2.5.

In Figures 2.5(a) and 2.5(b), we see that $\hat{\mu}^2$ and $\left(a - \frac{bc}{d}\right)^2$ intersect when $\mu = g_{\mathrm{L}}$ and $\mu = g_{\mathrm{L}}+g_{\mathrm{K}}$. For these respective values of μ, the equilibrium voltage tends to $-\infty$ and $+\infty$, and so the program cannot compute the equilibrium voltages, or the values of coefficients b, c, and d. However, we can show using limits that in fact $\left(a - \frac{bc}{d}\right)^2 \to \left(\frac{g_{\mathrm{L}}}{C}\right)^2$ as $\mu \to g_{\mathrm{L}}$. Recall that as $\mu \to g_{\mathrm{L}}$, $V^* \to -\infty$ and $n^* \to 0$. It immediately follows that, as $\mu \to g_{\mathrm{L}}$,

$$a = \frac{g_{\mathrm{L}} + g_{\mathrm{K}}n^*}{C} \quad \Rightarrow \quad a \to \frac{g_{\mathrm{L}}}{C} \quad \text{since} \quad n^* \to 0.$$

(a) $\mu < g_L = 3$.   (b) $\mu > g_L + g_K = 11$.
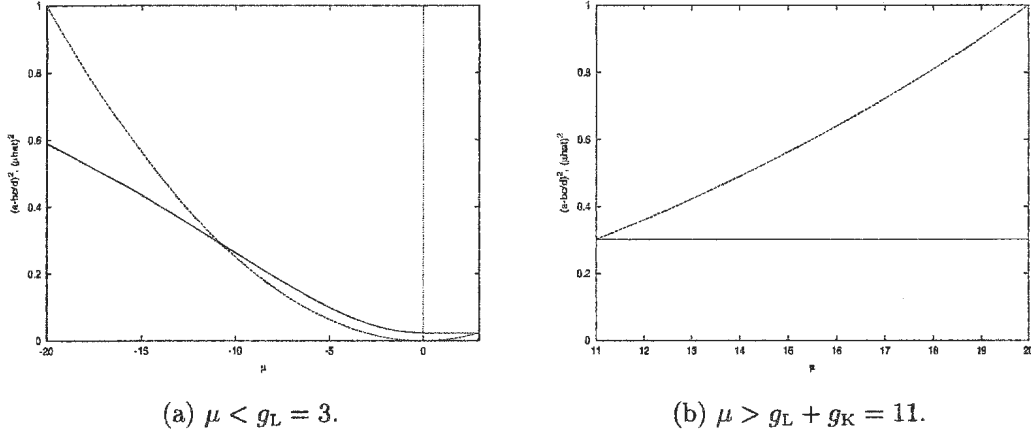
Figure 2.5: Plots of $\hat{\mu}^2$ (dashed curve) and $\left(a - \frac{bc}{d}\right)^2$ (solid curve) versus μ, for the two parameter ranges of μ where system (2.0.1) has a unique equilibrium point.

Next we show that $\frac{bc}{d} \to 0$ as $V^* \to -\infty$:

$$\frac{bc}{d} = \frac{\frac{\overline{\lambda_n}g_K}{2V_4 C}(V_K - V^*)\cosh\left(\frac{V^*-V_3}{2V_4}\right)\operatorname{sech}^2\left(\frac{V^*-V_3}{V_4}\right)}{\overline{\lambda_n}\cosh\left(\frac{V^*-V_3}{2V_4}\right)} = \frac{g_K}{2V_4 C}\frac{(V_K - V^*)}{\cosh^2\left(\frac{V^*-V_3}{V_4}\right)},$$

where we canceled the factor $\overline{\lambda_n}\cosh\left(\frac{V^*-V_3}{2V_4}\right)$, which is non–zero. Taking the limit we obtain

$$
\begin{aligned}
\lim_{V^* \to -\infty} \frac{bc}{d} &= \lim_{V^* \to -\infty} \frac{g_K}{2V_4 C}\frac{(V_K - V^*)}{\cosh^2\left(\frac{V^*-V_3}{V_4}\right)} \\
&= \frac{g_K}{2V_4 C}\lim_{V^* \to -\infty} \frac{-1}{2\cosh\left(\frac{V^*-V_3}{V_4}\right)\cdot \frac{1}{V_4}\sinh\left(\frac{V^*-V_3}{V_4}\right)} \\
&= \frac{g_K}{4C}\lim_{V^* \to -\infty} \frac{-1}{\sinh\left(\frac{2(V^*-V_3)}{V_4}\right)} = 0,
\end{aligned}
$$

since $\sinh(u) \to -\infty$ as $u \to -\infty$, and we applied l'Hôpitals Rule to evaluate the limit. Therefore

$$\lim_{V^* \to -\infty} \left(a - \frac{bc}{d}\right)^2 = \lim_{\substack{V^* \to -\infty \\ n^* \to 0}} \left(a - \frac{bc}{d}\right)^2 = \left(\frac{g_L}{C} - 0\right)^2 = \left(\frac{g_L}{C}\right)^2 = \lim_{\mu \to g_L} \hat{\mu}^2,$$

as desired. A similar limit computation with $\mu \to g_L + g_K$, and $V^* \to \infty$, $n^* \to 1$, verifies that the plots $\left(a - \frac{bc}{d}\right)^2$ and $\hat{\mu}^2$ in Figure 2.5(b) intersect as $\mu \to g_L + g_K$. For $\mu > g_L + g_K$, we find that $\hat{\mu}^2$ is always above $\left(a - \frac{bc}{d}\right)^2$, and so only Case 1 is possible with μ in this range.

Figure 2.5(a) indicates that there is a value of $\mu < 0$, which we denote by μ^*, for which $\hat{\mu}^2 > \left(a - \frac{bc}{d}\right)^2$ for all $\mu < \mu^*$, and $\hat{\mu}^2 < \left(a - \frac{bc}{d}\right)^2$ for all values of $\mu^* < \mu < g_L$. Therefore with $\mu < \mu^*$ the system is in Case 1 for which a single crossing of the imaginary axis is possible, and hence only one change in stability. More accurately, at most one crossing is possible, since the crossing is not automatic — it depends on the transversality condition (*cf.* Section 2.2.6) and the analysis with $\tau = 0$. Note that an exact numerical value for μ^* cannot be obtained, but using Maple we can approximate this value to two decimal places to obtain $\mu^* \approx -10.74$. This gives us the ranges

$$\mu < \mu^* \approx -10.74 \qquad \text{and} \qquad \mu > g_L + g_K = 11$$

for μ which lead to Case 1. To address the Case 2 dynamics of the system, we must determine if the additional criteria (a) and (b) are satisfied for all $\mu \in (\mu^*, g_L)$, or only for a subinterval. Again, this is done graphically by computing the quantities in criteria (a) and (b) of Case 2 for $\mu \in (\mu^*, g_L)$, and then plotting the results. Figure 2.6 contains plots which are used to check conditions (a) and (b).
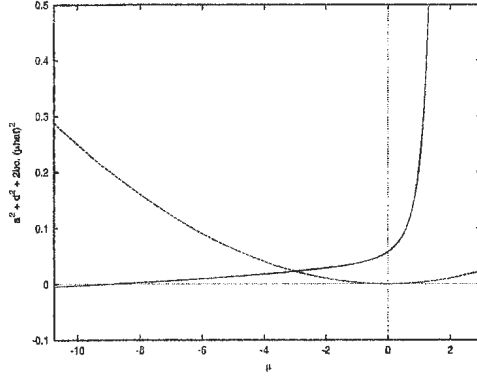
(a) Condition (a).
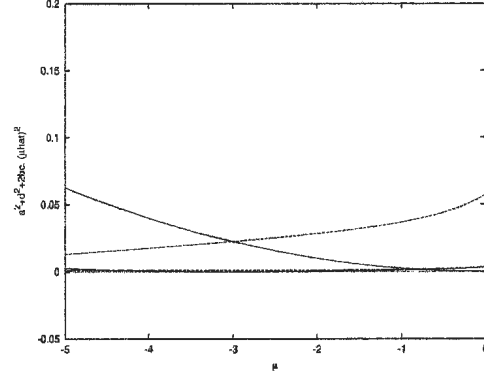
(b) Magnification of 2.6(a).
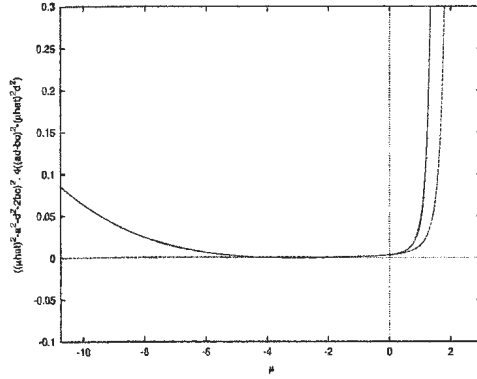
(c) Condition (b).
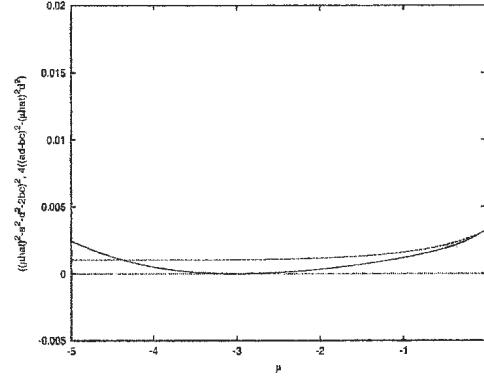
(d) Magnification of 2.6(c).

Figure 2.6: Checking conditions (a) and (b) for Case 2: Plots of $\hat{\mu}^2$ (dashed curve) and $a^2 + d^2 + 2bc$ (solid curve), versus μ, and plots of $\left(\hat{\mu}^2 - a^2 - d^2 - 2bc\right)^2$ (solid curve) and $4\left((ad - bc)^2 - \hat{\mu}^2 d^2\right)$ (dashed curve) versus μ. Magnifications of both are also included.

From Figure 2.6(a), we see that condition (a) is not met for all $\mu \in (\mu^*, g_L)$. A similar situation appears in Figure 2.6(c), in that condition (b) is not satisfied on the entire interval. There are two sub–intervals where condition (b) is met, and one where it is not. Figures 2.6(b) and 2.6(d) are magnifications of Figures 2.6(a) and 2.6(c), and these diagrams indicate that the largest sub–interval of (μ^*, g_L) on which both conditions (a) and (b) of Case 2 are met simultaneously is (μ^*, μ^{**}). Like μ^*, we cannot find the exact numerical value of μ^{**}, but we can approximate this value as $\mu^{**} \approx -4.37$. Therefore with μ in the range $\mu^* < \mu < \mu^{**}$, there are two imaginary solutions $\lambda = i\omega_{\pm}$ of (2.2.13), with $\omega_+ > \omega_- > 0$, and it is in this interval where we may apply the theory for Case 2 presented in [6].

When μ is in the range (μ^{**}, g_L) the model does not fall under Cases 1 or 2. There is a subinterval of (μ^{**}, g_L), denoted by (μ^{**}, μ_i) for which the discriminant in (2.2.20) is negative, and so the roots of (2.2.19) are imaginary. This implies that there are no purely imaginary roots $\lambda = i\omega$ of characteristic equation (2.2.13), and therefore no change in stability of the equilibrium point. The same is true if μ is in (μ_i, g_L), only here the discriminant in (2.2.20) is positive (*i.e.* condition (b) is met), meaning that in (2.2.20) $\omega_{\pm}^2$ are real but negative (since condition (a) is not met). Hence the roots $\omega_{\pm}$ are all imaginary and so there are no purely imaginary roots of (2.2.13), and hence no change in equilibrium point stability with μ in this range.

The theory does not include any conclusions for the case $\hat{\mu}^2 = \left(a - \frac{bc}{d}\right)^2$. Consider the case where $\hat{\mu}^2 = \left(a - \frac{bc}{d}\right)^2 \neq 0$. Then (2.2.19) is reduced to

$$\omega^4 + \left[(a+d)^2 - 2(ad - bc) - \hat{\mu}^2\right]\omega^2 = 0,$$

the roots of which are the square roots of

$$\omega^2 = 0 \qquad \text{and} \qquad \omega^2 = -\left[(a+d)^2 - 2(ad-bc) - \hat{\mu}^2\right].$$

Thus, we obtain a double zero eigenvalue, $\lambda = 0$ (multiplicity two), and a pair of purely imaginary eigenvalues. We shall see that, in some cases, the zero eigenvalues occur for a different value of the delay than the pure imaginary pair, there is no degeneracy. The cases where this situation occurs are addressed as they arise in the analysis.

2.2.6   The Transversality Condition

The transversality condition indicates the direction of change of the real part of the eigenvalue on the imaginary axis, and is determined by the sign of the quantity

$$\left.\frac{d(\text{Re}\lambda)}{d\tau}\right|_{\lambda=i\omega}.$$

A positive sign indicates crossing of the imaginary axis from left to right, while a negative sign indicates crossing from the right to left. If all other eigenvalues besides the complex conjugate pair which cross the axis have negative real part, then this crossing marks a change in stability of the equilibrium point from stable to unstable if the crossing is from left to right, and from unstable to stable if it is right to left. Furthermore, a Hopf bifurcation occurs provided the sign of the derivative is non–zero, and if either all other eigenvalues (of the linear variational equation) have nonzero real parts, or if for (μ, τ) where the crossing occurs, there are no additional purely imaginary roots of (2.2.13) which are integer multiples of $i\omega_\pm$. At those values where a Hopf bifurcation occurs, a branch of periodic solutions emanates.

From Equation (2.2.13), we have

$$\frac{d\lambda}{d\tau} = \frac{-\hat{\mu}(\lambda + d)\lambda e^{-\lambda\tau}}{2\lambda + (a + d) + \hat{\mu}[\tau(\lambda + d) - 1]e^{-\lambda\tau}} \, ,$$

which, along with the fact that a, b, and d are not all zero, indicates that all purely imaginary roots are simple. Also,

$$\left(\frac{d\lambda}{d\tau}\right)^{-1} = \frac{\hat{\mu} - [2\lambda + (a + d)]e^{\lambda\tau}}{\hat{\mu}\lambda(\lambda + d)} - \frac{\tau}{\lambda}, \quad e^{\lambda\tau} = \frac{\hat{\mu}(\lambda + d)}{\lambda^2 + (a + d)\lambda + (ad - bc)} \, .$$

From [6], we know that

$$\text{sign}\left\{\frac{d(\text{Re}\lambda)}{d\tau}\right\}_{\lambda=i\omega} = \text{sign}\left\{\text{Re}\left(\frac{d\lambda}{d\tau}\right)^{-1}\right\}_{\lambda=i\omega}$$

$$= \text{sign}\left\{\text{Re}\left[\frac{-(2\lambda + (a + d))}{\lambda(\lambda^2 + (a + d)\lambda + (ad - bc))}\right]_{\lambda=i\omega}\right.$$

$$\left. + \text{Re}\left[\frac{1}{\lambda(\lambda + d)}\right]_{\lambda=i\omega}\right\}$$

$$= \text{sign}\left\{\frac{(a + d)^2 - 2((ad - bc) - \omega^2}{(a + d)^2\omega^2 + (\omega^2 - (ad - bc))^2} - \frac{1}{\omega^2 + d^2}\right\}$$

$$= \text{sign}\left\{(a + d)^2 - \hat{\mu}^2 - 2(ad - bc) + 2\omega^2\right\} \, ,$$

where Equation (2.2.19) was used in the last step. If we insert expression (2.2.20) for $\omega_{\pm}^2$, we obtain

$$\text{sign}\left\{\frac{d(\text{Re}\lambda)}{d\tau}\right\}_{\lambda=i\omega} = \text{sign}\left\{(a + d)^2 - \hat{\mu}^2 - 2(ad - bc) + \hat{\mu}^2 - (a + d)^2\right.$$

$$\left. + 2(ad - bc) \pm \sqrt{\Delta}\right\}$$

$$= \text{sign}\left\{\pm\sqrt{\Delta}\right\} \, ,$$

where $\Delta = \left(\hat{\mu}^2 - (a+d)^2 + 2(ad-bc)\right)^2 - 4\left((ad-bc)^2 - \hat{\mu}^2 d^2\right)$ is the discriminant of (2.2.20). Hence we see that the sign is positive for ω_+^2 and negative for ω_-^2.

2.2.7 Analysis of the System in Case 1

To summarize the results for the bifurcation analysis of the all–K$^+$ conductance system, we have

<u>Case 1</u> $\left(\hat{\mu}^2 > \left(a - \frac{bc}{d}\right)^2\right)$. This case is satisfied for $\mu < \mu^*$ and $\mu > g_L + g_K$, for which we have only one purely imaginary root $\lambda = i\omega_+$ (with $\omega_+ > 0$) of (2.2.13). Therefore only one crossing of the imaginary axis is possible, and by the transversality condition it follows that this crossing is left to right as τ is increased. This indicates that the only change in stability of the equilibrium point can be from stable to unstable. Consider first $\mu > g_L + g_K$. Since the equilibrium point is unstable for $\tau = 0$, we already have eigenvalues with positive real part (*i.e.* on the right–hand side of the imaginary axis) for $\tau > 0$, and so a left–to–right crossing of the imaginary axis has no bearing on the stability of the equilibrium point, and therefore cannot induce a change in stability. Hence an unstable zero solution of (2.2.6), and therefore an unstable non–zero equilibrium point of (2.0.1)) for $\tau = 0$ cannot become stable with increasing τ. Hence for $\mu > g_L + g_K$, (2.0.1) admits a unique equilibrium point which is unstable for all $\tau \geq 0$.

On the other hand, the equilibrium point (V^*, n^*) of (2.0.1) is stable for $\tau = 0$ provided $\mu < g_L$, and, in particular, for $\mu < \mu^*$, which is the range for Case 1. Hence the left–to–right crossing of the imaginary axis as τ is increased will induce a change in stability of (V^*, n^*), which becomes unstable at the

smallest value of τ for which an imaginary root exists, say τ^*, and remains unstable for all $\tau > \tau^*$. When $\tau = \tau^*$, the system possesses a pair of purely imaginary eigenvalues $\pm i\omega_+$, and all other eigenvalues have strictly negative real parts. Since the transversality condition is satisfied, the Hopf Bifurcation Theorem for DDEs [17] indicates that the system undergoes a Hopf bifurcation at (μ, τ^*), resulting in the emergence of periodic solutions. The calculation required to determine the direction and stability of the bifurcating periodic solutions is presented at the end of this chapter, in section 2.2.9.

The analysis of section 2.2.9 reveals that, for $\mu < \mu^*$, the Hopf bifurcation which occurs at (μ, τ^*) is supercritical, and the bifurcating periodic solutions are stable. Supercritical Hopf bifurcations are such that the bifurcating periodic solutions exist for $\tau > \tau^*$, and stability of the periodic solutions refers to orbital stability. Thus, for each $\mu < \mu^*$, there exists a $\tau^* > 0$, depending on μ, for which the solution of (2.0.1) is non–periodic for $\tau < \tau^*$, and periodic for $\tau > \tau^*$. Once τ is increased past τ^*, stability of the equilibrium point cannot be regained, since we have only one pair of purely imaginary eigenvalues.

The second equation in (2.2.18) can be used to obtain an expression of τ^*, the bifurcation value of τ for a given $\mu \leq -10.74$, in terms of the model parameters and root ω_+:

$$\tau_n = \frac{1}{\omega_+} \cos^{-1} \left\{ \frac{a\omega_+^2 + d(ad - bc)}{\hat{\mu}(\omega_+^2 + d^2)} \right\} + \frac{2\pi n}{\omega_+} \qquad (n = 0, 1, \ldots). \qquad (2.2.21)$$

Note that $\tau^* = \tau_0$ from this sequence of time delays, and that τ^* depends directly on μ. Therefore, expression (2.2.21) indicates how the pair of parameters (μ, τ) are related. If τ is increased past τ^*, then the terms in the sequence (2.2.21) past $\tau^* = \tau_0$ mark the delay times where additional eigenvalues cross the imaginary axis. These additional crossings do not change the stability of

the equilibrium point, which is unstable after the initial crossing, and cannot regain stability. The bifurcation delay times τ^* can be found using (2.2.21) for $\mu < \mu^*$, and from these times we can generate a bifurcation diagram for the system. This diagram, which plots τ^* with respect to μ, is shown in Figure 2.7. Note that, in order to find τ^* for a given $\mu < \mu^*$, we must first evaluate the root ω_+ using (2.2.20). These calculations support our estimate of μ^*, the critical value separating the Case 1 and Case 2 dynamics of the system. A single purely imaginary root is obtained provided $\mu \leq -10.74$, and $\mu = -10.73$ revealed two imaginary roots, $\lambda_\pm = i\omega_\pm$, indicating that the system is in the realm of Case 2.
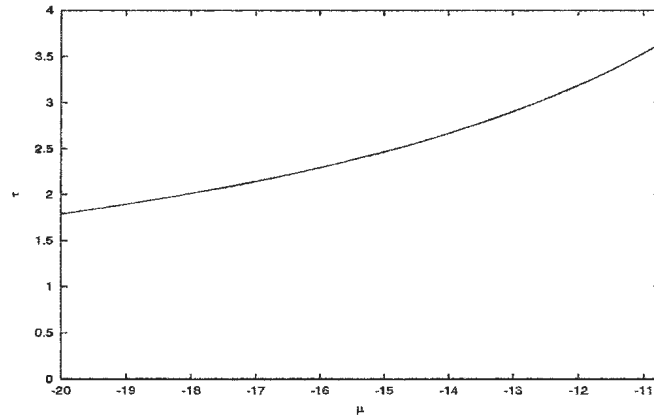
Figure 2.7: Bifurcation Diagram plotting τ^* vs. μ for system (2.0.1) with $\mu < \mu^* \approx -10.74$ (Case 1).

A final remark for this case is that periodic solutions emerging through Hopf bifurcation (in Case 1) in this conductance system are only possible for a feedback signal which is inhibitory, since $\mu^* \approx -10.74 < 0$.

Figure 2.8 illustrates the numerical results for Case 1, by showing the

numerical solution of (2.0.1) with $\mu = -10.8$ and different values of τ. Model parameters μ and τ are specified for each plot, and other model parameters are as in Table 2.1. The delay initial conditions, that is, the functions $V(\theta)$ and $n(\theta)$ for $-\tau \leq \theta \leq 0$, are set as the constant functions $V(\theta) = -50$ and

$$n(\theta) = n_\infty(V(\theta)) = n_\infty(-50) = \frac{1}{2}\left[1 + \tanh\left(\frac{-50 - V_3}{V_4}\right)\right],$$

chosen to correspond to the original initial conditions for this conductance system used by Morris and Lecar. The software package XPPAUT [11] was used for numerical simulations, and all results were confirmed using the DDE solver dde23 [36] for Matlab. All numerical simulations included in this thesis plot the numerical time–series solution $V(t)$ versus t, along with the delay phase plane $V(t - \tau)$ versus $V(t)$.

In Figure 2.8(b) we see that with $\mu = -10.8$ and a delay of $\tau = 3$, the system settles down to a stable equilibrium point after a few transient oscillations. However, by increasing the delay only slightly to $\tau = 4$ in Figure 2.8(d), we find that the stability of the equilibrium point has been lost, and the system exhibits periodicity; note the limit cycle in the delay phase plane in Figure 2.8(c). The simulations reveal that periodic solutions only appear as τ is increased through τ^*. Furthermore, the periodic solution is stable, and exists for $\tau > \tau^*$, in agreement with the detailed Hopf bifurcation analysis. Therefore the system passes through a Hopf bifurcation at $(\mu = -10.8, \tau^*)$, where $3 < \tau^* = 3.6 < 4$. Also, increasing τ further will not change the stability of the equilibrium point, and so (V^*, n^*) is unstable for all time delays $\tau > \tau^*$. The low Hopf bifurcation value of τ in this particular case is due to the relatively large magnitude of μ, which measures the strength of the feedback term.
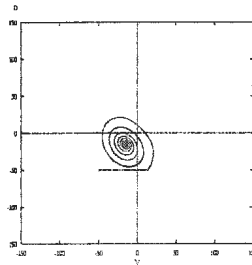
(a) $V(t - \tau)$ vs. V.
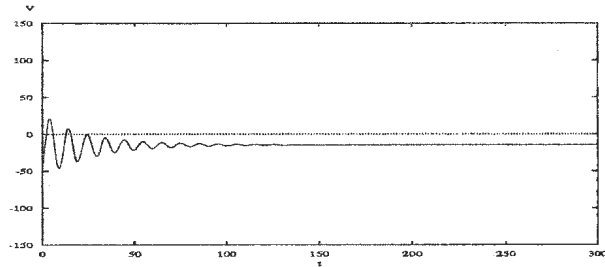
(b) $V(t)$ vs. t for $\tau = 3$.
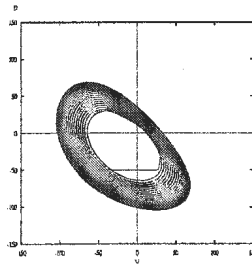
(c) $V(t - \tau)$ vs. V.
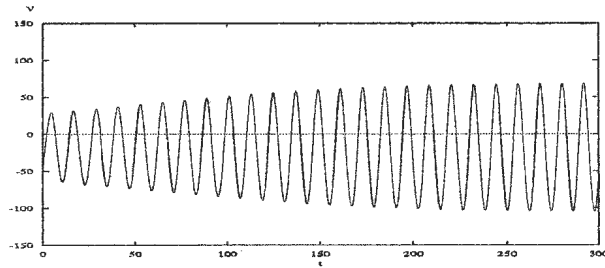
(d) $V(t)$ vs. t for $\tau = 4$.

Figure 2.8: Numerical simulation of (2.0.1) with the parameters in the range of Case 1: $\mu = -10.8$ with delay τ increased from $\tau = 3$ to $\tau = 4$ ms, illustrating a change in stability of the equilibrium voltage as τ is increased.

Before examining the Case 2 dynamics of (2.0.1), we comment on the values of μ for which $\hat{\mu}^2 = \left(a - \frac{bc}{d}\right)^2$. These values are $\mu = \mu^*$, which separates Case 1 from Case 2, and $\mu = g_L$, $\mu = g_L + g_K$, for which the equilibrium voltages approach $-\infty$ and $+\infty$, respectively. We are not concerned with the latter two cases, which are physiologically unrealistic. Consider the special case $\mu = \mu^*$. We saw in Section 2.2.5 that the condition $\hat{\mu}^2 = \left(a - \frac{bc}{d}\right)^2$ leads to a double zero eigenvalue and a pair of purely imaginary eigenvalues. By examining the equation defining τ^* of Case 1, (2.2.21), we find that the two zero eigenvalues occur for a different value of τ than the pure imaginary pair. In fact, as $\omega_+ \to 0$, it appears that $\tau^0 \to \infty$, where τ^0 represents the delay value where the zero eigenvalues occur. Therefore for $\tau = \tau^*$, which corresponds to the pair of purely imaginary eigenvalues, there is no degeneracy. As such, a change in equilibrium point stability and a Hopf bifurcation is expected as τ is increased through τ^*. For the approximate value $\mu^* \approx -10.74$, numerical simulations indicate that the equilibrium point (V^*, n^*) is stable for all $\tau < \tau^* = 3.6$, and loses stability at τ^* via a supercritical Hopf bifurcation, which gives rise to stable periodic solutions. That is, the dynamics are qualitatively similar to the Case 1 dynamics discussed in the previous section.

2.2.8 Analysis of the System in Case 2

Case 2 $\left(\hat{\mu}^2 < \left(a - \frac{bc}{d}\right)^2\right)$. The model satisfies the condition listed for all μ such that $\mu^* < \mu < g_L$. The additional conditions

(a) $\hat{\mu}^2 > (a + d)^2 - 2(ad - bc)$, and

(b) $\left(\hat{\mu}^2 - (a + d)^2 + 2(ad - bc)\right)^2 > 4\left((ad - bc)^2 - \hat{\mu}^2 d^2\right)$

are satisfied provided $\mu^* < \mu \leq \mu^{**} = -4.37$. Recall that, for these values of μ, the equilibrium point (V^*, n^*) of (2.0.1) is a stable spiral for $\tau = 0$. In Case 2 there are two purely imaginary roots $\lambda_\pm = i\omega_\pm$ of (2.2.13) with $\omega_+ > \omega_- > 0$, and that $\text{sign}\left\{ \frac{d(\text{Re}\,\lambda)}{d\tau} \right\}_{\lambda=i\omega}$ is positive for ω_+^2 and negative for ω_-^2. The crossing of the imaginary axis from left to right with increasing τ occurs whenever τ assumes a value corresponding to ω_+, and crossing from right to left occurs for values of the delay τ corresponding to ω_-. In this case, there are two sets of values of τ for which there are imaginary roots of the characteristic equation, obtained from Equation (2.2.18):

$$\tau_{n,1} = \frac{1}{\omega_+} \cos^{-1}\left\{ \frac{a\omega_+^2 + d(ad - bc)}{\hat{\mu}(\omega_+^2 + d^2)} \right\} + \frac{2\pi n}{\omega_+} \qquad (n = 0, 1, \cdots)$$

$$\tau_{n,2} = \frac{1}{\omega_-} \cos^{-1}\left\{ \frac{a\omega_-^2 + d(ad - bc)}{\hat{\mu}(\omega_-^2 + d^2)} \right\} + \frac{2\pi n}{\omega_-}. \tag{2.2.22}$$

Since the zero solution of (2.2.7) is stable for $\tau = 0$ with $\mu^* < \mu \leq \mu^{**}$, then we must have $\tau_{0,1} < \tau_{0,2}$. That is, the initial left–to–right crossing of the imaginary axis occurs as τ is increased through $\tau_{0,1}$, and the initial right–to–left crossing occurs as τ is further increased through $\tau_{0,2}$. Also, since

$$\tau_{n+1,1} - \tau_{n,1} = \frac{2\pi}{\omega_+} < \frac{2\pi}{\omega_-} = \tau_{n+1,2} - \tau_{n,2},$$

there can only be a finite number of switches between stability and instability, after which instability prevails (for more details on this stability switching, refer to [6]).

Consider $\mu \in (\mu^*, \mu^{**}]$. To determine the number of stability switches possible for a given value of μ in this interval, we compute the terms of the

sequences $\tau_{n,1}$, $\tau_{n,2}$, and look for two consecutive left to right crossings of the imaginary axis, *i.e.* find k such that $\tau_{k,1} < \tau_{k+1,1} < \tau_{k,2}$. When this occurs, $\tau_{k,1}$ will mark the final stability change, to give a total of $2k + 1$ stability switches. For $\mu \in (\mu^*, -5.02)$, only one change in stability is possible, from stable to unstable as τ is increased. With μ in this interval, the results are qualitatively similar to those reported for Case 1, in that as τ is increased through $\tau^* = \tau_0$, the equilibrium point (V^*, n^*) loses stability and remains unstable if τ is increased further. Also, the Hopf bifurcation which occurs at (μ, τ^*) is supercritical and branches to stable oscillations.

On the other hand, if $-5.02 \leq \mu \leq \mu^{**}$, multiple switches in stability are evident: for most values of μ in this range near the lower end of the interval, three changes in stability occur as τ is increased before instability persists. For values of μ in the upper portion of this interval, the number of stability switches increases to 5, 7, 9, 11, 13 as $\mu \to \mu^{**}$ from the left, and up to 27 stability switches are possible with $\mu = -4.37$, the approximate value of μ^{**}. These results were obtained by considering μ in this range accurate to two decimal places. As $|\mu|$ increases, the delay times marking the changes in stability decrease, and as the number of possible stability switches increases, the time delay where the final switch to instability occurs increases. For example, with $\mu = -4.37$, 27 stability changes are possible, and the final switch occurs when $\tau \approx 645$ ms. But for $\mu = -5.02$, only three changes in stability are observed, and the final switch occurs when $\tau \approx 41$ ms.

By computing the terms of the sequences in (2.2.22), we can generate bifurcation diagrams which describe how the delay times vary with μ. In Figures 2.9(a) and 2.9(b), the plots of $\tau_{0,1}$ and $\tau_{0,2}$ versus μ are shown for

$\mu \in (\mu^*, \mu^{**}]$. Since there is no gap between the values of μ which place the system in Cases 1 and 2, we expect the curve describing $\tau_{0,1}$ vs. μ to be a smooth continuation of the τ^* vs. μ curve obtained in Case 1, since both times correspond to the ω_+ root. This is confirmed in Figure 2.9(c), which combines the curves of $\tau* = \tau_{0,1}$ of Case 1 along with $\tau_{0,1}$ and $\tau_{0,2}$ of Case 2. Computing these roots and values of τ in the sequences supports our earlier estimation for $\mu^{**} \approx -4.37$, since no real roots were found for $\mu = -4.36$. The final bifurcation diagram we include demonstrates the stability switching properties of the model with $\mu \in [-5.02, -4.37]$: Figure 2.10 contains the terms of the sequences $\tau_{n,1}$ and $\tau_{n,2}$ which give rise to stability changes in the equilibrium point for μ in the indicated range, and up to 13 stability switches are included. Note that the intervals of μ exhibiting more stability changes get smaller as the number of switches increases.

We remark that no change(s) in stability occur at the cusp points in Figure 2.10. At these points, we have $\tau_{k,2} = \tau_{k+1,1}$ ($k \in \{0, 1, \ldots, 6\}$, since up to 13 switches are possible), and so as τ is increased through this common critical value, there are two pairs of purely imaginary eigenvalues, one pair corresponding to a left to right crossing of the imaginary axis, the other to a right to left crossing. The pair of eigenvalues which cross from right to left are the same pair which crossed from left to right at $\tau_{k,1}$. As τ is increased through $\tau_{k,2} = \tau_{k+1,1}$, the left to right crossing maintains the instability in the equilibrium point, and for those values of μ where a cusp point arises, the final stability switch occurs when $\tau = \tau_{k,1}$.

The system undergoes a Hopf bifurcation when the equilibrium point (V^*, n^*) changes stability, which occurs when the delay τ assumes the values $\tau_{0,1}$ and
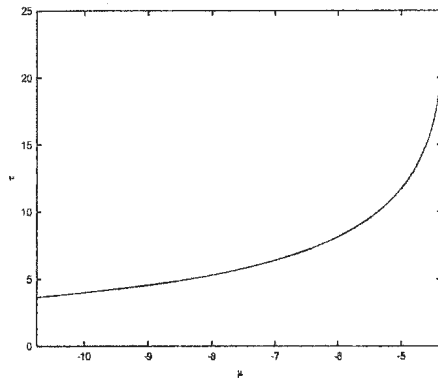
(a) $\tau_{0,1}$ vs. μ.
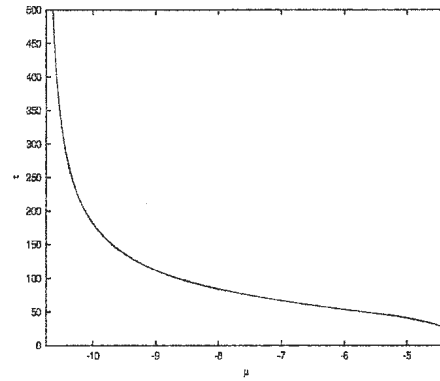
(b) $\tau_{0,2}$ vs. μ.
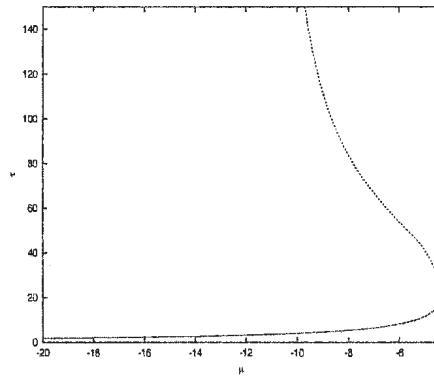
(c) τ^* (solid), $\tau_{0,1}$ (dashed), and
$\tau_{0,2}$ (dotted) vs. μ.

Figure 2.9: Bifurcation Diagrams: The values $\tau_{0,1}$ and $\tau_{0,2}$ versus μ for Case 2, and shown together along with the τ^* values of Case 1.
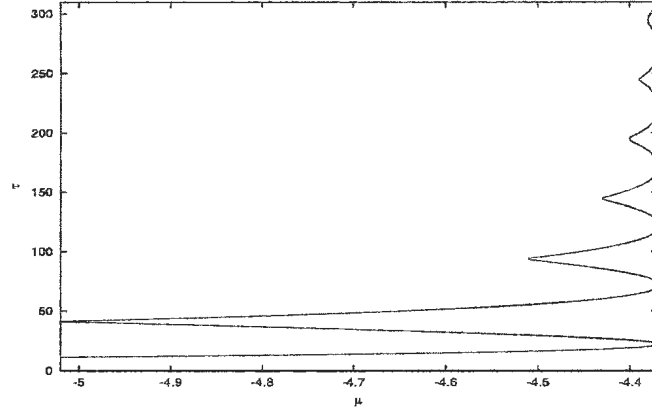
Figure 2.10: Bifurcation Diagram plotting the terms of $\tau_{n,1}$ and $\tau_{n,2}$ which give rise to stability changes for $\mu \in [-5.02, -4.37]$. The values of μ for which the model exhibits up to 13 stability switches are indicated.

$\tau_{0,2}$. The Hopf bifurcations which occur with the $\tau_{n,1}$, sequence are supercritical and branch to stable oscillations, while those associated with $\tau_{n,2}$ sequence are subcritical and branch to stable oscillations. These results are obtained from the detailed Hopf bifurcation analysis carried out in section 2.2.9. There is numerical evidence to suggest that the periodic solutions emanating from the subcritical Hopf bifurcation(s) at $\tau_{k,2}$ are from the same branch of stable solutions which appeared via the supercritical Hopf bifurcation at $\tau_{k,1}$. With τ just above $\tau_{0,1}$, the amplitude of the periodic solution increases, but further increasing τ causes the amplitude to decrease. As $\tau \to \tau_{0,2}$, the amplitude decreases and appears to approach zero.

To summarize, for $\mu \in [-5.02, \mu^{**}]$ system (2.0.1) possesses a single equilibrium point (V^*, n^*), which is stable for all $\tau < \tau_{0,1}$. When τ is increased through $\tau_{0,1}$, the equilibrium point loses stability, and a branch of stable pe-

riodic solutions emerges via a supercritical Hopf bifurcation. With $\tau_{0,1} < \tau <$ $\tau_{0,2}$, the system possesses an unstable equilibrium point and a stable limit cycle. As τ is increased through $\tau_{0,2}$, the equilibrium point regains stability and a branch of stable periodic solutions disappears through a subcritical Hopf bifurcation. Then, with $\tau_{0,2} < \tau < \tau_{1,1}$, the system admits only a stable equilibrium point, but a branch of stable periodic solutions emanates from a second supercritical Hopf bifurcation at $\tau_{1,1}$ when the equilibrium point loses stability. This trend continues until the final stability switch. Figure 2.11 contains a schematic bifurcation diagram illustrating this conjectured bifurcation sequence for the case where three stability switches are possible. Bifurcation diagrams such as Figure 2.11 concisely depict the behavior of a system as a parameter is varied. In schematic bifurcation diagrams appearing in this thesis, solid lines represent stable equilibria, and dashed lines represent unstable equilibria. Stable periodic orbits are represented by filled circles, and unstable periodic orbits by unfilled circles.
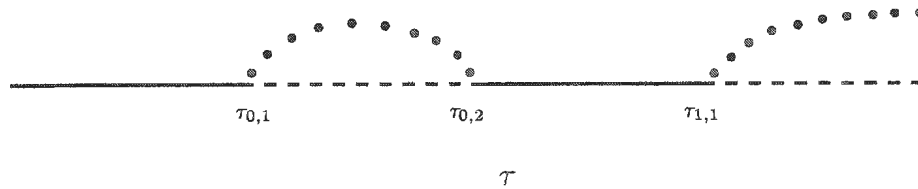
Figure 2.11: Conjectured bifurcation structure of system (2.0.1) with three stability switches as τ is increased.

Numerical simulations are included in Figure 2.12 to illustrate the stability–switching phenomenon predicted for this model. Here, we examine the spe-

cific case $\mu = -4.7$, which is in the range where we expect multiple stability switches. With $\mu = -4.7$, the Cooke–Grossman theory predicts changes in stability occur when the delay τ is increased through the values $\tau_{0,1} = 13.9$, $\tau_{0,2} = 34.8$, and $\tau_{1,1} = 48.4$. Included in Figure 2.12 are the time–series solutions for four different values of τ: $\tau = 10, 20, 43,$ and 55. With delay $\tau = 10$ ms, we find that the solution settles down to a stable constant equilibrium voltage after a few transient oscillations. Note that this initial time delay is less than $\tau_{0,1}$, which marks the first change in stability of the equilibrium point. The first stability change is observed by increasing the delay to $\tau = 20$, which is above $\tau_{0,1}$, and included in Figure 2.12(d). Here, we see that the equilibrium voltage is unstable, and the system exhibits stable periodic solutions, as a result of the supercritical Hopf bifurcation. Two further stability changes can be seen by taking $\tau = 43 \in [\tau_{0,2}, \tau_{1,1}]$ and $\tau = 55 > \tau_{1,1}$, the value where the final stability switch occurs. The equilibrium voltage cannot re–gain stability once τ is increased beyond this value. The sequence of figures shown here compliment the schematic bifurcation diagram in Figure 2.11, which depicted the dynamics of (2.0.1) with three stability switches. The initial functions in Figure 2.12 are $V(\theta) = -20$, $n(\theta) = n_\infty(-20)$, $\theta \in [-\tau, 0]$ to illustrate the local behavior of the system near the equilibrium point.

With $\mu \in (\mu^*, -5.02)$, the model satisfies all conditions of Case 2, but only one change in stability is possible, since $\tau_{1,1} < \tau_{0,2}$. In this respect, the results for the model with μ in this range are similar to the results for those $\mu < \mu^*$ where Case 1 occurs. Figure 2.13 is a numerical simulation of system (2.0.1) with $\mu = -8$, a representative of this case. Initial conditions are as in Figure 2.8. With a delay of $\tau = 4$ ms the equilibrium voltage is stable, and
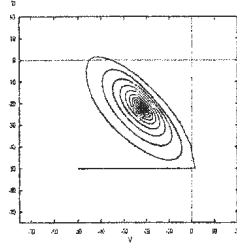
(a) $V(t-\tau)$ vs. V.
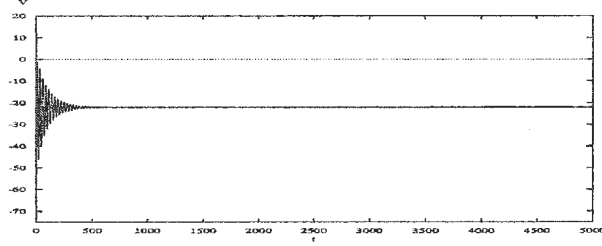
(b) $V(t)$ vs. t for $\tau = 10$ ms.
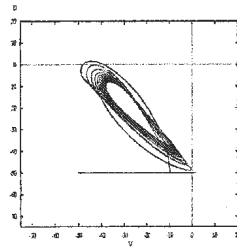
(c) $V(t-\tau)$ vs. V.
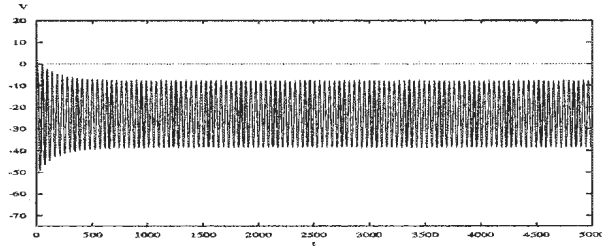
(d) $V(t)$ vs. t for $\tau = 20$.
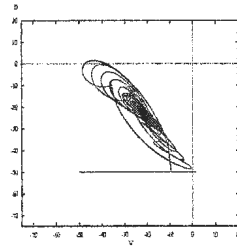
(e) $V(t-\tau)$ vs. V.
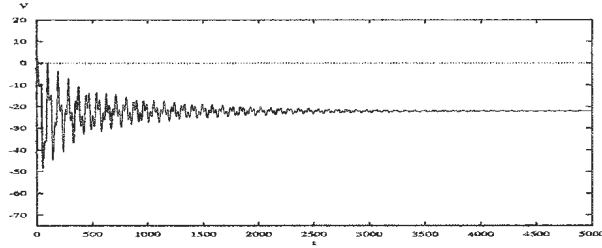
(f) $V(t)$ vs. t for $\tau = 43$.
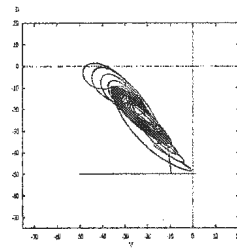
(g) $V(t-\tau)$ vs. V.
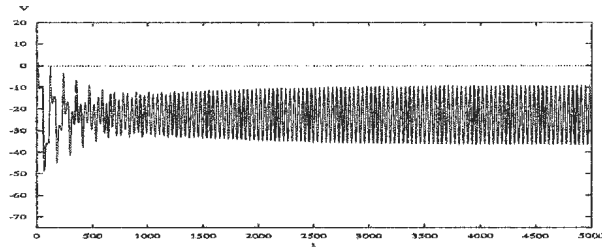
(h) $V(t)$ vs. t for $\tau = 55$.

Figure 2.12: Numerical simulation of of system (2.0.1) with $\mu = -4.7$ (Case 2), illustrating the stability switching of the (V^*, n^*) as τ is increased.

the solution approaches a constant value after a brief transient period. If the delay is increased to $\tau = 6$ ms, then stability of the equilibrium is lost, as the system has passed through a supercritical Hopf bifurcation (at $\tau = 5.3$) and a stable periodic solution has emerged.
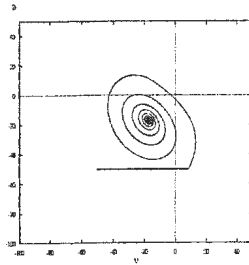
(a) $V(t-\tau)$ vs. V.
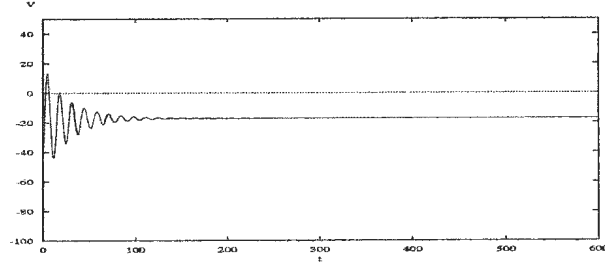
(b) $V(t)$ vs. t for $\tau = 4$.
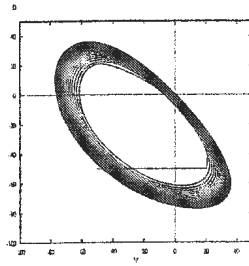
(c) $V(t-\tau)$ vs. V.
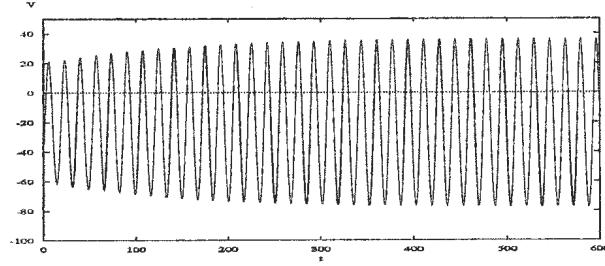
(d) $V(t)$ vs. t for $\tau = 6$.

Figure 2.13: Numerical simulation of (2.0.1) with the parameters in the range of Case 2: $\mu = -8$. With delay $\tau = 4$ the equilibrium point is stable, but becomes unstable if we increase the delay to $\tau = 6$. Periodic solutions arise as the system undergoes a Hopf bifurcation.

Since $\mu^{**} \approx -4.37 < 0$, stability switching is only possible for the all–K$^+$ conductance system (2.0.1) with inhibitory feedback. Therefore, sustained oscillations arising through Hopf bifurcation are possible in the all–K$^+$ con-

ductance system (2.0.1) with inhibitory feedback.

Finally, we consider μ in a range where the model does not satisfy the criteria for Case 1 or Case 2. This occurs for values $\mu^{**} < \mu < g_\mathrm{L}$, an interval which includes both inhibitory and excitatory feedback. Recall that, with μ in this range, the equilibrium is stable for $\tau = 0$. Since there are no purely imaginary roots of (2.2.13), then there are no crossings of the imaginary axis and hence no changes in equilibrium point stability. Thus we expect (V^*, n^*) to be stable for all $\tau > 0$, and do not anticipate periodic behavior. Figures 2.14 and 2.15 show the solution to the model with inhibitory feedback ($\mu = -2.5$) and excitatory feedback ($\mu = 2$), respectively, for values of μ in this range. In both cases, we find that the equilibrium voltage of the model is stable, and even a ten–fold increase in the magnitude of the delay has no affect on the long–term stability of the equilibrium. Here, the strength of the feedback is relatively weak, and it appears that no value of the delay τ, no matter how large, can cause the equilibrium to lose stability. Initial conditions for Figures 2.14 and 2.15 are as in Figure 2.8.

No additional behavior was detected for the all–potassium system. A large sample of initial conditions all led to the same behavior as the numerical simulations presented here, and hence we conjecture that the full dynamics of the system are accounted for by the Cooke–Grossman theory relating to equilibrium point stability, and by the Hopf bifurcation theory for DDEs. Of course, this is not true for those values of μ where the system does not have an equilibrium point, and for these cases we observed that in numerical simulations, the voltage approached $\pm\infty$. The biophysical interpretation of the voltage $V \to \pm\infty$ is discussed in Chapter 5.
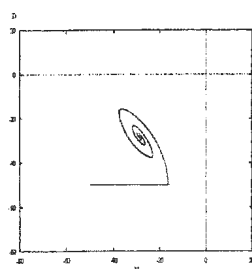
(a) $V(t - \tau)$ vs. V.
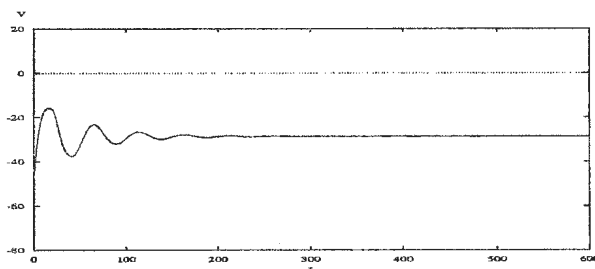
(b) $V(t)$ vs. t for $\tau = 20$.
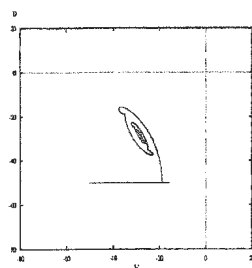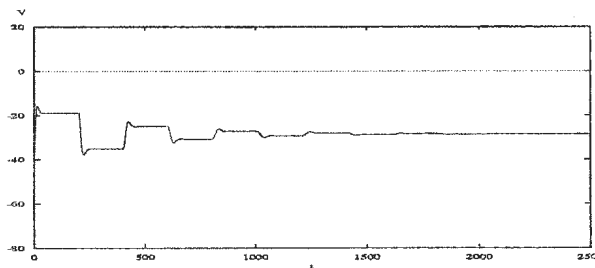
(c) $V(t - \tau)$ vs. V.

(d) $V(t)$ vs. t for $\tau = 200$.

Figure 2.14: Numerical simulation of system (2.0.1) for weak inhibitory feed-back. Here, $\mu = -2.5$, and the delay is increased from $\tau = 20$ to $\tau = 200$, illustrating that the equilibrium remains stable as the delay is increased.
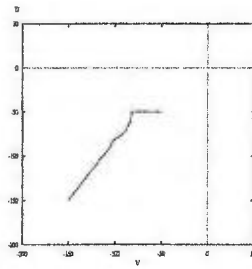
(a) $V(t-\tau)$ vs. V.
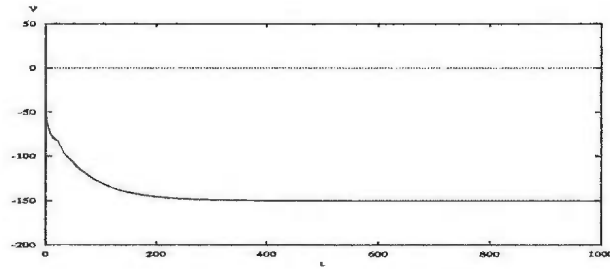
(b) $V(t)$ vs. t for $\tau = 20$.
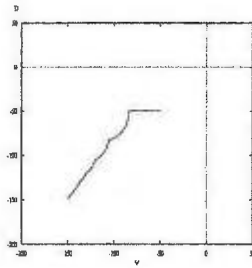
(c) $V(t-\tau)$ vs. V.
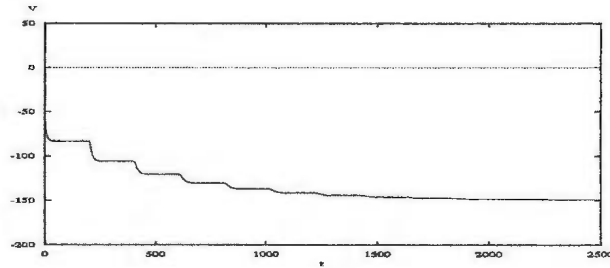
(d) $V(t)$ vs. t for $\tau = 200$.

Figure 2.15: Numerical simulation of system (2.0.1) for weak excitatory feedback. Here, $\mu = 2$, and the delay is increased from $\tau = 20$ to $\tau = 200$, illustrating that the equilibrium remains stable as the delay is increased.

The main results of this chapter (including Section 2.2.9), with respect to equilibrium point stability and Hopf bifurcation, can be summarized by the following theorem:

Theorem 2.2.8.1. *Assume that parameters in system (2.0.1) are as in Table 2.1. Then we have the following:*

1. *If $\mu < \mu^*$, then (V^*, n^*) is stable for all $\tau \in [0, \tau^*)$, where μ^*, τ^* are defined earlier, and unstable for all $\tau > \tau^*$. A supercritical Hopf bifurcation occurs at $\tau = \tau^*$, and the emerging periodic solutions are orbitally stable.*

2. *If $\mu^* < \mu < \mu^{**}$, then (V^*, n^*) is capable of a finite number of stability switches before instability persists (μ^{**} defined earlier). Transitions from stability to instability occur with $\tau_{n,1}$ terms of (2.2.22), while those from instability to stability occur with $\tau_{n,2}$ terms, $n = 0, 1, \ldots$. A total of $2k+1$ switches is possible, where k satisfies $\tau_{k,1} < \tau_{k+1,1} < \tau_{k,2}$. At each $\tau_{n,1}$ ($\tau_{n,2}$) where a stability change occurs, a supercritical (subcritical) Hopf bifurcation occurs, and the emerging periodic solutions are orbitally stable (stable).*

3. *If $\mu^{**} < \mu < g_L$, then (V^*, n^*) is stable for all $\tau \geq 0$.*

4. *If $\mu > g_L + g_K$, then (V^*, n^*) is unstable for all $\tau \geq 0$.*

The following section 2.2.9 contains the detailed Hopf bifurcation analysis of system (2.0.1), while physiological implications of the results presented here are addressed in Chapter 5.

2.2.9 Direction and Stability of Hopf Bifurcation

The previous sections indicate that system (2.0.1) is capable of undergoing Hopf bifurcation when $\mu < \mu^{**}$. Furthermore, whenever stability of the equilibrium point (V^*, n^*) changed, a Hopf bifurcation occurred. In this section, we present a detailed Hopf bifurcation analysis to study the direction, stability, and the period of bifurcating periodic solutions. We wish to verify that, for $\mu < -5.02$, only one supercritical Hopf bifurcation takes place as τ is increased past τ^*, and that alternating super– and sub–critical Hopf bifurcations occur as τ is increased through the values $\tau_{n,1}$, $\tau_{n,2}$, $n = 0, 1, \ldots$, respectively, if μ is in the range $-5.02 \le \mu \le -4.37$. The method used to analyse these features is based on the normal form method and the center manifold theory developed by Hassard, Kazarinoff, and Wan [20].

Consider system (2.0.1) with $\mu < \mu^{**}$. Recall that the Cooke–Grossman theory ensures that all eigenvalues other than $\pm i\omega_+$ have negative real parts when $\tau = \tau_{0,1}$. Similarly, when $\tau = \tau_{0,2}$, the system possesses a pair of purely imaginary eigenvalues $\pm i\omega_-$, and all other characteristic roots have strictly negative real parts. In Section 2.2.6 we verified that the transversality condition is satisfied in each case. The system (2.0.1) also satisfies the required conditions on the continuity of the nonlinearity, and so all hypotheses for the DDE Hopf bifurcation theorem [17] (Theorem 11.1) are met. Therefore we conclude that a Hopf bifurcation occurs for system (2.0.1) when $\tau = \tau_{0,1}$ and $\tau = \tau_{0,2}$. The same is true as τ is increased through the delay times $\tau_{n,1}$, and $\tau_{n,2}$, $n = 1, 2 \ldots$, while $\tau_{k,2} < \tau_{k+1,1}$, $k = 1, 2, \ldots$, the condition which specifies the number of stability switches. We noted earlier that, for the cusp points in Figure 2.10, no change in stability takes place since there is a simultaneous

left to right and right to left crossing of the imaginary axis. Since there are two pairs of purely imaginary eigenvalues in these cases, the Hopf bifurcation theorem for DDEs is not met, and hence no Hopf bifurcation occurs at these points. Such Hopf–Hopf interaction points have been studied in neural network models with delay [37], but we do not investigate these points of our model further.

Having determined that Hopf bifurcation(s) are possible when $\tau = \tau_{n,1}$ and $\tau_{n,2}$, $n = 0, 1, \ldots$, we turn to the direction and stability of periodic orbits emanating from these bifurcations. The analysis which follows is similar to that by Plant [32] and Wei and Ruan [40]. We consider the eigenvalues to be a function of τ, and when $\tau = \tau_{n,1}$, $n = 0, 1, \ldots$, the root

$$\lambda(\tau) = \alpha(\tau) + i\omega(\tau)$$

of (2.2.13) satisfies $\alpha(\tau_{n,1}) = 0$, $\omega(\tau_{n,1}) = \omega_+$, and has the property

$$\frac{d\alpha(\tau_{n,1})}{d\tau} > 0,$$

where $n = 0, 1, \ldots$, which is simply the transversality condition considered earlier. In the case of $\tau = \tau_{n,2}$, the root $\lambda(\tau)$ satisfies $\alpha(\tau_{n,2}) = 0$, $\omega(\tau_{n,1}) = \omega_-$, and has the property

$$\frac{d\alpha(\tau_{n,2})}{d\tau} < 0,$$

where $n = 0, 1, \ldots$. If we let $\tau = \tau_{n,1} + \gamma$, $\gamma \in \mathbb{R}$, $n = 0, 1, \ldots$, then $\gamma = 0$ is the Hopf bifurcation value for (2.0.1). The same is true if we let $\tau = \tau_{n,2} + \gamma$. For convenience, assume that $\tau = \tau_{n,1}$ or $\tau = \tau_{n,2}$, $n = 0, 1, \ldots$, and let ω be the corresponding root of (2.2.19), that is $\omega = \omega_+$ or $\omega = \omega_-$, to carry out the analysis. The actual values of τ and ω are only important once the calculation

is complete. We choose the phase space to be $C = C([-\tau, 0], \mathbb{R}^2)$, and concern ourselves with only real solutions. Expanding the hyperbolic trigonometric functions, we may write (2.2.6), the nonlinear system with equilibrium point shifted to the origin, in the form

$$
\begin{aligned}
\frac{dx}{dt} &= -ax + by + \hat{\mu}x(t - \tau) - \alpha xy \\
\frac{dy}{dt} &= cx - dy - \frac{c}{V_4}\left(\beta_v - \frac{1}{2}\beta_u\right)x^2 - \frac{d}{2V_4}\beta_u xy \\
&\quad - \frac{c}{V_4^2}\left[\frac{5}{24} + \beta_v\left(\frac{1}{2}\beta_u - \beta_v\right)\right]x^3 - \frac{d}{8V_4^2}x^2 y + O(x^4),
\end{aligned}
\tag{2.2.23}
$$

where

$$
\beta_u = \tanh(u), \quad \beta_v = \tanh(v), \quad u = \frac{V^* - V_3}{2V_4}, \quad v = \frac{V^* - V_3}{V_4}, \quad \alpha = \frac{g_K}{C},
$$

and the coefficients a, b, c, d and $\hat{\mu}$ were defined earlier for the linearised system (2.2.8). For $\phi = [\phi_1, \phi_2]^{\mathrm{T}} \in C$, let

$$
L_\gamma \phi = \begin{bmatrix} -a & b \\ c & -d \end{bmatrix} \phi(0) + \begin{bmatrix} \hat{\mu} & 0 \\ 0 & 0 \end{bmatrix} \phi(-\tau),
\tag{2.2.24}
$$

and define

$$
\begin{aligned}
F(\gamma, \phi) &= \begin{bmatrix} -\alpha\phi_1(0)\phi_2(0) \\[2ex] -\dfrac{c}{V_4}\left(\beta_v - \dfrac{1}{2}\beta_u\right)\phi_1^2(0) - \dfrac{d}{2V_4}\beta_u\phi_1(0)\phi_2(0) \end{bmatrix} \\[3ex]
&\quad + \begin{bmatrix} 0 \\[2ex] -\dfrac{c}{V_4^2}\left[\dfrac{5}{24} + \beta_v\left(\dfrac{1}{2}\beta_u - \beta_v\right)\right]\phi_1^3(0) - \dfrac{d}{8V_4^2}\phi_1^2(0)\phi_2(0) \end{bmatrix} + O(x^4)
\end{aligned}
$$

By the Riesz representation theorem, there exists a 2×2 matrix–valued function $\eta(\cdot, \gamma) : [-\tau, 0] \to \mathbb{R}^{2^2} = \mathbb{R}^4$ whose components are functions of bounded variation such that

$$L_\gamma \phi = \int_{-\tau}^{0} d\eta(\theta, \gamma) \phi(\theta)$$

for all $\phi \in C$. Specifically, we choose

$$\eta(\theta, \gamma) = \begin{cases} \begin{bmatrix} -a & b \\ c & -d \end{bmatrix}, & \theta = 0, \\[2em] \begin{bmatrix} \hat{\mu} & 0 \\ 0 & 0 \end{bmatrix} \delta(\theta + \tau), & \theta \in [-\tau, 0), \end{cases}$$

where δ is the Dirac–delta function. For $\phi \in C^1([-\tau, 0], \mathbb{R}^2)$, define

$$A(\gamma) \phi(\theta) = \begin{cases} \dfrac{d\phi(\theta)}{d\theta}, & \theta \in [-\tau, 0), \\[1.5em] \displaystyle\int_{-\tau^*}^{0} d\eta(\theta, \gamma) \phi(\theta), & \theta = 0, \end{cases}$$

and

$$R(\gamma) \phi(\theta) = \begin{cases} 0, & \theta \in [-\tau, 0) \\[1.5em] F(\gamma, \theta), & \theta = 0. \end{cases}$$

Hence, we can rewrite (2.2.23) in the form

$$\dot{X}_t = A(\gamma) X_t + R(\gamma) X_t, \qquad\qquad (2.2.25)$$

where $X = [x, y]^{\mathrm{T}}$ and $X_t = X(t + \theta)$ for $\theta \in [-\tau, 0]$. Let $C^* = C^1([0, \tau], \mathbb{R}^2)$

and define, for $\psi \in C^*$, the adjoint operator $A^*(0)$ of $A(0)$ by

$$
A^*(0)\psi(s) = \begin{cases} -\dfrac{d\psi(s)}{ds}, & s \in (0,\tau], \\[2em] \displaystyle\int_{-\tau}^0 d\eta^{\mathrm{T}}(s,0)\psi(-s), & s = 0, \end{cases}
$$

where η^{T} is the transpose of η. For $\phi \in C$ and $\psi \in C^*$, define the bilinear

form

$$
\langle \psi, \phi \rangle = \bar{\psi}(0)\phi(0) - \int_{-\tau}^0 \int_{\xi=0}^\theta \bar{\psi}^{\mathrm{T}}(\xi - \theta)d\eta(\theta)\phi(\xi)d\xi, \tag{2.2.26}
$$

where $\eta(\theta) = \eta(\theta, 0)$. Therefore, $A(0)$ and $A^*(0)$ are adjoint operators, and as

usual, we have

$$
\langle \psi, A(0)\phi \rangle = \langle A^*(0)\psi, \phi \rangle.
$$

If we assume that $\lambda(0) = i\omega$ is an eigenvalue of $A(0)$, then it follows that $-i\omega$

is an eigenvalue of $A^*(0)$. Then

$$
A(0)q(\theta) = i\omega q(\theta), \quad \text{and} \quad A^*(0)q^*(s) = -i\omega q^*(s),
$$

where $q(\theta)$ and $q^*(s)$ are the eigenfunctions corresponding to eigenvalues $i\omega$ of

$A(0)$ and $-i\omega$ of $A^*(0)$, respectively. We directly compute the eigenfunction

$q(\theta)$, and obtain

$$
q(\theta) = \begin{bmatrix} 1 \\ \beta \end{bmatrix} e^{i\omega\theta}, \qquad \text{where} \qquad \beta = \frac{cd - ic\omega}{d^2 + \omega^2}.
$$

To find $q^*(s)$, we let $q(s) = [\nu_1, \nu_2]e^{i\omega s}$, and the equations $\langle q^*, q \rangle = 1$ and

$\langle q^*, \bar{q} \rangle = 0$ under the standard inner product (2.2.26) lead to

$$1 = \bar{\nu}_1 + \beta \bar{\nu}_2 - \int_{-\tau}^{0} \int_{0}^{\theta} e^{-i\omega(\xi-\theta)} [\bar{\nu}_1, \bar{\nu}_2] \begin{bmatrix} \hat{\mu} & 0 \\ 0 & 0 \end{bmatrix} \delta(\theta + \tau) \begin{bmatrix} 1 \\ \beta \end{bmatrix} e^{i\omega\xi} d\xi d\theta,$$

$$0 = \bar{\nu}_1 + \bar{\beta} \bar{\nu}_2 - \int_{-\tau}^{0} \int_{0}^{\theta} e^{-i\omega(\xi-\theta)} [\bar{\nu}_1, \bar{\nu}_2] \begin{bmatrix} \hat{\mu} & 0 \\ 0 & 0 \end{bmatrix} \delta(\theta + \tau) \begin{bmatrix} 1 \\ \beta \end{bmatrix} e^{-i\omega\xi} d\xi d\theta.$$

Integration of these equations yields

$$\bar{\nu}_1 [1 + \hat{\mu}\tau \cos(\omega\tau) - i\hat{\mu}\tau \sin(\omega\tau)] + \beta \bar{\nu}_2 = 1,$$

$$\bar{\nu}_1 \left[1 + \frac{\hat{\mu}}{\omega} \sin(\omega\tau) \right] + \bar{\beta} \bar{\nu}_2 = 0.$$

Solving these equations for $\bar{\nu}_1$, $\bar{\nu}_2$, we obtain

$$\bar{\nu}_1 = \frac{\bar{\beta}}{\bar{\beta} e_1 - \beta e_2}, \qquad \text{and} \qquad \bar{\nu}_2 = -\frac{e_2}{\bar{\beta} e_1 - \beta e_2},$$

where $e_1 = 1 + \hat{\mu}\tau \cos(\omega\tau) - i\hat{\mu}\tau \sin(\omega\tau)$ and $e_2 = 1 + \frac{\hat{\mu}}{\omega} \sin(\omega\tau)$. Taking the complex conjugates of $\bar{\nu}_1$ and $\bar{\nu}_2$, we obtain

$$\begin{cases} \nu_1 = \dfrac{(dL_1 + \omega L_2) - i(\omega L_1 - dL_2)}{L_1^2 + L_2^2}, \\[3mm] \nu_2 = \dfrac{-(d^2 + \omega^2)e_2 L_1 - i(d^2 + \omega^2)e_2 L_2}{c(L_1^2 + L_2^2)}, \end{cases}$$

where

$$L_1 = \hat{\mu} \left[d\tau \cos(\omega\tau) + \sin(\omega\tau) \left(\omega\tau - \frac{d}{\omega} \right) \right],$$

$$L_2 = \omega \left(2 + \hat{\mu}\tau \cos(\omega\tau) \right) + \hat{\mu} \sin(\omega\tau)(1 - d\tau).$$

A centre manifold $\mathcal{C}_0$ for (2.2.25) at $\gamma = 0$ is a locally invariant, attracting two–dimensional manifold in C, whose coordinates are computed as follows.

Let X_t be the solution of (2.2.25), and define

$$z(t) = \langle q^*, X_t \rangle, \qquad \text{and} \qquad W(t, \theta) = X_t(\theta) - 2\text{Re}\{z(t)q(\theta)\}.$$

Then, for $\gamma = 0$, on the centre manifold $\mathcal{C}_0$ we have

$$W(t, \theta) = W(z(t), \bar{z}(t), \theta) = W_{20}(\theta)\frac{z^2}{2} + W_{11}z\bar{z} + W_{02}(\theta)\frac{\bar{z}^2}{2} + W_{21}(\theta)\frac{z^2\bar{z}}{2} + \cdots,$$

where z and $\bar{z}$ are local coordinates for the centre manifold $\mathcal{C}_0$ in C, in the direction of q^* and $\bar{q}^*$. Note that we are only interested in real solutions, and if X_t is real, then W is real.

According to [25], the existence of the centre manifold allows us to reduce (2.2.25) to an ordinary differential equation

$$
\begin{aligned}
\dot{z}(t) &= \langle q^*, A(0)X_t + RX_t \rangle \\
&= i\omega z + \langle q^*(\theta), F(W + 2\text{Re}\{z(t)q(\theta)\}) \rangle \\
&= i\omega z + \bar{q}^*(0)F(W((z, \bar{z}, 0) + 2\text{Re}\{z(t)q(0)\}) \\
&\overset{\text{def}}{=} i\omega z + \bar{q}^*(0)F_0(z, \bar{z}).
\end{aligned}
\tag{2.2.27}
$$

We rewrite this as

$$\dot{z}(t) = i\omega z(t) + g(z, \bar{z}),$$

where

$$g(z, \bar{z}) = \bar{q}^*(0)F_0(z, \bar{z}) = g_{20}\frac{z^2}{2} + g_{11}z\bar{z} + g_{02}\frac{\bar{z}^2}{2} + g_{21}\frac{z^2\bar{z}}{2} + \cdots. \tag{2.2.28}$$

From (2.2.25) and (2.2.27), we have

$$
\dot{W} = \dot{X}_t - \dot{z}q - \dot{\bar{z}}\bar{q} =
\begin{cases}
A(\gamma)W - 2\text{Re}\{\bar{q}^*(0)F_0 q(\theta)\}, & \theta \in [-\tau, 0) \\
A(\gamma)W - 2\text{Re}\{\bar{q}^*(0)F_0 q(0)\} + F_0, & \theta = 0,
\end{cases}
$$

$$\overset{\text{def}}{=} A(\gamma)W + H(z, \bar{z}, \theta),$$

where

$$H(z, \bar{z}, \theta) = H_{20}(\theta)\frac{z^2}{2} + H_{11}(\theta)z\bar{z} + H_{02}(\theta)\frac{\bar{z}^2}{2} + H_{21}(\theta)\frac{z^2\bar{z}}{2} + \cdots . \quad (2.2.29)$$

Expanding the above series and equating like coefficients, we obtain

$$(A(\gamma) - 2i\omega)W_{20}(\theta) = -H_{20}(\theta),$$

$$A(\gamma)W_{11}(\theta) = -H_{11}(\theta), \qquad\qquad (2.2.30)$$

$$(A(\gamma) + 2i\omega)W_{02}(\theta) = -H_{02}(\theta), \cdots .$$

Note that $q^*(0) = [\nu_1, \nu_2]$, and

$$x(t) = W^{(1)}(t, 0) + q_1(0)z(t) + \bar{q}_1(0)\bar{z}(t) = W^{(1)}(0) + z + \bar{z},$$

$$y(t) = W^{(2)}(t, 0) + q_2(0)z(t) + \bar{q}_2(0)\bar{z}(t) = W^{(2)}(0) + \beta z + \bar{\beta}\bar{z},$$

since $q(0) = [q_1(0), q_2(0)]^{\mathrm{T}} = [1, \beta]^{\mathrm{T}}$, where

$$W^{(1)}(0) = W^{(1)}(t, 0) = W^{(1)}_{20}(0)\frac{z^2}{2} + W^{(1)}_{11}(0)z\bar{z} + W^{(1)}_{02}(0)\frac{\bar{z}^2}{2} + \cdots ,$$

$$W^{(2)}(0) = W^{(2)}(t, 0) = W^{(2)}_{20}(0)\frac{z^2}{2} + W^{(2)}_{11}(0)z\bar{z} + W^{(2)}_{02}(0)\frac{\bar{z}^2}{2} + \cdots ,$$

and

$$F_0 = \begin{bmatrix} -\alpha x(t)y(t) \\ \\ Ax^2(t) - Bx(t)y(t) \end{bmatrix} + \begin{bmatrix} 0 \\ \\ -Dx^3(t) - Gx^2(t)y(t) \end{bmatrix} + \cdots ,$$

where

$$A = -\frac{c}{V_4}\left(\beta_v - \frac{1}{2}\beta_u\right), \quad B = \frac{d}{2V_4}\beta_u,$$

$$D = \frac{c}{V_4^2}\left[\frac{5}{24} + \beta_v\left(\frac{1}{2}\beta_u - \beta_v\right)\right], \quad G = \frac{d}{8V_4^2},$$

for convenience. Therefore, it follows that

$$
\begin{aligned}
g(z, \bar{z}) &= \bar{q}^*(0)F_0 \\
&= -\alpha x(t)y(t)\bar{\nu}_1 + \left[Ax^2(t) - Bx(t)y(t) - Dx^3(t) - Gx^2(t)y(t)\right]\bar{\nu}_2 \\
&\quad +O(x^4) \\
&= \left[A\bar{\nu}_2 - \beta(\alpha\bar{\nu}_1 + B\bar{\nu}_2)\right]z^2 + \left[2A\bar{\nu}_2 - (\beta + \bar{\beta})(\alpha\bar{\nu}_1 + B\bar{\nu}_2)\right]z\bar{z} \\
&\quad +\left[A\bar{\nu}_2 - \bar{\beta}(\alpha\bar{\nu}_1 + B\bar{\nu}_2)\right]\bar{z}^2 + \left[W_{20}^{(1)}(0)\frac{1}{2}\left(2A\bar{\nu}_2 - \bar{\beta}(\alpha\bar{\nu}_1 + B\bar{\nu}_2)\right)\right. \\
&\quad +W_{11}^{(1)}(0)\left(2A\bar{\nu}_2 - \beta(\alpha\bar{\nu}_1 + B\bar{\nu}_2)\right) - W_{20}^{(2)}(0)\frac{1}{2}(\alpha\bar{\nu}_1 + B\bar{\nu}_2) \\
&\quad +\left. W_{11}^{(2)}(0)(\alpha\bar{\nu}_1 + B\bar{\nu}_2) - \bar{\nu}_2\left(G(2\beta + \bar{\beta}) + 3D\right)\right]z^2\bar{z}.
\end{aligned}
$$

Comparing this to the expansion of $g(z, \bar{z})$, i.e. (2.2.28), and equating like coefficients, we have

$$
\begin{aligned}
g_{20} &= 2[A\bar{\nu}_2 - \beta(\alpha\bar{\nu}_1 + B\bar{\nu}_2)], \\
g_{11} &= 2A\bar{\nu}_2 - (\beta + \bar{\beta})(\alpha\bar{\nu}_1 + B\bar{\nu}_2), \\
g_{02} &= 2[A\bar{\nu}_2 - \bar{\beta}(\alpha\bar{\nu}_1 + B\bar{\nu}_2)], \\
g_{21} &= 2\left[W_{20}^{(1)}(0)\frac{1}{2}\left(2A\bar{\nu}_2 - \bar{\beta}(\alpha\bar{\nu}_1 + B\bar{\nu}_2)\right)\right. \\
&\quad +W_{11}^{(1)}(0)\left(2A\bar{\nu}_2 - \beta(\alpha\bar{\nu}_1 + B\bar{\nu}_2)\right) - W_{20}^{(2)}(0)\frac{1}{2}(\alpha\bar{\nu}_1 + B\bar{\nu}_2) \\
&\quad \left. -W_{11}^{(2)}(0)(\alpha\bar{\nu}_1 + B\bar{\nu}_2) - \bar{\nu}_2\left(G(2\beta + \bar{\beta}) + 3D\right)\right].
\end{aligned}
\tag{2.2.31}
$$

To compute $W_{20}(\theta)$ and $W_{11}(\theta)$ for $\theta \in [-\tau, 0)$, we have

$$
\begin{aligned}
H(z, \bar{z}, \theta) &= 2\text{Re}\{\bar{q}^*(0)F_0 q(\theta)\} = -gq(\theta) - \bar{g}\bar{q}(\theta) \\
&= -\left(g_{20}\frac{z^2}{2} + g_{11}z\bar{z} + g_{02}\frac{\bar{z}^2}{2} + \cdots\right)q(\theta) \\
&\quad -\left(\bar{g}_{20}\frac{\bar{z}^2}{2} + \bar{g}_{11}z\bar{z} + \bar{g}_{02}\frac{z^2}{2} + \cdots\right)\bar{q}(\theta).
\end{aligned}
$$

Equating like coefficients with (2.2.29) gives

$$H_{20}(\theta) = -g_{20}q(\theta) - \bar{g}_{02}\bar{q}(\theta), \quad \text{and} \quad H_{11}(\theta) = -g_{11}q(\theta) - \bar{g}_{11}\bar{q}(\theta).$$

From (2.2.30), it follows that

$$\dot{W}_{20}(\theta) = 2i\omega W_{20}(\theta) - g_{20}q(0)e^{i\omega\theta} - \bar{g}_{02}\bar{q}(0)e^{-i\omega\theta},$$

and solving this differential equation for $W_{20}(\theta)$ we obtain

$$W_{20}(\theta) = -\frac{g_{20}}{i\omega}q(0)e^{i\omega\theta} - \frac{\bar{g}_{02}}{3i\omega}\bar{q}(0)e^{-i\omega\theta} + Ee^{2i\omega\theta}. \qquad (2.2.32)$$

Similarly, we obtain

$$W_{11}(\theta) = \frac{g_{11}}{i\omega}q(0)e^{i\omega\theta} - \frac{\bar{g}_{11}}{i\omega}\bar{q}(0)e^{-i\omega\theta} + F. \qquad (2.2.33)$$

In (2.2.32) and (2.2.33), $E = [E_1, E_2]^{\mathrm{T}}$ and $F = [F_1, F_2]^{\mathrm{T}}$ are two–dimensional vectors, and can be determined by setting $\theta = 0$ in H. Since

$$H(z, \bar{z}, 0) = -2\mathrm{Re}\{\bar{q}^*(0)F_0q(0)\} + F_0,$$

this gives

$$H_{20}(0) = -g_{20}q(0) - \bar{g}_{02}\bar{q}(0) + \begin{bmatrix} -2\alpha\beta \\ 2(A - \beta B) \end{bmatrix}, \qquad (2.2.34)$$

and

$$H_{11}(0) = -g_{11}q(0) - \bar{g}_{11}\bar{q}(0) + \begin{bmatrix} -\alpha(\beta + \bar{\beta}) \\ 2A - B(\beta + \bar{\beta}) \end{bmatrix}, \qquad (2.2.35)$$

where $q(0) = [1, \beta]^{\mathrm{T}}$, and A and B were defined above. From (2.2.30) and the definition of $A(\gamma)$, we have

$$\begin{bmatrix} -a & b \\ c & -d \end{bmatrix} W_{20}(0) + \begin{bmatrix} \hat{\mu} & 0 \\ 0 & 0 \end{bmatrix} W_{20}(-\tau) = 2i\omega W_{20}(0) - H_{20}(0), \quad (2.2.36)$$

and

$$\begin{bmatrix} -a & b \\ c & -d \end{bmatrix} W_{11}(0) + \begin{bmatrix} \hat{\mu} & 0 \\ 0 & 0 \end{bmatrix} W_{11}(-\tau) = -H_{11}(0). \qquad (2.2.37)$$

Substituting (2.2.32) into (2.2.36), we obtain

$$\begin{bmatrix} -a + \hat{\mu}e^{-2i\omega\tau} - 2i\omega & b \\ c & -(d + 2i\omega) \end{bmatrix} E = -g_{20}q(0) - \bar{g}_{02}\bar{q}(0) - H_{20}(0),$$

since

$$\begin{bmatrix} -a + \hat{\mu}e^{-i\omega\tau} - i\omega & b \\ c & -d - i\omega \end{bmatrix} q(0) = 0.$$

With $H_{20}(0)$ given in (2.2.34), we obtain

$$\begin{bmatrix} -a + \hat{\mu}e^{-2i\omega\tau} - 2i\omega & b \\ c & -(d + 2i\omega) \end{bmatrix} E = - \begin{bmatrix} -2\alpha\beta \\ 2(A - \beta B) \end{bmatrix},$$

which gives the set of equations

$$\left(-a + \hat{\mu}e^{-2i\omega\tau} - 2i\omega \right) E_1 + bE_2 = 2\alpha\beta,$$

$$cE_1 - (d + 2i\omega)E_2 = -2(A - \beta B).$$

Solving these equations for E_1 and E_2 gives

$$E_1 = \frac{2\alpha\beta(d + 2i\omega) - 2b(A - \beta B)}{bc + (d + 2i\omega) \left[\hat{\mu}e^{-2i\omega\tau} - (a + 2i\omega) \right]}$$

and

$$E_2 = \frac{2\alpha\beta c + 2(A - \beta B) \left[\hat{\mu}e^{-2i\omega\tau} - (a + 2i\omega) \right]}{bc + (d + 2i\omega) \left[\hat{\mu}e^{-2i\omega\tau} - (a + 2i\omega) \right]}.$$

Solving for the components of F in a similar manner, we obtain

$$\begin{bmatrix} -a + \hat{\mu} & b \\ c & -d \end{bmatrix} F = - \begin{bmatrix} -\alpha(\beta + \bar{\beta}) \\ 2A - B(\beta + \bar{\beta}) \end{bmatrix},$$

which leads to

$$F_1 = \frac{b(2A - B(\beta + \bar{\beta})) - \alpha d(\beta + \bar{\beta})}{(ad - bc) - \hat{\mu}d},$$

$$F_2 = \frac{(a - \hat{\mu})(2A - B(\beta + \bar{\beta})) - \alpha c(\beta + \bar{\beta})}{(ad - bc) - \hat{\mu}d}.$$

Now we see that all of the g_{ij}'s in (2.2.31) are determined by the parameters and delay in the nonlinear system (2.2.6). We employ the formulas of Hassard, Kazarinoff and Wan [20] to compute the quantities

$$C_1(0) = \frac{i}{2\omega} \left(g_{20}g_{11} - 2|g_{11}|^2 - \frac{1}{3}|g_{02}|^2 \right) + \frac{g_{21}}{2},$$

$$\mu_2 = -\frac{\text{Re}\{C_1(0)\}}{\text{Re}\{\lambda'(0)\}}, \qquad (2.2.38)$$

$$\beta_2 = 2\text{Re}\{C_1(0)\},$$

$$T_2 = -\frac{1}{\omega} \left(\text{Im}\{C_1(0)\} + \mu_2 \text{Im}\{\lambda'(0)\} \right),$$

where $\lambda(\gamma) = \alpha(\gamma) + i\omega(\gamma)$ is a solution of (2.2.13), where $\tau = \tau_{n,1} + \gamma$, or $\tau = \tau_{n,2} + \gamma$, $n = 0, 1, \ldots$, satisfying $\alpha(0) = 0$, $\omega(0) = \omega$. Applying the results of Hassard, Kazarinoff and Wan [20], we know that μ_2 determines the direction of the Hopf bifurcation: if $\mu_2 > 0$ (< 0), then the Hopf bifurcation is supercritical (subcritical) and the bifurcating periodic solutions exist for $\tau > \tau^*$ ($< \tau^*$). The stability of periodic solutions on the centre manifold are determined by the sign of the Floquet exponent β_2: the bifurcating periodic solutions are orbitally stable if $\beta_2 < 0$, and unstable if $\beta_2 > 0$. Finally, the period of the bifurcating periodic solutions is given by T_2, and the period increases if $T_2 > 0$, and decreases if $T_2 < 0$. We are mainly concerned with the direction and stability of the bifurcating periodic solutions.

To conclude this chapter, we present some sample calculations to illustrate the results of the Hopf bifurcation analysis. The first example is for $\mu < \mu^*$, where the model is in Case 1. Under this case, stability of the equilibrium point is lost for good when $\tau = \tau^* = \tau_{0,1}$, and a branch of periodic solutions emerges from a Hopf bifurcation. Consider $\mu = -10.8$ as a representative from Case 1. For this value of μ, the purely imaginary root is $\lambda_+ = i\omega_+ = i \times 0.5441$, and the delay time for the bifurcation is $\tau^* = \tau_{0,1} = 3.6$ ms. The component β of the eigenfunction $q(\theta)$ is $\beta = 0.000283 - i \times 0.00206$, and ν_1, ν_2 of $q^*(s)$ are $\nu_1 = 0.274 + i \times 0.273$, $\nu_2 = 9.37 - i \times 12.39$. For the g_{ij} coefficients, we obtain $g_{20} = 0.00123 + i \times 0.00150$, $g_{11} = 0.000715 + i \times 0.00109$, $g_{02} = 0.000205 + i \times 0.000680$, and $g_{21} = -0.00222 + i \times 0.00284$. This gives $C_1(0) = -0.00111 + i \times 0.00142$, and hence $\mu_2 = (0.00111)(\text{Re}\{\lambda'(0)\})^{-1} > 0$, since $\text{Re}\{\lambda'(0)\} > 0$, and $\beta_2 = -0.00223 < 0$. Therefore, the Hopf bifurcation at $\tau_{0,1}$ for $\mu = -10.8$ is supercritical ($\mu_2 > 0$) and the bifurcating periodic solutions branch to stable oscillations ($\beta_2 < 0$). Similar results were obtained for a large sample of values of $\mu < \mu^*$. These results are consistent with numerical simulations for this case.

Next consider $\mu = -4.7$, an example discussed in detail in section 2.2.8. For this value of μ we found that three stability changes are possible, and occur as we increase τ through the values $\tau_{0,1} = 13.9$, $\tau_{0,2} = 34.8$, and $\tau_{1,1} = 48.4$. At each of these bifurcation values we also obtain a branch of periodic solutions from a Hopf bifurcation. Note that both $\tau_{0,1} = 13.9$ and $\tau_{1,1} = 48.4$ correspond to the ω_+ root, which has value $\omega_+ = i \times 0.182$, while $\tau_{0,2} = 34.8$ corresponds to the ω_- root, where $\omega_- = i \times 0.0875$. Tables 2.2 and 2.3 report the values for important quantities to determine the direction and stability for all three

Hopf bifurcations.

Value	$\tau_{0,1} = 13.9$	$\tau_{0,2} = 34.8$
β	$0.00121 - i \times 0.00260$	$0.00329 - i \times 0.00339$
ν_1	$0.201 + i \times 0.107$	$0.106 + i \times 0.0177$
ν_2	$1.12 - i \times 21.7$	$-9.63 - i \times 13.9$
g_{20}	$0.000289 + i \times 0.00162$	$-0.000625 + i \times 0.00127$
g_{11}	$-0.00138 + i \times 0.00121$	$-0.000845 + i \times 0.000862$
g_{02}	$-0.000565 + i \times 0.000802$	$-0.00106 + i \times 0.000455$
g_{21}	$-0.00261 + i \times 0.00282$	$-0.00203 + i \times 0.00112$
$C_1(0)$	$-0.00131 + i \times 0.00140$	$-0.00101 + i \times 0.000558$
μ_2	$(0.00131)(\text{Re}\{\lambda'(0)\})^{-1}$	$(0.00101)(\text{Re}\{\lambda'(0)\})^{-1}$
β_2	-0.00261	-0.00201

Table 2.2: Detailed Hopf bifurcation analysis: sample calculations for the first two Hopf bifurcations which occur for $\mu = -4.7$ (Case 2, multiple stability switches).

For the Hopf bifurcation which occurs at $\tau = \tau_{0,1} = 13.9$, $\mu_2 > 0$ since $\text{Re}\{\lambda'(0)\} > 0$, and so the Hopf bifurcation is supercritical, and since $\beta_2 < 0$, the bifurcating periodic solutions branch to stable oscillations. The same is true for the bifurcation at $\tau = \tau_{1,1} = 48.4$. While the bifurcation at $\tau_{0,2} = 34.8$ branches to stable oscillations ($\beta_2 < 0$), we find that $\mu_2 < 0$, since $\text{Re}\{\lambda'(0)\} < 0$, and so the the direction of the Hopf bifurcation is subcritical. A large sample of values of $\mu \in [-5.02, -4.37]$ (approximately 20–25 values) were tested and all produced similar results. That is, Hopf bifurcations occurring with delay times $\tau_{n,1}$, $n = 0, 1, \ldots$ are all supercritical and branch to stable

Value	$\tau_{1,1} = 48.4$
β	$0.00121 - i \times 0.00260$
ν_1	$0.0680 + i \times 0.0427$
ν_2	$0.948 - i \times 7.58$
g_{20}	$0.000143 + i \times 0.000561$
g_{11}	$-0.0000174 + i \times 0.000482$
g_{02}	$-0.000178 + i \times 0.000296$
g_{21}	$-0.000845 + i \times 0.00105$
$C_1(0)$	$-0.000423 + i \times 0.000525$
μ_2	$(0.000423)(\mathrm{Re}\{\lambda'(0)\})^{-1}$
β_2	-0.000846

Table 2.3: Detailed Hopf bifurcation analysis: sample calculations for the third Hopf bifurcation which occurs for $\mu = -4.7$ (Case 2, multiple stability switches).

oscillations, while those for $\tau_{n,2}$, $n = 0, 1, \ldots$ are subcritical and branch to stable oscillations. Also, numerical simulations presented in section 2.2.8 are in agreement with the results reported here.

Chapter 3

The all–Ca^{2+} Conductance System

In this chapter, we explore the dynamics of the all–Ca^{2+} conductance system. This investigation will illustrate how the all–Ca^{2+} and all–K$^+$ conductance systems with delay differ from each other, how the dynamics of the all–Ca^{2+} system with delay differ from the original model without delay, and will help demonstrate how the all–Ca^{2+} with delay contributes to the full–2D model with delay. The equations are similar in form to those describing the all–K$^+$ system, and so the analysis of the all–Ca^{2+} conductance system is very similar to that of the all–K$^+$ system.

The original single–ion conductance systems of the Morris–Lecar model without delay exhibit qualitatively different behavior. The all–K$^+$ system exhibits a graded response with a transient peak followed by a decay to a voltage plateau, while the all–Ca^{2+} system has bistable responses and a characteristic threshold [24]. These differences are due largely in part to differences in pa-

rameter values. It is important to note that Morris and Lecar [24] change the values of some parameters which overlap between the all–K^+ and all–Ca^{2+} systems, most importantly the leakage equilibrium voltage. In the original all–K^+ system without delay, they set $V_L = -50$ mV, but used the value $V_L = -35$ mV for the original all–Ca^{2+} system without delay. This was done to illustrate different behaviors displayed by the the two isolated conductance systems, and in the system where both systems are active. For consistency, we shall use $V_L = -50$ for both single–ion conductance systems. This will also allow us to better compare the dynamics of the conductance systems with delay.

The all–Ca^{2+} conductance system with delay is governed by the system

$$C\dot{V}(t) = -g_L(V - V_L) - g_{Ca}m(V - V_{Ca}) + \mu V(t - \tau)$$

$$\tag{3.0.1}$$

$$\dot{m}(t) = \lambda_m(V)\left[m_\infty(V) - m\right],$$

with voltage–dependent functions $m_\infty(V)$, $\lambda_m(V)$ described by

$$\begin{cases} m_\infty(V) = \dfrac{1}{2}\left[1 + \tanh\left(\dfrac{V - V_1}{V_2}\right)\right], \\[2ex] \lambda_m(V) = \overline{\lambda_m}\cosh\left(\dfrac{V - V_1}{2V_2}\right). \end{cases} \tag{3.0.2}$$

This system is obtained by setting n, the fraction of open K^+ channels, to zero in the three-dimensional Morris Lecar system with delay (1.3.5). Before addressing the dynamics of (3.0.1), we present a brief overview of the behavior of the original system without delay.

3.1 The all–Ca^{2+} Conductance System without Delay

In the absence of delay, the calcium conductance system displays more complicated dynamics than the potassium system. While voltage oscillations are still not possible in this isolated system, Morris and Lecar found that the all–Ca^{2+} system exhibits bistable responses and a characteristic threshold. With $\mu = 0$, system (3.0.1) is reduced to the original Ca^{2+} conductance system without delay:

$$C\dot{V}(t) = -g_{\mathrm{L}}(V - V_{\mathrm{L}}) - g_{\mathrm{Ca}}m(V - V_{\mathrm{Ca}})$$

$$(3.1.1)$$

$$\dot{m}(t) = \lambda_m(V)\left[m_\infty(V) - m\right],$$

with $\lambda_m(V)$ and $m_\infty(V)$ as in (3.0.2). For system (3.1.1), three equilibria are obtained in the (V, m)–phase plane, given by the intersection of the nullclines

$$V(m) = \frac{g_{\mathrm{L}}V_{\mathrm{L}} + g_{\mathrm{Ca}}V_{\mathrm{Ca}}m}{g_{\mathrm{L}} + g_{\mathrm{Ca}}m} \quad \text{and} \quad m(V) = m_\infty(V) = \frac{1}{2}\left[1 + \tanh\left(\frac{V - V_1}{V_2}\right)\right].$$

The $\dot{m} = 0$ nullcline, is a monotone increasing function $m = m_\infty(V)$ which is similar in shape to the $n(V)$ nullcline of the all–K$^+$ system, differing only in steepness and a slight shift along the voltage axis. The nature of the $\dot{V} = 0$ nullcline is the cause for the different behavior between the Ca^{2+} and K$^+$ conductance systems without delay. With $V_{\mathrm{K}} < V_{\mathrm{L}}$, the $\dot{V} = 0$ nullcline of the all–K$^+$ system is monotone decreasing and hence the nullclines can intersect at most once. On the other hand, since $V_{\mathrm{Ca}} > V_{\mathrm{L}}$, the $\dot{V} = 0$ nullcline of the all–Ca^{2+} system is monotone increasing, and so the nullclines can intersect one, two, or three times, depending on the value of the applied stimulus.

With $I = 0$, the system admits three equilibrium points, as indicated by the phase plane diagram depicted in Figure 3.1(b). We shall refer to the lower equilibrium point as (V_1, m_1), the middle as equilibrium point as (V_2, m_2), and the upper as (V_3, m_3).

Morris and Lecar state that the upper and lower equilibrium points are stable nodes while the middle equilibrium point is an unstable saddle. They also add that this pattern of equilibria leads to bistable behavior since the separatrix solutions associated with the saddle point separate the phase plane, so that trajectories starting in different regions are attracted to different stable equilibrium points. To verify the stability of each equilibrium, we first linearise the system about the origin. Let (V^*, m^*) be an equilibrium point of (3.1.1). Taking $x = V - V^*$, $y = m - m^*$ and linearising, we obtain

$$\dot{x} = -ax + by$$

$$\dot{y} = cx - dy,$$

where a, b, c, and d are given by

$$a = \frac{g_L + g_{Ca}m^*}{C}, \qquad b = \frac{g_{Ca}(V_{Ca} - V^*)}{C}, \qquad d = \overline{\lambda_m} \cosh\left(\frac{V^* - V_1}{2V_2}\right),$$

$$c = \frac{\overline{\lambda_m}}{2V_2} \cosh\left(\frac{V^* - V_1}{2V_2}\right) \text{sech}^2\left(\frac{V^* - V_1}{V_2}\right).$$

The characteristic equation is simply

$$\lambda^2 + (a + d)\lambda + (ad - bc) = 0,$$

and by the Routh–Hurwitz conditions [3], (V^*, m^*) is stable provided

(i). $a + d > 0 \quad \Rightarrow \quad a > -d$, and

(ii). $ad - bc > 0 \quad \Rightarrow \quad ad > bc$.

For the model parameters of system (3.0.1), we use a standard parameter listed in Table 3.1.

Parameter Set	
$C = 20 \ \mu\text{F/cm}^2$	$\overline{\lambda_m} = \frac{1}{10} \ \text{s}^{-1}$
$g_{\text{L}} = 3 \ \text{mmho/cm}^2$	$g_{\text{Ca}} = 4 \ \text{mmho/cm}^2$
$V_{\text{L}} = -50 \ \text{mV}$	$V_{\text{Ca}} = 100 \ \text{mV}$
$V_1 = 10.0 \ \text{mV}$	$V_2 = 15.0 \ \text{mV}$

Table 3.1: Morris–Lecar parameter set for the all–Ca²⁺ conductance system.

From the definition of a, and since the conductance constants g_{L} and g_{Ca} and capacitance C are non–negative, it follows that a is positive. Furthermore, d is also non–negative since $\overline{\lambda_m} > 0$. Therefore, like the all–potassium case system without delay, condition (i) is always satisfied for each of the three equilibria of the all–calcium system without delay (3.1.1), and specifically for the parameter set in Table 3.1.

To check condition (ii), we examine each of the three equilibrium points separately. The lower equilibrium point $(V_1^*, m_1^*) = (-49.932, 0.000)$, and so $V_1^* < V_{\text{Ca}} \Rightarrow b > 0$. Computing the coefficients a, b, c, and d we find that $ad > bc$, confirming (ii), and so (V_1^*, m_1^*) is a stable equilibrium point. To show

that (V_1^*, m_1^*) is a stable node, we must show that the roots of the characteristic equation,

$$\lambda_\pm = \frac{-(a+d) \pm \sqrt{(a+d)^2 - 4(ad - bc)}}{2}, \tag{3.1.2}$$

are real–valued. This is true provided the discriminant $\Delta_1 = (a+d)^2 - 4(ad - bc)$ of (3.1.2) for (V_1^*, m_1^*) is positive. For (V_1^*, m_1^*), we find that $\Delta_1 = 0.053 > 0$, and it follows that $\lambda_- < \lambda_+ < 0$, and both roots are real, indicating that (V_1^*, m_1^*) is in fact a stable node. Similarly, for $(V_3^*, m_3^*) = (34.299, 0.962)$, we find that $ad > bc \Rightarrow$ condition (ii) is met, hence (V_3^*, m_3^*) is stable, and for this singular point $\Delta_3 = 0.077 > 0$, which confirms that we have a stable node. On the other hand, for $(V_2^*, m_2^*) = (10, 0.5)$, $ad - bc < 0$, and since condition (ii) is violated then (V_2^*, m_2^*) is unstable. Furthermore, both eigenvalues $\lambda_\pm$ of the system corresponding to (V_2^*, m_2^*) are real, since the discriminant $\Delta_2 = 0.263 > 0$. This implies that $\lambda_- < 0$ and $\lambda_+ > 0$ from which it follows that (V_2^*, m_2^*) is an unstable saddle point.

3.2   The all–Ca^{2+} Conductance System with Delay

We return now to the conductance system with delay (3.0.1). To determine the number and location of equilibria of the all–calcium system (3.0.1), we analyse how the nullclines in the (V, m)–plane change as the parameter μ is varied.

3.2.1   The Nullclines of the all–Ca^{2+} System

The nullclines of system (3.0.1) in the (V, m)–plane are obtained by setting $\dot{V} = 0$, and $\dot{m} = 0$. This gives

$$V(m) = \frac{g_{\mathrm{L}} V_{\mathrm{L}} + g_{\mathrm{Ca}} V_{\mathrm{Ca}} m}{g_{\mathrm{L}} + g_{\mathrm{Ca}} m - \mu} \qquad (3.2.1)$$

$$m(V) = m_{\infty}(V) = \frac{1}{2}\left[1 + \tanh\left(\frac{V - V_1}{V_2}\right)\right]. \qquad (3.2.2)$$

The function $V(m)$ represents the $\dot{V} = 0$ nullcline, while $m(V)$ represents the $\dot{m} = 0$ nullcline. Since $0 \le m \le 1$, the voltage of the system varies between the limits

$$V(0) = \frac{g_{\mathrm{L}} V_{\mathrm{L}}}{g_{\mathrm{L}} - \mu} \qquad \text{and} \qquad V(1) = \frac{g_{\mathrm{L}} V_{\mathrm{L}} + g_{\mathrm{Ca}} V_{\mathrm{Ca}}}{g_{\mathrm{L}} + g_{\mathrm{Ca}} - \mu}.$$

For certain values of μ these voltage limits may become infinite, in which case the voltage itself may approach infinite values.

The $m(V)$ nullcline is a sigmoidal shaped, monotone increasing function of V, with limit 1 as $V \to +\infty$ and 0 as $V \to -\infty$. This nullcline differs only slightly from the $\dot{n} = 0$ nullcline of the all–potassium system, in steepness and position on the voltage axis. This nullcline does not depend on μ, and so any change in the number of equilibria must be attributed to changes in the $V(m)$ nullcline. The qualitative behavior of $V(m)$ changes as μ is varied. $V(m)$ nullcline is a hyperbola, separated by a vertical asymptote at $V = V_{\mathrm{Ca}}$, except for one degenerate case, where it is reduced to a pair of vertical and horizontal lines. Since $m \in [0, 1]$, we are only interested in the portions of the hyperbola which lie in this range. We have already seen that for $\mu = 0$, the system admits three equilibria, a saddle point between two stable nodes. For large values of μ, both positive and negative, $V(m) \to 0$ and $m(V) \to m_{\infty}(0) \approx 0.21$.

There are several regions to consider for finite μ. If

$$\mu < g_{\mathrm{L}} \left(1 - \frac{V_{\mathrm{L}}}{V_{\mathrm{Ca}}} \right) ,$$

then $V(m)$ is an increasing function of m, and is the portion of the upper branch of the hyperbola which lies in the range $0 \leq m \leq 1$. We do not consider the lower branch, since it is below the V–axis. With μ in this range, either one, two, or three equilibria are possible. A saddle–node bifurcation occurs at a value of $\mu < 0$, say $\bar{\mu}$, so that the system has a single equilibrium point (V_1^*, m_1^*) if $\mu < \bar{\mu}$, and three equilibria (V_i^*, m_i^*), $i = 1, 2, 3$, if $\bar{\mu} < \mu < g_{\mathrm{L}}$, where $g_{\mathrm{L}} < g_{\mathrm{L}} \left(1 - \frac{V_{\mathrm{L}}}{V_{\mathrm{Ca}}} \right)$. The bifurcation is of the saddle–node variety because the emerging equilibria are a saddle point and a node: we shall see later that, for system (3.0.1) with zero time delay, (V_2^*, m_2^*) is a saddle point and (V_3^*, m_3^*) is a node. With the parameter set specified in Table 3.1, $g_{\mathrm{L}} = 3$, $g_{\mathrm{L}} \left(1 - \frac{V_{\mathrm{L}}}{V_{\mathrm{Ca}}} \right) = \frac{9}{2}$, and the value of $\bar{\mu}$ is approximately -2.22. Also, for μ in this range, all equilibrium voltages V_i^*, $i = 1, 2, 3$ are below V_{Ca}. Furthermore, note that $V_1^* \to -\infty$ as $\mu \to g_{\mathrm{L}}$, and the lower equilibrium point (V_1^*, m_1^*) is lost once $\mu \geq g_{\mathrm{L}}$. Thus, for $g_{\mathrm{L}} < \mu < g_{\mathrm{L}} \left(1 - \frac{V_{\mathrm{L}}}{V_{\mathrm{Ca}}} \right)$, system (3.0.1) has two equilibria, an unstable saddle (V_2^*, m_2^*) and a stable node (V_3^*, m_3^*), with $V_2^*, V_3^* < V_{\mathrm{Ca}}$. This claim is proved in a later section. Figure 3.1 contains plots of the nullclines for the all–Ca^{2+} conductance system, for values of μ, including representative values for the three separate cases for $\mu < g_{\mathrm{L}} \left(1 - \frac{V_{\mathrm{L}}}{V_{\mathrm{Ca}}} \right)$. Also, once $\mu > g_{\mathrm{L}}$, the lower branch of the hyperbola is above the V–axis and in the interval of interest $[0, 1]$, but does not intersect the sigmoidal $m(V)$ nullcline. With both branches of the hyperbola significant, the voltage of the system is no longer bounded, and by rearranging $V(m)$ and solving for m, we can find

the value of m where the voltage becomes infinite:

$$m(V) = \frac{g_L(V_L - V) + \mu V}{g_{Ca}(V - V_{Ca})}$$

$$\lim_{V \to \pm\infty} m(V) = \frac{\mu - g_L}{g_{Ca}}. \tag{3.2.3}$$

With $\mu > g_L$, the limit in (3.2.3) is greater than 0, and so for each $\mu \in \left(g_L, g_L\left(1 - \frac{V_L}{V_{Ca}}\right)\right)$, there is a value of $m \in [0,1]$ where the voltage V of the system becomes infinite.

The nullclines reduce to a pair of lines $V = V_{Ca} = 100$ and $m = -\frac{g_L V_L}{g_{Ca} V_{Ca}} = \frac{3}{8} < 0$, if

$$\mu = g_L\left(1 - \frac{V_L}{V_{Ca}}\right) = \frac{9}{2}.$$

For this value of μ there are two equilibria, a stable node (V_3^*, m_3^*), with $V_3^* = V_{Ca} = 100$, and a saddle (V_2^*, m_2^*), with $V_2^* < V_{Ca}$. Stability here refers to the stability of the equilibria of system (3.0.1) with zero time delay. The nullclines for this special case is displayed in Figure 3.1(d).

With μ in the range

$$g_L\left(1 - \frac{V_L}{V_{Ca}}\right) < \mu < g_L + g_{Ca},$$

the $V(m)$ nullcline is a decreasing function for $m \in [0,1]$, and both upper and lower branches of the hyperbola are significant and intersect the sigmoidal $m(V)$ nullcline. There are two equilibria, a saddle point (V_2^*, m_2^*) with $V_2^* < V_{Ca}$, and a stable node (V_3^*, m_3^*), with $V_3^* > V_{Ca}$. Using the parameter values in Table 3.1, this range is $\frac{9}{2} < \mu < 7$, and the nullclines for a representative case are shown in Figure 3.1(e).

As $\mu \to g_L + g_{Ca}$, $V_3^* \to +\infty$, and so once μ passes this value then the upper equilibrium point (V_3^*, m_3^*) disappears. Furthermore, with $\mu > g_L + g_{Ca}$, the

(a) $\mu = -5$.

(b) $\mu = 0$.

(c) $\mu = 4$

(d) $\mu = \frac{9}{2}$.

(e) $\mu = 5$.

(f) $\mu = 8$.
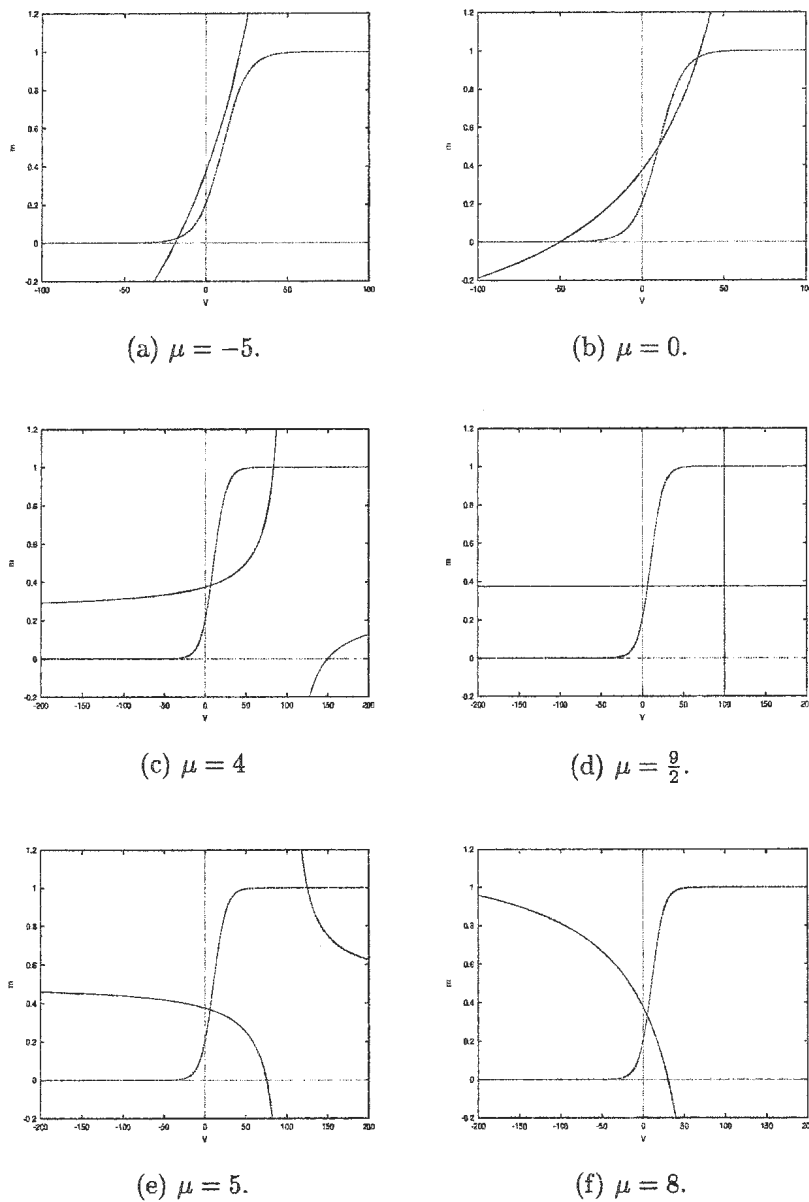
Figure 3.1: Plots of the $V(m)$ (solid) and $m(V)$ (dashed) nullclines of the all–Ca²⁺ system (3.0.1) for representative values of μ.

upper branch of the hyperbola is above the line $m = 1$, and so is not in the interval of interest. The lower branch is significant, is monotone decreasing for $m \in [0,1]$, and intersects the $m(V)$ sigmoidal nullcline to yield a single unstable saddle point (V_2^*, m_2^*), with $V_2^* < V_{Ca}$. Refer to Figure 3.1(f) for an example of the nullclines with μ in this range.

This analysis has shown that, as μ is varied, the shape and position of the $V(m)$ nullcline changes, which in turn influences the number of equilibria of the system. Figure 3.1 shows a sequence of nullcline plots to indicate the evolution of the nullclines in the (V,m)–plane as μ is varied. The number of equilibria for a given value of μ can be concisely depicted in bifurcation diagrams as a branch of steady–state solutions, and are presented in Figure 3.2. Figure 3.2(a) indicates how the equilibrium voltage(s) V^* change as μ is varied, while Figure 3.2(b) shows how the equilibrium fraction of open Ca²⁺ channels, m^* varies with μ.

As a final note in this section, we remark that for weak inhibitory and excitatory feedback, the all–Ca²⁺ system with delay (3.0.1) admits multiple equilibria. Moreover, the system exhibits bistability in this case, with two stable nodes (V_1^*, m_1^*) and (V_3^*, m_3^*) separated by an unstable saddle (V_2^*, m_2^*). Again, the stability we refer to is in the case of zero time delay, and these claims are verified in the following section. These observations can be clearly drawn from Figure 3.2(a). If the feedback strength is increased, then only a single equilibrium point remains in the inhibitory case, while a single unstable steady state exists if the feedback is excitatory.

(a) V vs. μ.

(b) m vs. μ.
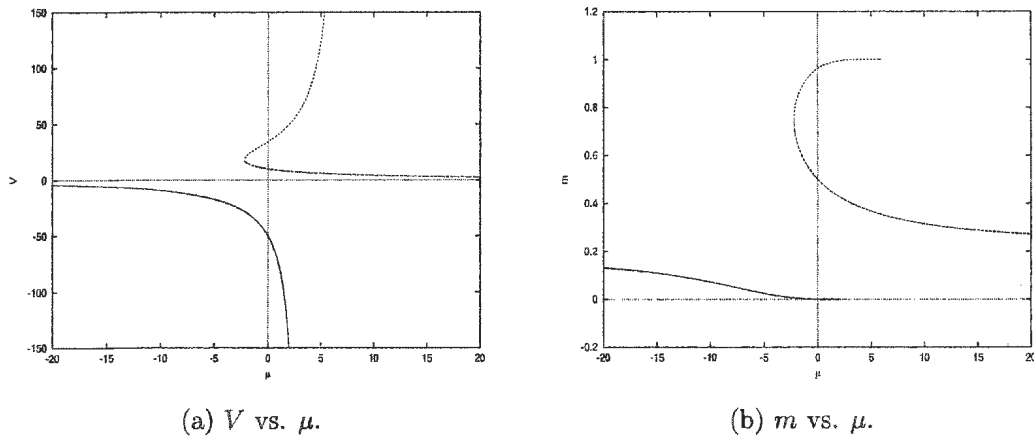
Figure 3.2: Bifurcation diagrams describing how V^* and m^* of the all–Ca²⁺ conductance system change as μ is varied. The solid curve represents (V_1^*, m_1^*) the dashed curve represents (V_2^*, m_2^*), and the dotted curve represents (V_3^*, m_3^*). Stability of equilibria is not indicated.

The results of this section, stated as a theorem, are given by:

Theorem 3.2.1.1. *With parameters listed in Table 3.1, system (3.0.1) admits up to three equilibrium points as μ is varied:*

1. *If $\mu < \bar{\mu}$, then (V_1^*, m_1^*) is the only equilibrium point of the system, with $V_1^* < V_{Ca}$;*

2. *A saddle–node bifurcation of steady states takes place at $\mu = \bar{\mu}$, giving rise to two additional equilibria. If $\bar{\mu} < \mu < g_L$, then system (3.0.1) admits three equilibria, (V_i^*, m_i^*), $i = 1, 2, 3$, with each of $V_i^* < V_{Ca}$, $i = 1, 2, 3$;*

3. *If $g_L < \mu < g_L \left(1 - \frac{V_L}{V_{Ca}}\right)$, then system (3.0.1) admits two equilibrium points, (V_2^*, m_2^*) and (V_3^*, m_3^*) with $V_2^*, V_3^* < V_{Ca}$;*

4. *If $\mu = g_L \left(1 - \frac{V_L}{V_{Ca}}\right)$, then system (3.0.1) admits two equilibrium points, (V_2^*, m_2^*) and (V_3^*, m_3^*) with $V_2^* < V_{Ca}$, $V_3^* = V_{Ca}$;*

5. *If $g_L \left(1 - \frac{V_L}{V_{Ca}}\right) < \mu < g_L + g_{Ca}$, then system (3.0.1) admits two equilibrium points, (V_2^*, m_2^*) and (V_3^*, m_3^*) with $V_2^* < V_{Ca}$, $V_3^* > V_{Ca}$;*

6. *If $\mu > g_L + g_{Ca}$, then system (3.0.1) possesses a single equilibrium point (V_2^*, m_2^*) where $V_2^* < V_{Ca}$.*

For all cases, $m_i \in [0, 1]$, $i = 1, 2, 3$.

3.2.2 Local Stability and Bifurcation Analysis of the all–Ca²⁺ System

In this section, we address the delay–dependent stability of the equilibria of (3.0.1). In the previous section, we referred to stability of the equilibria for zero time delay, that is system (3.0.1) with $\tau = 0$. Here, we prove the claims pertaining to the stability and type of equilibria for the model with zero time delay. We then examine the stability of (V_i^*, m_i^*), $i = 1, 2, 3$ for $\tau > 0$, and also determine whether or not the all–Ca²⁺ conductance system with delay (3.0.1) is capable of supporting stable oscillations.

We begin by linearising system (3.0.1) about the origin, noting that, for all $\mu \in \mathbb{R}$, the system admits at least one equilibrium point (V^*, m^*) in the (V, m)–phase plane. The linearised system is similar to that obtained for the all–K⁺ system. Let $x = V - V^*$ and $y = m - m^*$ and linearise to obtain

$$\dot{x}(t) = -ax + by + \hat{\mu}x(t - \tau)$$

$$(3.2.4)$$

$$\dot{y}(t) = cx - dy,$$

with the coefficients

$$a = \frac{g_{\mathrm{L}} + g_{\mathrm{Ca}}m^*}{C}, \qquad b = \frac{g_{\mathrm{Ca}}(V_{\mathrm{Ca}} - V^*)}{C}, \qquad d = \overline{\lambda_m} \cosh\left(\frac{V^* - V_1}{2V_2}\right),$$

$$c = \frac{\overline{\lambda_m}}{2V_2} \cosh\left(\frac{V^* - V_1}{2V_2}\right) \operatorname{sech}^2\left(\frac{V^* - V_1}{V_2}\right), \qquad \hat{\mu} = \frac{\mu}{C},$$

as the linearised system with equilibrium at the origin. In the event the system admits more than one equilibrium point, a separate stability analysis is required for each equilibrium. Note that (3.2.4), the linearisation of (3.0.1), is

identical in form to the linearised version of the all–K$^+$ conductance system, with the exception of the parameters appearing in the coefficients. This is not surprising, since the equations in the nonlinear systems have almost identical forms, and hence we expect a similar representation in the linearisation. Also, the coefficients depend on the equilibrium point (V^*, m^*) of the nonlinear system, which in turn depends on the delay parameter μ.

Since $0 \leq m \leq 1$, the voltage $V = V(t)$ satisfies $V(0) < V < V(1)$ if $\mu < g_{\mathrm{L}}$, and $V(1) < V < V(0)$ if $\mu > g_{\mathrm{L}} + g_{\mathrm{Ca}}$. The voltage is unbounded if $g_{\mathrm{L}} < \mu < g_{\mathrm{L}}\left(1 - \frac{V_{\mathrm{L}}}{V_{\mathrm{Ca}}}\right)$, and may become infinite through the horizontal asymptote of the $V(m)$ nullcline. The coefficients a and c are bounded for any value of μ, with

$$\frac{g_{\mathrm{L}}}{C} \leq a \leq \frac{g_{\mathrm{L}} + g_{\mathrm{Ca}}}{C} \quad \text{and} \quad 0 < c < \frac{\overline{\lambda_m}}{2V_2},$$

which are simply

$$\frac{3}{20} \leq a \leq \frac{7}{20}, \quad \text{and} \quad 0 < c < \frac{\frac{1}{10}}{2(15)} = \frac{1}{300}$$

for our parameter set (Table 3.1). While the numerical ranges do depend on the parameter set used, these ranges specified in terms of the parameters are true for any general parameter set where the conductance constants are non–negative, and as long as the capacitance C and parameters V_2 and $\overline{\lambda_m}$ are all positive.

The coefficient d is bounded if the voltage is, and the bounds depend on the values of $|V(0)|$ and $|V(1)|$. In this case we obtain inequalities similar to (2.2.9) and (2.2.10), with $\overline{\lambda_n}, V_3$, and V_4 replaced with $\overline{\lambda_m}, V_1$, and V_2, respectively. Thus $d \geq \overline{\lambda_m} > 0$ for all μ. Also, in the linearisation of the system about (V_1^*, m_1^*), $V_1^* \to -\infty$ as $\mu \to g_{\mathrm{L}}$, and so $d \to \infty$. Similarly, in the linearisation

of the system about (V_3^*, m_3^*), $V_3^* \to +\infty$ as $\mu \to g_L + g_{Ca}$, and $d \to +\infty$. Since the value of V_2^* is always finite, the coefficient d in the linearisation about (V_2^*, m_2^*) is always bounded, above and below. The range $d \in [0.1, 0.106]$ is obtained by considering the limiting case $V_2^* = 0$.

If V is bounded, then b is bounded, and we obtain inequalities similar to (2.2.11) and (2.2.12), replacing g_K with g_{Ca} and V_K with V_{Ca}. In the linearisation of (3.0.1) about (V_1^*, m_1^*), the sign of b does not change, since $V_1^* < V_{Ca}$ for all μ where (V_1^*, m_1^*) exists, and so $b > 0$. The lower bound on b can be obtained by considering the limiting case $V_1^* = 0$, and so we have $b > \frac{g_{Ca}(V_{Ca} - V_1^*)}{C} = \frac{g_{Ca}V_{Ca}}{C} = 20$. As $\mu \to g_L$, $V_1^* \to -\infty$, and so $b \to +\infty$.

For the middle equilibrium point, (V_2^*, m_2^*), b is finite because V_2^* is always finite, and positive since $V_2^* < V_{Ca}$ for all μ where (V_2^*, m_2^*) is an equilibrium point of (3.0.1). We find that b is confined to the approximate range $(16.5, 20)$, where the upper bound is found using the limiting case $V_2^* = 0$, and the lower bound is obtained using $\mu = \bar{\mu}$, the point where (V_2^*, m_2^*) is generated via a saddle–node bifurcation.

In the linearisation about the upper equilibrium point (V_3^*, m_3^*), we find that b is positive if $\mu < g_L \left(1 - \frac{V_L}{V_{Ca}}\right)$, since $V_3^* < V_{Ca}$, $b = 0$ when $\mu = g_L \left(1 - \frac{V_L}{V_{Ca}}\right)$, since $V_3^* = V_{Ca}$ here, and $b < 0$ for $\mu > g_L \left(1 - \frac{V_L}{V_{Ca}}\right)$, since $V_3^* > V_{Ca}$. As $\mu \to g_L + g_{Ca}$, $V_3^* \to +\infty$ and $b \to -\infty$, and so b is unbounded from below. Using $\mu = \bar{\mu}$, we obtain the upper bound 16.5 for b, and so in the linearisation about (V_3^*, m_3^*), $b < 16.5$.

Motivated by the results obtained for the all–K$^+$ conductance system, we expect the bifurcation structure of the all–Ca^{2+} system to rely on the pair of delay parameters μ and τ. Considering the linearised system (3.2.4), we make

the usual ansatz $x = \xi_1 e^{\lambda t}$, $y = \xi_2 e^{\lambda t}$ and obtain the characteristic equation

$$\lambda^2 + (a + d)\lambda + (ad - bc) - \hat{\mu}\lambda e^{-\lambda \tau} - \hat{\mu} d e^{-\lambda \tau} = 0. \qquad (3.2.5)$$

Aside from the definitions of the coefficients a, b, c, and d, equation (3.2.5) is of the exact same form of the characteristic equation obtained for the all–K$^+$ system, (2.2.13), since both characteristic equations were obtained from identical linearised systems. We apply the Cooke–Grossman theory to study the delay–dependent stability of the all–calcium system with delay.

Before seeking purely imaginary roots, we first determine the stability of the equilibrium point(s) of system (3.0.1) with zero time delay.

3.2.3 The $\tau = 0$ Case

Given $\mu \in \mathbb{R}$, we must determine the stability of the equilibrium point(s) of system (3.0.1). The stability of an equilibrium point (V^*, m^*) is preserved in the linearisation, and so the problem is reduced to studying the stability of the zero solution of the linearised system (3.2.4). With $\tau = 0$ the system is reduced to two ordinary differential equations, and the characteristic becomes the quadratic polynomial

$$\lambda^2 + (a + d - \hat{\mu})\lambda + [(ad - bc) - \hat{\mu} d] = 0, \qquad (3.2.6)$$

with roots

$$\lambda_{\pm} = \frac{\hat{\mu} - (a + d) \pm \sqrt{[(a + d) - \hat{\mu}]^2 - 4[(ad - bc) - \hat{\mu} d]}}{2} . \qquad (3.2.7)$$

The zero solution of (3.2.4) is stable provided the Routh–Hurwitz conditions are met. These conditions are

(i). $a + d - \hat{\mu} > 0 \quad \Rightarrow \quad \hat{\mu} < a + d$, and

(ii). $(ad - bc) - \hat{\mu}d > 0 \quad \Rightarrow \quad \hat{\mu} < a - \frac{bc}{d}$.

Recall that the coefficients of system (3.2.4) arising from the linearisation of (3.0.1) about an equilibrium point (V^*, m^*) depend on the equilibrium point of the nonlinear system, which in turn depends on the value of μ. So all of a, b, c, and d are functions of μ. To check conditions (i) and (ii), we follow the same procedure outlined in the all–potassium section. We compute the coefficients and quantities in conditions (i) and (ii) for a large range of μ and then plot the results in Figure 3.3. These figures show that the plots of $\hat{\mu}$ and $a - \frac{bc}{d}$ intersect when $\mu = g_{\mathrm{L}}$ for (V_1^*, m_1^*), when $\mu = \bar{\mu}$ (the saddle–node bifurcation point) for (V_2^*, m_2^*), and when $\mu = \bar{\mu}$ and $g_{\mathrm{L}} + g_{\mathrm{Ca}}$ for (V_3^*, m_3^*). Since $V_1^* \to -\infty$ as $\mu \to g_{\mathrm{L}}$ and $V_3^* \to +\infty$ as $\mu \to g_{\mathrm{L}} + g_{\mathrm{Ca}}$, we use limits to show that the $a - \frac{bc}{d}$ and $\hat{\mu}$ curves intersect when μ assumes these values.

Both Routh–Hurwitz conditions are met for (V_1^*, m_1^*) and (V_3^*, m_3^*). Figure 3.3(a) plots both the conditions for the lower equilibrium point (V_1^*, m_1^*) for $-20 < \mu < g_{\mathrm{L}} = 3$, while the conditions are shown for (V_3^*, m_3^*) on $-2.22 \approx \bar{\mu} < \mu < g_{\mathrm{L}} + g_{\mathrm{Ca}} = 7$, its entire interval of definition, in Figure 3.3(c). Therefore, both (V_1^*, m_1^*) and (V_3^*, m_3^*) are stable for (3.0.1) with $\tau = 0$. Meanwhile, from Figure 3.3(b) we can see that condition (ii) is never met, and so (V_2^*, m_2^*) is unstable for (3.0.1) with zero time delay. The conditions are plotted on the sample interval $-2.22 < \mu < 20$. Furthermore, it is easy to classify (V_2^*, m_2^*) as an unstable saddle point. Let $\Delta_2 = [(a + d) - \hat{\mu}]^2 - 4[(ad - bc) - \hat{\mu}d]$, the discriminant of the roots (3.2.7) obtained in the linearisation about (V_2^*, m_2^*). Since condition (ii) is never met, then the discriminant of the roots is always positive $\Delta_2 > 0$, and so the roots of the characteristic equation $\lambda_{\pm}$ are both
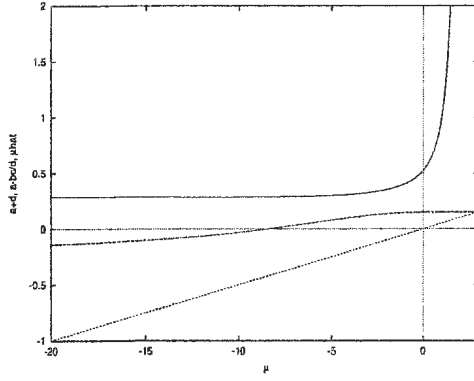
(a) Conditions for (V_1^*, m_1^*) with $-20 < \mu < g_\mathrm{L} = 3$.
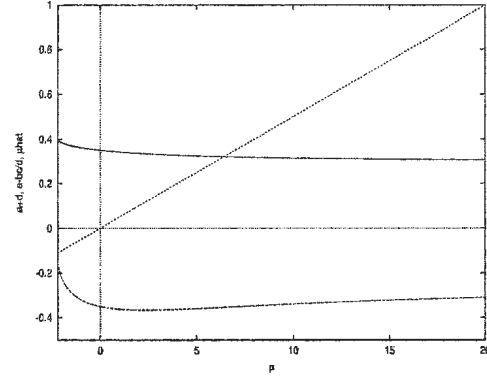
(b) Conditions for (V_2^*, m_2^*) with $-2.22 \approx \bar{\mu} < \mu < 20$.
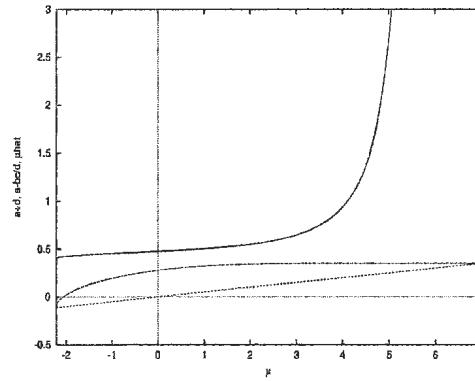
(c) Conditions for (V_3^*, m_3^*) with $-2.22 \approx \bar{\mu} < \mu < g_\mathrm{L} + g_\mathrm{Ca} = 7$.

Figure 3.3: Checking the Routh–Hurwitz conditions: Plots of $a + d$ (solid curve), $a - \frac{bc}{d}$ (dashed curve), and $\hat{\mu}$ (dotted line) against μ for each of the equilibrium points (V_i^*, m_i^*), $i = 1, 2, 3$.

always real–valued. Initially, we see that condition (i) is met, $\hat{\mu} < a + d$, and then after some point this condition is violated, that is $\hat{\mu} > a + d$. In either case, it follows that $\lambda_+ > 0$ while $\lambda_- < 0$, indicating that (V_2^*, m_2^*) is an unstable saddle point for all values of $\mu > \bar{\mu}$.

To classify the stable equilibria (V_1^*, m_1^*) and (V_3^*, m_3^*), we calculate the value of the discriminant corresponding to each point to see whether it is positive or negative. A positive discriminant indicates a stable node, while a negative discriminant yields a stable spiral. Let Δ_1 and Δ_3 denote the discriminant of the roots of (3.2.5) obtained by linearising about (V_1^*, m_1^*) and (V_3^*, m_3^*), respectively. We plot the quantities $[(a+d) - \hat{\mu}]^2$ and $4[(ad - bc) - \hat{\mu}d]$ versus μ for both (V_1^*, m_1^*) and (V_3^*, m_3^*) in Figure 3.4. In each case, we see that $[(a + d) - \hat{\mu}]^2 > 4[(ad - bc) - \hat{\mu}d]$, and so $\Delta_1 > 0$ and $\Delta_3 > 0$. Hence both eigenvalues $\lambda_\pm$ for each of (V_1^*, m_1^*) and (V_3^*, m_3^*) are real, with $\lambda_+ < 0$ and $\lambda_- < 0$ for each equilibrium point. It follows that both (V_1^*, m_1^*) and (V_3^*, m_3^*) are stable nodes. This classification of the equilibria (V_i^*, m_i^*), $i = 1, 2, 3$ for the (3.0.1) with $\tau = 0$ is only according to the particular parameter set included in Table 3.1.

These results for (3.0.1) with $\tau = 0$ are similar to the all–calcium system in the original Morris–Lecar system without delay, in that, when three equilibria exist, the middle equilibrium point is always an unstable saddle, while the upper and lower equilibria are stable nodes. Also, in the lower parameter region, $\mu < \bar{\mu}$, there is only a single equilibrium point (V_1^*, m_1^*) which is a stable node. The main differences in system (3.0.1) with zero time delay and the original Morris–Lecar calcium system is the parameter regions where there are two equilibria (V_2^*, m_2^*) and (V_3^*, m_3^*), which is the case if $g_{\rm L} < \mu <$

(a) Δ_1 for (V_1^*, m_1^*).

(b) Δ_3 for (V_3^*, m_3^*).
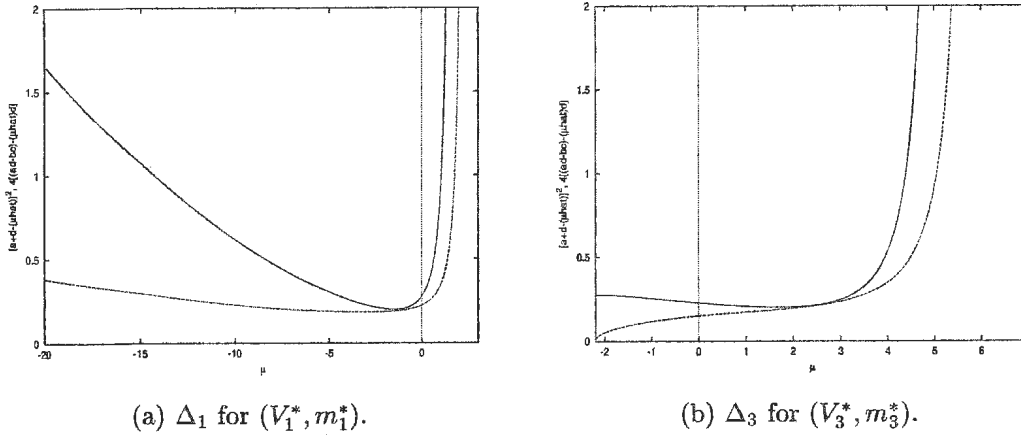
Figure 3.4: Plots of $[(a+d) - \hat{\mu}]^2$ (solid curve) and $4[(ad - bc) - \hat{\mu}d]$ (dashed curve) versus μ to determine the sign of the discriminant for equilibrium points (V_1^*, m_1^*) and (V_3^*, m_3^*).

$g_L + g_{Ca}$, and the upper parameter range $\mu > g_L + g_{Ca}$ where there is a single unstable saddle point (V_2^*, m_2^*). Neither of these situations is encountered in the original calcium system without delay. Note that, when the system has two equilibria, the existence of the saddle (V_2^*, m_2^*) gives rise to the behavior in which stability of the node (V_3^*, m_3^*) is only local, and not global. The separatrix solutions associated with (V_2^*, m_2^*) separate the (V, m)–plane, and trajectories from some initial conditions escape to $-\infty$ instead of approaching (V_3^*, m_3^*). Refer to Figures 3.1(c) and 3.1(e) for the nullcline plots where this situation is encountered.

We note that the theory is only valid for values of μ such that $\hat{\mu} \neq a + d$ or $\hat{\mu} \neq a - \frac{bc}{d}$. From Figure 3.3(b), we see that $\hat{\mu} = a + d$ for $\mu \approx 6.3$, in the linearisation of (3.0.1) about (V_2^*, m_2^*), and in this case the roots in (3.2.9)

become

$$\omega_{\pm}^2 = (ad - bc) \pm \hat{\mu}d < 0,$$

and so there are no positive real roots of (3.2.8). Also, from Figure 3.3, we find that $\hat{\mu} = a - \frac{bc}{d}$ when $\mu = g_{\mathrm{L}}$ for (V_1^*, m_1^*), for $\mu = \bar{\mu}$ for (V_2^*, m_2^*), and for $\mu = \bar{\mu}$, $\mu = g_{\mathrm{L}} + g_{\mathrm{Ca}}$ for (V_3^*, m_3^*). We neglect the physiologically unrealistic cases $\mu = g_{\mathrm{L}}$ and $\mu = g_{\mathrm{L}} + g_{\mathrm{Ca}}$, and comment more on the special case $\mu = \bar{\mu}$ in Section 3.2.7.

3.2.4 The System with Non–zero Delay $\tau > 0$

In this section, we apply the Cooke–Grossman theory to investigate the delay–dependent stability of the equilibria of the all–Ca^{2+} conductance system. We apply the results in [6] to analyse the degree–two transcendental characteristic equation of system (3.0.1). To look for purely imaginary roots of (3.2.5), we set $\lambda = i\omega$ in characteristic equation (3.2.5). We discuss the results for a general equilibrium (V^*, m^*) of system (3.0.1), and then address the specific details of each equilibrium point separately. The equations obtained are identical to those from the all–potassium system analysis, so after substitution, setting the resulting real and imaginary parts to zero, squaring both equations and adding, we obtain a quartic equation

$$\omega^4 + \left[(a + d)^2 - 2(ad - bc) - \hat{\mu}^2\right]\omega^2 + (ad - bc)^2 - \hat{\mu}^2 d^2 = 0, \qquad (3.2.8)$$

with roots

$$\omega_{\pm}^2 = \frac{1}{2}\left(\hat{\mu}^2 - a^2 - d^2 - 2bc\right)$$

$$\pm \left\{\frac{1}{4}\left(\hat{\mu}^2 - a^2 - d^2 - 2bc\right)^2 - \left((ad - bc)^2 - \hat{\mu}^2 d^2\right)\right\}^{\frac{1}{2}}. \quad (3.2.9)$$

Purely imaginary roots $\lambda = i\omega$ of (3.2.5) with $\omega > 0$ correspond to positive real roots of (3.2.8), *i.e.* the positive square roots of ω_+^2 and ω_-^2 that are real, which we denote by ω_+ and ω_-, respectively.

Recall that there are two cases to consider:

1. Delay–dominant case: $\hat{\mu}^2 > \left(a - \frac{bc}{d}\right)^2$, which leads to one imaginary root $\lambda_+ = i\omega_+$, with $\omega_+ > 0$.

2. Case of non–dominant delay: $\hat{\mu}^2 < \left(a - \frac{bc}{d}\right)^2$, with additional conditions

    (a) $\hat{\mu}^2 > a^2 + d^2 + 2bc$, and

    (b) $\left(\hat{\mu}^2 - a^2 - d^2 - 2bc\right)^2 > 4\left((ad - bc)^2 - \hat{\mu}^2 d^2\right)$.

    If all three criteria are met for this case, then there are two imaginary solutions $\lambda_\pm = i\omega_\pm$, with $\omega_+ > \omega_- > 0$.

The discussion of why each case leads to one or two purely imaginary roots was addressed at length in the all–potassium chapter. The method of approach is the same, in that we look for the values of the parameter μ such that the system falls under the dynamics described by Case 1 or Case 2. However, since multiple equilibria are possible for this system, we do this separately for each of the lower, middle, and upper equilibrium points. For each equilibrium point we compute the values of $\hat{\mu}^2$ and $\left(a - \frac{bc}{d}\right)^2$ for a large range of μ, or in the case of (V_3^*, m_3^*), where the equilibrium point is defined, and plot the results. Comparing the curves resulting from these plots, we obtain the parameter ranges where Cases 1 and 2 occur. The relevant plots are included in Figure 3.5.
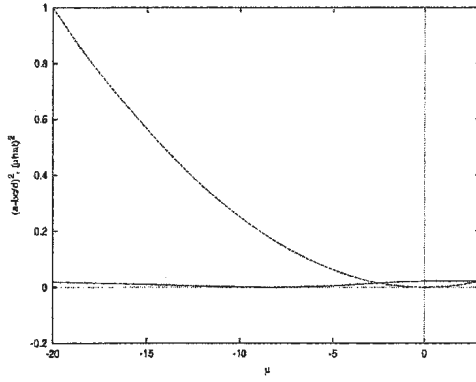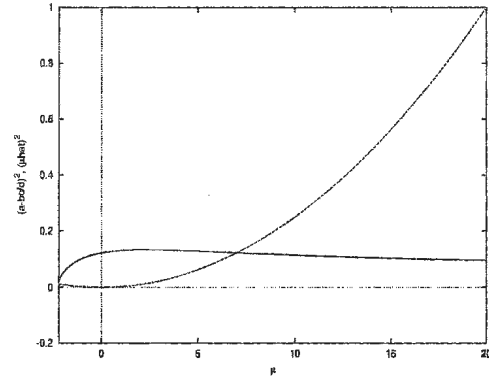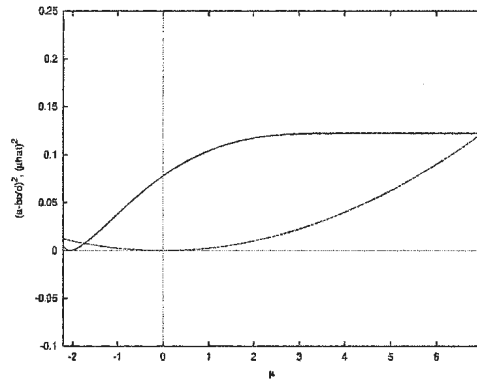
(a) Checking the cases for (V_1^*, m_1^*).

(b) Checking the cases for (V_2^*, m_2^*).

(c) Checking the cases for (V_3^*, m_3^*).

Figure 3.5: Plots of $\hat{\mu}^2$ (dashed curve) and $\left(a - \frac{bc}{d}\right)^2$ (solid curve) versus μ, for each of the three equilibrium points (V_i^*, m_i^*), $i = 1, 2, 3$.

3.2.5 Results for the lower Equilibrium Point (V_1^*, m_1^*)

Figure 3.5(a) contains the plots of $\hat{\mu}^2$ and $\left(a - \frac{bc}{d}\right)^2$ versus μ for coefficients a, b, c, and d arising in the linearisation of system (3.0.1) about the lower equilibrium point (V_1^*, m_1^*). Note that (V_1^*, m_1^*) is an equilibrium point of (3.0.1) provided $\mu < g_L$, and is the only equilibrium point of the system if $\mu < \bar{\mu}$. As in the case with zero delay, the curves intersect when $\mu = g_L$, corresponding to $V_1^* = -\infty$, which we verified using limits. There is a value of μ, say μ^-, such that $\hat{\mu}^2 > \left(a - \frac{bc}{d}\right)^2$, if $\mu < \mu^-$, but $\hat{\mu}^2 < \left(a - \frac{bc}{d}\right)^2$ for $\mu^- < \mu < g_L$. Therefore, if $\mu < \mu^-$, then Case 1 is satisfied, and if $\mu^- < \mu < g_L$ then the first condition of Case 2 is met. The value separating the cases is approximately $\mu^- \approx -2.52 < \bar{\mu}$, and so Case 1 occurs for the lower equilibrium point (V_1^*, m_1^*) in a range where it is the only equilibrium point of the system. Also, since $\mu^- < 0$, the Case 1 dynamics of system (3.0.1) linearised about (V_1^*, m_1^*) occur for inhibitory feedback only.

Consider first system (3.0.1) with $\mu < \mu^-$. Here, the system is in Case 1, and it follows that for every μ less than μ^-, there is a single purely imaginary eigenvalue $\lambda_+ = i\omega_+$, with $\omega_+ > 0$. This eigenvalue comes from $\omega_+^2 > 0$ of (3.2.9), while $\omega_-^2 < 0$ and therefore does not yield any positive real roots of (3.2.8). Therefore for every $\mu < \mu^-$, there is a value of τ for which the system has a purely imaginary eigenvalue, and a pair of complex conjugate eigenvalues cross the imaginary axis. The value of τ depends on the value of μ, and on the value of the ω_+ root. To determine the direction of the crossing, we check the transversality condition, the sign of the derivative of Re λ with respect to τ at $\lambda = \lambda_+$. This derivative is identical in form to that computed in Section 2.2.6

for the all–potassium case, and so we have

$$\mathrm{sign}\left\{\frac{d(\mathrm{Re}\lambda)}{d\tau}\right\}_{\lambda=i\omega} = \mathrm{sign}\left\{\pm\sqrt{\Delta}\right\}, \qquad (3.2.10)$$

where $\Delta = \left(\hat{\mu}^2 - (a+d)^2 + 2(ad-bc)\right)^2 - 4\left((ad-bc)^2 - \hat{\mu}^2 d^2\right)$ is the discriminant of (3.2.9). From (3.2.10), the sign is positive for ω_+^2 and negative for ω_-^2. In this case, only ω_+^2 is significant, and so the crossing of the imaginary axis is from left to right. Recall that, for system (3.0.1) with $\tau = 0$, (V_1^*, m_1^*) is a stable node. Therefore, considering $\mu < \mu^-$ and increasing τ, (V_1^*, m_1^*) becomes unstable at the smallest value of $\tau > 0$ for which ω_+ is a root of (3.2.8), and remains unstable if τ is increased further. There is a sequence of time delays, τ_n, given by

$$\tau_n = \frac{1}{\omega_+}\cos^{-1}\left\{\frac{a\omega_+^2 + d(ad-bc)}{\hat{\mu}(\omega_+^2+d^2)}\right\} + \frac{2\pi n}{\omega_+} \qquad (n=0,1,\ldots), \qquad (3.2.11)$$

for which we expect purely imaginary roots. The only significant crossing occurs with the first term, τ_0, which we label τ^*. A two–parameter bifurcation diagram illustrating how τ^* varies with μ for $\mu < \mu^-$ appears in Figure 3.6. Also, solving for ω_+ to obtain the value of τ^* for $\mu < \mu^-$ supports our earlier estimate of the value of $\mu^- \approx -2.52$.

In addition to the change in stability, for $\mu < \mu^-$, system (3.0.1) undergoes Hopf bifurcation when τ is increased through τ^*. To see this, note that all eigenvalues of system (3.0.1) with $\tau = 0$ have negative real parts. Also, since the first and only crossing of the imaginary axis occurs when $\tau = \tau^*$, all eigenvalues of system (3.0.1) have strictly negative real parts while $\tau \in [0, \tau^*)$. There is only a single pair of complex conjugate eigenvalues with positive real parts when $\tau > \tau^*$, and all other eigenvalues have strictly negative real parts. This is the pair that migrated across the imaginary axis for $\tau = \tau^*$. And since
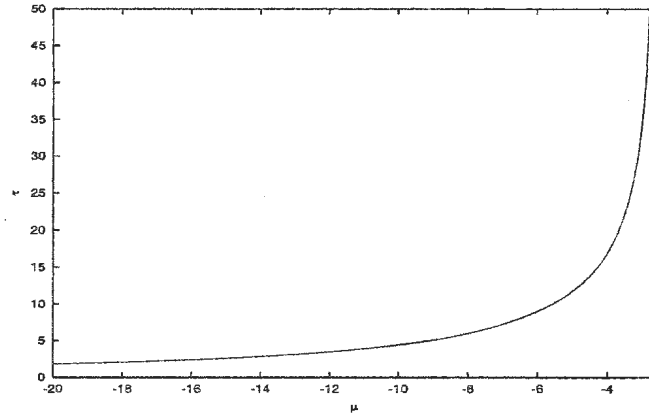
Figure 3.6: Bifurcation Diagram plotting τ^* vs. μ for system (3.0.1) linearised about (V_1^*, m_1^*), with $\mu \leq -2.52$ (Case 1).

the transversality condition (*c.f.* Section 2.2.6) is satisfied, all hypotheses of the Hopf bifurcation theorem for DDEs are met, and so (3.0.1) with $\mu < \mu^-$ does indeed undergo Hopf bifurcation as τ is increased through τ^*. The calculation to determine the stability and direction of the Hopf bifurcation is addressed at the end of this chapter in section 3.2.8, which also includes some sample calculations illustrating the results discussed here.

Interestingly enough, two qualitatively different types of Hopf bifurcation occur for system (3.0.1) with $\mu < \mu^-$. If $\mu \leq -3.7$ then the Hopf bifurcation which occurs as τ is increased through τ^* is supercritical, and the emerging periodic solutions branch to stable oscillations. Figure 3.7 demonstrates these results for the representative value $\mu = -5$. Here, we see that (V_1^*, m_1^*) loses stability as τ is increased through $\tau^* = 11.7$ ms, and stable periodic solutions emerge via a supercritical Hopf bifurcation. The initial functions used in this simulation were the constant functions $V(\theta) = -17$, and $m(\theta) = m_\infty(-17)$,

$-\tau \leq \theta \leq 0$, selected close to the equilibrium point to demonstrate the change in stability.
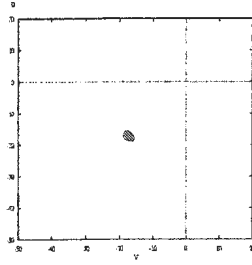
(a) $V(t-\tau)$ vs. V.
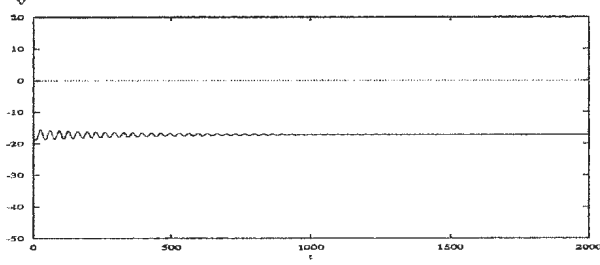
(b) $V(t)$ vs. t for $\tau = 11$.
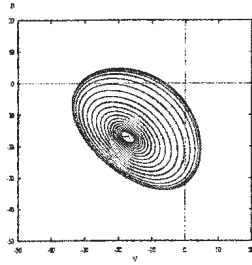
(c) $V(t-\tau)$ vs. V.
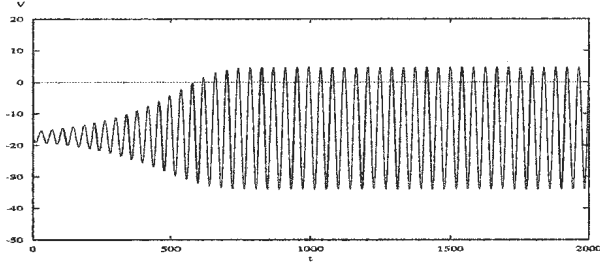
(d) $V(t)$ vs. t for $\tau = 13$.

Figure 3.7: Numerical simulation of system (3.0.1) with $\mu = -5$ (Case 1). The delay is increased from $\tau = 11$ to $\tau = 13$, illustrating the loss of stability of the equilibrium voltage, and the onset of stable oscillations.

However, if $-3.7 < \mu < \mu^- \approx -2.52$, then the Hopf bifurcation is sub-critical, and the emerging periodic solutions are orbitally unstable. Hence for some $\tau < \tau^*$, the system possesses unstable periodic orbits along with the stable equilibrium point (V_1^*, m_1^*). Moreover, numerical simulations of (3.0.1) with $\mu \in (-3.7, \mu^-)$ indicate the presence of stable periodic solutions for some $\tau < \tau^*$. Since the system admits only the single equilibrium point (V_1^*, m_1^*)

with μ in this range, it must lie inside the nested periodic orbits, with the unstable limit cycle inside the stable limit cycle. In this way the system exhibits bistability with coexistence of a stable equilibrium and a stable limit cycle. Trajectories with initial conditions in the basin of attraction of (V_1^*, m_1^*) will approach the stable equilibrium point, while those outside this region will tend to the stable limit cycle. At $\tau = \tau^*$, the equilibrium point loses stability, and the unstable limit cycle disappears via a subcritical Hopf bifurcation. The stable limit cycle remains, appears to be globally attractive, and is well–formed with a finite (and somewhat large) amplitude. This behavior is consistent with the emergence of a stable limit cycle prior to τ^*, which grows in amplitude as τ is increased. These observations lead us to propose the following conjecture:

Conjecture 3.2.5.1. *Assume the parameter set listed in Table 3.1 for system (3.0.1). Then (3.0.1) linearised about (V_1^*, m_1^*) with $\mu \in (-3.7, \mu^-)$ (Case 1) undergoes a periodic saddle–node bifurcation (PSNB) at some value of the delay $\tau_{PSN} < \tau^*$, where τ^* is given by the τ_0 term of sequence (3.2.11). A pair of stable and unstable periodic orbits are generated at τ_{PSN}, and the system exhibits bistability with a stable equilibrium point (V_1^*, m_1^*) and a stable limit cycle for $\tau_{PSN} < \tau < \tau^*$. Furthermore, the unstable periodic orbit formed at τ_{PSN} is lost in a subcritical Hopf bifurcation at $\tau = \tau^*$.*

The conjectured qualitative dynamics of system (3.0.1) for $-3.7 < \mu < \mu^-$ are illustrated in the schematic bifurcation diagram in Figure 3.8. Note in particular the PSNB at τ_{PSN} prior to τ^*, and the subcritical Hopf bifurcation at τ^*. Without actually computing the branch of periodic solutions emanating from the Hopf bifurcation using a numerical continuation technique, we cannot verify that a PSNB is responsible for the observed behaviour. As such, we

cannot obtain an accurate estimate of the delay value where periodic solutions arise for (3.0.1) for a given $\mu \in (-3.7, \mu^-)$ (τ_{PSN} if the orbits are generated by a PSNB). Even if a PSNB is responsible, we cannot determine the basin of attraction of the stable limit cycle while τ is close to τ_{PSN}, since it will have a small region of attraction in comparison to the stable equilibrium point. Numerical simulations of (3.0.1) with $\mu \in (-3.7, \mu^-)$ provide only a rough estimate of τ_{PSN}, but more importantly they reveal existence of stable periodic orbits for $\tau < \tau^*$, which, along with an unstable subcritical Hopf bifurcation at τ^*, provide evidence for a PSNB. Problems detecting stable limit cycles associated with a small basin of attraction were avoided by selecting initial conditions far away from the equilibrium point. Also, decreasing the strength of the inhibitory feedback signal decreased the value of the delay where periodic orbits arise. For example, with $\mu = -3.7$, $\tau^* = 19.6$, stable periodic orbits were detected at $\tau = 19.4$ ms, just before the Hopf bifurcation. But with $\mu = -2.52$, $\tau^* = 652$ ms, stable periodic orbits were detected for $\tau = 36$ ms, long before the stability of the equilibrium point changes.

In Figure 3.9, we present a numerical simulation highlighting the dynamics of system (3.0.1) described above. With $\mu = -3$, the system is in Case 1, and we have $\tau^* = 34.6$, the delay value where the equilibrium point loses stability. A stable limit cycle is present when $\tau = 28 < \tau^*$, and the Hopf bifurcation at τ^* is subcritical and unstable, which we verify in §3.2.8. With the delay just below τ^* and initial conditions close to the equilibrium point in Figure 3.9(d), we see that (V_1^*, m_1^*) is stable, and coexists with the stable
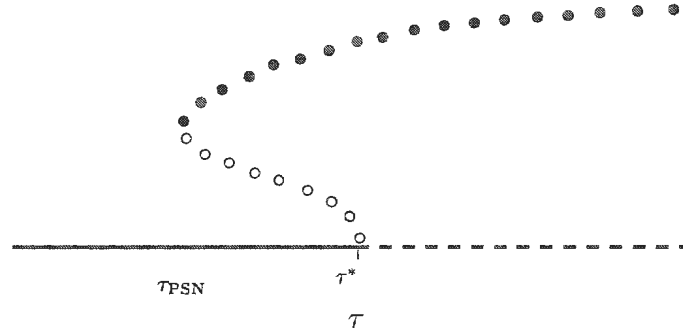
Figure 3.8: Conjectured bifurcation structure of system (3.0.1) with parameters in the range of Case 1 $(-3.7 < \mu < \mu^-)$, as τ is increased.

limit cycle. Increasing τ just above τ^* leads to instability of the equilibrium point, and trajectories starting close to (V_1^*, m_1^*) eventually approach a stable limit cycle, see Figures 3.9(g) and 3.9(h). Numerical evidence suggests that it is the same limit cycle which formed earlier at $\tau = 28$, which has changed and grown in amplitude with the increase in delay.

Multiple stability switches can only occur if the system has two purely imaginary eigenvalues. This is only possible for the Case 2 Cooke–Grossman results. Figure 3.5(a) indicates that the primary requirement for Case 2, *i.e.* $\hat{\mu}^2 < \left(a - \frac{bc}{d}\right)^2$, is satisfied for all μ such that $\mu^- < \mu < g_{\mathrm{L}}$. The plots required to check the additional criteria (a) and (b) associated with Case 2 are included in Figure 3.10(a), where we find that $\hat{\mu}^2 < a^2 + d^2 + 2bc$ for all $\mu \in (\mu^-, g_{\mathrm{L}})$. Hence condition (a) of Case 2 is not satisfied for any $\mu^- < \mu < g_{\mathrm{L}}$, while condition (b) is satisfied for all μ in this interval. This implies that, for $\mu^- < \mu < g_{\mathrm{L}}$, both ω_+^2 and ω_-^2 are real, but negative, and so there are no positive real roots of (3.2.8).
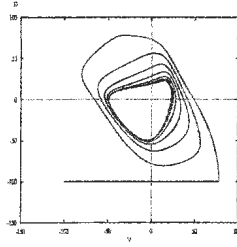
(a) $V(t-\tau)$ vs. V.
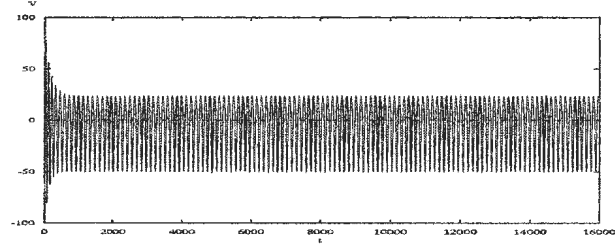
(b) $V(\theta) = -100, n(\theta) = n_\infty(-100)$ with $\tau = 28$.
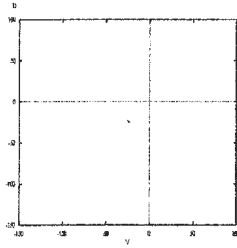
(c) $V(t-\tau)$ vs. V.
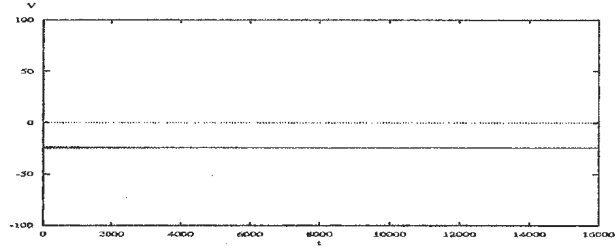
(d) $V(\theta) = -25, n(\theta) = n_\infty(-25)$ with $\tau = 33$.
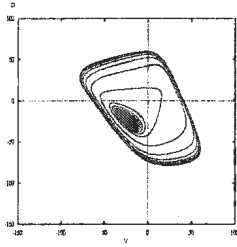
(e) $V(t-\tau)$ vs. V.

(f) $V(\theta) = -25, n(\theta) = n_\infty(-25)$ with $\tau = 35$.
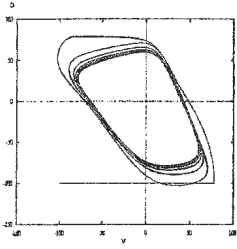
(g) $V(t-\tau)$ vs. V.
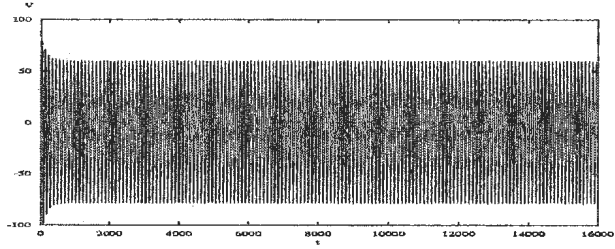
(h) $V(\theta) = -100, n(\theta) = n_\infty(-100)$ with $\tau = 35$.

Figure 3.9: Numerical simulation of system (3.0.1) with $\mu = -3$ (Case 1), illustrating that a stable limit cycle emerges before the equilibrium point loses stability as τ is increased.

Therefore, system (3.0.1) linearised about (V_1^*, m_1^*) with μ in this range admits no purely imaginary eigenvalues, and consequently there is no change in the stability of (V_1^*, m_1^*). Since this equilibrium point was shown to be stable for $\tau = 0$, we conclude that the lower equilibrium point (V_1^*, m_1^*) of system (3.0.1) for a given $\mu^- < \mu < g_L$ is stable for all $\tau \geq 0$. Also, for those $\mu \in (\mu^-, g_L)$ where (V_1^*, m_1^*) is the only equilibrium point of (3.0.1), i.e. for $\mu^- < \mu < \bar{\mu}$, the system cannot undergo Hopf bifurcation. As such, any periodic solutions of the system must arise from a different bifurcation. Stability of (V_1^*, m_1^*) for increasing τ is illustrated in the numerical simulations presented in Figures 3.11. Here, we consider $\mu = -2.3$, and plot the solution for two different time delays, $\tau = 50$ and $\tau = 200$ ms. No change in stability was detected, even with a four–fold increase in the magnitude of the delay. With the higher time delay, more transient oscillations are observed initially, but the solution eventually settles down to the constant equilibrium voltage V_1^*. The initial conditions $V(\theta) = -25$ and $n(\theta) = n_\infty(-25)$ are selected close to $(V_1^*, m_1^*) = (-27.67, 0.0065)$ to specifically demonstrate its local stability properties.

Figure 3.11 also indicates some interesting additional dynamics of (3.0.1) with $\mu^- < \mu < \bar{\mu}$. While (V_1^*, m_1^*) remains stable for all $\tau \geq 0$, this stability is only local, and (V_1^*, m_1^*) is not globally attractive for all $\tau > 0$. Instead, the system exhibits bistability, with a stable equilibrium point and a stable limit cycle. We conjecture that the stable periodic orbit emerges via a PSNB for some value of the delay τ_{PSN}, similar to that observed in the Case 1 for $\mu \in (-3.7, \mu^-)$. However, for system (3.0.1), there is less evidence to support this conjecture than Conjecture 3.2.5.1, since for $\mu \in (\mu^-, \bar{\mu})$ there is no loss of

(a) Condition (a).
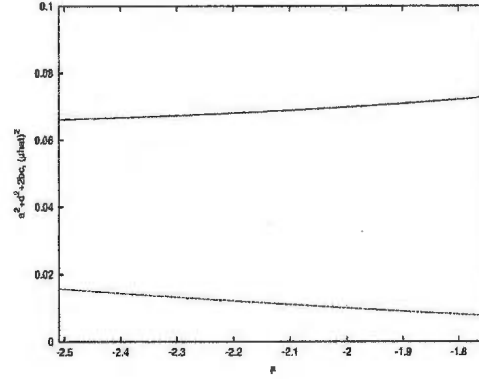
(b) Magnification of 3.10(a).
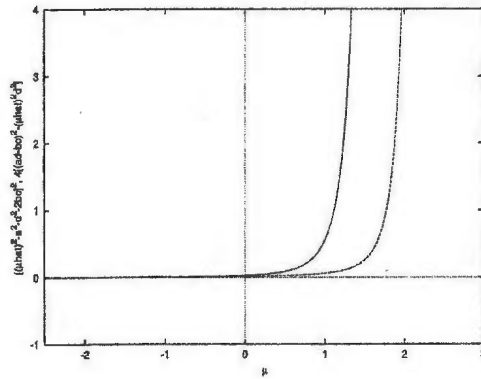
(c) Condition (b).
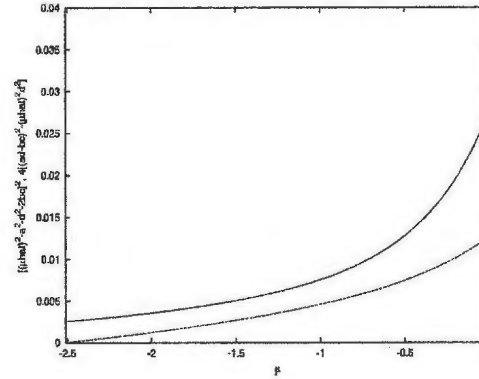
(d) Magnification of 3.10(c).

Figure 3.10: Checking conditions (a) and (b) of Case 2 for (V_1^*, m_1^*): Plots of $\hat{\mu}^2$ (dashed curve) and $a^2 + d^2 + 2bc$ (solid curve), versus μ, and plots of $(\hat{\mu}^2 - a^2 - d^2 - 2bc)^2$ (solid curve) and $4\left((ad - bc)^2 - \hat{\mu}^2 d^2\right)$ (dashed curve) versus μ. Magnifications of both are also included.
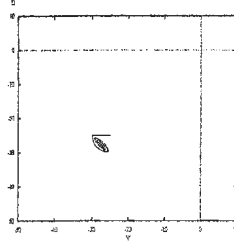
(a) $V(t-\tau)$ vs. V.
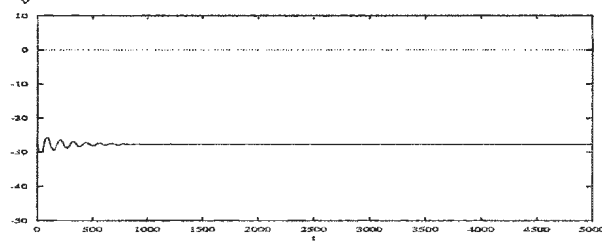
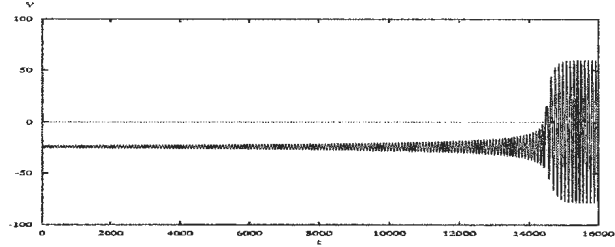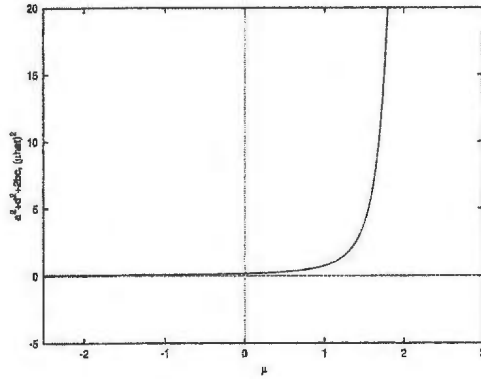(b) $V(\theta) = -25, n(\theta) = n_\infty(-25)$ with $\tau = 50$.
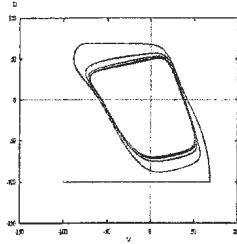
(c) $V(t-\tau)$ vs. V.
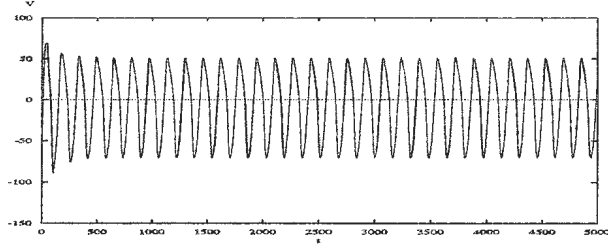
(d) $V(\theta) = -100, n(\theta) = n_\infty(-100)$ with $\tau = 50$.
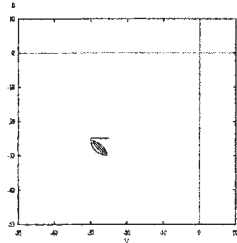
(e) $V(t-\tau)$ vs. V.
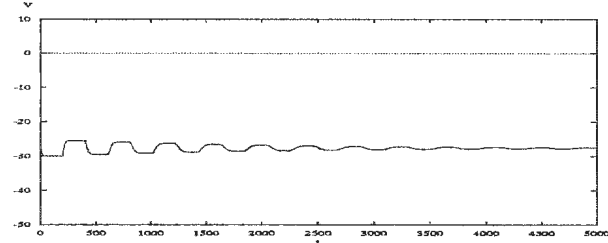
(f) $V(\theta) = -25, n(\theta) = n_\infty(-25)$ with $\tau = 200$.
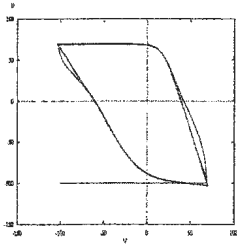
(g) $V(t-\tau)$ vs. V.
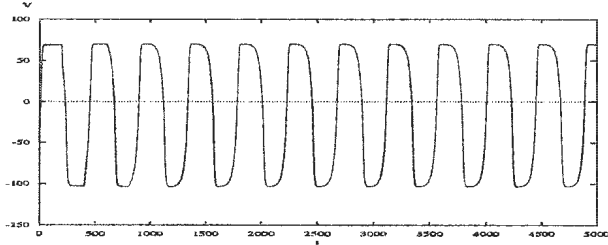
(h) $V(\theta) = -100, n(\theta) = n_\infty(-100)$ with $\tau = 200$.

Figure 3.11: Numerical simulation of system (3.0.1) with $\mu = -2.3$, and the delay increased from $\tau = 50$ to $\tau = 200$ ms. Initial data are specified in each sub–figure.

an unstable periodic orbit via a subcritical Hopf bifurcation subsequent to the appearance of stable periodic orbits. As such, we cannot be sure that a pair of stable/unstable orbits are generated together. If we do suppose that a PSNB occurs, then the unstable periodic orbit generated at τ_{PSN} must be present for $\tau > \tau_{\text{PSN}}$, since there are no purely imaginary eigenvalues to facilitate its vanishing through a subcritical Hopf bifurcation. Therefore with $\mu^- < \mu < \bar{\mu}$, the stable equilibrium (V_1^*, m_1^*) persists along with the stable limit cycle for all $\tau > \tau_{\text{PSN}}$, and the system displays bistability over a large range of delay. Also, numerical simulations showed no indication of decrease in the amplitude of the stable limit cycle. The schematic bifurcation diagram in Figure 3.12 illustrates the qualitative dynamics conjectured here. This behavior was detected for system (3.0.1) with $\mu \in (\mu^-, \bar{\mu})$, the interval whereby system (3.0.1) is outside Case 1 for which (V_1^*, m_1^*) is the only equilibrium point of the system. There is some additional behavior to report for the system with $\bar{\mu} < \mu < g_{\text{L}}$, but we leave a discussion of these results until the stability of the upper equilibrium point, (V_3^*, n_3^*), with non–zero time delay, has been addressed.

Note that for $\mu = \mu^-$, and $\mu = g_{\text{L}}$, we have $\hat{\mu}^2 = \left(a - \frac{bc}{d} \right)^2$, and the Cooke–Grossman theory makes no assertions pertaining to equilibrium point stability. The latter case $\mu = g_{\text{L}}$ is unphysical, since $V_1^* \to -\infty$ as $\mu \to g_{\text{L}}$. The value $\mu = \mu^-$ marks the end of the Case 1 dynamics for system (3.0.1) linearised about (V_1^*, m_1^*), and this situation resembles the $\mu = \mu^*$ case for the all–K$^+$ system (c.f. Chapter 2). Here we obtain a double zero eigenvalue, along with a pair of purely imaginary eigenvalues. The zero eigenvalues occur for
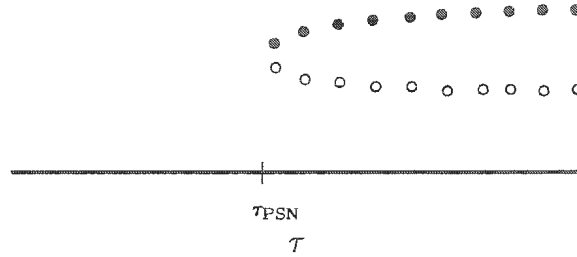
Figure 3.12: Bifurcation diagram illustrating the behavior conjectured for system (3.0.1) with $\mu \in (\mu^-, \bar{\mu})$, as τ is increased.

infinite values of τ, different from the τ^* value where the purely imaginary pair occur. Since there is no degeneracy, the lower equilibrium point does undergo a stability change and a Hopf bifurcation as τ is increased past τ^*. For the approximate value of $\mu^- \approx -2.52$, numerical simulations indicate that (V_1^*, m_1^*) is stable for $\tau < \tau^* = 652$, and loses stability at τ^* via a subcritical Hopf bifurcation, and that the bifurcating periodic solutions are orbitally unstable. Numerical results also indicate the presence of stable periodic solutions for $\tau < \tau^*$, and so we again conjecture that the stable/unstable limit cycle pair is generated via a PSNB for some $\tau_{\mathrm{PSN}} < \tau^*$.

We summarize the results proved in this section, along with the results presented in section 3.2.8, in the following theorem:

Theorem 3.2.5.2. *Assume that parameters in system (3.0.1) are as in Table 3.1. Then for $\mu < \mu^-$, (V_1^*, m_1^*) is stable for all $\tau \in [0, \tau^*)$, where μ^-, τ^* are defined earlier. For all $\tau > \tau^*$, (V_1^*, m_1^*) is unstable, and the system undergoes a Hopf bifurcation at $\tau = \tau^*$. If $\mu \leq -3.7$ ($-3.7 < \mu < \mu^-$), the Hopf bifurcation at τ^* is supercritical (subcritical), and the emerging periodic*

solutions are orbitally stable (unstable). If $\mu^- < \mu < g_L$, then (V_1^*, m_1^*) is stable for all $\tau \geq 0$.

3.2.6 Results for the middle Equilibrium Point (V_2^*, m_2^*)

We first recall that (V_2^*, m_2^*) is an equilibrium point of (3.0.1) for all $\mu > \bar{\mu}$, and that this middle equilibrium point is unstable for $\tau = 0$. Stability switching of such an equilibrium point is only possible if the system satisfies all the requirements of Case 2, so that both $\lambda_+ = i\omega_+$ and $\lambda_- = i\omega_-$ are roots of the characteristic equation, for which both left to right and right to left crossings of the imaginary axis are possible. An unstable equilibrium point with $\tau = 0$ may undergo multiple (finite) stability switches before instability persists, provided the initial crossing is in the right to left direction. When the system falls under Case 1, there is only a single crossing of the imaginary axis with $\lambda_+ = i\omega_+$, and this crossing is left to right by the transversality condition Lemma 2.2.6. Since (V_2^*, m_2^*) is unstable with $\tau = 0$, the system linearised about (V_2^*, m_2^*) must have at least one eigenvalue with positive real part for $\tau \geq 0$. Therefore, a left to right crossing as τ increases will have no bearing on the stability of the equilibrium point.

In Figure 3.5(b), we see that $\hat{\mu}^2 > \left(a - \frac{bc}{d}\right)^2$ for $\mu > 7^+$, which indicates the single requirement for Case 1 is satisfied. By the reasoning above, the predicted crossing of the imaginary axis does not affect stability of the equilibrium point, and so the unstable equilibrium point cannot become stable with increasing τ. Therefore, with μ in this range, the middle equilibrium point (V_2^*, m_2^*) is unstable for all $\tau \geq 0$. Note that (V_2^*, m_2^*) is the only equilibrium point of system (3.0.1) for $\mu > g_L + g_{Ca}$.

The primary requirement for Case 2, $\hat{\mu}^2 < \left(a - \frac{bc}{d}\right)^2$, is met for $\bar{\mu} < \mu < g_\text{L} + g_\text{Ca}$, as indicated in Figure 3.5(b). The plots required to check the additional criteria associated with Case 2 are included in Figure 3.13. From Figure 3.13(a), it is clear that $\hat{\mu}^2 < a^2 + d^2 + 2bc$ for all $\mu \in (\bar{\mu}, g_\text{L} + g_\text{Ca})$, meaning that (a) is never satisfied. Therefore, the characteristic equation has no purely imaginary roots, since both ω_+^2 and ω_-^2 are both real but negative. Hence stability changes in the equilibrium point are not possible with increasing τ. Thus for any $\mu \in (\bar{\mu}, g_\text{L} + g_\text{Ca})$, the middle equilibrium point (V_2^*, m_2^*) is unstable for all $\tau \geq 0$. Moreover, this equilibrium point is unstable for all $\tau \geq 0$ whenever it is an equilibrium point of the system, *i.e.* for $\mu > \bar{\mu}$. These results lead to the following theorem:

Theorem 3.2.6.1. *Assume that parameters in system (3.0.1) are as in Table 3.1. Then (V_2^*, m_2^*) of system (3.0.1) is unstable for all $\mu > \bar{\mu}$, for all $\tau \geq 0$.*

When $\mu = \bar{\mu}$ and $\mu = 7^+$, we have $\hat{\mu}^2 = \left(a - \frac{bc}{d}\right)^2$, and the system possesses a double zero eigenvalue, and a pair of purely imaginary eigenvalues. In each case, the equilibrium voltages are finite, but for $\mu = 7^+$, (V_2^*, m_2^*) is unstable for all $\tau \geq 0$, and so whether or not the zero eigenvalues occur for a different value of τ than the purely imaginary eigenvalues is not really relevant. The results for $\mu = \bar{\mu}$ are addressed in the following Section 3.2.7 which deals with the results for the upper equilibrium point (V_3^*, m_3^*).

(a) Condition (a).
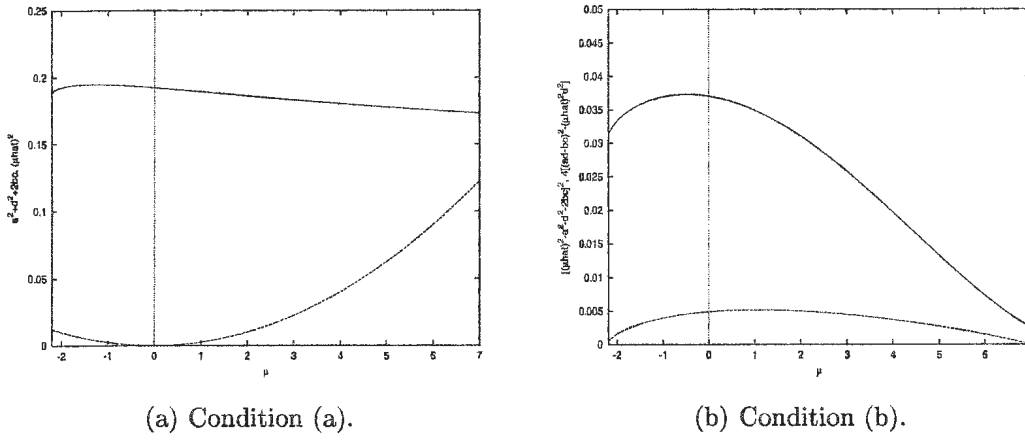
(b) Condition (b).

Figure 3.13: Checking conditions (a) and (b) of Case 2 for (V_2^*, m_2^*): Plots of $\hat{\mu}^2$ (dashed curve) and $a^2 + d^2 + 2bc$ (solid curve), versus μ, and $(\hat{\mu}^2 - a^2 - d^2 - 2bc)^2$ (solid curve) and $4((ad - bc)^2 - \hat{\mu}^2 d^2)$ (dashed curve) versus μ.

3.2.7   Results for the upper Equilibrium Point (V_3^*, m_3^*)

In this section we address the delay–dependent stability of the upper equilibrium point, (V_3^*, m_3^*). This equilibrium point exists for the system when $\bar{\mu} < \mu < g_{\text{L}} + g_{\text{Ca}}$, and was found to be stable for $\tau = 0$. According to Figure 3.5(c), there is a small interval where the criterion for Case 1 is met, $\bar{\mu} < \mu < \mu^{--} \approx -1.73$. With μ in this interval, we obtain one purely imaginary root of the characteristic equation, $\lambda_+ = i\omega_+$. Along with the transversality condition, this indicates a left to right crossing of the imaginary axis by an eigenvalue of the system. Since all eigenvalues of the system linearised about (V_3^*, m_3^*) have negative real part with $\tau = 0$, a transition to instability is expected at the smallest value of the sequence (3.2.11). That is, for $\mu \in (\bar{\mu}, \mu^{--})$, there exists a $\tau^* = \tau_0$ of sequence (3.2.11), depending on μ, such that (V_3^*, m_3^*) is stable for all $\tau < \tau^*$, and unstable for $\tau > \tau^*$. Furthermore, stability of the equilibrium point cannot be regained once $\tau > \tau^*$, since no right to left crossings of the imaginary axis occur. Calculating the initial terms τ_0 of the sequence (3.2.11), we obtain a bifurcation diagram of τ^* versus μ for $\bar{\mu} < \mu < \mu^{--}$, which appears in Figure 3.14. This figure describes how τ^* varies with the strength of the feedback signal, μ, and indicates where stability of (V_3^*, m_3^*) changes in terms of the bifurcation pair (μ, τ^*).

For $\mu \in (\bar{\mu}, \mu^{--})$, the system exhibits some additional interesting dynamics. As τ is increased past τ^*, the upper equilibrium point (V_3^*, m_3^*) loses stability, and the system undergoes a Hopf bifurcation. However, with μ in this range, the system admits two additional equilibria, (V_1^*, m_1^*), which is stable for all $\tau \geq 0$, and (V_2^*, m_2^*), which is unstable for all $\tau \geq 0$. If we consider the system with $\tau < \tau^*$, then both (V_1^*, m_1^*) and (V_3^*, m_3^*) are stable equilibrium points,
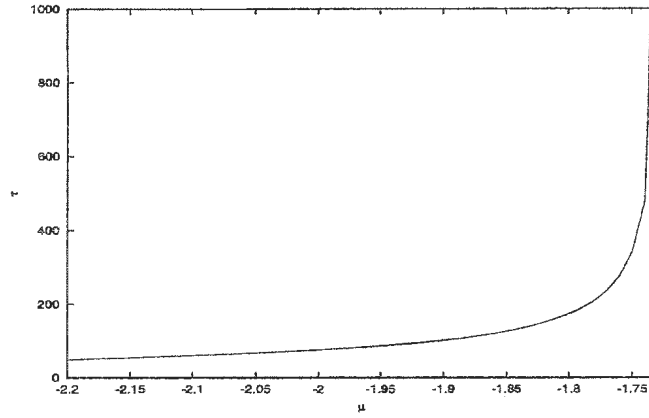
Figure 3.14: Bifurcation Diagram plotting τ^* vs. μ for system (3.0.1) linearised about (V_3^*, m_3^*), with $\bar{\mu} < \mu < \mu^{--}$ (Case 1).

and so the system exhibits multistability. Furthermore, numerical simulations also indicate the emergence of periodic solutions of system (3.0.1) prior to the loss of stability of (V_3^*, m_3^*) at τ^*. The mechanism is believed to be the same as that observed for (V_1^*, m_1^*) in Case 1, that is, via a PSNB at for some value of the delay $\tau_{\text{PSN}} < \tau^*$:

Conjecture 3.2.7.1. *Assume the parameter set listed in Table 3.1 for system (3.0.1). Then (3.0.1) linearised about (V_3^*, m_3^*) with $\mu \in (\bar{\mu}, \mu^{--})$ (Case 1) undergoes a periodic saddle–node bifurcation (PSNB) at some value of the delay $\tau_{PSN} < \tau^*$, where τ^* is given by the τ_0 term of sequence (3.2.11). A pair of stable and unstable periodic orbits are generated at τ_{PSN}, and the system exhibits tristability with a two stable equilibria (V_1^*, m_1^*), (V_3^*, m_3^*) and a stable limit cycle for $\tau_{PSN} < \tau < \tau^*$. Furthermore, the unstable periodic orbit formed at τ_{PSN} is lost in a subcritical Hopf bifurcation at $\tau = \tau^*$.*

As mentioned in Conjecture 3.2.7.1, the Hopf bifurcation at τ^* was found

to be subcritical and unstable, which would facilitate the loss of an unstable periodic orbit generated at τ_{PSN}, thereby supporting our claim. Therefore, we propose that the system is bistable with two locally stable equilibria for $0 \leq \tau < \tau_{\text{PSN}}$, and for $\tau_{\text{PSN}} < \tau < \tau^*$ the system is tristable with two locally stable equilibria and a locally stable limit cycle around the upper equilibrium point. Stability of (V_3^*, m_3^*) is lost if τ is increased past τ^*, and the system reverts back to a bistable state, only this time we have a locally stable limit cycle coexisting with the locally stable equilibrium (V_1^*, m_1^*). In numerical simulations with τ just above τ^*, trajectories starting with initial conditions close to (V_3^*, m_3^*) appeared to approach the same stable limit cycle generated at τ_{PSN}, which had grown in amplitude with the increase in delay. This further supports our PSNB conjecture.

To demonstrate the occurrence of tristability in system (3.0.1), we present a numerical simulation of system (3.0.1) with $\mu = -2.2$ in Figure 3.15. For this value of μ, $\tau^* = 47.7$, the value of the delay where $(V_3^*, m_3^*) = (19.29, 0.78)$ loses stability. If we take $\tau = 45$ ms, then trajectories were observed to approach one of the two stable equilibria, and periodic solutions were not detected. But if we consider $\tau = 46 < \tau^*$, with initial conditions $V(\theta) = -100$, $m(\theta) = m_\infty(-100)$, then the trajectory approaches a stable limit cycle (dotted curve). If we use $V(\theta) = -35$, $m(\theta) = m_\infty(-35)$ with $\tau = 46$, then the trajectory tends to the stable equilibrium point (V_1^*, m_1^*) (solid curve), and with with $V(\theta) = 20$, $m(\theta) = m_\infty(20)$, and $\tau = 46$ then the trajectory approaches (V_3^*, m_3^*) (dashed curve). The three solutions with these initial data are included in Figure 3.15.

As a final remark for system (3.0.1) with $\mu \in (\bar{\mu}, \mu^{--})$, we note that the
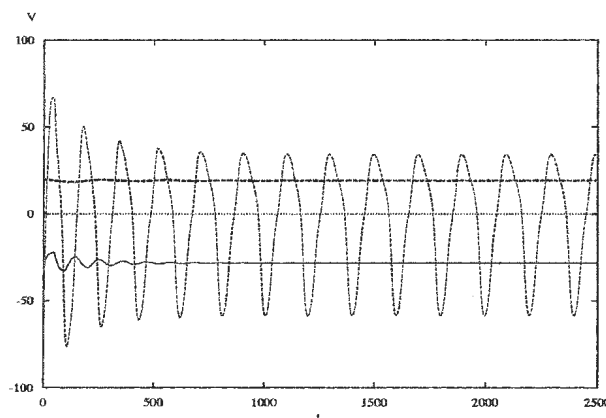
Figure 3.15: Numerical simulation of system (3.0.1) with $\mu = -2.2$ and $\tau = 46 < \tau^*$, illustrating the occurrence of tristability in the all–Ca^{2+} system.

domains of attraction of the locally stable equilibrium points (V_1^*, m_1^*) and (V_3^*, m_3^*) are delay–dependent. As a consequence, trajectories starting from the same initial data can be made to approach different stable equilibria simply by increasing the delay. A numerical simulation presented in Figure 3.16 of system (3.0.1) with $\mu = -2$ illustrates this point. For this value of μ, $\tau^* = 67.6$. With initial conditions $V(\theta) = 50$, $m(\theta) = m_\infty(50)$ and $\tau = 15$, the trajectory tends to (V_3^*, m_3^*) (dashed curve), but with $\tau = 20$ we find that the solution with the same initial conditions approaches the lower equilibrium (V_1^*, m_1^*) (solid curve).

In Figure 3.5(c), it is clear that $\hat{\mu}^2 < \left(a - \frac{bc}{d}\right)^2$ for all μ such that $\mu^{--} < \mu < g_L + g_{Ca}$, the remainder of the interval where the upper equilibrium point (V_3^*, m_3^*) exists. However, checking conditions (a) and (b) of Case 2 in Figure 3.17 reveals that (b) is satisfied while (a) is not, implying that both ω_+^2 and ω_-^2 are real but negative. Thus, there are no purely imaginary roots of
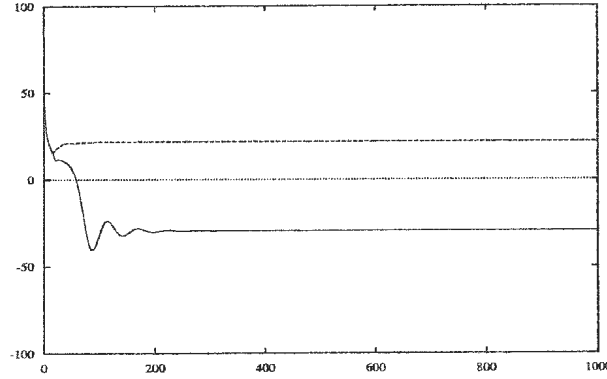
Figure 3.16: Numerical simulation of system (3.0.1) with $\mu = -2$, with the delay increased from $\tau = 15$ to $\tau = 20$, using the same initial conditions. This illustrates the domain of attraction of the equilibria are delay–dependent.

the characteristic equation, and so (V_3^*, m_3^*) does not change stability as τ is increased, and is locally stable for all $\tau \geq 0$.

However, with $\mu \in (\mu^{--}, g_L + g_{Ca})$, the complete dynamics of the system are not governed simply by the one stable equilibrium (V_3^*, m_3^*) if $\mu \in (g_L, g_L + g_{Ca})$, or the two stable equilibria (V_1^*, m_1^*) and (V_3^*, m_3^*) if $\mu \in (\mu^{--}, g_L)$. There are sub–intervals of $(\mu^{--}, g_L + g_{Ca})$ where the system admits different qualitative dynamics.

Consider $\mu^{--} < \mu < g_L$. We can further sub–divide this interval into two regions, $\mu^{--} < \mu \leq -1.4$, and $-1.4 < \mu < g_L$. With $\mu^{--} < \mu \leq -1.4$, and small delay, the system appears to be bistable with two stable equilibria, (V_1^*, m_1^*) and (V_3^*, m_3^*). However, increasing the delay leads to the onset of stable periodic solutions which coexist with the stable equilibria, and the system is tristable. We conjecture that a PSNB at some value $\tau_{PSN} > 0$ is
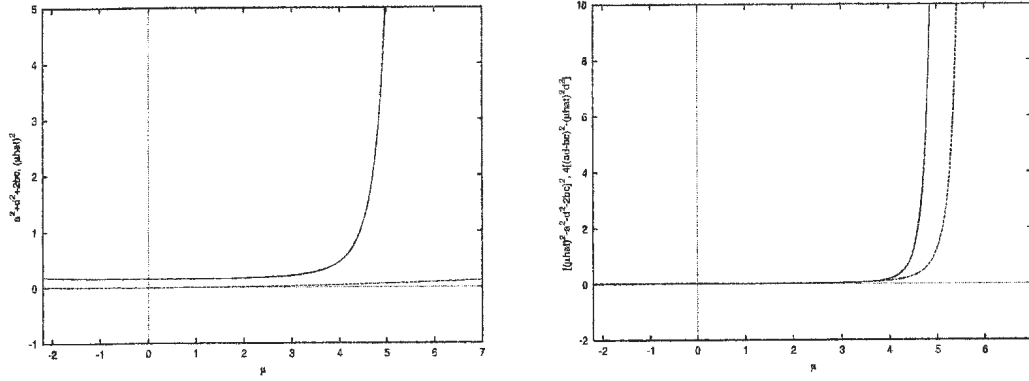
(a) Condition (a).

(b) Condition (b).
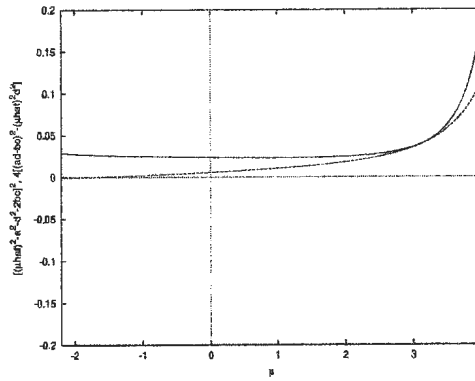
(c) Magnification of 3.17(b).

Figure 3.17: Checking conditions (a) and (b) of Case 2 for (V_3^*, m_3^*): Plots of $\hat{\mu}^2$ (dashed curve) and $a^2 + d^2 + 2bc$ (solid curve), versus μ, and plots of $(\hat{\mu}^2 - a^2 - d^2 - 2bc)^2$ (solid curve) and $4\left((ad - bc)^2 - \hat{\mu}^2 d^2\right)$ (dashed curve) versus μ, and a magnification of 3.17(b).

responsible for this. The system exhibits tristability for a large range of the delay, $\tau > \tau_{\text{PSN}}$, since an unstable periodic orbit which might be generated at τ_{PSN} cannot be lost in a subsequent subcritical Hopf bifurcation.

We were not able to find any numerical evidence of a delay–induced PSNB with $-1.4 < \mu < g_{\text{L}}$. No periodic solutions were observed with μ in this range, and the system is bistable with two stable equilibria and one unstable equilibrium. If $g_{\text{L}} < \mu < g_{\text{L}} + g_{\text{Ca}}$, then the lower equilibrium (V_1^*, m_1^*) is no longer present, and the system admits two equilibria, (V_2^*, m_2^*), which is unstable for all $\tau \geq 0$, and (V_3^*, m_3^*), which is stable for all $\tau \geq 0$.

The values of μ for which $\hat{\mu}^2 = \left(a - \frac{bc}{d} \right)^2$ are $\mu = \bar{\mu}$, $\mu = \mu^{--}$, and $\mu = g_{\text{L}} + g_{\text{Ca}}$. It was shown earlier that this situation leads to a double zero eigenvalue and a pair of purely imaginary eigenvalues. We disregard the latter case, since $V_3^* \rightarrow +\infty$ as $\mu \rightarrow g_{\text{L}} + g_{\text{Ca}}$. The value $\mu = \mu^{--}$ marks the end of Case 1 dynamics for system (3.0.1) linearised about (V_3^*, m_3^*). Qualitatively, the results for this parameter value are similar to the results obtained in Section 3.2.5 for μ^-, in that the double zero eigenvalue and pure imaginary pair occur for different values of τ. The double zero roots appear as $\tau \rightarrow +\infty$, and since there is no degeneracy, we predict that a stability change and Hopf bifurcation occur as τ is increased past $\tau^* = 1473$, the delay value corresponding to the pair of purely imaginary eigenvalues. However, the situation surrounding $\mu = \bar{\mu}$ is more interesting: as $\mu \rightarrow \bar{\mu}$, the Hopf bifurcation and steady–state saddle–node bifurcation coalesce in what appears to be a Takens–Bogdanov interaction [37]. Here, we expect τ^0, the delay value corresponding to the zero eigenvalues, to approach a finite limit, $\bar{\tau}^0$, as $\omega \rightarrow 0$. This differs from other cases where $\hat{\mu}^2 = \left(a - \frac{bc}{d} \right)^2$, where $\tau^0 \rightarrow \infty$ as $\omega \rightarrow 0$. Since we cannot

obtain an exact numerical representation for $\bar{\mu}$, and since the limit is difficult to evaluate analytically, we estimate the limit using the approximate value $\bar{\mu} \approx -2.22$. With this value we obtain $\bar{\tau}^0 = 46$, and conjecture that the point $(\bar{\mu}, \bar{\tau}^0)$ is a Takens–Bogdanov point.

The phenomenon of bistability was observed in the original all–calcium conductance system studied by Morris and Lecar, in which the $V(m)$ nullcline was monotone increasing and the system possessed three equilibria, an unstable saddle between two stable nodes. They showed that a trajectory starting with initial conditions could be made to approach different stable equilibria by including an impulse of current to raise the voltage past the region where the separatrix of the saddle point intersects the voltage axis. However, this requires non–zero applied current ($I \neq 0$). We were able to obtain bistability in the all–calcium system with delayed recurrent feedback and no applied current, indicating that the feedback alone is capable of producing bistability. Furthermore, the all–calcium system with delay, (3.0.1), is even capable of demonstrating tristability, between two stable equilibria and a stable limit cycle. The original system without delay did not exhibit such diverse and complex behavior.

This concludes the detailed analysis of the all–calcium conductance system with delay. Addressed here, at length, was the stability of the equilibria, as well as other more complicated dynamics of the model. The all–calcium system with delayed recurrent feedback exhibits a diverse spectrum of dynamical phenomena, and are much more rich than these of the original model without delay. Figure 3.18 provides a summary of the dynamics observed for system (3.0.1) as a sequence of schematic bifurcation diagrams. In the next chap-

ter, we shall combine both conductance systems and study a two–dimensional model with delay, obtained from a simplification of the full three–dimensional system.
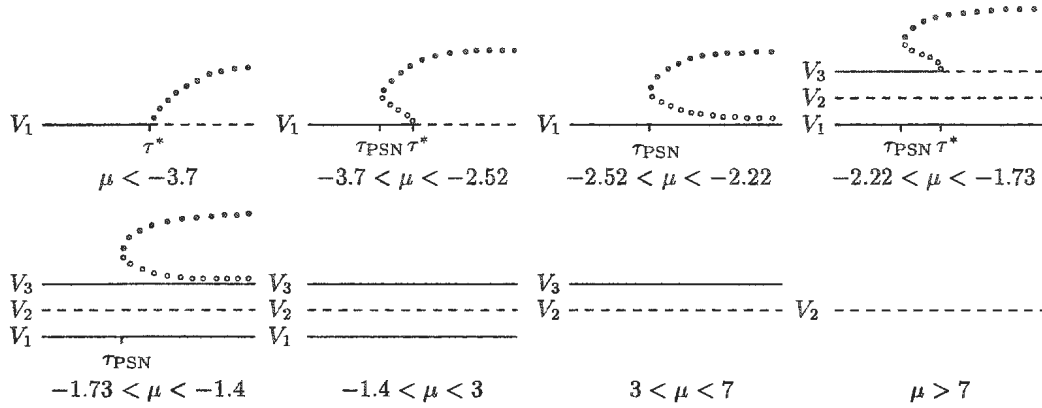
Figure 3.18: Sequence of schematic bifurcation diagrams outlining the conjectured bifurcation structure of system (3.0.1) as μ and τ are varied. Delay times for Hopf bifurcation (τ^*) and PSNB (τ_{PSN}) are indicated.

The following theorem summarizes the results proved in this section:

Theorem 3.2.7.2. *Assume that parameters in system (3.0.1) are as in Table 3.1. Then for $\bar{\mu} < \mu < \mu^{--}$, (V_3^*, m_3^*) is stable for all $\tau \in [0, \tau^*)$, where $\bar{\mu}$, μ^{--}, τ^* are defined earlier. For all $\tau > \tau^*$, (V_3^*, m_3^*) is unstable, and the system undergoes a subcritical Hopf bifurcation at $\tau = \tau^*$, and the emerging periodic solutions are orbitally unstable. If $\mu^{--} < \mu < g_L + g_{Ca}$, then (V_3^*, m_3^*) is stable for all $\tau \geq 0$.*

3.2.8 Direction and Stability of Hopf Bifurcation

In this section we examine the stability and direction of the Hopf bifurcation for the all–calcium conductance system with delay (3.0.1). Since the equations are identical in form to those of the all–potassium system with delay, aside from the parameters, the analysis required to determine the details of the bifurcating periodic solutions is identical to that presented in the chapter on the all–K$^+$ system. The previous sections have shown that the system admits at most one pair of purely imaginary roots $\pm i\omega_+$, and hence multiple stability switches are not possible for any equilibria of the system. Therefore, at most one (significant) Hopf bifurcation is expected for those μ where the system linearised about the lower or upper equilibrium points has a pair of purely imaginary eigenvalues. Furthermore, we know from the transversality condition computed in Section 2.2.6 that any crossing of the imaginary axis is from left to right, i.e. if $\lambda(\tau) = \alpha(\tau) + i\omega(\tau)$, then $\alpha(\tau^*) = 0$, $\omega(\tau^*) = \omega_+$, and

$$\frac{d\alpha(\tau^*)}{d\tau} > 0.$$

The lower and upper equilibrium points are capable of at most one change in stability, while the middle equilibrium point is unstable for all $\tau \geq 0$. Therefore, let (V^*, m^*) be an equilibrium point of (3.0.1). Specifically, $(V^*, m^*) = (V_1^*, m_1^*)$ if $\mu < \mu^-$, and $(V^*, m^*) = (V_3^*, m_3^*)$ if $\bar{\mu} < \mu < \mu^{--}$. The nonlinear system with equilibrium point shifted to the origin, and with the hyperbolic

trigonometric functions expanded is

$$
\begin{aligned}
\frac{dx}{dt} &= -ax + by + \hat{\mu}x(t-\tau) - \alpha xy \\
\frac{dy}{dt} &= cx - dy - c\left(\beta_v - \frac{1}{2}\beta_u\right)x^2 - \frac{d}{2V_4}\beta_u xy \\
&\quad - \frac{c}{V_4^2}\left[\frac{5}{24} + \beta_v\left(\frac{1}{2}\beta_u - \beta_v\right)\right]x^3 - \frac{d}{8V_4^3}x^2 y + O(x^4).
\end{aligned}
\tag{3.2.12}
$$

Here,

$$
\beta_u = \tanh(u), \quad \beta_v = \tanh(v), \quad u = \frac{V^* - V_1}{2V_2}, \quad v = \frac{V^* - V_1}{V_2}, \quad \alpha = \frac{g_{Ca}}{C},
$$

and the coefficients a, b, c, d and $\hat{\mu}$ were defined earlier for the linearised system (3.2.4). The calculation on the centre manifold is the same, and we obtain the same expressions for the g_{ij} terms, and hence the expressions for μ_2, β_2 and T_2, the coefficients which determine the stability, direction and period of the bifurcating periodic solutions, are also identical. One must simply replace the coefficients for the all-potassium system with those of the all-calcium system, given above for (3.2.12), to reproduce the analysis.

Now we turn to the results of this important calculation. For the lower equilibrium point (V_1^*, m_1^*), system (3.0.1) has a pair of complex conjugate, purely imaginary eigenvalues $\pm i\omega_+$ for (μ, τ^*), where $\mu < \mu^- \approx -2.52$, and τ^* is given by (3.2.11). Recall that for $\mu \leq -3.7$, the onset of stable periodic solutions was observed only as τ was increased through τ^*, corresponding to the loss of stability of (V_1^*, m_1^*), the sole equilibrium point of the system. If we consider the specific example $\mu = -5$, then we expect to find a supercritical Hopf bifurcation ($\mu_2 > 0$) at $\tau = \tau^*$, and that the bifurcating periodic solutions are orbitally stable ($\beta_2 < 0$). For this example, the purely imaginary root is $\lambda_+ = i\omega_+ = i \times 0.1786$, and the delay time for the bifurcation is $\tau^* = 11.7$

ms. For the $q(\theta)$ eigenfunction, we obtain $\beta = 0.00132 - i \times 0.00164$, and for $q^*(s)$ we have $\nu_1 = 0.2145 + i \times 0.2075$, $\nu_2 = -2.74 + i \times 30.37$. For the g_{ij} coefficients, we obtain $g_{20} = -0.00045 - i \times 0.001147$, $g_{11} = -0.000242 - i \times 0.001318$, $g_{02} = -0.000034 - i \times 0.001489$, and $g_{21} = -0.00317 - i \times 0.00395$. Computing $C_1(0)$ we obtain $C_1(0) = -0.00159 - i \times 0.00198$, and hence $\mu_2 = (0.00159)(\text{Re}\{\lambda'(0)\})^{-1} > 0$, since $\text{Re}\{\lambda'(0)\} > 0$, and $\beta_2 = -0.00317 < 0$. Thus our predictions as to the direction and stability of the Hopf bifurcation are confirmed. Similar results were obtained for a sample of value of $\mu \leq -3.7$.

On the other hand, for $-3.7 < \mu \leq \mu^-$, stable periodic solutions were observed prior to the loss of stability of (V_1^*, m_1^*), that is for $\tau < \tau^*$. We conjectured that these stable periodic solutions were generated by a PSNB for some value $\tau_{\text{PSN}} < \tau^*$, along with an unstable periodic orbit. In this case, we expect to see a subcritical Hopf bifurcation ($\mu_2 < 0$), and that the bifurcating periodic solutions are orbitally unstable ($\beta_2 > 0$). Considering $\mu = -3$, we find that $\lambda_+ = i\omega_+ = i \times 0.0733$, $\tau^* = 34.6$ ms, $\beta = 0.00117 - i \times 0.00050$, $\nu_1 = 0.1455 + i \times 0.0769$, $\nu_2 = 13.77 + i \times 16.96$, $g_{20} = 0.000268 - i \times 0.00049$, $g_{11} = 0.000331 - i \times 0.000456$, $g_{02} = 0.000394 - i \times 0.000421$, and $g_{21} = 0.00218 - i \times 0.00395$. For $C_1(0)$ we obtain $C_1(0) = 0.00109 - i \times 0.00198$, which yields $\mu_2 = (-0.00109)(\text{Re}\{\lambda'(0)\})^{-1} < 0$, and $\beta_2 = 0.00218 > 0$. This verifies that the Hopf bifurcation at $\tau^* = 34.6$ is subcritical, and that the bifurcating periodic solutions are orbitally unstable. A sample of values of $\mu \in (-3.7, \mu^-)$ yielded similar results.

With $\bar{\mu} < \mu < \mu^{--}$, (V_1^*, m_1^*) is stable for all $\tau \geq 0$, but (V_3^*, m_3^*) loses stability as τ is increased through the (Hopf) bifurcation value τ^*. Also, stable periodic solutions were detected for $\tau < \tau^*$ most likely arising via PSNB.

For this case, we expect to find that the unstable periodic orbit formed at some $\tau_{\mathrm{PSN}} < \tau^*$ is lost via a subcritical Hopf bifurcation at τ^*. To see if this is the case, we calculate the coefficients μ_2 and β_2 for the sample value $\mu = -2.2$. For this value of μ we have $\lambda_+ = i\omega_+ = i \times 0.0215$, $\tau^* = 48.8$ ms, $\beta = 0.0223 - i \times 0.00458$, $\nu_1 = 0.1133 + i \times 0.2517$, $\nu_2 = 9.10 + i \times 40.62$, $g_{20} = -0.00177 + i \times 0.00972$, $g_{11} = -0.00262 + i \times 0.00942$, $g_{02} = -0.00347 + i \times 0.00913$, and $g_{21} = 0.00651 - i \times 0.0192$. Computing $C_1(0)$ we obtain $C_1(0) = 0.00423 - i \times 0.0116$. This gives $\mu_2 = (-0.00423)(\mathrm{Re}\{\lambda'(0)\})^{-1} < 0$, which indicates that the Hopf bifurcation is subcritical, and $\beta_2 = 0.00846 > 0$, which implies that the bifurcating periodic solutions are orbitally unstable, as expected. Checking a large sample of values of $\bar{\mu} < \mu < \mu^{--}$ produced similar results.

The results of this detailed analysis are consistent with results obtained from numerical simulations, and verifies our earlier claims. The subcritical Hopf bifurcation branching to unstable oscillations was observed with $-3.7 < \mu < \mu^-$ for (V_1^*, m_1^*), and with $\bar{\mu} < \mu < \mu^{--}$ for (V_3^*, m_3^*). Along with numerically–detected stable periodic orbits for $\tau < \tau^*$, the subcritical, unstable Hopf bifurcation(s) support our PSNB conjecture. However, this detailed Hopf bifurcation analysis cannot provide evidence for a PSNB of the system with $\mu^{--} < \mu < g_{\mathrm{L}} + g_{\mathrm{Ca}}$, since there is no Hopf bifurcation of the system for these values of μ. Hence this phenomenon is a trend observed for $\bar{\mu} < \mu < \mu^{--}$, and is believed to persist with $\mu \in (\mu^{--}, -1.4]$, based on results from numerical simulations.

Chapter 4

The Full–2D Model with Delay

With both the calcium and potassium conductance systems operational, Morris and Lecar [24] found that the original model without delay is capable of supporting voltage oscillations. Analysis of the full three–dimensional model requires simultaneous adjustment of several parameters, making it even difficult to establish requirements for oscillations from numerical study of the full system in some generality. To facilitate their study of the model with both conductance systems active, Morris and Lecar successfully reduced the dimension of the system, invoking an inequality of Tikhonov [38] which allows reduction of the dimension of the phase space without changing the character of the singular point of the system. They then were able to apply the Poincaré–Bendixson theorem to prove the existence of periodic orbits of the reduced system. The physiological justification of such a reduction lies in the difference in relaxation times of the Ca^{2+} and K^+ conductances. The calcium conductance operates on a much faster time scale than the potassium conductance, and so by assuming that g_{Ca} is instantaneously in steady state at all

times, *i.e.* $m = m_\infty(V)$, we obtain the reduced two–dimensional system with delay

$$C\dot{V}(t) = -g_{\mathrm{L}}(V - V_{\mathrm{L}}) - g_{\mathrm{K}}n(V - V_{\mathrm{K}}) - g_{\mathrm{Ca}}m_\infty(V)(V - V_{\mathrm{Ca}})$$
$$+ \mu V(t - \tau)$$

$$(4.0.1)$$

$$\dot{n}(t) = \lambda_n(V)\left[n_\infty(V) - n\right],$$

with $m_\infty(V)$, $n_\infty(V)$, and $\lambda_n(V)$ given by

$$
\begin{cases}
m_\infty(V) = \dfrac{1}{2}\left[1 + \tanh\left(\dfrac{V - V_1}{V_2}\right)\right], \\[2ex]
n_\infty(V) = \dfrac{1}{2}\left[1 + \tanh\left(\dfrac{V - V_3}{V_4}\right)\right], \\[2ex]
\lambda_n(V) = \overline{\lambda_n}\cosh\left(\dfrac{V - V_3}{2V_4}\right).
\end{cases}
\qquad (4.0.2)
$$

System (4.0.1) with $\mu = 0$ is the original V, N reduced system studied by Morris and Lecar. In this thesis, we refer to the delayed system (4.0.1) as the full–2D Morris–Lecar model with delay. In effect, m has been removed as a dependent variable. Inspection of system (4.0.1) reveals that it is basically the all–potassium system with delay (2.0.1), with an extra nonlinear term in the DDE to account for the steady–state calcium conductance.

We have already established that each conductance system in isolation is capable of supporting voltage oscillations in the presence of delayed recurrent feedback. Since the original conductance systems were incapable of displaying periodic behavior, we conclude that the addition of a delay allows for more complex dynamics. The purpose of this chapter is to analyse the two–

dimensional reduced model with delayed recurrent feedback, so that we may gain some insight to the effects of adding a delay to this more complex system.

4.1 The Full–2D model without Delay

With $\mu = 0$, we obtain the original V, N reduced system proposed by Morris and Lecar:

$$C\dot{V}(t) = -g_{\mathrm{L}}(V - V_{\mathrm{L}}) - g_{\mathrm{K}}n(V - V_{\mathrm{K}}) - g_{\mathrm{Ca}}m_{\infty}(V)(V - V_{\mathrm{Ca}})$$

$$(4.1.1)$$

$$\dot{n}(t) = \lambda_n(V)\left[n_{\infty}(V) - n\right],$$

with $m_{\infty}(V)$, $n_{\infty}(V)$, and $\lambda_n(V)$ as given in (4.0.2). The $\dot{n} = 0$ nullcline is the same as that in the all–potassium system,

$$n(V) = n_{\infty}(V) = \frac{1}{2}\left[1 + \tanh\left(\frac{V - V_3}{V_4}\right)\right].$$

The equation of the $\dot{V} = 0$ nullcline is

$$V(n) = \frac{g_{\mathrm{Ca}}V_{\mathrm{Ca}}m_{\infty}(V) + g_{\mathrm{K}}V_{\mathrm{K}}n + g_{\mathrm{L}}V_{\mathrm{L}}}{g_{\mathrm{Ca}}m_{\infty}(V) + g_{\mathrm{L}} + g_{\mathrm{K}}n},$$

which is no longer a hyperbola, due to the hyperbolic tangent term. However, with $\mu = 0$ the nullclines still intersect only once in the (V, n)–plane, and so the system admits a single equilibrium point (V^*, n^*). This is evident in Figure 4.1(b), which contains a plot of the nullclines of (4.1.1). The parameter set used in the investigation of the full system is included in Table 4.1.

To determine the local stability of the equilibrium point (V^*, n^*), we let

Parameter Set		
$g_{Ca} = 4$ mmho/cm^2	$g_K = 8$ mmho/cm^2	$g_L = 3$ mmho/cm^2
$V_{Ca} = 100$ mV	$V_K = -70$ mV	$V_L = -50$ mV
$V_1 = 10$ mV	$V_3 = -1.0$ mV	$C = 20$ μF/cm^2
$V_2 = 15$ mV	$V_4 = 14.5$ mV	$\overline{\lambda_n} = \frac{1}{15}$ s^{-1}

Table 4.1: Morris–Lecar parameter set for the full two–dimensional system.

$x = V - V^*$ and $y = n - n^*$, and linearise to obtain

$$
\frac{dx}{dt} = -\frac{1}{C}\left[g_L + g_K n^* + g_{Ca}\left(m_\infty(V^*) + \frac{(V^* - V_{Ca})}{2V_2}\operatorname{sech}^2\left(\frac{V^* - V_1}{V_2}\right)\right)\right]x
$$
$$
+\frac{g_K}{C}(V_K - V^*)y
$$

$$
\frac{dy}{dt} = \frac{\overline{\lambda_n}}{2V_4}\cosh\left(\frac{V^* - V_3}{2V_4}\right)\operatorname{sech}^2\left(\frac{V^* - V_3}{V_4}\right)x - \overline{\lambda_n}\cosh\left(\frac{V^* - V_3}{2V_4}\right)y.
$$

Setting

$$
a = \frac{1}{C}\left[g_L + g_K n^* + g_{Ca}\left(m_\infty(V^*) + \frac{(V^* - V_{Ca})}{2V_2}\operatorname{sech}^2\left(t\right)\right)\right],
$$

$$
c = \frac{\overline{\lambda_n}}{2V_4}\cosh\left(u\right)\operatorname{sech}^2\left(v\right), \quad b = \frac{g_K(V_K - V^*)}{C}, \quad d = \overline{\lambda_n}\cosh\left(u\right),
$$

where $u = \frac{V^* - V_3}{2V_4}$, $v = \frac{V^* - V_3}{V_4}$, $t = \frac{V^* - V_1}{V_2}$, where t in this case is a parameter, not the independent (time) variable of the system. With these substitutions,

we obtain

$$\lambda^2 + (a+d)\lambda + (ad - bc) = 0$$

as the characteristic equation of (4.1.1). By the Routh–Hurwitz conditions, (V^*, n^*) is stable provided (i) $a > -d$ and (ii) $ad > bc$.

The equilibrium of system (4.1.1) is $(V^*, n^*) = (-49.995, 1.16 \times 10^{-3})$. With this point and the parameter values cited in Table 4.1, we compute the coefficients a through d of the linearised system, which appear in Table 4.2. Since a and d are both positive, condition (i) $a > -d$ is satisfied. Also, since b is negative and c is positive, condition (ii) is met as well, implying that both eigenvalues of the system have negative real parts. Furthermore, since the discriminant $\Delta = (a+d)^2 - 4(ad - bc) = 4.52 \times 10^{-4} > 0$ of the characteristic equation is positive, it follows that the single equilibrium point is a stable node.

Parameter Value
$a = 0.149$
$b = -8.00$
$c = 2.98 \times 10^{-5}$
$d = 0.187$

Table 4.2: The values of the coefficients of the linearised system of (4.1.1).

4.2 The Full–2D model with Delay

Consider (4.0.1) with non–zero μ. As with the conductance systems, we begin our analysis of the full two–dimensional model with delay by examining how

the nullclines of the system change as the parameter μ is varied. This will indicate the number and position of the equilibria of the system in the (V, n)–plane.

4.2.1 The Nullclines of the System

Since the second equation of (4.0.1) does not contain the parameter μ, the $\dot{n} = 0$ nullcline is simply

$$n(V) = n_\infty(V) = \frac{1}{2}\left[1 + \tanh\left(\frac{V - V_3}{V_4}\right)\right], \qquad (4.2.1)$$

which is a monotone increasing sigmoidal function with horizontal asymptotes -1 and 1 as $V \to -\infty$ and $+\infty$, respectively. This is the same as the nullcline obtained in the all–potassium conductance system.

For the all–potassium conductance system, we obtained V as an explicit function of n for the $\dot{V} = 0$ nullcline. In the case of the full system, such an explicit representation is not possible, due to the hyperbolic tangent term containing V. Therefore the nullcline V as a function of n is defined implicitly as

$$V(n) = \frac{g_{Ca}V_{Ca}m_\infty(V) + g_K V_K n + g_L V_L}{g_{Ca}m_\infty(V) + g_L + g_K n - \mu}. \qquad (4.2.2)$$

However, it is possible to express the $\dot{V} = 0$ nullcline with n as an explicit function of V, which is convenient to study the nullclines in the (V, n)–plane. We obtain

$$n(V) = \frac{g_L(V_L - V) + g_{Ca}m_\infty(V)(V_{Ca} - V) + \mu V}{g_K(V - V_K)}. \qquad (4.2.3)$$

For convenience, we shall label the $\dot{n} = 0$ nullcline $n_1(V)$, and the $\dot{V} = 0$ nullcline $n_2(V)$. Note that the $\dot{V} = 0$ nullcline is no longer a simple hyperbola,

but it still consists of two distinct parts, separated by a vertical asymptote at
$V = V_K$. There are two horizontal asymptotes for $n_2(V)$, which we find by
taking the limits as $V \to \pm\infty$:

$$\lim_{V \to -\infty} n_2(V) = \frac{\mu - g_L}{g_K},$$

$$\lim_{V \to +\infty} n_2(V) = \frac{\mu - g_L - g_{Ca}}{g_K}.$$

To evaluate these limits, we used l'Hôpitals rule along with the fact that
$\tanh\left(\frac{V-V_1}{V_2}\right) \to -1$ and 1 as $V \to -\infty$ and ∞, respectively, $\text{sech}^2\left(\frac{V-V_1}{V_2}\right) \to 0$
as $V \to \pm\infty$, and

$$V \, \text{sech}^2\left(\frac{V - V_1}{V_2}\right) \to 0 \qquad \text{as} \qquad V \to \pm\infty.$$

The behavior of the $n_2(V)$ nullcline as μ is varied is very similar to that of
the $\dot{V} = 0$ nullcline of the all–K^+ conductance system. When we refer to the
nullcline in each parameter region, we mean the portion of the nullcline which
is in the interval of interest $0 \leq n \leq 1$. If

$$\mu < g_{Ca}m_\infty(V_K)\left(1 - \frac{V_{Ca}}{V_K}\right) + g_L\left(1 - \frac{V_L}{V_K}\right)$$

then the portion of the $n_2(V)$ nullcline left of the vertical asymptote is below
the V–axis, and is merely shifted vertically as μ is varied. The part to the
right of $V = V_K$ is in the interval of interest, and changes significantly as we
vary μ in this range. For large negative μ, say $\mu < -9$, this part is monotone
decreasing and the $n_1(V)$, $n_2(V)$ nullclines intersect once. As μ approaches
$g_{Ca}m_\infty(V_K)\left(1 - \frac{V_{Ca}}{V_K}\right) + g_L\left(1 - \frac{V_L}{V_K}\right)$, then the right–most part of $n_2(V)$ has a
cubic–like shape, due to the approximation of rapid activation of the calcium
current ($m = m_\infty(V)$). Such an N–shaped instantaneous current–voltage

relation is common of models of excitable membranes for which the voltage–gated channels carrying inward current activate rapidly [34]. For some values of μ the knee of the N–shaped nullcline rises above the V–axis, but does not lead to any additional equilibria. Therefore, for all $\mu < g_{\text{Ca}} m_\infty(V_{\text{K}}) \left(1 - \frac{V_{\text{Ca}}}{V_{\text{K}}}\right) + g_{\text{L}} \left(1 - \frac{V_{\text{L}}}{V_{\text{K}}}\right)$, system (4.0.1) admits a single equilibrium point (V^*, n^*) in the (V, n)–plane, with $V^* > V_{\text{K}}$. Using the parameter values included in Table 4.1, we find that

$$g_{\text{Ca}} m_\infty(V_{\text{K}}) \left(1 - \frac{V_{\text{Ca}}}{V_{\text{K}}}\right) + g_{\text{L}} \left(1 - \frac{V_{\text{L}}}{V_{\text{K}}}\right) = \frac{40}{7} + \frac{34}{7} \tanh\left(\frac{-16}{3}\right) \approx 0.857369283,$$

which is very close in value to $\frac{6}{7}$. In the all–potassium system, the value $\mu = \frac{6}{7}$ separated the parameter range where the $\dot{V} = 0$ nullcline was monotone increasing from that where it was monotone decreasing, and marked the parameter value where the nullcline was reduced to a pair of vertical and horizontal lines. A sample nullcline plot in the (V, n)–plane with μ in this range is included in Figure 4.1(a).

When $\mu = g_{\text{Ca}} m_\infty(V_{\text{K}}) \left(1 - \frac{V_{\text{Ca}}}{V_{\text{K}}}\right) + g_{\text{L}} \left(1 - \frac{V_{\text{L}}}{V_{\text{K}}}\right)$, the n_2 nullcline is reduced to a vertical line at $V = V_{\text{K}}$, and an additional part given by

$$n_2(V) = \frac{-g_{\text{L}} V_{\text{L}}}{g_{\text{K}} V_{\text{K}}} + \frac{g_{\text{Ca}} \left[m_\infty(V_{\text{K}}) \left(1 - \frac{V_{\text{Ca}}}{V_{\text{K}}}\right) V + m_\infty(V)(V_{\text{Ca}} - V)\right]}{g_{\text{K}}(V - V_{\text{K}})}. \quad (4.2.4)$$

The vertical line intersects the $n_1(V)$ nullcline, leading to the equilibrium point $(V^*, n^*) \approx (-70, 0)$, since the $n_1(V)$ nullcline is nearly zero there. The additional part (4.2.4) lies mostly below the V–axis, but does protrude into the interval of interest. However, it does not lead to additional equilibria. Figure 4.1(c) shows the nullclines in the (V, n)–plane for this value of μ.

The part of the $n_2(V)$ nullcline of interest is monotone increasing when μ

(a) $\mu = -1$.

(b) $\mu = 0$.

(c) $\mu = \frac{40}{7} + \frac{34}{7} \tanh\left(\frac{-16}{3}\right)$.

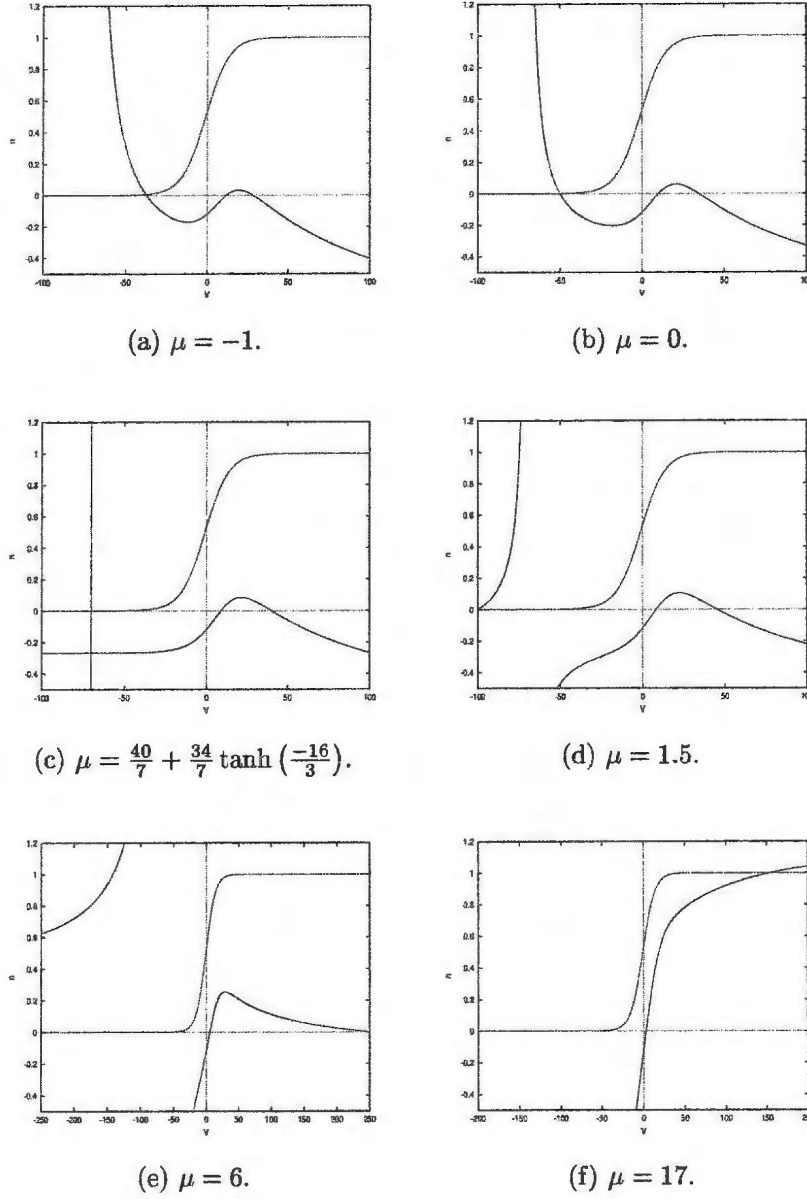(d) $\mu = 1.5$.

(e) $\mu = 6$.

(f) $\mu = 17$.

Figure 4.1: Plots of the $V(n)$ (solid) and $n(V)$ (dashed) nullclines of the full–2D system (4.0.1) for representative values of μ.

is in the range

$$g_{\text{Ca}} m_\infty(V_{\text{K}}) \left(1 - \frac{V_{\text{Ca}}}{V_{\text{K}}} \right) + g_{\text{L}} \left(1 - \frac{V_{\text{L}}}{V_{\text{K}}} \right) < \mu < g_{\text{L}},$$

and consists of the branch left of $V = V_{\text{K}}$. To the right of $V = V_{\text{K}}$, $n_2(V)$ does not intersect the $\dot{n} = 0$ nullcline. Here, we again have a single equilibrium point (V^*, n^*) but the equilibrium voltage is below V_{K}. Figure 4.1(d) contains the nullclines for a value of μ in this region.

As $\mu \to g_{\text{L}}$, $V^* \to -\infty$, since the horizontal asymptote of $n_2(V)$ as $V \to -\infty$ approaches zero. When $\mu = g_{\text{L}}$ the nullclines do not intersect in the (V, n)–plane, and there is no finite equilibrium point. The same is true while $g_{\text{L}} \le \mu \le g_{\text{L}} + g_{\text{K}} + g_{\text{Ca}}$, because with μ in this range, the lower horizontal asymptote of $n_2(V)$ is above zero, and the upper horizontal asymptote is between zero and one, inclusive. This can be seen in Figure 4.1(e), where the $n_1(V)$ and $n_2(V)$ nullclines are positioned in such a way that they do not intersect. Note though, that when $\mu = g_{\text{L}} + g_{\text{K}} + g_{\text{Ca}}$, the horizontal asymptote of $n_2(V)$ as $V \to +\infty$ has value $n = 1$. As μ is increased above $g_{\text{L}} + g_{\text{K}} + g_{\text{Ca}}$, the right branch of $n_2(V)$ intersects $n_1(V)$, and the system has a single equilibrium point, (V^*, n^*), with n^* close to 1 and $V^* > 0 > V_{\text{K}}$. Since the left branch of the $n_2(V)$ nullcline is above the interval of interest (the lower horizontal asymptote rose above $n = 1$ with $\mu > g_{\text{L}} + g_{\text{K}}$), it is not important. The upper branch flattens out at around $\mu = 10$, and becomes monotone increasing and concave down on the interval of interest. Figure 4.1(f) shows the nullclines of the system with $\mu = 17$. Here, the left branch is well above $n = 1$, and the right branch does indeed intersect the n_1 nullcline.

Comparing Figure 4.1 to Figure 2.1 of Chapter 2, we see that the qualitative behavior of the nullclines of the full–2D system (4.0.1) is similar to that of the

all–potassium conductance system (2.0.1). As such, system (4.0.1) with model parameters in Table 4.1 admits at most one equilibrium point in the (V, n)–plane for any $\mu \in \mathbb{R}$. Furthermore, the equilibrium point (V^*, n^*) of the full–2D model (4.0.1) for a specific value of μ is very close to the corresponding equilibrium point of the all–K$^+$ conductance system (2.0.1) for the same μ. Also, there is a parameter region of μ where the system does not have any equilibrium point. This range depends on the model parameters appearing in the expressions for the horizontal asymptotes of $n_2(V)$. These similarities are not surprising, since in the reduction of the full model we assumed that the potassium conductance system played a more prominent role than the calcium conductance.

The results discussed in this section are summarized in Figure 4.2, which contains steady–state bifurcation diagrams indicating how V^* and n^* change with μ. Stability of the equilibrium point (for $\tau = 0$) is also included, where solid lines represent stable equilibrium values and dashed lines unstable values. Stability properties of the equilibrium point of the model with zero time delay are verified in the next section. Notice the similarity between the bifurcation diagrams in Figure 4.2 to those for the all–potassium system depicted in Figure 2.2. It is evident that the full 2D model under this simplification is dominated by the potassium conductance, and it appears that the contribution of the calcium conductance is minimal, serving only to slightly raise the equilibrium voltage for a given value of μ.
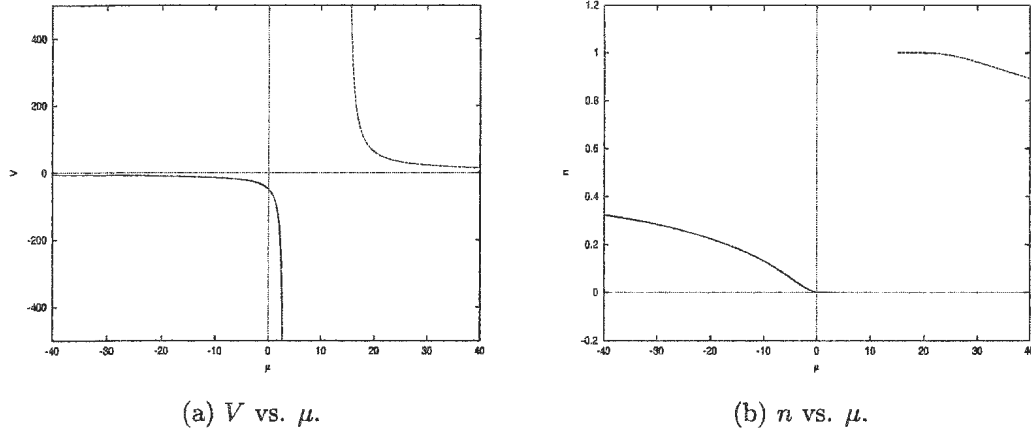
(a) V vs. μ.   (b) n vs. μ.

Figure 4.2: Bifurcation diagrams describing how V^* and n^* of the full–2D model change as μ is varied. Solid lines indicate stable equilibrium points while dashed lines represent unstable ones.

With the results of this section, we have essentially established the following theorem:

Theorem 4.2.1.1. *With parameters listed in Table 4.1, system (4.0.1) admits at most one equilibrium point (V^*, n^*) for all $\mu \in \mathbb{R}$. The value $n^* \in [0, 1]$, and $V^* > V_K$ if $\mu < g_{Ca} m_\infty(V_K) \left(1 - \frac{V_{Ca}}{V_K}\right) + g_L \left(1 - \frac{V_L}{V_K}\right)$ or $\mu > g_L + g_K + g_{Ca}$, $V^* < V_K$ if $g_{Ca} m_\infty(V_K) \left(1 - \frac{V_{Ca}}{V_K}\right) + g_L \left(1 - \frac{V_L}{V_K}\right) < \mu < g_L$, and $V^* = V_K$ if $\mu = g_{Ca} m_\infty(V_K) \left(1 - \frac{V_{Ca}}{V_K}\right) + g_L \left(1 - \frac{V_L}{V_K}\right)$. Furthermore, if $g_L \leq \mu \leq g_L + g_K + g_{Ca}$, then (4.0.1) does not possess an equilibrium point.*

4.2.2 Local Stability and Bifurcation Analysis of the Full–2D Model with Delay

Equilibrium points (V^*, n^*) of system (4.0.1) are given by the intersection of the nullclines (4.2.1) and (4.2.3). In the previous section 4.2.1, we established that the system admits at most one equilibrium point. In particular, there is one equilibrium point with finite equilibrium voltage provided $\mu \notin [g_{\mathrm{L}}, g_{\mathrm{L}} + g_{\mathrm{K}} + g_{\mathrm{Ca}}]$, and no equilibrium point if μ is in this range.

Consider system (4.0.1) with $\mu \notin [g_{\mathrm{L}}, g_{\mathrm{L}} + g_{\mathrm{K}} + g_{\mathrm{Ca}}]$. To determine the local stability of the equilibrium point (V^*, n^*), we linearise the system. The nonlinear system with equilibrium point shifted to the origin is

$$
C\frac{dx}{dt} = -\left\{ g_{\mathrm{L}} + g_{\mathrm{K}}n^* + \frac{g_{\mathrm{Ca}}}{2}\left[1 + \tanh\left(\frac{x + V^* - V_1}{V_2}\right)\right]\right\} x \qquad (4.2.5)
$$
$$
-\frac{g_{\mathrm{Ca}}}{2}(V^* - V_{\mathrm{Ca}})\left[1 + \tanh\left(\frac{x + V^* - V_1}{V_2}\right)\right] + g_{\mathrm{K}}(V_{\mathrm{K}} - V^*)y
$$
$$
-g_{\mathrm{K}}xy + \mu x(t - \tau) - V^*(g_{\mathrm{L}} + g_{\mathrm{K}}n^* - \mu) + (g_{\mathrm{L}}V_{\mathrm{L}} + g_{\mathrm{K}}V_{\mathrm{K}}n^*)
$$

$$
\frac{dy}{dt} = \overline{\lambda_n}\cosh\left(\frac{x + V^* - V_3}{2V_4}\right) \times \qquad (4.2.6)
$$
$$
\left[\frac{1}{2}\left(1 + \tanh\left(\frac{x + V^* - V_3}{V_4}\right)\right) - y - n^*\right].
$$

Linearising, we obtain

$$
\frac{dx}{dt} = -\frac{1}{C}\left[g_{\mathrm{L}} + g_{\mathrm{K}}n^* + g_{\mathrm{Ca}}\left(m_\infty(V^*) + \frac{(V^* - V_{\mathrm{Ca}})}{2V_2}\operatorname{sech}^2(t)\right)\right] x
$$
$$
+ \frac{g_{\mathrm{K}}}{C}(V_{\mathrm{K}} - V^*)y + \frac{\mu}{C}x(t - \tau)
$$

$$
(4.2.7)
$$

$$
\dot{y}(t) = \frac{\overline{\lambda_n}}{2V_4}\cosh(u)\operatorname{sech}^2(v) - \overline{\lambda_n}\cosh(u)\, y.
$$

where $u = \frac{V^* - V_3}{2V_4}$, $u = \frac{V^* - V_3}{V_4}$, and $t = \frac{V^* - V_1}{V_2}$. If we set

$$a = \frac{1}{C} \left[g_L + g_K n^* + g_{Ca} \left(m_\infty(V^*) + \frac{(V^* - V_{Ca})}{2V_2} \, \mathrm{sech}^2(t) \right) \right],$$

$$c = \frac{\overline{\lambda_n}}{2V_4} \cosh(u) \, \mathrm{sech}^2(v), \quad b = \frac{g_K(V_K - V^*)}{C}, \quad d = \overline{\lambda_n} \cosh(u), \quad \hat{\mu} = \frac{\mu}{C},$$

then system (4.2.7) becomes

$$\dot{x}(t) = -ax + by + \hat{\mu} x(t - \tau)$$

$$(4.2.8)$$

$$\dot{y}(t) = cx - dy,$$

which is identical in form to (2.2.8), the potassium conductance system lin-earised about the origin. Therefore, the characteristic equation for system (4.0.1) is of the same form for the all–potassium conductance system, and we can apply the results of Cooke and Grossman to analyse stability of the equilibrium point. Comparing (4.2.8) to (2.2.8), coefficient a has a different definition, while all other coefficients have the same form but differ slightly in value from those of the all–potassium system for any given μ due to the change in equilibrium point from the single–conductance system to the full system. Since the behavior of the nullclines is qualitatively the same for both systems as μ is varied, the ranges for coefficients b, c, and d specified in the all–potassium chapter are valid for these coefficients appearing in (4.2.8). One must simply replace the values $g_L \left(1 - \frac{V_L}{V_K} \right)$ and $g_L + g_K$ in the all–potassium system with $g_{Ca} m_\infty(V_K) \left(1 - \frac{V_{Ca}}{V_K} \right) + g_L \left(1 - \frac{V_L}{V_K} \right)$ and $g_L + g_K + g_{Ca}$, respectively, for the full two–dimensional system. We still find that b and d are unbounded as $\mu \to g_L$ and $g_L + g_K + g_{Ca}$, both c and d are always positive constants, and b changes sign at a slightly different value than before.

We consider a separately, since it has a different form. Again, $V^* \to -\infty$ and $n^* \to 0$ as $\mu \to g_L$. In this limit, the extra terms appearing in the definition of a tend to zero, and so we find that $a \to \frac{g_L}{C}$. Also, as $\mu \to g_L + g_K + g_{Ca}$, $V^* \to +\infty$ and $n^* \to 1$, and so $a \to \frac{g_L + g_K + g_{Ca}}{C}$. For large values of μ, positive and negative, $V^* \to 0$ and $n^* \to n_\infty(0) \approx 0.53$, and substituting these values in for V^* and n^* into the expression for a, we obtain $a \approx -3.47 \times 10^{-2}$, which is less than zero. While a can assume negative values, we note that this can only occur for large values of $|\mu|$ which are physiologically unrealistic, say $\mu = -100$ and $\mu = 80$. Also, since the lowest value a can assume is very small in magnitude, it does not interfere with any of the analytical results. For our purposes, we may consider a to be a positive constant which is bounded above by the value $\frac{g_L + g_K + g_{Ca}}{C} = 0.75$.

The characteristic equation of (4.0.1) is

$$\lambda^2 + (a+d)\lambda + (ad - bc) - \hat{\mu}\lambda e^{-\lambda\tau} - \hat{\mu}de^{-\lambda\tau} = 0, \qquad (4.2.9)$$

with a, b, c, and d defined above. Consider first the system with zero time delay, (4.0.1) with $\tau = 0$. In this case, the system is reduced to a pair of coupled ODEs, and has a quadratic polynomial characteristic with roots

$$\lambda_\pm = \frac{\hat{\mu} - (a+d) \pm \sqrt{[(a+d) - \hat{\mu}]^2 - 4[(ad - bc) - \hat{\mu}d]}}{2}. \qquad (4.2.10)$$

The trivial solution of (4.2.7) is stable provided the Routh–Hurwitz conditions (i) $\hat{\mu} < a+d$ and (ii) $\hat{\mu} < a - \frac{bc}{d}$ are both satisfied. These conditions are plotted in Figure 4.3, where we find that both (i) and (ii) are satisfied provided $\mu < g_L$. Therefore, with μ in this range, (V^*, n^*) of (4.0.1) is a stable equilibrium point. Further investigation reveals that the equilibrium point is a stable node for most parameter values, but a stable focus for $-1.21 < \mu < -0.04$, which can

be determined from the plots of the discriminant $\Delta = [(a + d) - \hat{\mu}]^2 - 4[(ad - bc) - \hat{\mu}d]$ of (4.2.10) in Figure 4.4.

(a) $\mu < g_{\mathrm{L}} = 3$.   (b) $g_{\mathrm{L}} + g_{\mathrm{K}} + g_{\mathrm{Ca}} = 15 < \mu$.
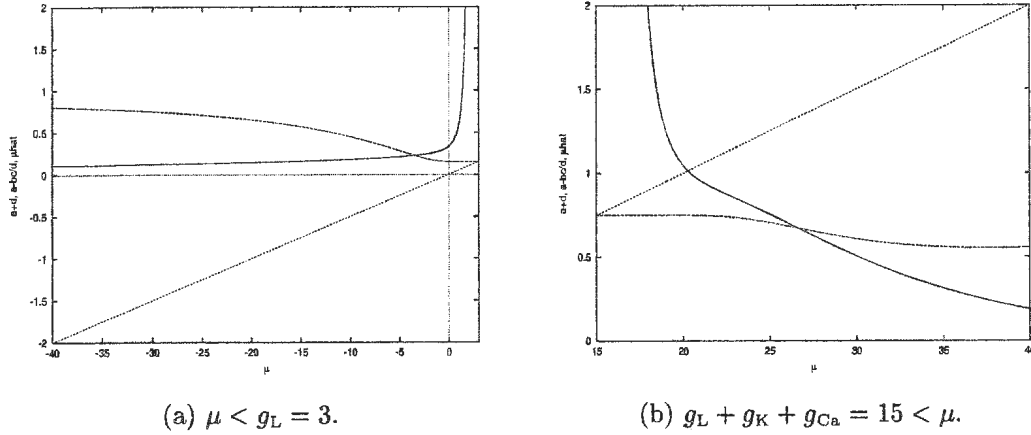
Figure 4.3: Checking the Routh–Hurwitz conditions: Plots of $a + d$ (solid curve), $a - \frac{bc}{d}$ (dashed curve), and $\hat{\mu}$ (dotted line) against μ for the two parameter ranges where system (4.0.1) (with $\tau = 0$) has a unique equilibrium point.

For $\mu > g_{\mathrm{L}} + g_{\mathrm{K}} + g_{\mathrm{Ca}}$, condition (ii) is never met and so the equilibrium point (V^*, n^*) is unstable. In fact, from Figure 4.3(b), it is clear that $\hat{\mu} \geq a - \frac{bc}{d}$ for all $\mu \geq g_{\mathrm{L}} + g_{\mathrm{K}} + g_{\mathrm{Ca}}$, from which it follows that $(ad - bc) - \hat{\mu}d \leq 0$ for all $\mu \geq g_{\mathrm{L}} + g_{\mathrm{K}} + g_{\mathrm{Ca}}$. This implies that the discriminant $\Delta \geq 0$ for all μ in this range, and so both roots $\lambda_{\pm}$ are real with $\lambda_+ > 0$, $\lambda_- < 0$ and so (V^*, n^*) is an unstable saddle point for all μ in this range. The Cooke–Grossman theory does not apply when $\mu \approx 21.0$, since for this value of μ, we have $\hat{\mu} = a + d$. As in the previous chapters (Chapters 2 and 3), in this case there are no purely imaginary roots of the characteristic equation (4.2.9). The theory also fails if
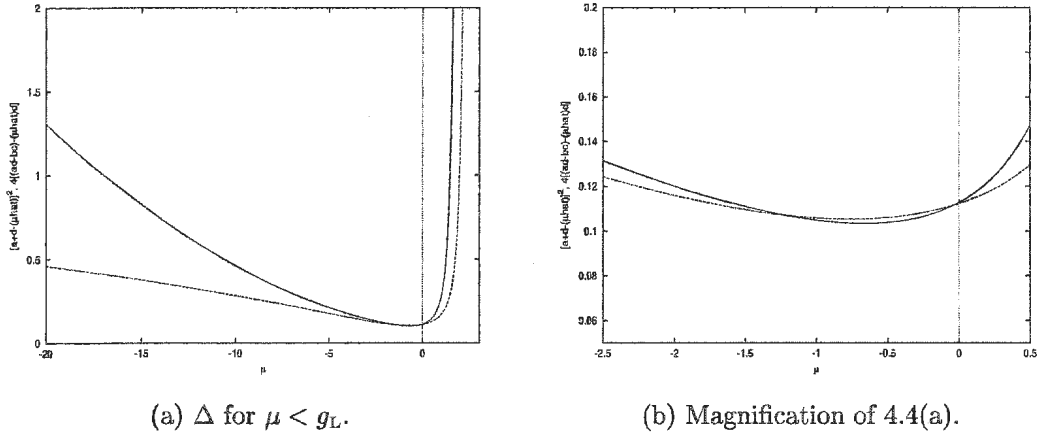
(a) Δ for $\mu < g_{\mathrm{L}}$.

(b) Magnification of 4.4(a).

Figure 4.4: Plots of $[(a+d) - \hat{\mu}]^2$ (solid curve) and $4[(ad - bc) - \hat{\mu}d]$ (dashed curve) versus μ to determine the sign of the discriminant. Figure 4.4(a) magnified in 4.4(b) to distinguish the ranges of μ for which the discriminant is positive from those where it is negative.

$\hat{\mu} = a - \frac{bc}{d}$ which occurs when $\mu = g_{\mathrm{L}}$ and $g_{\mathrm{L}} + g_{\mathrm{K}} + g_{\mathrm{Ca}}$, but these cases are physiologically unrealistic.

Turning now to the model with delay, $\tau > 0$, we substitute $\lambda = i\omega$ into (4.2.9) to search for purely imaginary roots of the transcendental characteristic equation. From previous analysis, we know that this leads to the quartic equation

$$\omega^4 + \left[(a + d)^2 - 2(ad - bc) - \hat{\mu}^2\right]\omega^2 + (ad - bc)^2 - \hat{\mu}^2 d^2 = 0, \qquad (4.2.11)$$

the roots of which are the $\pm$ square roots of $\omega_{\pm}^2$, given by

$$\begin{aligned} \omega_{\pm}^2 &= \frac{1}{2}\left(\hat{\mu}^2 - a^2 - d^2 - 2bc\right) \\ &\pm \left\{\frac{1}{4}\left(\hat{\mu}^2 - a^2 - d^2 - 2bc\right)^2 - \left((ad - bc)^2 - \hat{\mu}^2 d^2\right)\right\}^{\frac{1}{2}}.(4.2.12) \end{aligned}$$

Purely imaginary roots $\lambda = i\omega$ (with $\omega > 0$) of (4.2.9), occur with positive real roots of (4.2.11). To determine if system (4.0.1) admits purely imaginary eigenvalues, we check to see if the system satisfies the criteria for the cases outlined by Cooke and Grossman [6].

<u>Case 1</u> $\left(\hat{\mu}^2 > \left(a - \frac{bc}{d}\right)^2\right)$. In this case, we obtain one purely imaginary root $\lambda_+ = i\omega_+$ of (4.2.9), corresponding to the single positive real root of (4.2.11), $\omega_+ > 0$. To determine the range on the parameter μ for which this case is satisfied, we plot $\hat{\mu}^2$ and $\left(a - \frac{bc}{d}\right)^2$ versus μ in Figure 4.5.

Figure 4.5(b) indicates that the single criterion for Case 1 is satisfied for all $\mu > g_{\mathrm{L}} + g_{\mathrm{K}} + g_{\mathrm{Ca}}$. The plots for $\mu < g_{\mathrm{L}}$ appear in Figure 4.5(a), where we find that there is a $\mu^* < 0$ such that $\hat{\mu}^2 > \left(a - \frac{bc}{d}\right)^2$, i.e. Case 1, provided $\mu < \mu^*$, but $\hat{\mu}^2 < \left(a - \frac{bc}{d}\right)^2$ for $\mu^* < \mu < g_{\mathrm{L}}$, which is the primary requirement
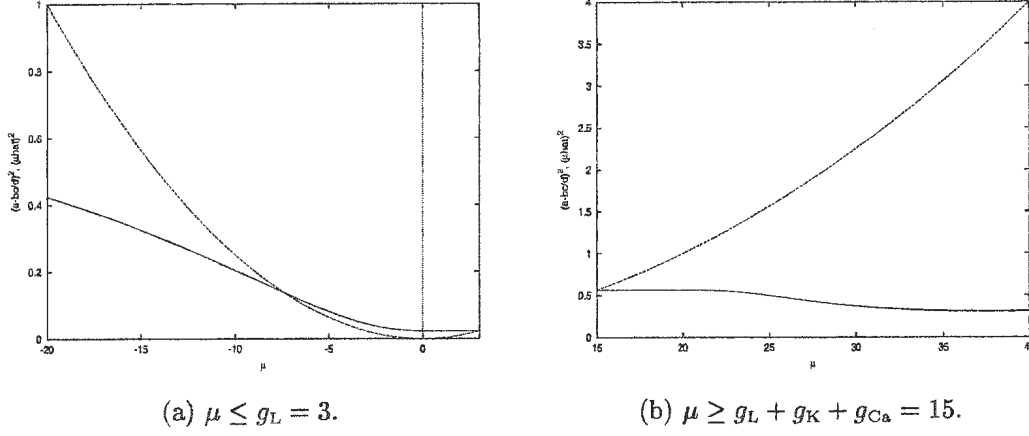
(a) $\mu \leq g_L = 3$.

(b) $\mu \geq g_L + g_K + g_{Ca} = 15$.

Figure 4.5: Plots of $\hat{\mu}^2$ (dashed curve) and $\left(a - \frac{bc}{d}\right)^2$ (solid curve) versus μ, for the two parameter ranges of μ for which the system (4.0.1) has a unique equilibrium point.

for Case 2. As in Chapter 2, we cannot obtain the exact numerical value of μ^*, but we can estimating the value to obtain $\mu^* \approx -7.39$. Recall that the symbol μ^* was used in the chapter on the all–potassium conductance system, and represented the value of μ which separated the Case 1 and Case 2 dynamics of the model. We re–use this label here to serve the same purpose.

In this section we focus on the Case 1 dynamics of the model, for which the system has a single purely imaginary root $\lambda_+ = i\omega_+$, $\omega_+ > 0$. By the transversality condition computed earlier, we know that $\text{sign}\left\{\frac{d(\text{Re}\lambda_+)}{d\tau}\right\} = \text{sign}\left\{+\sqrt{\Delta}\right\} > 0$ for λ_+, where Δ is the discriminant of (4.2.12). It follows that the crossing of the imaginary axis occurring with the purely imaginary root λ_+ must be from left to right. With $\mu > g_L + g_K + g_{Ca}$, the equilibrium point of the system is an unstable saddle for $\tau = 0$. Therefore, with μ in this

range, stability of the equilibrium point cannot be obtained by increasing τ, and so (V^*, n^*) is unstable for all $\tau \geq 0$.

Consider next the case where $\mu < \mu^*$. With μ in this range we obtain a single equilibrium point in the (V, n)–plane, which is stable for $\tau = 0$. Therefore (V^*, n^*) loses stability as τ is increased though the smallest value for which

$$\tau_n = \frac{1}{\omega_+} \cos^{-1} \left\{ \frac{a\omega_+^2 + d(ad - bc)}{\hat{\mu}(\omega_+^2 + d^2)} \right\} + \frac{2\pi n}{\omega_+} \qquad (n = 0, 1, \ldots).$$

Denote this value by $\tau^* = \tau_0$. Since there is only one purely imaginary root and one crossing, this is the only change in stability of the equilibrium point. Therefore, for every $\mu < \mu^*$, there exists a time delay τ^* for which the equilibrium point (V^*, n^*) of (4.0.1) is stable for all delays $\tau < \tau^*$, but unstable if τ is greater than τ^*. Stability of the equilibrium point cannot be regained by further increasing the delay. Figure 4.6 plots the bifurcation times τ^* versus μ for $\mu < \mu^*$.
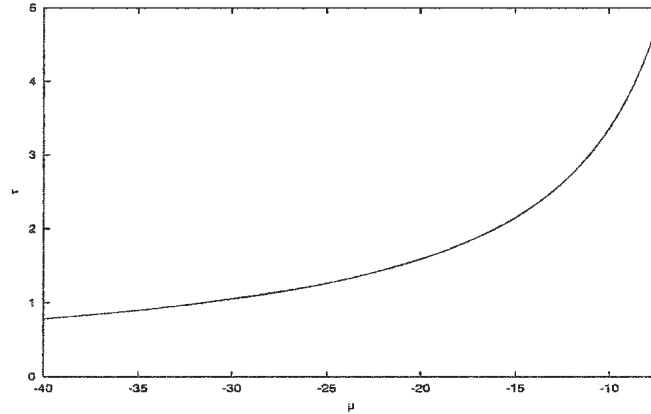

Figure 4.6: Bifurcation Diagram plotting τ^* vs. μ for system (4.0.1) with $\mu < \mu^* \approx -7.39$ (the model is in Case 1).

When $\tau = \tau^*$, the system satisfies all requirements for the Hopf bifurcation

theorem for DDEs [17]. As the equilibrium point (V^*, n^*) loses stability, the system also undergoes a Hopf bifurcation as τ is increased past τ^*. Numerical simulations indicate the emergence of stable periodic solutions prior to the loss of equilibrium point stability. The system is originally monostable with a stable equilibrium point, but for some values of the delay less than τ^* the system exhibits bistability with a locally stable limit cycle and a locally stable equilibrium point. To illustrate these results, we consider system (4.0.1) with $\mu = -8 < \mu^*$, and so the system is in Case 1. For this value of μ, $\tau^* = 4.4$ ms. In Figure 4.7 we plot the solution $V(t)$ versus t and delay phase plane $V(t-\tau)$ versus $V(t)$ for $\tau = 4 < \tau^*$, and $\tau = 5 > \tau^*$, and two different initial conditions for each time delay. The initial conditions $V(\theta) = -16$, $n(\theta) = n_\infty(-16)$, $\theta \in [-\tau, 0]$ demonstrate the stability properties of the equilibrium point $(V^*, n^*) = (-16.53, 0.11)$, while the conditions $V(\theta) = -50$, $n(\theta) = n_\infty(-50)$ highlight the presence of a stable periodic orbit before and after the bifurcation value τ^*.

These results are consistent with those obtained for the all–calcium conductance system, and so it seems plausible that the stable periodic orbits for $\tau < \tau^*$ are generated by the same mechanism, namely a PSNB. Hence we propose the following conjecture

Conjecture 4.2.2.1. *Assume model parameters are as in Table 4.1. Then system (4.0.1) with $\mu < \mu^*$ (Case 1) undergoes a periodic saddle–node bifurcation (PSNB) at some value of the delay $\tau_{PSN} < \tau^*$, where τ^* is given by the τ_0 term of sequence (3.2.11). A pair of stable and unstable periodic orbits are generated at τ_{PSN}, and the system exhibits bistability with a stable equilibrium point (V^*, n^*) and a stable limit cycle for $\tau_{PSN} < \tau < \tau^*$. Furthermore, the*
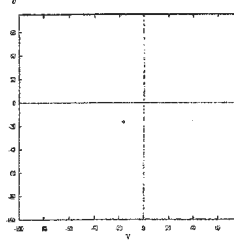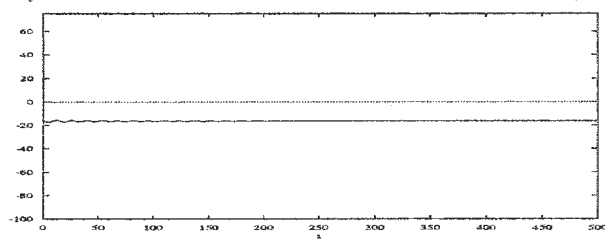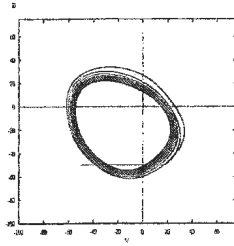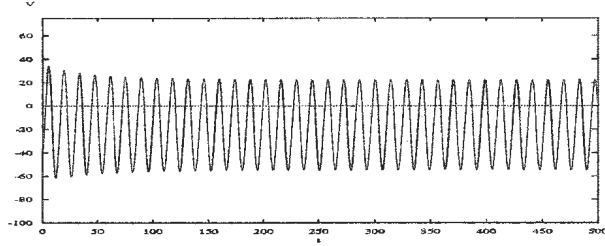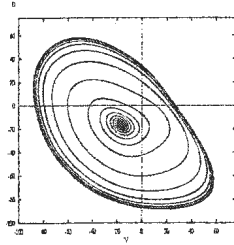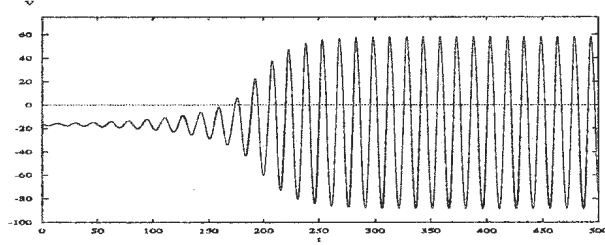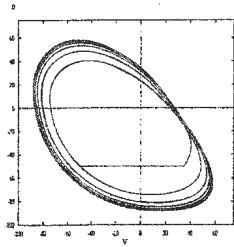
(a) $V(t-\tau)$ vs. V.

(b) $V(\theta) = -16, n(\theta) = n_{\infty}(-16)$ with $\tau = 4$.

(c) $V(t-\tau)$ vs. V.

(d) $V(\theta) = -50, n(\theta) = n_{\infty}(-50)$ with $\tau = 4$.
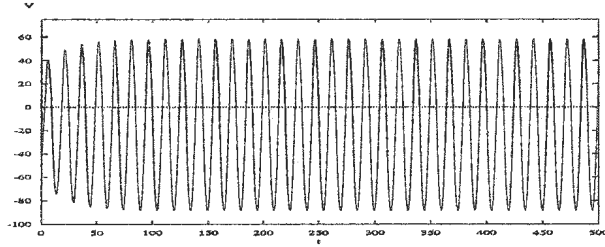
(e) $V(t-\tau)$ vs. V.

(f) $V(\theta) = -16, n(\theta) = n_{\infty}(-16)$ with $\tau = 5$.

(g) $V(t-\tau)$ vs. V.

(h) $V(\theta) = -50, n(\theta) = n_{\infty}(-50)$ with $\tau = 5$.

Figure 4.7: Numerical simulation of system (4.0.1) with $\mu = -8$ (Case 1). The delay is increased from $\tau = 4$ to 5 ms, demonstrating evidence for a periodic saddle–node bifurcation.

unstable periodic orbit formed at τ_{PSN} is lost in a subcritical Hopf bifurcation at $\tau = \tau^*$.

Refer to Figure 3.8 of Chapter 3 for the schematic bifurcation diagram depicting this behavior. Since there is only a single equilibrium point, a PSNB would generate a pair of nested stable and unstable periodic orbits which surround (V^*, n^*). Recall for the all–calcium conductance system (3.0.1), we found that the unstable periodic orbit produced prior to τ^* was lost via a subcritical Hopf bifurcation at τ^*, indicated by the detailed Hopf bifurcation analysis in section 3.2.8. The Hopf bifurcation analysis for the full–2D model (4.0.1) appears at the end of this chapter in section 4.2.3. However, the results from this analysis indicate that the Hopf bifurcation at τ^* is supercritical and branching to stable oscillations, contrary to the expected result. It also does not guarantee the existence of an unstable periodic orbit for time delays below τ^*, and therefore cannot offer any support to our PSNB conjecture for the full–2D model (4.0.1). Thus there is a discrepancy between the Hopf bifurcation analysis and numerical results for system (4.0.1). However, it seems apparent from numerical simulations that the Hopf bifurcation is not supercritical and branches to stable oscillations. If it were, then we should be able to detect a stable small amplitude periodic solution for system (4.0.1) when τ is just above τ^*, and with initial conditions close to (V^*, n^*). No such stable periodic solutions were detected. Instead, trajectories with initial conditions very close to (V^*, n^*) approached a stable large amplitude periodic solution. Moreover, the large amplitude periodic solution for $\tau > \tau^*$ appears to be the same limit cycle generated prior to τ^*, which had since grown in amplitude as the delay increased. This is also illustrated in Figure 4.7.

We were unable to account for the discrepancies between the numerical results and detailed Hopf bifurcation analysis. It is likely that there may be an error in the Hopf bifurcation analysis of section 4.2.3 that we could not find, given the tedious nature of the computation. As a result, the analysis revealed a Hopf bifurcation structure of (4.0.1) which was qualitatively identical to that obtained for the all–potassium conductance system with delay. However, the numerical results seem to indicate that the bifurcation structure mimics that of the delayed all–calcium conductance system, depicted in Figure 3.8. From our experience with the previous chapters, we are more inclined to accept the numerical results, especially given the ease at which errors may creep into the Hopf bifurcation analysis. However, this does not preclude the possibility that more complicated dynamical phenomena might be present. It might be that both the Hopf bifurcation analysis and numerical results are correct, giving a more complex bifurcation structure which differs significantly from both conductance systems.

The emergence of stable periodic solutions of (4.0.1) for delay values below τ^* was observed for a sample of values of $\mu < \mu^*$. As $|\mu|$ increases, τ^* decreases and the value of τ_{PSN} estimated using numerical simulations gets closer to τ^*. That is, the range of the delay over which the system exhibits bistability decreases as $|\mu|$ increases. In general, estimating the value of τ_{PSN} is difficult since the stable limit cycle will have a very small basin of attraction just after it forms. A more accurate estimation of τ_{PSN} can only be obtained using a numerical continuation package for delay differential equations. However, such numerical packages have been developed only recently, and one was not available for this thesis research.

Before discussing the Case 2 dynamics of the full–2D model with delay, we comment on the dynamics of system (4.0.1) for values of μ where the Cooke–Grossman theory is not applicable. These values are $\mu = \mu^*$, $\mu = g_{\mathrm{L}}$, and $\mu = g_{\mathrm{L}} + g_{\mathrm{K}} + g_{\mathrm{Ca}}$, for which $\hat{\mu}^2 = \left(a - \frac{bc}{d}\right)^2$. For the values $\mu = g_{\mathrm{L}}$ and $g_{\mathrm{L}} + g_{\mathrm{K}} + g_{\mathrm{Ca}}$, $V^* \to -\infty$ and $+\infty$, respectively, and so these cases are physiologically unrealistic. The value μ^* separates the Case 1 and Case 2 dynamics of the model, and in this case we have a double zero eigenvalue along with a pair of purely imaginary eigenvalues. But like the case for μ^* in Chapter 2, the zero eigenvalues occur at a different value of τ (actually as $\omega \to 0$, $\tau^0 \to \infty$) than the purely imaginary eigenvalues. Thus, when $\tau = \tau^*$, the delay value corresponding to the purely imaginary pair, there is no degeneracy. Hence as τ is increased through τ^* the equilibrium point changes stability and a Hopf bifurcation occurs, and the result resembles the Case 1 dynamics. For the approximate value $\mu^* = -7.39$, numerical simulations of indicate that the equilibrium loses stability as τ is increased past $\tau^* = 4.8$. Also, the system exhibits bistability, as a stable periodic orbit emerges for some $\tau < \tau^*$, possibly via a PSNB.

Case 2 $\left(\hat{\mu}^2 < \left(a - \frac{bc}{d}\right)^2\right)$. In this case, we obtain two purely imaginary roots $\lambda_{\pm} = i\omega_{\pm}$ of (4.2.9), corresponding to the positive real roots ω_+ and ω_- of (4.2.11). The primary requirement for Case 2, $\hat{\mu}^2 < \left(a - \frac{bc}{d}\right)^2$, is satisfied for all μ such that $\mu^* < \mu < g_{\mathrm{L}}$, where $\mu^* \approx -7.39$. Checking the additional conditions (a) and (b) associated with Case 2 indicates that both conditions are simultaneously met when $\mu^* < \mu < \mu^{**}$, where $\mu^{**} \approx -3.66$. The plots used to determine this range are included in Figure 4.8.

Therefore, if $\mu^* < \mu \leq \mu^{**}$, then there are two purely imaginary roots of
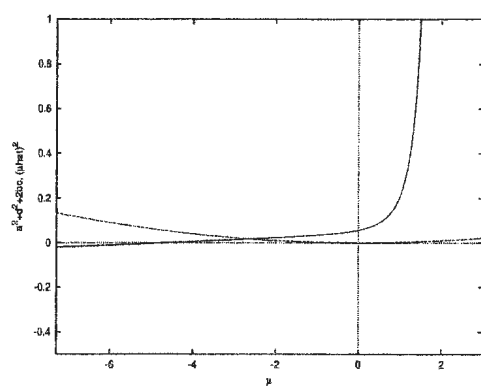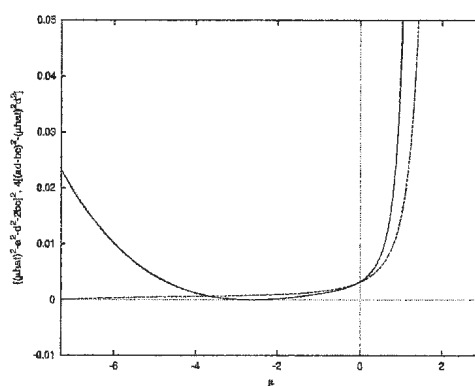
(a) Condition (a).   (b) Condition (b).

Figure 4.8: Verifying conditions (a) and (b) for Case 2: Plots of $\hat{\mu}^2$ (dashed curve) and $a^2 + d^2 + 2bc$ (solid curve), versus μ, and plots of $(\hat{\mu}^2 - a^2 - d^2 - 2bc)^2$ (solid curve) and $4((ad - bc)^2 - \hat{\mu}^2 d^2)$ (dashed curve) versus μ.

the characteristic equation, $\lambda_{\pm} = i\omega_{\pm}$, and two crossings of the imaginary axis are possible. By the transversality condition, a left to right crossing occurs with the λ_+ root, while a right to left crossing occurs with the λ_- root. We obtain two sequences of delay times, $\tau_{n,1}$, which denote the time delays where a left to right crossing takes place, and $\tau_{n,2}$, which marks the right to left crossings. These sequences are given by

$$\tau_{n,1} = \frac{1}{\omega_+}\cos^{-1}\left\{\frac{a\omega_+^2 + d(ad - bc)}{\hat{\mu}(\omega_+^2 + d^2)}\right\} + \frac{2\pi n}{\omega_+} \qquad (n = 0, 1, \cdots)$$

$$\tau_{n,2} = \frac{1}{\omega_-}\cos^{-1}\left\{\frac{a\omega_-^2 + d(ad - bc)}{\hat{\mu}(\omega_-^2 + d^2)}\right\} + \frac{2\pi n}{\omega_-}.$$

(4.2.13)

Hence with μ in this range, multiple stability switches of the equilibrium point are possible as τ is increased. Not every crossing of the imaginary axis leads to a change in stability of (V^*, n^*), and a finite number of stability switches from stability to instability may occur before instability persists. The number of switches depends on the model parameters, and the switching behavior terminates with two consecutive left to right crossings.

Only one stability change is possible if $\mu^* < \mu < -4.11$, since for these values of μ, $\tau_{1,1} < \tau_{0,2}$, and we have two consecutive left to right crossings of the imaginary axis prior to the first right to left crossing. With μ in this range the dynamics are similar to those encountered in Case 1. The equilibrium point (V^*, n^*) loses stability when $\tau = \tau^*$ as a purely imaginary root migrates across the imaginary axis. In addition, the numerics indicate that a stable periodic solution emerges for some $\tau = \tau_{\mathrm{PSN}} < \tau^*$, and the system exhibits bistability for all $\tau \in (\tau_{\mathrm{PSN}}, \tau^*)$. We conjecture that a PSNB occurs at τ_{PSN}, and generates a pair of stable and unstable periodic orbits. When stability of (V^*, n^*) is lost,

only a stable limit cycle remains. However, similar discrepancies between the Hopf bifurcation analysis and the numerical results were also encountered for μ in this range, and so we have no concrete proof that an unstable subcritical Hopf bifurcation occurs at $\tau_{0,2}$.

A number of numerical simulations were run with samples of $\mu \in (\mu^*, -4.11)$, and all revealed the same qualitative behavior. In Figure 4.10 we consider the example $\mu = -5$, for which $(V^*, n^*) = (-20.79, 0.06)$ and $\tau^* = 8.6$. Initial conditions are $V(\theta) = -100$, $n(\theta) = n_\infty(-100)$ and $V(\theta) = -20$, $n(\theta) = n_\infty(-20)$, $\theta \in [-\tau, 0]$, with the delay increased from $\tau = 7$ to $\tau = 9$. With $\tau < 7$, the system is initially monostable with a stable equilibrium point, and no stable periodic solutions were detected. This can be seen in Figure 4.9, where we plot the solution for $\mu = -5$, $\tau = 6$ and initial conditions $V(\theta) = -100$, $n(\theta) = n_\infty(-100)$. If $\tau = 7$, the system is bistable with a stable equilibrium and stable limit cycle, but if τ is increased past τ^* then stability of the equilibrium point is lost, and only a stable limit cycle remains. Note the detection of a stable periodic orbit as the delay was increased from $\tau = 6$ to $\tau = 7$. We do not claim that $\tau_{\mathrm{PSN}} \in (6, 7)$, and it is possible that $\tau < 6$. Rather, we have merely identified that, for a given initial condition, a stable periodic orbit becomes evident for $\tau < \tau^*$.

If $-4.11 \leq \mu \leq \mu^{**}$, the equilibrium point (V^*, n^*) of system (4.0.1) undergoes multiple changes in stability before instability persists. A total of $2k + 1$ stability switches take place, where $k \in \mathbb{N}$ is the smallest value for which $\tau_{k,1} < \tau_{k+1,1} < \tau_{k,2}$, and the final stability change occurs when $\tau = \tau_{k,1}$. The number of stability switches increases as $\mu \to \mu^{**}$. If μ is close to -4.11, then only three switches are possible, while as many as 31 switches are predicted

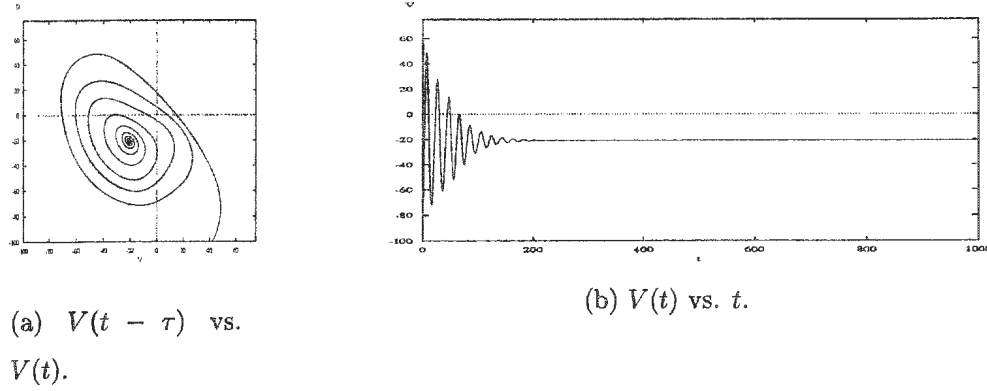(a) $V(t - \tau)$ vs.
$V(t)$.

(b) $V(t)$ vs. t.

Figure 4.9: Numerical simulation of system (4.0.1) with $\mu = -5$, $\tau = 6$ ms, illustrating a stable equilibrium point.

for $\mu = -3.66$, the approximate value of μ^{**}. The number of stability switches (up to 11) for a given $\mu \in [-4.11, \mu^{**}]$, as well as the values of the delay where the switches occur, are reported in Figure 4.11. As in Figure 2.10 in the all–K$^+$ chapter, neither stability switching nor Hopf bifurcation(s) occur at the cusp points of Figure 4.11, due to the presence of two pairs of purely imaginary eigenvalues. The initial terms $\tau_{0,1}$ and $\tau_{0,2}$ of the sequences (4.2.13) are plotted for $-4.11 < \mu \le \mu^{**}$ in Figures 4.12(a) and 4.12(b), and similar plots can be constructed for any terms in these sequences. In Figure 4.12(c) we show that the $\tau_{0,1}$ bifurcation curve of Case 2 is simply a continuous extension of the $\tau^* = \tau_0$ curve of Case 1, and that the $\tau_{0,1}$ and $\tau_{0,2}$ curves of Case 2 also combine to form a smooth, continuous curve.

To demonstrate the local stability switching of the equilibrium point (V^*, n^*) for a given $\mu \in [-4.11, \mu^{**}]$, we present a numerical simulation carried out for $\mu = -3.8$. For this value of μ, three changes in stability of the equilibrium
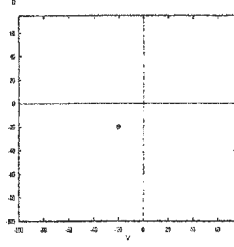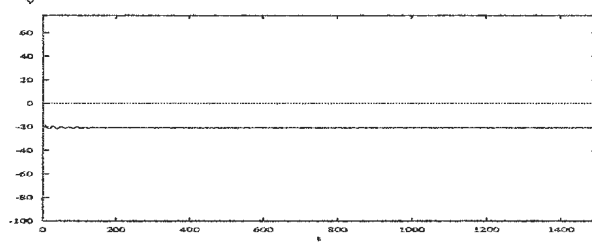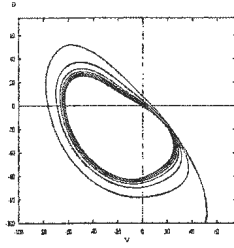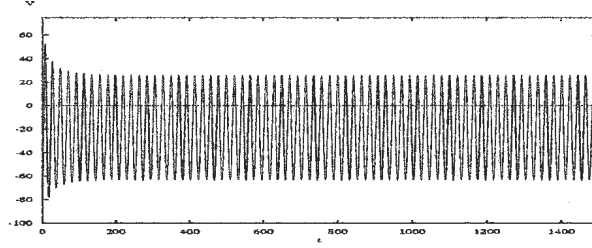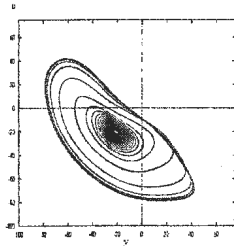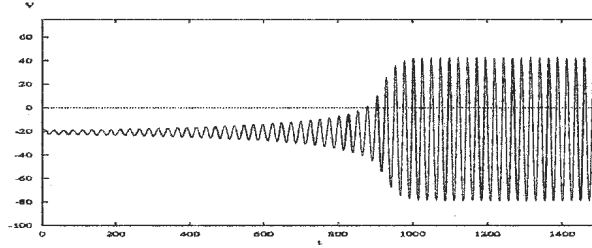
(a) $V(t-\tau)$ vs. V.

(b) $V(\theta) = -20, n(\theta) = n_\infty(-20)$ with $\tau = 7$.

(c) $V(t-\tau)$ vs. V.

(d) $V(\theta) = -100, n(\theta) = n_\infty(-100)$ with $\tau = 7$.
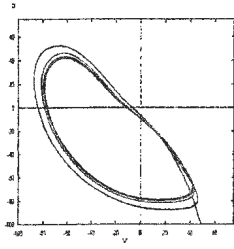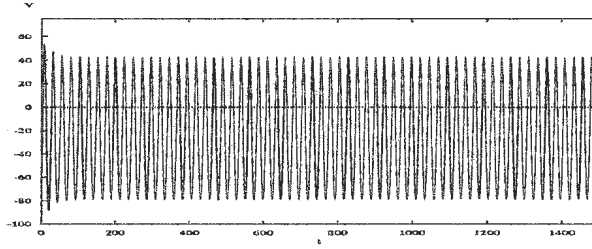
(e) $V(t-\tau)$ vs. V.

(f) $V(\theta) = -20, n(\theta) = n_\infty(-20)$ with $\tau = 9$.

(g) $V(t-\tau)$ vs. V.

(h) $V(\theta) = -100, n(\theta) = n_\infty(-100)$ with $\tau = 9$.

Figure 4.10: Numerical simulation of system (4.0.1) with $\mu = -5$ (Case 2). Only one stability change is possible and a periodic solution emerges prior to the loss of stability of (V^*, n^*).
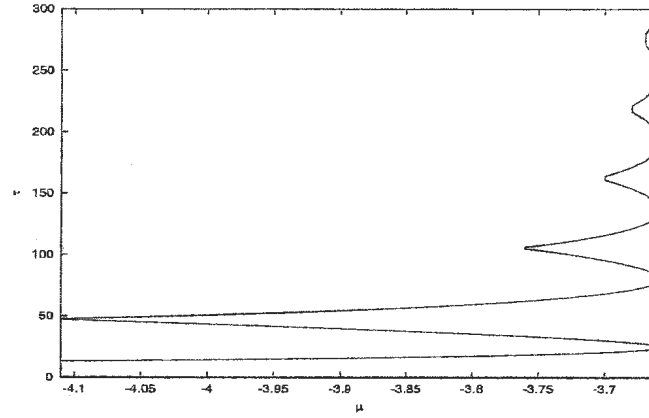
Figure 4.11: Bifurcation Diagram plotting the terms of $\tau_{n,1}$ and $\tau_{n,2}$ which give rise to stability changes for $\mu \in [-4.11, -3.66]$. The values of μ for which the model exhibits up to 11 stability switches are indicated.

$(V^*, n^*) = (-23.57, 0.04)$ are possible, and these occur for the delay times $\tau = 17.3, 35.5$, and 59.5. To witness the stability changes, we increase the delay τ through the values 15, 25, 50, and 70 in the numerical simulations in Figure 4.13. Initial conditions $V(\theta) = -20$, $n(\theta) = n_\infty(-20)$, $\theta \in [-\tau, 0]$, are selected close to the equilibrium point, to emphasize that the stability of (V^*, n^*) is only a local phenomenon.

Along with multiple changes in equilibrium point stability, we also observed some additional, more complicated dynamics. The bifurcation structure of the model appears to change significantly as $\mu \to \mu^{**}$. With μ near the lower end of the interval, say $-4.11 \le \mu \le 4$, the stability of the equilibrium point (V^*, n^*) changes three times, when τ is increased through $\tau_{0,1}$, $\tau_{0,2}$, and $\tau_{1,1}$, and at each of these delay times a Hopf bifurcation occurs. Stable periodic solutions were detected for values of $\tau \in (0, \tau_{0,1})$, while (V^*, n^*) is stable. There were no small

(a) $\tau_{0,1}$ vs. μ.

(b) $\tau_{0,2}$ vs. μ.

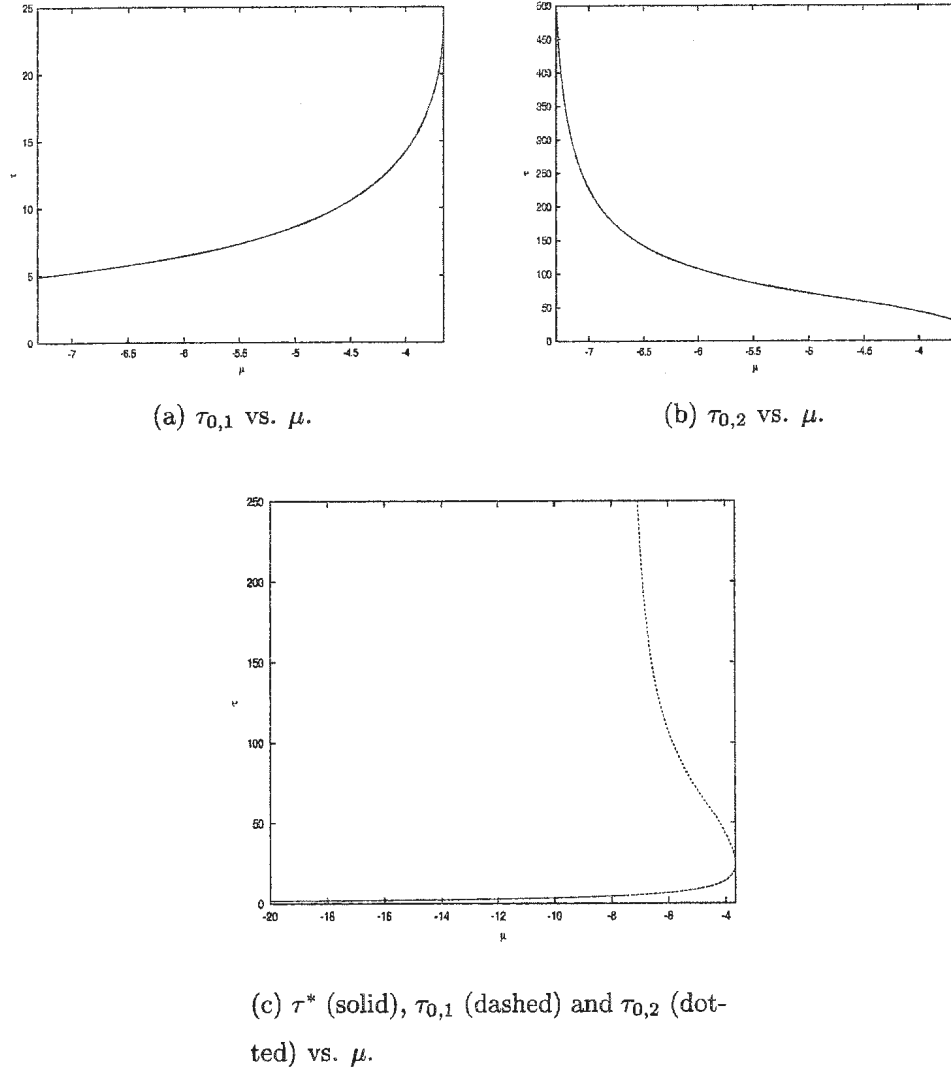(c) τ^* (solid), $\tau_{0,1}$ (dashed) and $\tau_{0,2}$ (dotted) vs. μ.

Figure 4.12: Bifurcation Diagrams: The values $\tau_{0,1}$ and $\tau_{0,2}$ versus μ for Case 2, and shown together along with the τ^* curve of Case 1.
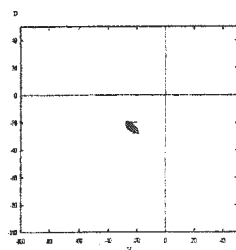
(a) $V(t-\tau)$ vs. V.
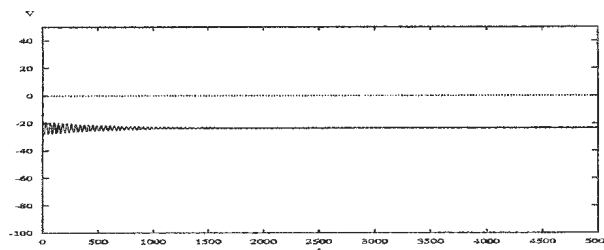
(b) $V(t)$ vs. t for $\tau = 15$.
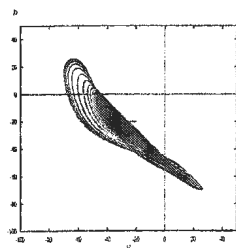
(c) $V(t-\tau)$ vs. V.
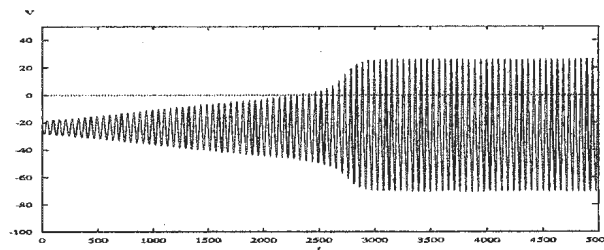
(d) $V(t)$ vs. t for $\tau = 25$.
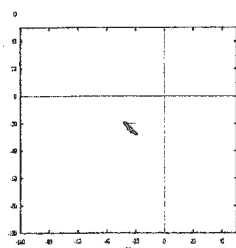
(e) $V(t-\tau)$ vs. V.
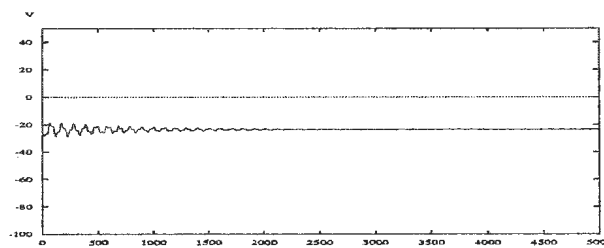
(f) $V(t)$ vs. t for $\tau = 50$.
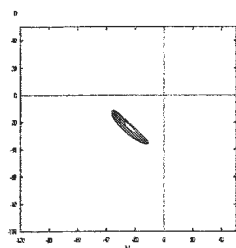
(g) $V(t-\tau)$ vs. V.
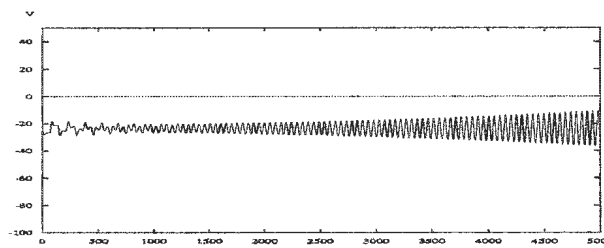
(h) $V(t)$ vs. t for $\tau = 70$.

Figure 4.13: Numerical simulation of system (4.0.1) with $\mu = -3.8$ (Case 2). The delay τ is increased from $\tau = 15, 25, 50$ to 70 ms, to illustrate multiple stability changes.

amplitude periodic solutions detected using initial conditions close to (V^*, n^*) for τ just above $\tau_{0,1}$, rather trajectories approached a large amplitude limit cycle. We conjecture that a PSNB occurs for some $\tau_{\text{PSN}} < \tau^*$, which generates a pair of nested stable and unstable periodic orbits surrounding the equilibrium, and that the unstable periodic orbit is lost in a subcritical Hopf bifurcation at $\tau = \tau_{0,1}$. Numerical simulations indicate that the system is bistable for all $\tau \in (\tau_{\text{PSN}}, \tau_{0,1})$, which is consistent with our conjecture. With $\tau \in (\tau_{0,1}, \tau_{0,2})$, the equilibrium point is unstable, and the system is initially monostable with a large amplitude limit cycle for τ just above $\tau_{0,1}$. Interestingly, based on numerical evidence, we propose that a second PSNB takes place for some $\tau_{\text{PSN2}} \in (\tau_{0,1}, \tau_{0,2})$, whereby we have nested stable, unstable, and stable periodic orbits of increasing amplitude surrounding an unstable equilibrium for $\tau \in (\tau_{\text{PSN2}}, \tau_{0,2})$. To support this conjecture we include a numerical simulation with $\mu = -4.06$, for which stability of (V^*, n^*) changes at the delay times $\tau_{0,1} = 13.5$, $\tau_{0,2} = 45.3$, and $\tau_{1,1} = 48.8$ ms. Figures 4.14(b) and 4.14(d) illustrate that, for $\tau = 40 \in (\tau_{0,1}, \tau_{0,2})$, the system has two stable limit cycles of different amplitude. Initial conditions are specified in each plot.

The smaller–amplitude stable limit cycle we believe is generated at τ_{PSN2} decreases in amplitude as $\tau \to \tau_{0,2}$, and we propose that it is lost via a subcritical Hopf bifurcation at $\tau = \tau_{0,2}$. With $\tau_{0,2} < \tau < \tau_{1,1}$, the system is bistable with nested unstable and stable periodic orbits surrounding a stable equilibrium point. Stability of the (V^*, n^*) is lost for good when τ is increased past $\tau_{1,1}$, and trajectories close to (V^*, n^*) with τ just above $\tau_{1,1}$ approach the large amplitude limit cycle generated at τ_{PSN}, as indicated in Figure 4.16. Thus, we suspect that an unstable periodic orbit generated at τ_{PSN2} is lost via

(a) $V(t - \tau)$ vs. V.
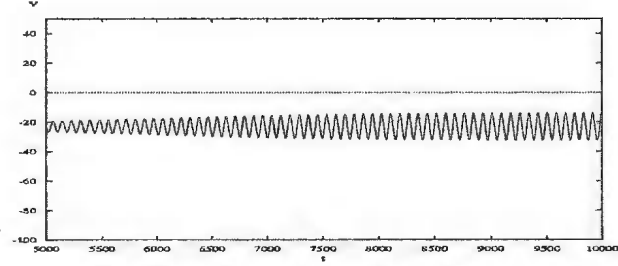
(b) $V(t)$ vs. t with $V(\theta) = -23$, $n(\theta) = n_\infty(-23)$.
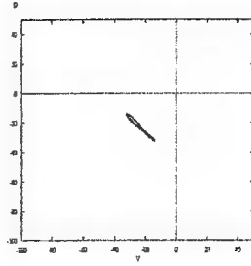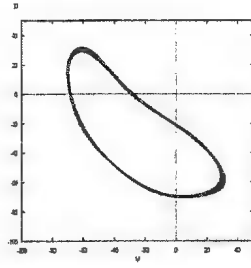

(c) $V(t - \tau)$ vs. V.
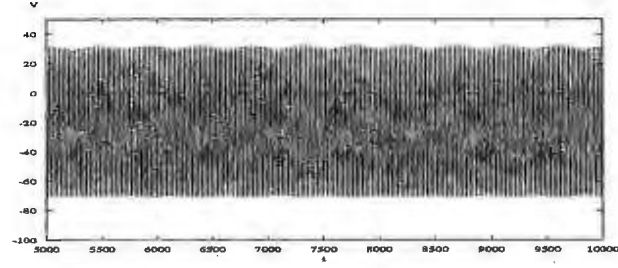
(d) $V(t)$ vs. t, with $V(\theta) = -50$, $n(\theta) = n_\infty(-50)$.

Figure 4.14: Numerical simulation of system (4.0.1) with $\mu = -4.06$ (Case 2), and $\tau = 40$ ms, illustrating the presence of two different stable limit cycles Simulations run from $t = 5000$ to 10000 ms to discard transient behavior.

a subcritical Hopf bifurcation at $\tau_{1,1}$, and so the system is monostable with a large amplitude periodic solution for all $\tau > \tau_{1,1}$. No additional bifurcations were detected after the final switching time. Considering the sequence of bifurcations described here, we propose the bifurcation structure depicted in Figure 4.15 for system (4.0.1) with $-4.11 \le \mu \le -4.0$.
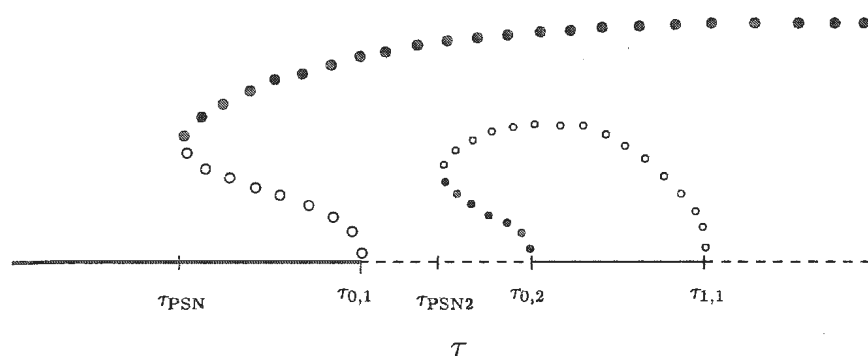
Figure 4.15: Conjectured bifurcation diagram illustrating the behavior of the full–2D model (4.0.1) for $\mu \in [-4.11, -4.0]$.

If $-4.0 < \mu < -3.76$, then a different series of bifurcations appear to take place for system (4.0.1) as τ is increased. There are still only three stability changes possible for (V^*, n^*), and we still observe a similar PSNB phenomenon for $0 < \tau_{\text{PSN}} < \tau_{0,1}$. Also, we conjecture that an unstable periodic orbit generated at τ_{PSN} is lost via a subcritical Hopf bifurcation at $\tau_{0,1}$, so that for $\tau \in (\tau_{0,1}, \tau_{0,2})$, the system has an unstable equilibrium point and a stable limit cycle. But unlike the results witnessed for $-4.11 \le \mu \le -4.0$, numerical simulations seem to indicate that a stable limit cycle formed at τ_{PSN} decreases in amplitude as $\tau \to \tau_{0,2}$, where we believe it is lost in a subcritical Hopf
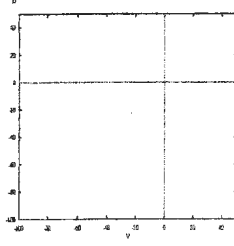
(a) $V(t-\tau)$ vs. V.
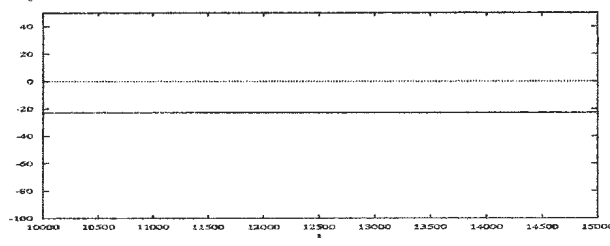
(b) $V(t)$ vs. t for $\tau = 48$, $V(\theta) = -23$, $n_\infty(-23)$.
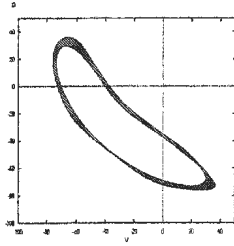
(c) $V(t-\tau)$ vs. V.
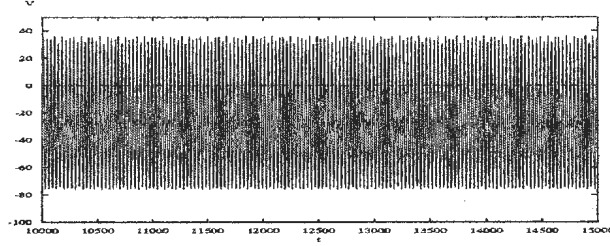
(d) $V(t)$ vs. t for $\tau = 48$, $V(\theta) = -50$, $n_\infty(-50)$.

(e) $V(t-\tau)$ vs. V.

(f) $V(t)$ vs. t for $\tau = 52$, $V(\theta) = -23$, $n_\infty(-23)$.

(g) $V(t-\tau)$ vs. V.
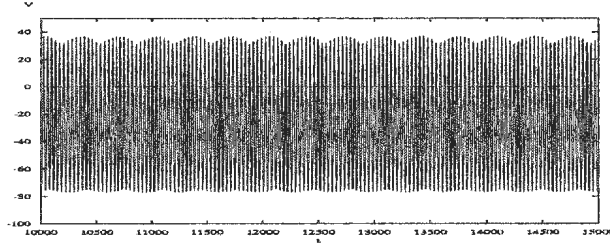
(h) $V(t)$ vs. t for $\tau = 52$, $V(\theta) = -50$, $n_\infty(-50)$.

Figure 4.16: Numerical simulation of system (4.0.1) with $\mu = -4.06$ (Case 2). Increasing τ from 48 to 52 ms, illustrates the system is bistable for $\tau < \tau_{1,1}$, but monostable for $\tau > \tau_{1,1}$. We believe that an unstable periodic orbit is lost

bifurcation. We believe that, with τ just above $\tau_{0,2}$, the system is monostable with a stable equilibrium (V^*, n^*), and no periodic solutions were detected. Based on numerical evidence, we conjecture that a second PSNB occurs for some value $\tau_{\mathrm{PSN2}} \in (\tau_{0,2}, \tau_{1,1})$, which generates a pair of nested stable and unstable periodic orbits surrounding the stable equilibrium. The system is bistable for all $\tau \in (\tau_{\mathrm{PSN2}}, \tau_{1,1})$. Because large amplitude periodic solutions were detected for τ just above $\tau_{1,1}$, we speculate that an unstable periodic orbit generated at τ_{PSN2} is lost in a subcritical Hopf bifurcation at $\tau_{1,1}$. Furthermore, for $\tau > \tau_{1,1}$, we gathered evidence to support a third PSNB for some $\tau_{\mathrm{PSN3}} > \tau_{1,1}$, and with τ above this value the system exhibits bistability with large and small amplitude periodic solutions. Figure 4.17 indicates that, for $\mu = -3.8$, the system appears to be monostable for $\tau = 75 > \tau_{1,1} = 59.5$, as trajectories with significantly different initial conditions approach the same stable limit cycle. However, with the delay increased to $\tau = 85$, different long–term behavior is observed for different initial conditions. Hence the system is (at least) bistable, and there must be an unstable periodic orbit separating the small and large–amplitude stable oscillations. The bifurcation sequence we propose for (4.0.1) with μ in this range is concisely depicted in Figure 4.18.

Numerical simulations indicate that the bifurcation structure of the full–2D system (4.0.1) becomes increasingly more complex as $\mu \to \mu^{**}$. Some very rich dynamics arise as the number of stability switches of (V^*, n^*) increases, and we make no attempt to classify all the behavior here. Figure 4.19 is a schematic bifurcation diagram outlining the qualitative dynamics conjectured
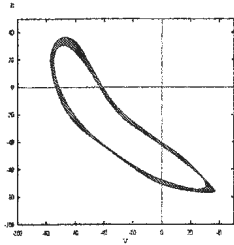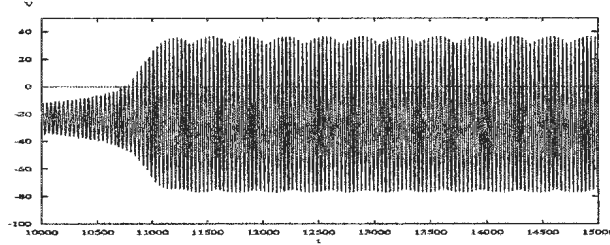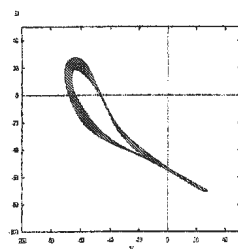
(a) $V(t-\tau)$ vs. V.
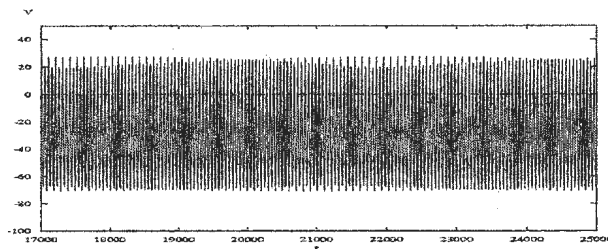
(b) $V(t)$ vs. t for $\tau = 75$, $V(\theta) = -23$, $n_\infty(-23)$.
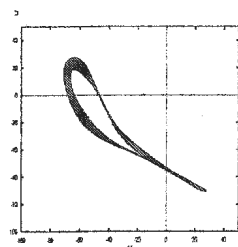
(c) $V(t-\tau)$ vs. V.
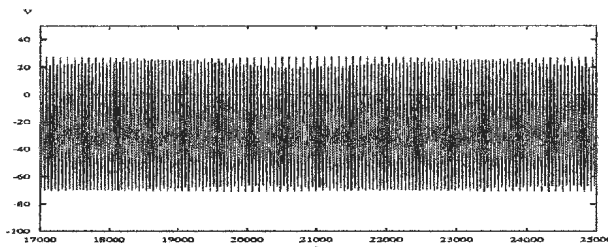
(d) $V(t)$ vs. t for $\tau = 75$, $V(\theta) = -100$, $n_\infty(-100)$.
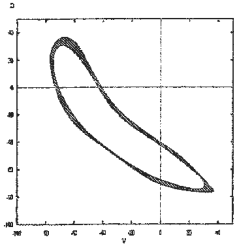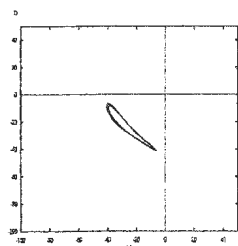
(e) $V(t-\tau)$ vs. V.
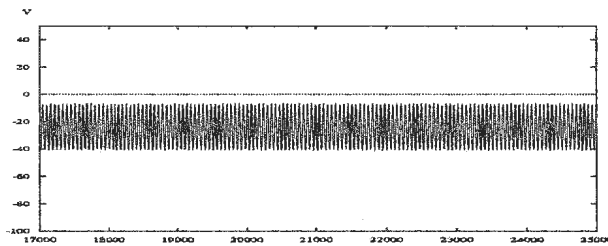
(f) $V(t)$ vs. t for $\tau = 85$, $V(\theta) = -23$, $n_\infty(-23)$.
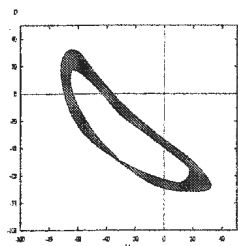
(g) $V(t-\tau)$ vs. V.
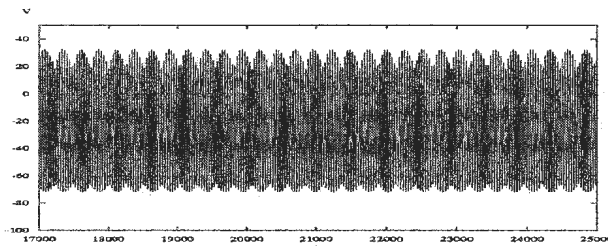
(h) $V(t)$ vs. t for $\tau = 85$, $V(\theta) = -100$, $n_\infty(-100)$.

Figure 4.17: Numerical simulations of system (4.0.1) with $\mu = -3.8$ (Case 2). Increasing τ from 75 to 85 ms demonstrates a PSNB takes place for some $\tau_{\text{PSN3}} > \tau_{1,1}$. Simulations run from $t = 17000$ to 25000 to discard transients.
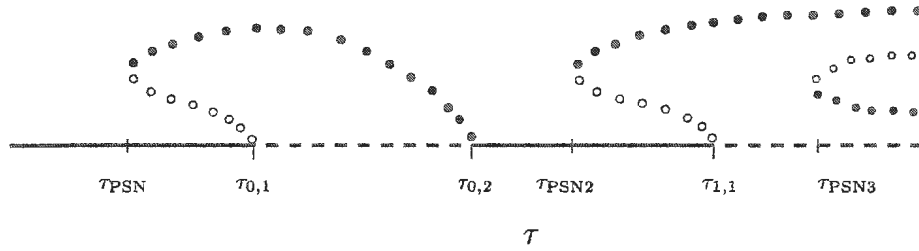
Figure 4.18: Conjectured bifurcation diagram illustrating the behavior observed for the full-2D model (4.0.1) for $\mu \in (-4.0, -3.76)$ (Case 2), where three stability switches are possible.

for system (4.0.1) with $\mu = -3.75 \in (-3.76, -3.7)$, for which five changes in equilibrium point stability occur. Combinations of PSNB and subcritical Hopf bifurcations (stable and unstable) are suspected to largely govern the dynamics of the system with μ in this range. The results discussed here for $\mu \in [-4.11, -3.66]$ are based on observation from numerical simulations, and there are discrepancies between the numerical results and Hopf bifurcation analysis that we were unable to account for. A more complete picture of the bifurcation structure of the model could be elucidated with the use of an an appropriate numerical continuation package for delay differential equations, which would allow one to accurately estimate the delay times where PSNB(s) take place, and would indicate the existence and location of unstable periodic orbits.

All that remains in the analysis of the full-2D model is to comment on the dynamics of system (4.0.1) for $\mu^{**} < \mu < g_L$. With μ in this range, the primary requirement of Case 2 is met, but the sub-conditions (a) and (b) are not
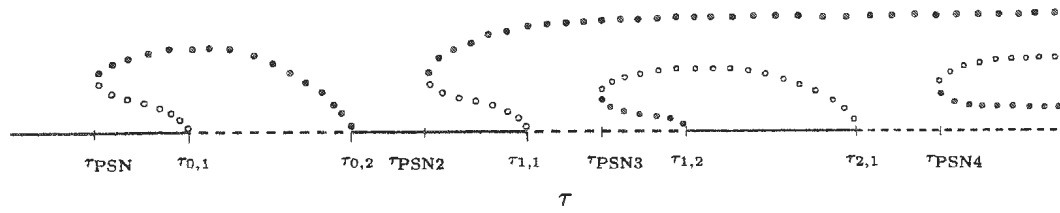
Figure 4.19: Conjectured bifurcation diagram outlining the dynamics of the full–2D model (4.0.1) for $-3.76 < \mu < -3.7$ (Case 2), where five stability changes are possible.

simultaneously satisfied. This implies that there there are no purely imaginary roots of the characteristic equation, and hence no changes in stability of the equilibrium point are possible. Since (V^*, n^*) is stable for $\tau = 0$, it follows that (V^*, n^*) is stable for all $\tau \geq 0$. Numerical results support this conclusion, and two examples are illustrated in Figure 4.20, one for weak inhibitory feedback ($\mu = -2.5$) and one for weak excitatory feedback ($\mu = 1.5$). For $\mu = -2.5$, we use initial conditions $V(\theta) = -20$, $n(\theta) = n_\infty(-20)$ and $V(\theta) = -50$, $n(\theta) = n_\infty(-50)$ for $\mu = 1.5$. In each case, the stability of the equilibrium point does not change, even with a 10–fold increase in the delay.

However, for some values of $\mu \in (\mu^{**}, g_{\mathrm{L}})$, the system exhibits bistability over a range of the time delay. With μ near the lower end of the interval, say $\mu^{**} < \mu < -3.37$, numerical simulations indicate the existence of a stable limit cycle along with a locally stable equilibrium point. Since there is no Hopf bifurcation to account for a stable periodic solution, we speculate that a PSNB at some value of the delay $\tau_{\mathrm{PSN}} > 0$ is responsible. However, if we further increase τ then the equilibrium appears to be globally attracting, and no periodic solutions were detected. We propose that a reversing PSNB
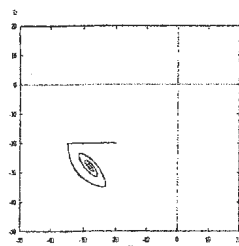
(a) $V(t-\tau)$ vs. V.
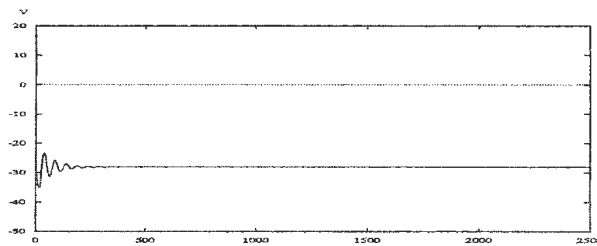
(b) $V(t)$ vs. t for $\mu = -2.5$, $\tau = 20$.
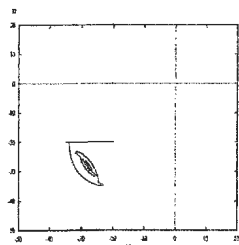
(c) $V(t-\tau)$ vs. V.
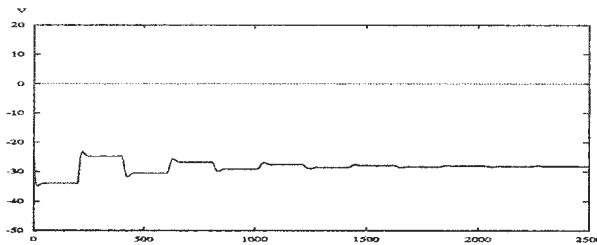
(d) $V(t)$ vs. t for $\mu = -2.5$, $\tau = 200$.
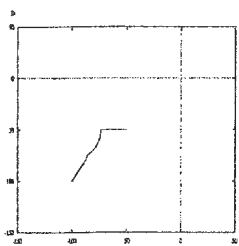
(e) $V(t-\tau)$ vs. V.
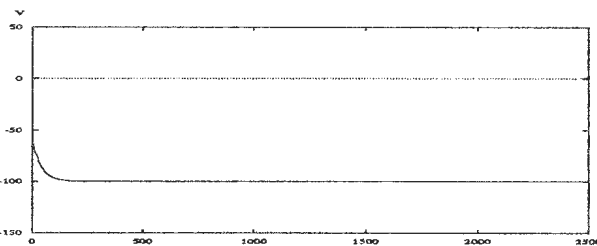
(f) $V(t)$ vs. t for $\mu = 1.5$, $\tau = 20$.
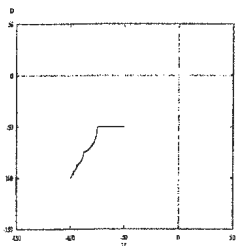
(g) $V(t-\tau)$ vs. V.
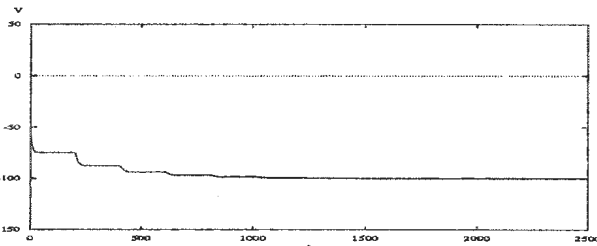
(h) $V(t)$ vs. t for $\mu = 1.5$, $\tau = 200$.

Figure 4.20: Numerical simulation of system (4.0.1) with weak inhibitory and excitatory feedback. The values of μ and τ, are specified for each plot. In each case, stability of the equilibrium does not change as the delay is increased.

occurs as the delay is increased, whereby a pair of unstable and stable periodic orbits coalesce and annihilate each other, leaving only the globally attractive equilibrium point. A schematic bifurcation diagram describing these possible qualitative dynamics appears in Figure 4.21. This behavior seems to persist for a larger interval of the delay as $|\mu|$ increases. For example, with $\mu = -3.65$, we detected a stable periodic orbit for $\tau = 12$ to 26 ms, but for $\mu = -3.37$ we could only detect a stable periodic orbit for $\tau = 17$ to 20 ms.
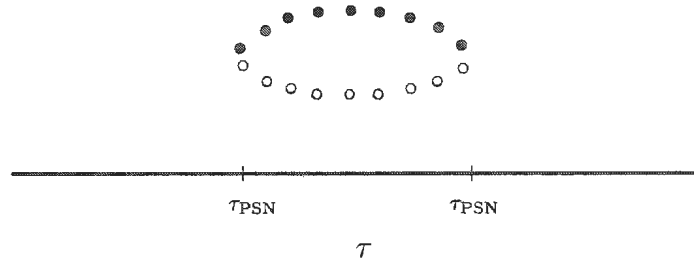
Figure 4.21: Conjectured bifurcation diagram illustrating the behavior observed for system (4.0.1) with $\mu^{**} < \mu < -3.37$ (neither Case 1 nor Case 2).

To illustrate these dynamics, we consider the example $\mu = -3.5$. The equilibrium point $(V^*, n^*) = (-24.44, 0.04)$ is stable for all $\tau \geq 0$, but a stable limit cycle becomes evident as τ is increased past 14, as demonstrated in Figure 4.22. Trajectories with initial conditions close to the equilibrium point tend to (V^*, n^*), while those with significantly different initial conditions approach a stable limit cycle. We believe that a PSNB occurs for some $\tau < 14$. If we increase τ further, the equilibrium point remains stable but the stable

limit cycle cannot be detected for $\tau \geq 24$ ms.

This concludes the analysis of the full–2D Morris–Lecar model with delay. Our investigation indicates that the model with both conductances operational displays a wide range of rich dynamics, and contributions of both conductance systems are evident. In the final chapter, Chapter 5, we interpret our results biophysically, address the contribution of each conductance system to the full–2D model, and comment on how the Morris–Lecar model with delay compares to the original non–delayed model. A detailed Hopf bifurcation analysis of the full–2D model (4.0.1) is presented in the following Section 4.2.3.

To close this section, we summarize the proven results in the following theorem:

Theorem 4.2.2.2. *Assume that parameters in system (4.0.1) are as in Table 4.1. Then we have the following:*

1. *If $\mu < \mu^*$, then (V^*, n^*) is stable for all $\tau \in [0, \tau^*)$, where μ^*, τ^* are defined earlier. For all $\tau > \tau^*$, (V^*, n^*) is unstable, and a Hopf bifurcation occurs at $\tau = \tau^*$.*

2. *If $\mu^* < \mu < \mu^{**}$, then (V^*, n^*) is capable of a finite number of stability switches, before instability persists (μ^{**} defined earlier). Transitions from stability to instability occur with $\tau_{n,1}$ terms of (4.2.13), while those from instability to stability occur with $\tau_{n,2}$ terms, $n = 0, 1, \ldots$. A total of $2k+1$ switches is possible, where k satisfies $\tau_{k,1} < \tau_{k+1,1} < \tau_{k,2}$. At values of $\tau_{n,1}$, $\tau_{n,2}$ where a stability change occurs, system (4.0.1) undergoes a Hopf bifurcation.*

3. *If $\mu^{**} < \mu < g_L$, then (V^*, n^*) is stable for all $\tau \geq 0$.*
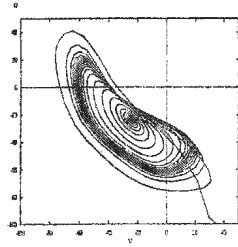
(a) $V(t-\tau)$ vs. V.
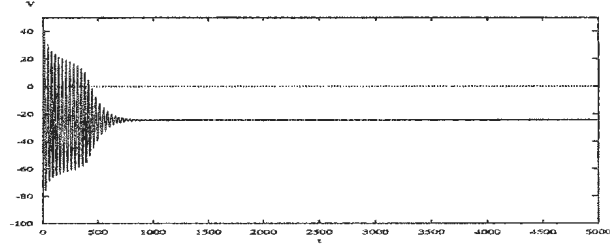
(b) $V(\theta) = -100$, $n(\theta) = n_\infty(-100)$ with $\tau = 13$.
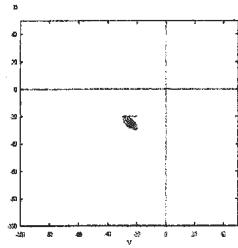
(c) $V(t-\tau)$ vs. V.
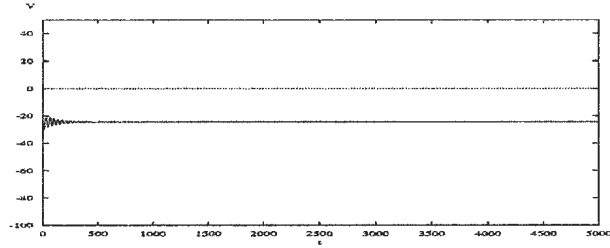
(d) $V(\theta) = -20$, $n(\theta) = n_\infty(-20)$ with $\tau = 14$.
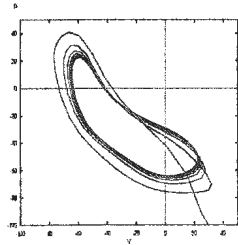
(e) $V(t-\tau)$ vs. V.
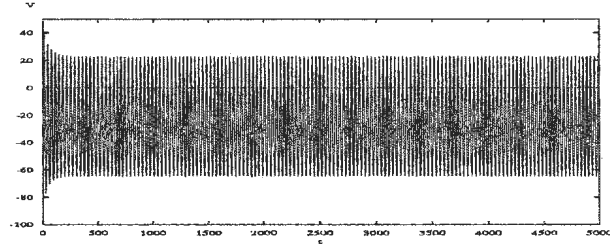
(f) $V(\theta) = -100$, $n(\theta) = n_\infty(-100)$ with $\tau = 14$.
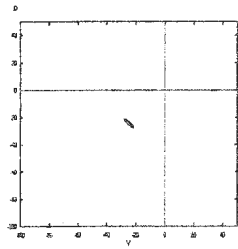
(g) $V(t-\tau)$ vs. V.
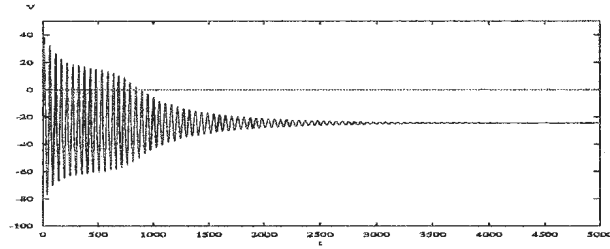
(h) $V(\theta) = -100$, $n(\theta) = n_\infty(-100)$ with $\tau = 24$.

Figure 4.22: Numerical simulation of system (4.0.1) with $\mu = -3.5$, to illustrate a double PSNB.

4. If $\mu > g_L + g_K + g_{Ca}$, then (V^*, n^*) is unstable for all $\tau \geq 0$.

4.2.3 Direction and Stability of Hopf Bifurcation

We turn now to the direction and stability of the Hopf bifurcation associated with (4.0.1), the two–dimensional Morris–Lecar model with delay. The detailed Hopf bifurcation analysis of this system is similar to that presented for the individual conductance systems, and follows the same steps presented in the all–K$^+$ chapter. However, the delay differential equation of (4.0.1) has an additional nonlinear term representing a steady–state calcium conductance, which affects the calculations. Therefore, in this section we merely highlight the important changes. We note in particular that the conditions on the continuity of the nonlinearity of the system required by the Hopf bifurcation theorem for DDEs is met. Also, we comment that Hopf bifurcations do not occur at the cusp points of Figure 4.11. These are Hopf–Hopf interaction points where there are two pairs of purely imaginary eigenvalues, and the situation is similar to that encountered for the all–K$^+$ conductance system in Chapter 2.

Consider (4.2.7), the nonlinear system with equilibrium point shifted to the origin. Expanding the hyperbolic trigonometric functions in powers of x, we obtain

$$
\begin{aligned}
\frac{dx}{dt} &= -ax + by + \hat{\mu}x(t - \tau) - \alpha xy + Jx^2 + Kx^3 + O(x^4) \\
\frac{dy}{dt} &= cx - dy + Ax^2 - Bxy - Dx^3 - Gx^2y + O(x^4)
\end{aligned}
\tag{4.2.14}
$$

where $\beta_u = \tanh(u)$, $\beta_v = \tanh(v)$, $\beta_s = \operatorname{sech}^2(t)$,

$$
u = \frac{V^* - V_3}{2V_4}, \quad v = \frac{V^* - V_3}{V_4}, \quad t = \frac{V^* - V_1}{V_2}, \quad \alpha = \frac{g_K}{C}, \quad G = \frac{d}{8V_4^2},
$$

$$A = -\frac{c}{V_4}\left(\beta_v - \frac{1}{2}\beta_u\right), \quad B = \frac{d}{2V_4}\beta_u, \quad D = \frac{c}{V_4^2}\left[\frac{5}{24} + \beta_v\left(\frac{1}{2}\beta_u - \beta_v\right)\right],$$

$$J = \frac{g_{Ca}\beta_s}{2V_2C}\left[\frac{(V^* - V_{Ca})}{V_2}\beta_t - 1\right], \quad K = \frac{g_{Ca}\beta_s}{2V_2^2C}\left[\beta_t + \frac{V^* - V_{Ca}}{3V_2}(\beta_s - 2\beta_t^2)\right],$$

and the coefficients a, b, c, d and $\hat{\mu}$ were defined earlier for the linearised system (4.2.8). For $\phi = [\phi_1, \phi_2]^T \in C$, the definition of $L_\gamma\phi$ does not change, since the form of (4.0.1) linearised about the origin is identical to that of (2.0.1). However, in this case we define

$$F(\gamma, \phi) \;=\; \begin{bmatrix} -\alpha\phi_1(0)\phi_2(0) + J\phi_1^2(0) \\[2em] A\phi_1^2(0) - B\phi_1(0)\phi_2(0) \end{bmatrix} + \begin{bmatrix} K\phi_1^3(0) \\[2em] -D\phi_1^3(0) - G\phi_1^2(0)\phi_2(0) \end{bmatrix} + O(x^4).$$

The eigenfunctions $q(\theta) = [1, \beta]^T e^{i\omega\theta}$ and $q^*(s) = [\nu_1, \nu_2]e^{i\omega s}$, with β, ν_1 and ν_2 defined earlier, also assume the same form, since these are found using only the linear components of (4.2.14). Most important are the coefficients g_{ij} for the full system, and we find these by evaluating $g(z, \bar{z}) = \bar{q}^*(0)F_0$. This gives

$$g_{20} = 2[\bar{\nu}_1(J - \alpha\beta) + \bar{\nu}_2(A - \beta B)],$$

$$g_{11} = \bar{\nu}_1(2J - \alpha(\beta + \bar{\beta})) + \bar{\nu}_2(2A - B(\beta + \bar{\beta})),$$

$$g_{02} = 2[\bar{\nu}_1(J - \alpha\bar{\beta}) + \bar{\nu}_2(A - \bar{\beta}B)],$$

$$g_{21} = 2\left[W_{20}^{(1)}(0)\left(\bar{\nu}_1\left(J - \frac{1}{2}\alpha\bar{\beta}\right) + \bar{\nu}_2\left(A - \frac{1}{2}\bar{\beta}B\right)\right)\right.$$
$$+ 2W_{11}^{(1)}(0)\left(\bar{\nu}_1\left(J - \frac{1}{2}\alpha\beta\right) + \bar{\nu}_2\left(A - \frac{1}{2}\beta B\right)\right) - W_{20}^{(2)}(0)\frac{1}{2}(\alpha\bar{\nu}_1 + B\bar{\nu}_2)$$
$$\left. - W_{11}^{(2)}(0)(\alpha\bar{\nu}_1 + B\bar{\nu}_2) + 3K\bar{\nu}_1 - \bar{\nu}_2\left(G(2\beta + \bar{\beta}) + 3D\right)\right],$$

where $W_{20}(\theta)$, $W_{11}(\theta)$ are given by

$$W_{20}(\theta) = -\frac{g_{20}}{i\omega}q(0)e^{i\omega\theta} - \frac{\bar{g}_{02}}{3i\omega}\bar{q}(0)e^{-i\omega\theta} + Ee^{2i\omega\theta},$$

and

$$W_{11}(\theta) = \frac{g_{11}}{i\omega}q(0)e^{i\omega\theta} - \frac{\bar{g}_{11}}{i\omega}\bar{q}(0)e^{-i\omega\theta} + F.$$

The vectors $E = [E_1, E_2]^{\mathrm{T}}$ and $F = [F_1, F_2]^{\mathrm{T}}$ have components

$$E_1 = \frac{2(\alpha\beta - J)(d + 2i\omega) - 2b(A - \beta B)}{bc + (d + 2i\omega)\left[\hat{\mu}e^{-2i\omega\tau} - (a + 2i\omega)\right]},$$

$$E_2 = \frac{2c(\alpha\beta - J) + 2(A - \beta B)\left[\hat{\mu}e^{-2i\omega\tau} - (a + 2i\omega)\right]}{bc + (d + 2i\omega)\left[\hat{\mu}e^{-2i\omega\tau} - (a + 2i\omega)\right]},$$

$$F_1 = \frac{b(2A - B(\beta + \bar{\beta})) - d(\alpha(\beta + \bar{\beta}) - 2J)}{(ad - bc) - \hat{\mu}d},$$

$$F_2 = \frac{(a - \hat{\mu})(2A - B(\beta + \bar{\beta})) - c(\alpha(\beta + \bar{\beta}) - 2J)}{(ad - bc) - \hat{\mu}d}.$$

With the coefficients g_{ij} as functions of the model parameters only, we may compute $C_1(0)$, along with μ_2, and β_2, which indicate the direction and stability of the bifurcating periodic solutions, respectively.

The results complied from numerical simulations of the full–2D model indicate that the Hopf bifurcations associated with terms of the $\tau_{n,1}$, $n = 0, 1, \ldots$ sequence are subcritical and branch to unstable oscillations, while those associated with the terms of the $\tau_{n,2}$, $n = 0, 1, \ldots$ sequence are subcritical and branch to stable oscillations.

This is where we find discrepancies between our numerical results and Hopf bifurcation analysis. The results of the Hopf bifurcation analysis for the all–K$^+$ and all–Ca^{2+} conductance systems matched perfectly with numerical results, and these methods complimented each other nicely. However, this is not the case for the analysis of the full–2D model with delay, as the following calculations illustrate.

We consider first an example where $\mu < \mu^*$. For these values of μ the model is in Case 1, and one Hopf bifurcation occurs when the equilibrium point loses stability, that is when τ is increased through τ^*. We present a set of calculations for $\mu = -8$, a representative value of this case considered earlier. For this value of μ, the purely imaginary root is $\lambda_+ = i\omega_+ = i \times 0.4292$, and the delay time for the bifurcation is $\tau^* = 4.4$ ms. The component β of the eigenfunction $q(\theta)$ is $\beta = 0.000399 - i \times 0.00224$, and ν_1, ν_2 of $q^*(s)$ are $\nu_1 = 0.293 + i \times 0.306$, $\nu_2 = 12.3 - i \times 16.77$. For the g_{ij} coefficients, we obtain $g_{20} = 0.00419 - i \times 0.00102$, $g_{11} = 0.00355 - i \times 0.00147$, $g_{02} = 0.00290 - i \times 0.00193$, and $g_{21} = -0.002152 + i \times 0.00324$. This gives $C_1(0) = -0.00106 + i \times 0.00164$, and hence $\mu_2 = (0.00106)(\text{Re}\{\lambda'(0)\})^{-1} > 0$, since $\text{Re}\{\lambda'(0)\} > 0$, and $\beta_2 = -0.00213 < 0$. This calculation indicates that the Hopf bifurcation at $\tau^* = 4.4$ for $\mu = -8$ is supercritical ($\mu_2 > 0$) and the bifurcating periodic solutions branch to stable oscillations ($\beta_2 < 0$). Similar results were obtained for a sample of values with $\mu < \mu^*$ using this calculation. However, numerical simulations of (4.0.1) with μ in this range provide evidence for a PSNB followed by a subcritical Hopf bifurcation, contrary to what our Hopf bifurcation calculations show.

With $\mu^* < \mu < \mu^{**}$, the system is in Case 2, and multiple changes in stability of (V^*, n^*) are possible. Only one stability change occurs if $\mu^* < \mu < -4.11$, and calculations with μ in this range indicate results similar to those for $\mu < \mu^*$. For an example where multiple stability switches are possible, we consider $\mu = -3.8$, for which three changes in stability occur for the delay times $\tau_{0,1} = 17.3$, $\tau_{0,2} = 35.5$, and $\tau_{1,1} = 59.5$. At each of these delay times we also obtain a branch of periodic solutions from a Hopf bifurcation. Note

that both $\tau_{0,1} = 17.3$ and $\tau_{1,1} = 59.5$ correspond to the ω_+ root, which has value $\omega_+ = i \times 0.149$, while $\tau_{0,2} = 35.5$ corresponds to the ω_- root, where $\omega_- = i \times 0.0838$. Tables 4.3 and 4.4 report the values for important quantities to determine the direction and stability for all three Hopf bifurcations.

Value	$\tau_{0,1} = 17.3$	$\tau_{0,2} = 35.5$
β	$0.00145 - i \times 0.00246$	$0.00295 - i \times 0.00281$
ν_1	$0.201 + i \times 0.105$	$0.125 + i \times 0.0285$
ν_2	$-1.23 - i \times 24.3$	$-10.8 - i \times 16.3$
g_{20}	$0.000995 + i \times 0.00121$	$-0.000086 + i \times 0.00119$
g_{11}	$0.00055 + i \times 0.00080$	$-0.000331 + i \times 0.000793$
g_{02}	$0.000106 + i \times 0.000392$	$-0.000576 + i \times 0.000393$
g_{21}	$-0.00279 + i \times 0.00319$	$-0.00247 + i \times 0.00158$
$C_1(0)$	$-0.00140 + i \times 0.00159$	$-0.00123 + i \times 0.000783$
μ_2	$(0.00140)(\text{Re}\{\lambda'(0)\})^{-1}$	$(0.00123)(\text{Re}\{\lambda'(0)\})^{-1}$
β_2	-0.00280	-0.00246

Table 4.3: Detailed Hopf bifurcation analysis: sample calculations for two of the Hopf bifurcation which occur for $\mu = -3.8$ (Case 2, multiple stability switches).

Note that $\text{Re}\{\lambda'(0)\} > 0$ for $\tau_{0,1}$ and $\tau_{1,1}$, while $\text{Re}\{\lambda'(0)\} < 0$ for $\tau_{0,2}$. Our calculations indicate that the Hopf bifurcations which occur at $\tau_{0,1} = 17.3$ and $\tau_{1,1} = 59.5$ are supercritical and branch to stable oscillations, since $\mu_2 > 0$, $\beta_2 < 0$. On the other hand, the results in Table 4.4 indicate that the Hopf bifurcation at $\tau_{0,2} = 35.5$ is subcritical and branches to stable oscillations, since $\mu_2 < 0$, $\beta_2 < 0$. All values of $\mu \in (-4.11, \mu^{**})$ which we checked produced

Value	$\tau_{1,1} = 59.5$
β	$0.00145 - i \times 0.00246$
ν_1	$0.0690 + i \times 0.0415$
ν_2	$0.0657 - i \times 8.65$
g_{20}	$0.000377 + i \times 0.000407$
g_{11}	$0.000212 + i \times 0.000272$
g_{02}	$0.000046 + i \times 0.000137$
g_{21}	$-0.000924 + i \times 0.00118$
$C_1(0)$	$-0.000462 + i \times 0.000592$
μ_2	$(0.000462)(\mathrm{Re}\{\lambda'(0)\})^{-1}$
β_2	-0.000925

Table 4.4: Detailed Hopf bifurcation analysis: sample calculations for the third Hopf bifurcation which occurs for $\mu = -3.8$ (Case 2, multiple stability switches).

similar results, in that Hopf bifurcations occurring with members of the $\tau_{n,1}$, $n = 0, 1, \ldots$ sequence are supercritical and branch to stable oscillations, while those with the $\tau_{n,2}$, $n = 0, 1, \ldots$ sequence are subcritical and branch to stable oscillations. The results for bifurcations with the $\tau_{n,2}$, $n = 0, 1, \ldots$ sequence match the behavior indicated by numerical simulations, while those for the $\tau_{n,1}$, $n = 0, 1, \ldots$ sequence are opposite of what the numerics indicate.

The most likely cause of the discrepancies between the numerics and the Hopf bifurcation analysis is an error in the calculation for the full–2D model, due to the tedious nature and numerous steps involved with the algorithm. However, we were unable to identify mistake(s) in our calculations.

Chapter 5

Discussion

In this final chapter, we provide a biophysical interpretation of our results from previous chapters. Since our model describes the dynamics of the neuro-muscular feedback loop in terms of the potential across the membrane of the muscle fibre, our interpretations are based on membrane dynamics. We comment on the contribution of each conductance system to the behavior of the full–2D model, and how the conductance systems and full–2D model with delay compare to the systems of the original Morris–Lecar model. Some model limitations are also discussed, along with interesting avenues of possible future research.

The all–K^+ conductance system with delay is capable of more complicated dynamics than its non–delayed counterpart. Voltage oscillations were not possible in the all–potassium system without delay, which admitted at most one equilibrium point. With external stimulus, the system exhibits a graded response with a transient peak followed by a decay to a stable resting plateau, and with no stimulus the system simply approaches the steady state directly,

with no early peak in the voltage. The all–K$^+$ system with delay does support voltage oscillations for inhibitory synaptic feedback. In fact, for $\mu < 0$ the system with parameters in Table 2.1 is monostable for all delays $\tau \geq 0$, with either a single stable equilibrium point or a stable limit cycle surrounding an unstable equilibrium. The equilibrium point (V^*, n^*) corresponds to the membrane resting potential, which changes with the strength of synaptic feedback, $|\mu|$. A stable rest state in this case corresponds to quiescent behavior where the membrane is polarized, while stable oscillations about the rest state represent repetitive firing (graded depolarizations) of the membrane. In the case of $\mu < 0$, oscillatory solutions correspond to excitation due to recurrent inhibition. More specifically, it is due to the well–observed phenomenon of anode–break excitation, which is a form of post–inhibitory rebound [32, 35].

If the inhibitory feedback signal is weak, say $\mu^{**} < \mu < 0$, then the rest state (V^*, n^*) is stable for all $\tau \geq 0$, and no voltage oscillations occur. Conversely, if the delay term is dominant $(\mu < \mu^*)$, then the feedback is strong, and the stability of the equilibrium is delay–dependent. The rest state is stable for small delays below a critical value τ^*, and is unstable for all delays greater than τ^*. The value of τ^* depends on μ and other model parameters, and is very small when the delay is dominant. When the resting potential loses stability, stable oscillations emerge via a supercritical Hopf bifurcation. Oscillations arising in this manner are termed "soft" [16], [26], since they appear to grow from the rest state, in that they are small in amplitude if the delay τ is just above the bifurcation time τ^*, and grows as the delay is further increased. We note that the oscillations encountered in the all–K$^+$ conductance system do not have the same relaxation–oscillation shape typical of standard action poten-

tials. Instead, the oscillations are graded with depolarized and hyperpolarized phases, which are produced by an oscillating outward potassium current. Such graded action potentials are common in synthetic membrane models with a single voltage–dependent conductance system [24]. The sequence of events that produce a typical relaxation–oscillation action potential are determined by the dynamics of two gating variables, one with a fast–activation time course, and the other with a slow–activation time course. However, in this case the fast–acting calcium conductance is inoperative, and so the oscillations of the all–K^+ system are governed by only a single gating variable (n) and therefore only one (slow) time scale is operational.

The story is more interesting when the delay term of the system is not dominant, which is true if $\mu^* < \mu < \mu^{**}$. In this case, the feedback signal is strong enough to influence the dynamics of the system, but not strong enough to "take over" for small $\tau > 0$. If μ is near the lower end of this interval then the dynamics are similar to those for $\mu < \mu^*$, however the bifurcation value τ^* has a more modest value, and so the equilibrium point remains stable for larger delay values before relinquishing stability to a stable oscillation. However, a finite number of changes in stability of the equilibrium point are possible with more intermediate values of μ near the upper end of this range. For small delays the rest state is stable, and the membrane remains polarized. But as the rest state loses stability, a branch of stable soft oscillations appears and the membrane undergoes repetitive firing. Increasing the delay causes oscillations to cease via a subcritical Hopf bifurcation as the rest state regains stability. This sequence of events continues with increasing τ but eventually stability of the rest state is lost for good, and a globally attractive limit cycle dictates the

repetitive firing along the membrane.

No stable voltage oscillations were encountered for the all–K$^+$ system with excitatory feedback. This may seem somewhat counter–intuitive, since recurrent excitation might be expected to lead to repetitive firing, and has been observed in neural feedback models [32]. Instead, the system possesses a stable equilibrium point if $0 < \mu < g_{\mathrm{L}}$, no equilibrium if $g_{\mathrm{L}} \leq \mu \leq g_{\mathrm{L}} + g_{\mathrm{K}}$, and a single unstable equilibrium for $\mu > g_{\mathrm{L}} + g_{\mathrm{K}}$. The equilibrium point (V^*, n^*) for $0 < \mu < g_{\mathrm{L}}$ corresponds to a rest state where the membrane is polarized, while that for $\mu > g_{\mathrm{L}} + g_{\mathrm{K}}$ represents an excited state where the membrane is depolarized. The feedback signal is not strong enough to induce stable oscillations if $0 < \mu < g_{\mathrm{L}}$ and the rest state is stable for all positive time delays. With $\mu > g_{\mathrm{L}} + g_{\mathrm{K}}$ the signal strength is sufficient to cause the excited state to be unstable for all $\tau \geq 0$, and no stable oscillations were detected about this depolarized level. Solutions in numerical simulations for $\mu > g_{\mathrm{L}} + g_{\mathrm{K}}$ tended to $+\infty$ or $-\infty$, which is obviously not possible in an actual physiological setting. Rather, we interpret such behavior biologically as $V \rightarrow V(1)$ or $V(0)$, respectively, since the variable n represents the fraction of open K$^+$ channels and must lie in the interval $[0, 1]$. The case $V \rightarrow V(1)$ corresponds to a state where all potassium–ion channels are open, and so the conductance system is 100% operational. The opposite is true in the case $V \rightarrow V(0)$, where the potassium–conductance essentially shuts down, and all K$^+$ channels are closed.

The all–potassium conductance system does not admit an equilibrium point if $\mu \in [g_{\mathrm{L}}, g_{\mathrm{L}} + g_{\mathrm{K}}]$. Trajectories in this case can escape to $+\infty$ or $-\infty$ for a value of $n \in [0, 1]$, which we also interpret as $V \rightarrow V(0)$, or $V(1)$, depending on their values. That our model of recurrent excitation does not admit an

equilibrium point for even modest feedback strength is unrealistic, and an unfortunate by–product of how the delay was incorporated into the original Morris–Lecar equations. Therefore, we speculate that, while the Morris–Lecar model appears to describe the dynamics of recurrent inhibition nicely, it is incapable of supporting recurrent excitatory feedback as it has been proposed in our model. In addition, it is also unrealistic to have the equilibrium voltage $V^* \to -\infty$ and $+\infty$, which is the case for our model as $\mu \to g_L$ and $g_L + g_K$, respectively. Some suggestions on how to improve the model so that these unrealistic scenarios are avoided are addressed later in this chapter.

The isolated Ca^{2+} conductance system of the original Morris–Lecar model did not support voltage oscillations. Rather, the system had bistable responses with a characteristic threshold, with two stable equilibria separated by an unstable saddle point. Sustained oscillations are readily observed in the all–Ca^{2+} conductance system with delayed inhibitory feedback. With $\mu < 0$, the system admits up to three equilibria, and the number of equilibria can have a significant influence on the dynamics. For a moderate to strong feedback signal ($\mu < \mu^-$) the delay term in equations (3.0.1) is dominant, and there is only one equilibrium point, which corresponds to the rest state where the membrane is polarized. In fact, the rest state is the only steady state of the system for all $\mu < \mu^-$.

If the feedback is strong ($\mu < -3.7$) the rest state is stable for small to moderate values of the delay, but loses stability if the delay is increased past a critical value τ^*. When this happens, stable oscillations about the rest state ensue, driven by a supercritical Hopf bifurcation, which represents repetitive firing of the membrane. Recall that for soft oscillations arising in this manner,

the amplitude of oscillation is related to the magnitude of the delay above the critical value τ^*. As in the all–K^+ system with delay, stable oscillations for $\mu < 0$ result from excitation due to recurrent inhibition. The action potentials are graded due to the oscillatory nature of a single inward calcium current, which operates on a fast time scale. The slow–acting potassium conductance is not operational in this system. Therefore with strong inhibitory feedback the membrane operates in one of two stable modes: a stable rest state for small τ, and stable repetitive firing for large τ.

With intermediate feedback strength ($-3.7 \leq \mu \leq \mu^-$) the delay is still dominant, and the rest state becomes unstable as the delay is increased past the critical value τ^*. However, the system exhibits bistability with a stable rest state and a stable oscillation for some values of $\tau < \tau^*$. We conjecture that a PSNB occurs for some value of the delay ($0 < \tau_{\mathrm{PSN}} < \tau^*$), which generates a pair of nested stable and unstable periodic orbits which surrounding stable rest state. Trajectories with initial conditions inside the unstable periodic orbit approach the rest state, while those with initial conditions outside approach a stable periodic state. An unstable periodic orbit arising from a PSNB could act as a threshold for repetitive firing.

This threshold is believed to be lost along with stability of the rest state in a subcritical Hopf bifurcation at τ^*. When $\tau > \tau^*$, the system is monostable with a stable limit cycle, and the membrane fires repetitively. However, these oscillations are "hard" [16], [26] since they have large amplitude when the delay is just above τ^*, in contrast to soft oscillations. A trajectory with initial condition leading to rest for $\tau < \tau^*$ will suddenly undergo large amplitude oscillations if the delay is increased above τ^*. This type of bistability and

subsequent hard oscillation which may result from a combination periodic saddle–node bifurcation and a subcritical Hopf bifurcation is in fact a common phenomenon of the reduced–2D Morris–Lecar model without delay, but not of the non–delayed all–Ca^{2+} system. Similar behavior can be observed in the original Morris–Lecar model model by treating the applied current I as a bifurcation parameter, and with an appropriate parameter set for the other model parameters [34].

There is a range where the feedback strength is too weak to induce instabilities in the rest state, regardless of the magnitude of the time delay ($\mu^- < \mu < \bar{\mu}$), and for which the rest state is the only equilibrium point of the model. In this case the delay is not dominant, and the system is initially monostable with a stable rest state for small time delays. We again observe bistability in the model possibly arising through a PSNB at some $\tau_{PSN} > 0$, however since the rest state does not lose stability as τ is increased, bistability in the model persists over a large range of the delay, $\tau > \tau_{PSN}$.

A saddle–node bifurcation of steady states occurs at $\mu = \bar{\mu}$ ($\bar{\mu} \approx -2.22$), which gives rise to two additional equilibria in addition to the rest state. An unstable saddle point representing an intermediate, slightly depolarized state, and an excited state corresponding to a voltage plateau, which represents a fully depolarized state of the membrane. For all $\bar{\mu} < \mu < g_L$ the rest state is stable for all time delays, which incorporates weak inhibitory and excitatory feedback, and the saddle is unstable for all delays. The excited state can undergo a change in stability with weak inhibitory feedback, that is if $\mu \in (\bar{\mu}, \mu^{--})$. For certain parameter values we may obtain stable oscillations about the depolarized, excited state, which itself may or may not be stable.

With μ in this range and a small time delay, the system appears to be bistable with a stable rest state and a stable excited state. We believe that a PSNB takes place (at τ_{PSN}) as the delay is increased, after which the system is either tristable (for $\tau \in (\tau_{\mathrm{PSN}}, \tau^*)$) with a stable rest state, stable excited state, and a stable periodic state about the depolarized level, or bistable ($\tau > \tau^*$) with a stable rest state and a stable hard oscillation about the depolarized level. A threshold for repetitive firing, an unstable periodic orbit possibly formed at τ_{PSN}, which would allow for the tristability, is most likely lost along with stability of the excited state via a subcritical Hopf bifurcation at τ^*. However, if the feedback is slightly reduced ($\mu^{--} < \mu < -1.4$) so that the excited state does not lose stability as τ is increased, then tristability in the system appears to persist over a large range of the delay (for all $\tau > \tau_{\mathrm{PSN}}$). Tristability in the all–Ca^{2+} system with delay is an interesting feature of this system, and is not possible in the all–Ca^{2+} system without delay. However, the reduced–2D Morris–Lecar model without delay is capable of exhibiting tristability for certain model parameter sets and by treating the applied current I as a bifurcation parameter [34].

Stable oscillations about the excited state are abolished if the feedback strength is reduced further. For weak inhibitory and excitatory feedback ($-1.4 < \mu < g_{\mathrm{L}}$), the rest and excited states are both stable for all time delays, and the system seems to be bistable. No stable oscillations were detected. It is interesting that, while the rest state and excited state may change stability for certain (inhibitory) parameter ranges, neither state can undergo multiple changes in stability, a trend observed in the all–K^+ conductance system for non–dominant delay. Thus with inhibitory feedback the all–Ca^{2+} conductance

system displays a broad range of behavior, including multistability and hard oscillations, neither of which were possible in the all–K^+ system with delay.

However, problems start to creep into the model if we consider excitatory feedback. As $\mu \to g_L$, which corresponds to small feedback strength, the stable resting potential approaches $-\infty$. Also, as $\mu \to g_L + g_{Ca}$, the stable equilibrium voltage of the excited state approaches $+\infty$. For $g_L \leq \mu \leq g_L + g_{Ca}$ the system has only a stable excited state and an unstable saddle point, and trajectories can escape to $\pm\infty$. As in the all–K^+ system, these unphysical results are interpreted as the voltage assuming one of the limiting potentials $V(0)$ or $V(1)$. Furthermore with strong excitatory feedback ($\mu > g_L + g_{Ca}$) the system is unstable with only an unstable saddle with no stable rest or excited state(s), and no stable oscillations. Therefore, similar problems to those identified for the all–K^+ system with excitatory feedback are present in the all–Ca^{2+} system with delay.

Investigation of the full–2D model with delay revealed that it retained features specific to each of the single–ion conductance systems, and that each system contributes significantly to the dynamics of the full–2D model. However, the behavior observed was more complex than a straightforward combination of the K^+– and Ca^{2+}–conductances would account for. This trend was observed when the potassium and calcium systems without delay were incorporated into the reduced–2D original Morris–Lecar model. Despite having two very simple components, the original Morris–Lecar model was able to support sustained and damped oscillations rather than merely voltage–plateau responses. However, much of the diverse dynamical phenomena admitted by the original Morris–Lecar model was possible only through the application of

applied stimulus, that is by treating I as a bifurcation parameter. With $I = 0$, as we have here, the original Morris–Lecar model is in fact a very simple system, and with the parameters in Table 4.1 admits only a single stable rest state and exhibits no periodic behavior. Hence its dynamics are by no means as complex as even those of either single–ion conductance system with delay. We shall comment more on the dynamics of the original Morris–Lecar model with $I \neq 0$ after discussing the results of the full–2D model with delay.

One obvious feature of the full–2D model with delay is its similarity in form to the all–potassium conductance system with delay. Eliminating the calcium ion–gating variable m as a dependent variable of the full–3D system (1.3.5) reduced the model to system (4.0.1), the full–2D Morris–Lecar model with delay. Similarities in the form of systems (1.3.5) and (4.0.1), and in the steady–state bifurcation structure were addressed in Chapter 4

However, the all–K^+ system with delay was incapable of hard excitation and bistability, which were common in the all–Ca^{2+} system with delay. These phenomena were also readily observed in the full–2D model with delayed inhibitory feedback, and it stands to reason that these characteristics are contributions of the all–Ca^{2+} system to the full–2D model. With $\mu < 0$, the equilibrium point corresponds to a rest state where the membrane is polarized. In the presence of strong feedback ($\mu < \mu^*$) the rest state is stable for only small delays, and loses stability as τ is increased through a critical value τ^*. Also, we observe bistability with a stable rest state and a stable oscillation for some $\tau < \tau^*$. A PSNB at $\tau_{\mathrm{PSN}} < \tau^*$ is believed to be responsible. An unstable periodic orbit generated at τ_{PSN} could act as a threshold for repetitive firing, and may then be lost via a subcritical Hopf bifurcation at τ^*. For

$\tau > \tau^*$, numerical simulations indicate that the system is monostable with a stable hard oscillation. A similar sequence of events, namely a PSNB followed by a subcritical Hopf bifurcation, was proposed to cause similar behavior in the all–Ca^{2+} system with delay.

More reminiscent of the all–K^+ system is the multiple changes in stability possible for the rest state with intermediate feedback ($\mu^* < \mu < \mu^{**}$). In this case, the delay is non–dominant, and the rest state may change stability a finite number of times before instability prevails. With only a single change in stability the dynamics are similar to those for strong feedback. However, as the number of stability changes increases (as $\mu \to \mu^{**}$) the dynamics of the system become increasingly complex, involving the rest state and multiple periodic orbits. The system demonstrates bistability with a stable rest state and hard oscillations, or with two stable (hard) oscillations of different amplitude surrounding an unstable rest state, depending on the value of the delay. We speculate that a series of PSNBs along with subcritical Hopf bifurcations (some branching to stable oscillations, others unstable) may be responsible for the occurrence of bistability over large ranges in the delay for $\mu \in (\mu^*, \mu^{**})$. Numerical simulations indicate that the Hopf bifurcation structure (direction and stability) is similar to that of the all–Ca^{2+} system with delay. Thus for inhibitory feedback, bistability is a commonly encountered in the full–2D model. No instances of tristability were detected for the full–2D model.

With intermediate to weak feedback ($\mu^{**} < \mu < -3.37$) the system demonstrates bistability only over a small range of the delay. The system has a stable rest state for small delays, and also for large delays. There is a range of the delay where the system demonstrates bistability with a stable rest state and

stable periodic state. An unstable periodic orbit arising from a PSNB could provide a threshold for repetitive firing, and is believed to be lost in a second PSNB, whereby the nested stable and unstable periodic orbits from a first bifurcation coalesce and annihilate each other. For weak inhibitory feedback ($-3.37 < \mu < 0$), the rest state is stable for all values of the delay, and no stable voltage oscillations occur.

The results for recurrent excitation in the full–2D model with delay are essentially the same as those for the all–K^+ system with recurrent excitation. As in the two conductance systems, the full–2D model with delay displays diverse dynamics with recurrent inhibition, but problems arise in the case of recurrent excitation. These problems are a result of how the delay was incorporated in to the original Morris–Lecar equations. Our results and discussion indicate that the Ca^{2+}–conductance system has a much more substantial influence on the dynamics of the full–2D model than originally anticipated, and that the full–2D model with delay is more than merely a simple combination of both Ca^{2+}– and K^+–conductance systems.

There are many modifications and improvements one could add to the model we propose here to simulate delayed recurrent feedback in the Morris–Lecar model. However, there are still some interesting questions from our investigation that remain unanswered. First and foremost are the discrepancies between the Hopf bifurcation analysis and numerical simulations for the full–2D model with delay. Given the tedious nature of the Hopf bifurcation analysis, it is likely that an error in this calculation is responsible for these discrepancies. However, we were unable to identify any mistakes in our analysis. Secondly, although we hypothesize the occurrence of a PSNB in the all–Ca^{2+}

system and full–2D model, and have some evidence to support these claims, we cannot be certain that this is the mechanism generating stable and unstable periodic orbits in these systems. It seems plausible, especially since this type of bifurcation is commonly encountered in the original model without delay, by treating the applied current I as a bifurcation parameter. To confirm that this is the actual mechanism responsible would require the use of a numerical continuation package for delay differential equations, such as DDE–Biftool [10] for Matlab. Numerical continuation packages can be powerful aids in elucidating the dynamics and bifurcations of nonlinear differential equations, and can verify and compliment analytical results. While such packages are common for ODEs, numerical solvers capable of bifurcation continuation for DDEs have only recently been developed, and are presently in the beta–testing stage. This is why a package such as DDE–Biftool was not used in the thesis research presented here. However, once perfected, such packages should be reliable and have the capacity to reveal the existence and location of unstable periodic orbits, provide an accurate estimate for the value(s) of τ_{PSN}, and verify the direction and stability of Hopf bifurcations in systems of DDEs. With the methods discussed in this thesis, we have no way of accurately estimating τ_{PSN} bifurcation values, and are simply relying on thorough detective work with numerical simulations to identify the emergence of stable periodic orbits which might arise from a PSNB.

Another interesting aspect of this model which we did not pursue in detail in this thesis are the codimension two bifurcations which occur for the single–ion conductance systems and the full–2D model with delay. The cusp points of Figures 2.10 and 4.11 in Chapters 2 and 4, respectively, are codi-

mension two bifurcation points where Hopf–Hopf interactions occur, that is the system(s) admit two pairs of purely imaginary eigenvalues. Interaction of such bifurcations can result in a secondary Hopf bifurcation leading to the creation of a 2–torus [16]. References [4] and [37] discuss these points and their dynamical possibilities in more detail. For the all–Ca^{2+}, there is evidence of a Takens–Bogdanov interaction at $(\bar{\mu}, \bar{\tau}^{*})$, which occurs with a double zero eigenvalue and a purely imaginary pair of eigenvalues. We briefly investigated this point in Chapter 3, and found a finite delay value was approached as $\mu \to \bar{\mu}$, a steady–state saddle–node bifurcation point of the system. A similar situation arises in the Morris–Lecar model without delay, using the applied current I as a bifurcation parameter [11]. In this case, a steady–state saddle-node bifurcation emerges along with a large amplitude periodic solution at a common parameter value. Takens–Bogdanov bifurcations are common codimension two bifurcation points, and analysing these interactions may reveal some additional, complicated dynamics.

An obvious modification to address in the Morris–Lecar equations with delay is the behavior of the model with different parameter sets. Our analysis is based on a single parameter set, and so our results are highly specific to the parameter set used. Throughout the thesis however, we have attempted to generalize results wherever possible. Rinzel and Ermentrout [34] have found that the original Morris–Lecar model is capable of many different dynamical phenomena, and the dynamics vary considerably with the model parameters. Certain parameters have a more profound influence on the dynamics, while other have only small to moderate influence. By varying other model parameters besides the delay parameters μ and τ, one might uncover a different

spectrum of dynamics for the Morris–Lecar model with delay. The most significant change would be expected for the full–2D model with delay. With different parameter sets from the one used here, the N–shape in the $\dot{V} = 0$ nullcline is more pronounced, and the system can admit up to three equilibria. In some cases the system is excitable, with a stable rest state, and an unstable excited state separated by an unstable saddle. Here, the stable manifolds of the saddle point (for $\tau = 0$) define a separatrix curve that distinguishes sub–from super–threshold initial conditions. By tuning the bifurcation parameter μ, a range of repetitive firing can be realised as the stable rest state and unstable saddle coalesce and disappear via a saddle–node bifurcation. As such, repetitive firing might even be achieved in the full–2D model (4.0.1) with zero time delay using such a parameter set. Considering $\tau > 0$ in such a case could lead to some interesting and more complex dynamics than those reported in Chapter 4.

The original Morris–Lecar model displays an impressive array of behavior, especially for a relatively simple model employing only two noninactivating conductances. Most research on the original model has focused on how the dynamics change as the applied current, I, is varied (*e.g.* [34, 39]). By treating I as a bifurcation parameter, the model exhibits excitable dynamics, multistability (bistability and tristability), and sustained oscillations (repetitive firing of action potentials). Further variations in dynamics occur with different parameter sets. Here, we only considered recurrent input due to synaptic feedback, studying the dynamics of the model as the feedback parameters μ and τ were varied. With no applied current, solutions of the system represent the natural response and evolution of the membrane potential over time. It would

be interesting to consider the combined effects of synaptic feedback along with external stimulus (non–zero applied current) on the Morris–Lecar model by treating μ, τ, and I as bifurcation parameters. This is an obvious extension to our investigation, given the significance of I in the bifurcation structure of the original model without delay. What would make such an investigation interesting is that, for certain parameter ranges, an applied current might counterbalance the effects of synaptic feedback. For example, consider the all–K$^+$ conductance system with inhibitory feedback. With $\mu < 0$, the $\dot{V} = 0$ nullcline in the (V, n)–plane is monotone decreasing on the interval of interest. As $\mu \to 0$, the nullcline is shifted to the left, thereby lowering the equilibrium voltage. If we add a positive applied current $I > 0$, the $\dot{V} = 0$ nullcline will shift vertically, thereby raising the equilibrium voltage of the system. Raising the equilibrium voltage in turn changes the values of the coefficients a, b, c, and d in the linearisation, which influences the parameter ranges where the model obeys the dynamics of Cases 1 and 2 of the Cooke–Grossman theory. Thus, adding a positive applied current in this case could change the long–term behavior of the model, and eliminate stability switching of (V^*, n^*) which would have occurred with $I = 0$. Also, the values of $\omega_{\pm}$ and hence $\tau_{n,1}$, $\tau_{n,2}$ $(n = 0, 1, \ldots)$ in ranges where Case 1 and Case 2 are satisfied would change as I is varied. Therefore, even if the external stimulus is inadequate to change the qualitative behavior of the model, it will influence the quantitative results by changing the delay times where stability changes in (V^*, n^*) occur.

In addition, the number of equilibria in each of the all–K$^+$ system, the all–Ca^{2+} system, and the full–2D model with delay may change as I is varied. For example, while the all–K$^+$ system with delay only admits at most a single

equilibrium point for all $\mu \in \mathbb{R}$, the system can admit multiple equilibria for non–zero I, which could lead to totally different dynamics in the system. Moreover, incorporating I into the single–ion conductance systems and full–2D model with delay might also alleviate some of the problems encountered with excitatory feedback. Recall that neither of the all–K^+ conductance system and full–2D model with delay possessed an equilibrium point for a range of excitatory feedback strength, which was suggested as a limitation of our model. However, considering non–zero I with μ in these range(s) can shift the $\dot{V} = 0$ nullcline so that these systems do admit one or more equilibrium points, which may be stable or unstable. This may provide us with a way of studying the dynamics of recurrent excitation as they are proposed in our model, without too much modification.

By reducing the 3D Morris–Lecar model with delay (1.3.5) to a 2D–system (4.0.1), the analysis of the model becomes more tractable while retaining many key qualitative features of the full model. However, it is natural to wonder how well the full–2D model approximates the full–3D model? Surely the quantitative results would be expected to differ between the 3D model and its 2D counterpart, since the calcium–activation time course is not assumed to be instantaneous in the full–3D model. A more important question is whether or not some new dynamical phenomena arise in the 3D system so that there is a significant difference in the qualitative dynamics of the two systems. Such a question can only be answered through a thorough investigation into the dynamics of the full–3D Morris–Lecar model with delay (1.3.5), and comparing them with the results for the full–2D model presented here. However, for the full–3D model the transcendental characteristic equation of the system would

be a degree–three trigonometric polynomial, which is more difficult to analyse than the degree–two trigonometric polynomial characteristic equation of the full–2D model.

In [33], Rinzel considers spatio–temporal distribution of voltage and ionic permeabilities in the Hodgkin–Huxley neuron model. In our present treatment of the Morris–Lecar model with delay, we have ignored spatio–temporal aspects of the muscle fibre membrane, and so our results describing the the voltage across the membrane apply only to a space–clamped patch of sarcolemma membrane. Also, a spatially uniform cell, or a network of identical, perfectly synchronized cells might be modeled using the methods discussed in this thesis. Consideration of such spatio–temporal aspects in conjunction with delayed recurrent feedback would result in a system containing a time–delayed non–local partial differential equation, and might make for an interesting future study.

The model studied here involves a DDE with a single discrete time delay. Employing this type of delay presupposes that the recurrent inhibitory/excitatory (feedback) pathways all operate with an identical time delay of τ ms. A more realistic treatment of time–delayed effects on our neuro–muscular feedback loop would involve the use of an integro– or distributed–delay differential equation, to account for distribution of axonal diametres, conduction pathway lengths, and synaptic transmission times. An appropriate modification of the original Morris–Lecar model incorporating these considerations would involve using a relation of the form

$$F(V(t-\tau)) = \mu \int_{-\infty}^{t} V(u-\tau)k(t-u)du \qquad (5.0.1)$$

for the feedback function, rather than simply $F(V(t-\tau)) = \mu V(t-\tau)$. In

(5.0.1), $k(x)$ is an appropriate kernel function describing the distribution of transmission times. While the model with this type of delay would be more realistic, analysis of the Morris–Lecar model with distributed delay would be more involved than the work presented here for the discrete delay case. Whether or not using a distribution of time delays rather than a single delay would produce different qualitative behavior has not been determined, and is an interesting topic for future consideration.

To study the full range of dynamics of our model, we only required that the time delay be positive, $\tau > 0$. Many models concerning delayed recurrent feedback have been developed with additional conditions placed on the time delay, the most common being that it exceed the relaxation time of the system being considered. Our objection to this is that the relaxation time of a physiological system modeled using the Morris–Lecar equations with delay would be highly parameter–specific, and rely on accurate estimation of numerous model parameters. A study only considering delays of a certain magnitude may not detect some important dynamics present for small time delays. For example, Plant [32] and Foss *et al.* [14] were mainly concerned with time delays greater than the duration of a single action potential. Plant asserts that the relaxation time of systems similar in form to (2.0.1), (3.0.1), and (4.0.1) is roughly measured by the quantity $\frac{1}{d}$, where $d = \overline{\lambda_n} \cosh\left(\frac{V^*-V_3}{2V_4}\right)$ for systems (2.0.1) and (4.0.1), and $d = \overline{\lambda_m} \cosh\left(\frac{V^*-V_1}{2V_2}\right)$ for (3.0.1). Imposing the restriction

$$\tau > \frac{1}{d}$$

on our model might not reveal the presence of some important dynamical phenomena. For example, consider the all–K$^+$ system (2.0.1). If $\mu < \mu^*$, the system is in Case 1, the equilibrium point (V^*, n^*) loses stability when $\tau = \tau^*$,

and a stable limit cycle emerges. The value of τ^* for a given $\mu < \mu^*$ is very small, so that $\tau^* < \frac{1}{d}$. Considering only those delays $\tau > \frac{1}{d} > \tau^*$ would reveal an unstable equilibrium point with a stable limit cycle oscillation, and so we would not observe the transition from a stable equilibrium point to a stable oscillation. Furthermore, for system (2.0.1) in Case 2 ($\mu^* < \mu < \mu^{**}$), the value of $\frac{1}{d}$ is greater than the delay marking the final change in equilibrium point stability, then an analysis of the model for delays $\tau > \frac{1}{d}$ would not reveal the stability switching properties of the model for increasing τ. We would only find a monostable system consisting of an unstable equilibrium and a stable limit cycle, and therefore would be unable to discern any qualitative change in behavior from Case 1 to Case 2. If in Case 2 the value of $\frac{1}{d}$ is below the final switching time then a few (but not all) of the stability switches would be detected by considering only $\tau > \frac{1}{d}$. Of course, with $\mu > \mu^{**}$, the results obtained by considering only $\tau > \frac{1}{d}$ would be the same as those for $\tau > 0$, since the qualitative behavior of the system with μ in this range does not change with increasing τ.

Similar comments can be made pertaining to the limitations resulting from such an analysis of the all–Ca^{2+} conductance system and full–2D models. In these cases, however, the dynamics observed would depend on the value of $\frac{1}{d}$ in relation not only to the delay times where changes in equilibrium point stability occur, but also to the value(s) of τ_{PSN}, where the system is believed to undergo PSNB(s). In these cases, regions of monostability or multistability for certain ranges of μ might not be detected by considering only $\tau > \frac{1}{d}$, and would not provide a complete picture of the model dynamics. Thus there would be pitfalls in not analysing the sub–systems and full–2D model for all

$\tau > 0$. In any case, we have seen that studying the equations with zero time delay can be useful in the analysis of delay–dependent stability of equilibria. Therefore, to study the systems analytically it behooves us to consider the full range of positive discrete time delays $\tau > 0$.

In their treatment of the dynamics of recurrent inhibition, Mackey and an der Heiden [29] employ a type of mixed feedback, by using a feedback function which is non–monotone. This corresponds to feedback which is neither purely positive or negative. The feedback function used in our model, $F(V(t - \tau)) = \mu V(t - \tau)$ is monotone increasing if $\mu > 0$, and monotone decreasing if $\mu < 0$, thereby permitting pure positive and negative feedback, respectively. As we have seen, the dynamics of recurrent excitation are somewhat questionable for the model in its present form, and we have identified this as a possible limitation of our Morris–Lecar model with delay. It might be interesting to study the delayed Morris–Lecar model with mixed delayed feedback, by using a non–monotone feedback function, for example the one used by an der Heiden in [2] given by

$$F(V(t - \tau)) = \mu \frac{V(t - \tau)}{1 + [V(t - \tau)]^n}, \quad n \geq 2. \tag{5.0.2}$$

Problems arose in the all–K^+ system and full–2D model with delay for $\mu > 0$ due to the appearance of the parameter μ in the denominator of the $\dot{V} = 0$ nullcline, for example

$$V(n) = \frac{g_L V_L + g_K V_K n}{g_L + g_K n - \mu}$$

for the all–K^+ system. Considering a feedback function of the form (5.0.2), with say $n = 2$, we obtain for the $\dot{V} = 0$ nullcline

$$n(V) = \frac{-g_L(V - V_K)(1 + V^2) + \mu V}{g_K(V - V_K)(1 + V^2)}.$$

This modification might allow us to study a model with fewer limitations and problems like those encountered with the model we propose here. Also, analysis of nonlinear DDEs with mixed feedback of type (5.0.2) have revealed a rich structure of bifurcating periodic solutions and deterministic chaos [2, 29]. Another interesting and physiologically relevant type of feedback we could study would be nonlinear mixed feedback with delay. In such a model, an example of a nonlinear feedback function would be $F(V(t-\tau)) = \mu \tanh(V(t-\tau))$.

When Morris and Lecar [24] developed their original model, they used linear relations for the instantaneous current–voltage curves through open–channels. However, in their own experiments with barnacle muscle fibre they found evidence for a nonlinear instantaneous Ca^{2+} current–voltage relation, and therefore used a suitable relation when analysing the all–Ca^{2+} conductance system. However, when considering the reduced–2D model with both conductance systems operational, they reverted back to the linear relations. The motivation behind this was supported by results which indicated that the operational K^+–conductance system is enough to keep the Ca^{2+}–system in the (nearly) linear region. In our analysis of the all–Ca^{2+} conductance system with delay we used the linear relation, because studying the all–Ca^{2+} with a nonlinear current–voltage relation (such as the one suggested by Morris and Lecar) would have not provided a clear indication of the contribution of the all–Ca^{2+} system to the full–2D model, which employed the linear relation. Nevertheless, it might be interesting to examine the all–Ca^{2+} system with delay using a nonlinear instantaneous current–voltage relation, to see if it adds to the already rich dynamics of that system. Also, including the effects of Ca^{2+}–ion

accumulation in the analysis of the all–Ca^{2+} conductance system with delay, as considered in the original Morris–Lecar study, may prove fruitful.

Also concerning the individual conductance systems, some authors [35] have suggested a modified potassium conductance system for models of Hodgkin–Huxley type to account for calcium ion activation. Experimental results [24] indicate evidence for such a Ca^{2+}–activated potassium conductance, which might easily be implemented into our model with delayed recurrent feedback.

In closing we comment on the applicability of our Morris–Lecar model with delay. The purpose of our investigation was to determine the effects of time–delayed synaptic input on the dynamics of a muscle fibre model with two noninactivating conductances. The original Morris–Lecar model as a mathematical means to study voltage oscillations in muscle fibre had predictive power, in that it was able to accurately describe many different, experimentally–observed voltage behaviors. The subsequent work of Rinzel and Ermentrout [34] successfully identified new complex behavior capable of the Morris–Lecar model. However, Morris and Lecar [24] point out that there are aspects of the barnacle fibre voltage behavior which their model (1.2.1) was unable to account for. These included a bistable oscillation pattern, as well as the sort of oscillations which start small and grow in amplitude. Our model (1.3.5) is an improvement of the original model since it is able to account for these complex voltage responses. Figures 4.7(f), 4.10(f), and 4.13(d) in Chapter 4 are numerical simulations of the full–2D Morris–Lecar model with delay (4.0.1) which represent voltage oscillations which start small and grow in amplitude, while Figure 4.14 of the same chapter demonstrates bistable voltage oscillations. Therefore, our modification of the Morris–Lecar equations enhances the predictive power of

the original model.

The real test of the predictive power of our model (1.3.5) would lie in comparing the results gathered here to empirical results collected from a suitably–designed experiment involving an appropriate neuro–muscular feed-back loop. We noted in the introduction (Chapter 1) that the constriction and dilation mechanisms which control the pupil–light reflex operate using a neuro–muscular feedback loop, and represents an actual physiological process to which our model might be applied. Applying a voltage–clamp to a patch of the muscle fibre of this loop along with the appropriate neural connections would provide an ideal set–up to test our results experimentally. However, it is not known whether the components of such a neuro–muscular feedback loop are amenable to voltage–clamp analysis. Alternatives to using a complete physiological feedback loop on its own could include using components from different loops for which voltage–clamp analysis is possible, or to artificially simulate the effects of delayed recurrent feedback in an experimental set–up like the one used by Morris and Lecar [24].

Bibliography

[1] U. an der Heiden, Delays in Physiological Systems, *Journal of Mathematical Biology*, **8** (1979) 345–364.

[2] U. an der Heiden, On the Dynamics of Nonlinear Feedback Loops in Cell Membrane, Neural and Sensory Systems, *Fields Institute Communications*, Volume **21** (1999) 259–268.

[3] R. Bellman, K.L. Cooke, "Differential-Difference Equations" *Mathematics in Science and Engineering* Volume 6, Academic Press, London (1963).

[4] S.A. Campbell, Stability and Bifurcation in the Harmonic Oscillator with Multiple, Delayed Feedback Loops, *Dynamics of Continuous, Discrete and Impulsive Systems*, **5** (1999) 225–235.

[5] S.N. Chow, Existence of periodic solutions of autonomous functional differential equations, *Journal of Differential Equations*, **15** (1974) 350–378.

[6] K.L. Cooke & Z. Grossman, Discrete Delay, Distributed Delay and Stability Switches, *Journal of Mathematical Analysis and Applications*, **86** (1982) 592–627.

[7] R. Datko, A Procedure for determination of the Exponential Stability of certain differential–difference equations, *Quarterly Applied Mathematics*, **36** (1978) 279–292.

[8] R.D. Driver, "Ordinary and Delay Differential Equations" *Applied Mathematical Sciences* **20**, Springer-Verlag, New York (1977).

[9] K. Engelborghs, V. Lemaire, J. Bélair, D. Roose, Numerical bifurcation analysis of delay differential equations arising from physiological modeling, *Journal of Mathematical Biology*, **42** (2001) 361–385.

[10] K. Engelborghs, T. Luzyanina, D. Roose, Numerical bifurcation analysis of delay differential equations using DDE-BIFTOOL, *ACM Transactions on Mathematical Software*, Volume 28, **1** (2002) 1–21.

[11] G.B. Ermentrout, *Simulating, Analyzing, and Animating Dynamical Systems: A Guide to XPPAUT for Researchers and Students*, Siam, Philadelphia (2002).

[12] R. FitzHugh, Thresholds and plateaus in the Hodgkin–Huxley nerve equations, *Journal of General Physiology*, **1** (1960) 867-896.

[13] R. FitzHugh, Impulses and physiological states in theoretical models of nerve membranes, *Biophysics Journal*, **1** (1961) 445-466.

[14] J. Foss, A. Longtin, B. Mensour, J. Milton, Multistability and Delayed Recurrent Loops, *Physical Review Letters*, Volume 76, **4** (1996) 708–711.

[15] B.C. Goodwin, in *Advances in Enzyme Regulation*, (G. Weber, editor) Volume **3**, Oxford: Pergamon Press (1965) 425.

[16] J. Guckenheimer, P. Holmes, *Nonlinear Oscillations, Dynamical Systems, and Bifurcations of Vector Fields*, Springer–Verlag, New York (1983).

[17] J.K. Hale, *Theory of Functional Differential Equations*, Springer, New York (1987).

[18] J.K. Hale, *Theory of Functional Differential Equations*, Springer–Verlag, New York (1977).

[19] J.K. Hale, H. Koçak, *Dynamics and Bifurcations*, Springer-Verlag, New York (1991).

[20] B.D. Hassard, N.D. Kazarinoff, Y.H Wan, *Theory and Applications of Hopf Bifurcation*, Cambridge University Press, Cambridge (1981).

[21] A.L. Hodgkin, A.F. Huxley, A quantitative description of membrane current and its application to conduction and excitation in nerve, *Journal of Physiology (London)*, **117** (1952) 500–544.

[22] J. Keener, J. Sneyd, *Mathematical Physiology*, Springer-Verlag, New York (1998).

[23] H.D. Landahl, Some conditions for sustained oscillations in biochemical chains with feedback inhibition, *Bulletin of Mathematical Biophysics*, **31** (1969) 775–787.

[24] H. Lecar, C. Morris, Voltage Oscillations in the Barnacle Giant Muscle Fiber, *Biophysical Journal*, Volume 35 (1981) 193–213.

[25] N.D. Kararinoff, Y.H. Yan, P. Van Den Driessche, Hopf Bifurcation and Stability of Periodic Solutions of Differential–difference and Integro–differential Equations, *J. Inst. Maths Applics*, **21** (1978) 461–477.

[26] A. Longtin, J.G. Milton, Modeling Autonomous Oscillations in the Human Pupil Light Reflex using Non–Linear Delay–Differential Equations, *Bulletin of Mathematical Biology*, Volume 51, **5** (1989) 605–624.

[27] N. MacDonald, Time delay in a model of biochemical reaction sequence with end–product inhibition, *Journal of Theoretical Biology*, **67** (977) 549–556.

[28] M.C Mackey, L. Glass, Oscillation and chaos in physiological control systems, *Science*, **197** (1977) 287–289.

[29] M.C. Mackey, U. an der Heiden, The dynamics of recurrent inhibition, *Journal of Mathematical Biology*, **19** (1984) 211–225.

[30] J. Murray, "Mathematical Biology" *Biomathematics Texts*, Volume 19, Springer-Verlag, New York (1989).

[31] J. Nagumo, S. Arimoto, S. Yoshizawa, An active pulse transmission line simulating nerve axon, *Proceedings IRE*, **50** (1964) 2061-2070.

[32] R.E. Plant, A FitzHugh Differential–Difference Equation Modeling Recurrent Neural Feedback, *SIAM Journal on Applied Mathematics*, Volume 40, **1** (1981) 150–162.

[33] J. Rinzel, "Models in Neurobiology", *Mathematical Aspects of Physiology*, Lectures in Applied Mathematics, Volume 19, American Mathematical Society (1981) 281–297.

[34] J. Rinzel, G.B. Ermentrout, "Analysis of Neural Excitability and Oscillations", *Methods in Neuronal Modeling*, The MIT Press, Massachusetts (1990) 135–170.

[35] M.E. Rush, J. Rinzel, The Potassium A–Current, Low Firing Rates and Rebound Excitation in Hodgkin–Huxley Models, *Bulletin of Mathematical Biology*, Volume 57, **6** (1995) 899–929.

[36] L.F. Shampine, S. Thompson, Solving Delay Differential Equations with dde23 (available on–line), (2000).

[37] L.P. Shayer, S.A. Campbell, Stability, Bifurcation, and Multistability in a System of Two Coupled Neurons with Multiple Time Delays, *SIAM Journal on Applied Mathematics*, **61** (2000) 673–700.

[38] A.N. Tikhonov, On Systems of Equations Containing Parameters (In Russian), *Mater. Sb.*, **27** (1950) 147.

[39] K. Tsumoto, T. Yoshinaga, K. Aihara, H. Kawakami, Bifurcations in Morris–Lecar neuron model, *Proceedings of the International Symposium on Nonlinear Theory and its Applications* (2002).

[40] J. Wei, S. Ruan, Stability and bifurcation in a neural network model with two delays, *Physica D*, **130** (1999) 255–272.